On the Spectrometry of Laser-Accelerated Particle Bunches and Laser-Driven Proton Radiography

Matthias Würl

On the Spectrometry of Laser-Accelerated Particle Bunches and Laser-Driven Proton Radiography

Matthias Würl

DISSERTATION

an der Fakultät für Physik

der Ludwig-Maximilians-Universität München

vorgelegt von

Matthias Würl

geboren in Regensburg

München, den 9. August 2018

Erstgutachter: Prof. Dr. Katia Parodi

Zweitgutachter: Prof. Dr. Thomas Kuhr

Tag der mündlichen Prüfung: 14. September 2018

Zusammenfassung

Die vermehrte Verfügbarkeit von Hochleistungslasersystemen mit relativ hohen Puls-wiederholungsraten ($\sim 1\,\text{Hz}$), wie beispielsweise im Centre for Advanced Laser Applications (CALA), öffnen neue Wege für Anwendungen von Laser-Ionen-Beschleunigung, die über die Grundlagenforschung hinausreichen. Da sich die erzielten Energien von laser-beschleunigten Protonen den $100\,\text{MeV}$ annähern, steigt das Interesse an biomedizinischen Anwendungen wie beispielsweise Kleintierbestrahlungen und Bildgebung von biologischen Proben. Die Eigenschaften solcher laser-beschleunigter Ionenpulse sind einzigartig verglichen mit konventionell beschleunigten Teilchen von elektrostatischen oder von Beschleunigern basierend auf elektromagnetischen Wechselfeldern. Zu den Merkmalen zählen die hohen Intensitäten ($\sim 10^9\,\text{Protonen/ns}$), ein breites Energiespektrum ($\sim 100\%$) und der starke elektromagnetische Puls, der in der Laser-Plasma-Interaktion erzeugt wird. Aufgrund dieser besonderen Eigenschaften sind herkömmliche Strahlüberwachungssysteme, wie beispielsweise in klinischen Ionenstrahleinrichtungen eingesetzt, nicht geeignet. Bisher ist kein System verfügbar, welches eine Echtzeitstrahlüberwachung parallel zu einer Anwendung erlaubt.

Im Zuge dieser Arbeit wurden zwei Ansätze zur Charakterisierung laser-beschleunigter Protonenpulse hinsichtlich ihres Energiespektrums untersucht. Prototypen wurden entwickelt und getestet. Der erste Ansatz basiert auf der Flugzeitmessung (time-of-flight - TOF). Die kontinuierliche Energieverteilung wird aus dem gemessenen TOF-Signal herausgefaltet. Dieses wird mit Hilfe eines neuartigen dünnen Siliziumdetektors aufgezeichnet, der dem zeitlich auseinanderlaufenden polyenergetischen Protonenpuls exponiert ist. Die Ansprechfunktion des Detektors und der zugehörigen Ausleseelektronik wird hierbei berücksichtigt. Messungen wurden im Energiebereich bis $20\,\text{MeV}$ mit nanosekunden-kurzen und passiv Energie-modulierten Protonenpulsen eines Tandem-Beschleunigers, sowie mit laser-beschleunigten Protonenpulsen am Laboratory for Extreme Photonics, durchgeführt. Vielversprechende Übereinstimmungen wurden beim Vergleich der rekonstruierten Energieverteilung zu Monte-Carlo Simulationen und zu Messungen mit Hilfe eines Magnetspektrometers gefunden. Für den getesteten Energiebereich und TOF-Distanzen waren die Abweichungen zwischen Rekonstruktion und Erwartungen bei Teilchenzahl und mittlerer Energie kleiner als 12%, beziehungsweise 2%.

Im zweiten untersuchten Aufbau wurde die Sensorchipkante des hybriden Pixeldetektors Timepix mit Protonen im Energieintervall zwischen 17 und $20\,\text{MeV}$ bestrahlt. Räumliche Information entlang einer Achse senkrecht zur Strahlrichtung wurde aufgrund der Pixelierung des Detektors erhalten. Dieser spektrometrische Aufbau ist nur für niedrige Protonenfluenzen ($< 7 \times 10^3\,\text{Protonen/cm}^2$) pro Aufnahmebild, welche weit unter typischen Fluenzen in Laser-Ionen-Beschleunigung liegt, geeignet. Dennoch kann die in dieser Arbeit entwickelte Rekonstruktionsmethode für andere Detektortypen, mit höherer Sätti-

gungsgrenze als der Timepix-Detektor, angewandt werden.

Da diese Dissertation das Ziel einer biomedizinische Anwendung von laser-beschleunigten Protonenpulsen verfolgt, wurde eine Studie durchgeführt um die Machbarkeit von laserbeschleunigter Protonenradiographie von Millimeter- bis Zentimeter-großen Objekten und pixelierten Halbleiterdetektoren zu eruieren. Der Energiebereich der polyenergetischen Protonenpulse war hierbei bis 20 MeV und bis 100 MeV. Die Studie basiert auf Monte-Carlo Simulationen und wurde durch ein Proof-of-Principle Experiment mit einem Energie-modulierten Protonenstrahl von einem Tandembeschleuniger unterstützt. Die gefundene räumliche Auflösung und die Dichteauflösung war im sub-Millimeterbereich, bzw. besser als 3% für alle in dieser Studie getesteten Objekte und für die optimierten geometrischen Abstände.

Aufgrund der vielversprechenden Ergebnisse, die im Zuge dieser Arbeit gewonnen wurden, wird das Flugzeitspektrometer als diagnostisches System für die Laser-Ionen-Beschleunigung an CALA in naher Zukunft eingesetzt. Desweiteren ist ein Aufbau zur Bildgebung mittels laser-beschleunigter Protonen und einem pixelierten Siliziumdetektor, basierend auf den in dieser Arbeit erzielten Ergebnisse, vorgesehen.

Abstract

The increased availability of high-power laser systems operating with relatively high repetition rates ($\sim 1\,\mathrm{Hz}$), such as installed in the upcoming Centre for Advanced Laser Applications (CALA), are pushing laser-driven ion acceleration towards applications beyond fundamental research. With energies of laser-accelerated protons approaching $100\,\mathrm{MeV}$, great interest in the community is devoted to biomedical applications like small-animal irradiation and imaging of biological samples. Such laser-accelerated ion bunches exhibit unique properties as compared to conventionally accelerated particles from electrostatic or radio-frequency driven accelerators. Among these characteristics are high beam intensities ($\sim 10^9$ protons/ns), a broad energy distribution ($\sim 100\%$) and a strong electromagnetic pulse generated in the laser-plasma interaction. Due to these peculiar properties, conventional beam monitoring devices as installed e.g. in clinical ion beam facilities are not suitable for the characterization of laser-accelerated ion bunches and no system is available to date allowing for online beam monitoring simultaneous to an application.

Within the framework of this thesis, two approaches for characterization of laser-accelerated proton bunches in terms of energy spectrum have been investigated and prototype systems have been developed and tested. The first setup is based on the time-of-flight (TOF) technique. The continuous energy distribution is deconvolved from the TOF signal current measured by a novel thin silicon detector which is exposed to temporally divergent polyenergetic proton bunches, taking into account the finite response function of the detector and the associated readout electronics. Measurements were performed in the energy range up to $20\,\mathrm{MeV}$ using nanosecond-short and passively energy-modulated proton bunches from a Tandem accelerator, as well as using laser-accelerated proton bunches obtained in experiments at the Laboratory for Extreme Photonics. A comparison of the reconstructed energy spectra to Monte Carlo simulations and measurements using a magnetic spectrometer has shown promising agreement. In the studied energy range and for the tested TOF distances, the reconstructed particle number and the mean reconstructed energy agreed with expectations within 12% and 2%, respectively.

In the second investigated setup, the sensor chip of a hybrid pixel detector Timepix was irradiated edge-on with protons in the energy interval between 17 and $20\,\mathrm{MeV}$. Spatial information along one axis perpendicular to the proton beam direction was obtained due to the pixelation of the detector. Although this spectrometric setup is only suitable for low proton fluences ($< 7 \times 10^3$ protons/cm^2) per acquisition frame, which is far below typically obtained fluences from laser-ion acceleration experiments, the developed spectrum reconstruction method could be applied to other detector types providing a higher saturation limit than the used Timepix detector.

As this thesis is dedicated to biomedical applications using laser-accelerated proton bunches, a feasibility study was performed to assess the applicability of laser-driven pro-

ton radiography of millimeter to centimeter sized objects using pixelated semiconductor detectors and polyenergetic proton bunches in the energy ranges up to 20 MeV and up to 100 MeV. The study was based on Monte Carlo simulations and was supported by a proof of principle experiment with an energy-modulated proton beam from a conventional Tandem accelerator. Sub-mm spatial resolution and density resolution below 3% were found for all objects investigated within this study and the optimized geometric distances. Motivated by the promising results obtained within this thesis, the TOF spectrometer will be implemented as diagnostic device in the laser-ion acceleration setup at CALA in the near future. Moreover, a radiographic imaging setup using laser-accelerated proton bunches and pixelated silicon detector, based on the results obtained within this thesis, is foreseen.

Contents

List of Figures

List of Tables

Introduction

In 1960, Theodore H. Maiman at the Hughes Research Laboratories in Malibu, California, presented the first functional laser (**l**ight **a**mplification by **s**timulated **e**mission of **r**adiation), using a ruby crystal as its gain medium [Maiman, 1960]. His work was based on previous theoretical considerations, stating that *"the prospect is favorable for masers which produce oscillations in the infrared or optical regions"* [Schawlow and Townes, 1958]. This invention provided numerous scientific (and technological) possibilities, impossible to reach with any other man-made light source before.

Another milestone of applied physics, yet in an entirely different field, happened only a few years earlier and about $600\,\mathrm{km}$ further north. At Lawrence Berkeley Laboratory, the first human cancer patient received treatment with protons in 1954 [Tobias et al., 1958], encouraged by the proposal of Wilson [1946] that the properties of fast protons *"make it possible to irradiate intensely a strictly localized region within the body, with but little skin dose"*.

Driven by amongst others the interest in laser-induced nuclear fusion, research and development in laser technology advanced quickly within the following decades and new gain media allowed for more and more powerful laser systems. However, the damage threshold of optics and gain medium to high laser peak intensities damped the rapid increase in laser intensity. A new era was initiated by the invention of chirped pulse amplification (CPA) [Strickland and Mourou, 1985]. Table-top laser systems were then capable of delivering intensities almost $10^5 - 10^6$ times higher than in the pre-CPA era [Mourou et al., 2006]. Around the year 2000, several groups reported the acceleration of protons by high-power laser systems [Hatchett et al., 2000; Snavely et al., 2000; L. Clark et al., 2000; Maksimchuk et al., 2000]. By focusing multi-TW to PW class lasers onto thin solid targets, peak intensities in the order of $10^{20}\,\mathrm{W\,cm^{-2}}$ could be achieved and protons were accelerated from the laser-induced plasma.

Also around the turn of the millennium, developments in ion beam therapy gave rise to treatment modalities achieving an excellent dose conformity within the targeted tumor volume. Several companies became interested in this technology and many new clinical

ion beam therapy facilities have been built within the following years. Soon, the number of ion beam facilities for cancer treatment will exceed 100 [PTCOG]. Nevertheless, such high dose conformity can only be fully exploited, if the targeted volume is accurately covered. Misalignment of the patient on the treatment table or changes in the patient anatomy over the several weeks long treatment cycles are possible obstacles in achieving this goal. Another source of uncertainty is due to the fact that the treatment planning is done based on volumetric images acquired with x-ray CT (computed tomography) scanners. However, the energy loss of protons in tissue and x-ray attenuation are two entirely different physical processes. Established empirical conversion curves from x-ray Hounsfield Units (HU) to proton stopping power relative to water can thus result in additional range uncertainties of the proton beams. This adds up to a total range uncertainty of almost 3% [Paganetti, 2012]. One approach to circumvent this problem is to use proton CTs, such that the treatment can be planned on volumetric images inherently showing the proton energy loss relative to water. Moreover, proton radiography could prove beneficial for low-dose position verification prior to each treatment session.

At this point, the two research fields of modern and applied physics slowly started converging. Encouraged by the first measurement of fast laser-accelerated protons and theoretical scaling laws predicting proton energies far beyond 100 MeV being achievable in the near future, several groups started to investigate the feasibility of laser-induced proton therapy. They proposed visionary concepts of how facilities and treatment with laser-accelerated protons could look like (e.g. Malka et al. [2004]; Schell and Wilkens [2009]; Hofmann et al. [2011]). Nevertheless, besides the challenge of reaching ion energies sufficient to penetrate far enough into tissue for treating also deep-seated tumors, several issues regarding for instance beam stability and reproducibility, as critically pointed out in Linz and Alonso [2007, 2016], still remain to be solved. However, the unique features of laser-accelerated ions open up new possibilities for radiobiological studies, like investigating the dose-rate dependence when irradiating cancerous cells with such short and intense ion bunches [Bin et al., 2012].

At the research campus in Garching, the new Centre for Advanced Laser Applications (CALA) has recently been opened and will soon be ready for experiments. It is equipped with a 3 PW Ti:sapphire based laser system, the ATLAS-3000 (Advanced Titanium-Sapphire Laser), which is an upgrade of a 300 TW laser system formerly operational at the Laboratory for Extreme Photonics (LEX Photonics) in the neighboring building. As already denoted in its name, this facility is dedicated to applications [Lindner et al., 2017]. With ion energies expected at this facility reaching 100 MeV/n and a repetition rate of 1 Hz, radiobiological experiments with laser-accelerated ion bunches on small-animal models become possible. For reliable and quantitative results of such experiments, accurate and precise knowledge of the characteristics of these bunches is absolutely required on a shot-to-shot basis.

1.1 Envisioned Applications

Within this thesis, two crucial steps towards quantitative irradiation experiments using laser-accelerated ion bunches in this energy range are tackled.

As already pointed out previously, an absolute requirement for such experiments is a comprehensive characterization of the laser-accelerated ion bunches. One of the most important quantities in this context is the spatial distribution of the dose delivered to the investigated object. However, *in-vivo* dose measurement is not possible in most cases, hence the determination of the transversal distribution of the ion fluence and their kinetic energies can serve as a good substitute. The ideal detection system for such a task should therefore be position sensitive and used in transmission prior to the application. That implies that the material budget of this detector needs to be as small as possible to keep perturbation of the ion beam low. Of course, relatively high repetition rates can only be exploited, if the detection system provides feedback on the measured quantities in (almost) real-time. It is worth mentioning that a diagnostic device with such specifications is not only interesting for radiobiological studies, but can be of interest for any other application relying on laser-accelerated ions, where knowledge of their spatial and spectral distribution is required. Furthermore, for a sample the experimenter wants to irradiate, also its internal structure and its position with respect to the beam may be of importance. This is especially relevant in case of irradiation of a small-animal model.

A possible imaging setup related to future biomedical applications at CALA is therefore studied within the framework of this thesis. A simplified sketch of such a setup is shown in figure 1.1. The high-power laser is focused onto a thin foil target, turning it into a plasma from which electrons and ions are accelerated. The highly divergent beam propagates unperturbated up to a few meters in the experimental vacuum chamber, before leaving it through a thin vacuum window. There, a thin pixelated silicon detector is used in time-of-flight configuration to determine the spatially resolved kinetic energy distribution on a shot-to-shot basis. With a sufficiently small detector thickness, an application in transmission is possible without significantly perturbating the initial ion bunch. After passing the time-of-flight detector, the ion bunch reaches an object of interest, seated on a movable and rotatable table. From the initial polyenergetic ion spectrum, only ions with an energy sufficient to entirely penetrate the object can be detected by a further pixelated detector on the downstream side of the object. The second detector then gives a spatially resolved signal, proportional to the energy deposited by the residual proton bunch.

Based on this detector signal and in a first approximation, the total proton energy loss along straight lines connecting the target and the object can then be calculated and converted into a quantity of interest for medical radiation physics, the water-equivalent thickness or the proton stopping power relative to water. By rotating the object for at least 180°, this radiographic approach could then even be extended to proton computed tomography.
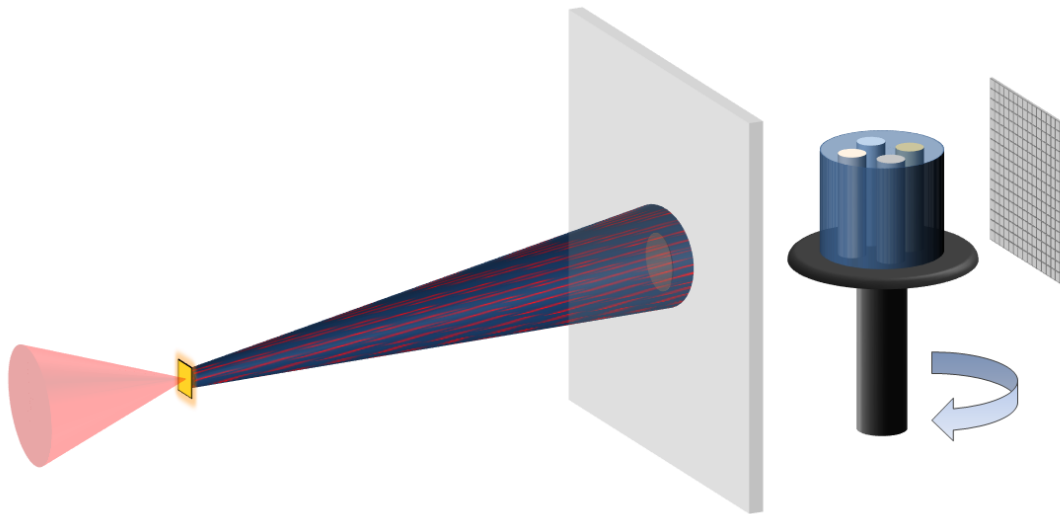
Figure 1.1: Simplified sketch of the envisioned setup for proton imaging using laser-accelerated protons. The laser (red) is focused onto a target foil (yellow), which is turned into a plasma from which ions and electrons (red-blue cone) are accelerated. A thin and pixelated silicon time-of-flight detector determines the energy and spatial distribution of the ion bunch. The object of interest (blue cylinder with inserts) is seated on a rotatable table. Low-energetic ions are stopped within the object, while high-energy particles reach a pixelated detector downstream of the object and carry information on its internal structures.

While the imaging setup relies on the unperturbated divergent ion beam, many other applications may require dedicated beam focusing devices based on magnetic quadrupole lenses or solenoids (see, for instance Busold et al. [2015]; Rösch et al. [2017]). Also in such applications, the use of an online transmission beam monitoring system based on the time-of-flight technique may be of great interest.

1.2 Outline of the Thesis

This work is an interdisciplinary project, involving various fields of modern physics. **Chapter 2** therefore provides a brief overview of the three topics relevant to this thesis, namely the mechanisms of laser-ion acceleration, the interaction of ionizing radiation with matter and fundamental properties of semiconductor detectors.

Several different types of diagnostic devices are currently used for the characterization of laser-accelerated ion bunches. The most common offline and online detection systems and recent developments are reviewed in **chapter 3**, showing the need for further improvements. Also, the state-of-the-art in proton radiography is presented, focusing on radiographic approaches that do not rely on the tracking of single particles.

Both Monte Carlo simulations and experiments were performed in the framework of this thesis. Materials and methods relevant throughout this work are introduced in **chapter 4**, starting with a description of the FLUKA Monte Carlo code. The three types of detectors used in the experimental parts of this project are presented, highlighting their main features and characteristics. Furthermore, the experimental facilities where most

of the experiments were performed are described. These feature the electrostatic Munich Tandem Van de Graaff accelerator, ion acceleration driven by the ATLAS-300 laser at LEX Photonics and the more compact and lower power ZEUS laser system.

One of the major goals of this project is the development of accurate time-of-flight spectrometry of laser-accelerated ion bunches, using semiconductor detectors. A preparatory step to achieve this goal is a thorough characterization of such detectors assessing their suitability for time-of-flight spectrometry of protons in the (near-)relativistic energy range. Especially, their timing properties are crucial for a possible implementation as diagnostic device. Characterization experiments and their results are presented and discussed in **chapter 5**.

Chapter 6 is dedicated to online time-of-flight spectrometry of short, polyenergetic proton bunches. A detailed description on how the spectrum is reconstructed from the measured time-of-flight signal current is provided. This is followed by showing experimental results obtained with conventionally accelerated quasi-mono- and polyenergetic proton bunches, as well as with laser-accelerated protons. The achievable accuracy is discussed and possible further improvements in future diagnostic devices are given.

A different approach for online spectrometry of a polyenergetic ion bunch is presented in **chapter 7**. It is based on edge-on irradiation of the sensor chip of the hybrid pixel detector Timepix. For calibration purposes, the energy deposition of individual protons penetrating the sensor chip parallel to the detector front surface was measured at the Tandem accelerator for proton energies up to 20 MeV. Based on these measured tracks at known energy, a method to extract spectral and 1D spatial information from an unknown polychromatic proton distribution is established.

Characterization of laser-accelerated ion bunches is driven by the goal to use such bunches for applications. In **chapter 8**, a detailed Monte Carlo study investigating the feasibility of quantitative proton radiography with laser-accelerated ion bunches is performed in energy ranges up to 20 MeV and up to 100 MeV. Two available pixelated silicon detectors are modeled as imaging detectors in the simulation geometry. Various parameters are varied within these investigations to obtain information on achievable spatial and density resolution. Results from a proof-of-principle experiment with an energy-modulated proton beam at the Tandem accelerator are also shown.

Finally, the main results of this thesis are summarized in **chapter 9**. A conclusion is drawn and perspectives for further developments are given, both on a short and on a longer time scale.

CHAPTER **2**

Theoretical Background

The interdisciplinary nature of the studies performed in the framework of this thesis involves various fields of modern physics. The addressed topics include plasma physics and the interaction of intense laser pulses with matter, giving rise to laser-ion acceleration. Moreover, the interaction of ionizing radiation with matter, which is fundamental in medical physics and for transmission imaging, is a substantial part of this project. Last but not least, radiation detection using semiconductor detectors is of great importance for the experiments presented thereafter. This chapter is intended to give an introduction to these three topics. For a deeper insight to the topics, references to literature are given where appropriate.

2.1 Laser-Driven Ion Acceleration

In this section, a brief overview of the fundamentals of the interaction of highly intense and ultra-short laser pulses with matter, and the resulting laser-ion acceleration process, is given. Special emphasis is set on the unique features of laser-accelerated particle bunches as compared to ion bunches from conventional accelerators. As this work is focused on the characterization of laser-accelerated ions from solid targets, this overview is restricted to interactions and mechanisms relevant in this context. A more elaborate description on this acceleration mechanism can be found in existing literature, e.g. in Gibbon [2005], Daido et al. [2012] and Macchi et al. [2013].

High-power laser systems delivering laser pulses with peak powers in the TW or even PW regime provide peak intensities required for particle acceleration processes. The invention of chirped pulse amplification (CPA) [Strickland and Mourou, 1985] provided the key technology to produce intensities sufficient for relativistic electron motion. By temporal stretching of the initially short ($\sim$ fs) laser pulse to several hundreds of ps before entering the gain medium, the peak intensity within the amplifier remains below its damage threshold. After amplification, the long pulse is re-compressed to obtain a pulse duration typically in the order of a few tens to hundreds of femtoseconds.

The specified duration of the laser pulse only holds for the main peak intensity. In practice, such short pulses are accompanied by a pedestal that can extend over several hundreds of ps. This pedestal originates from unavoidable amplified spontaneous emission (ASE), which is caused by spontaneously emitted light, amplified in the gain medium. Moreover, several pre-pulses can be present picoseconds before the main pulse. They are caused by imperfections of optical elements causing spurious reflections. The ratio between the intensity of the main pulse and pre-pulses is denoted by the *temporal laser contrast* or *pulse contrast*. A high laser contrast is essential for efficient laser-ion acceleration employing thin target foils, as otherwise pre-expansion starts prematurely. The contrast can be improved by the use of double plasma mirrors [Wittmann et al., 2006; Speicher et al., 2018].

Regardless of the target material exposed to the highly intense laser pulse, the most abundant ion species in laser-ion acceleration experiments are protons. These protons often originate from thin surface contamination layers (mainly water and hydrocarbons) on the target foils. If laser-acceleration of heavier ions is desired, their contribution can be reduced by dedicated heating of the target [Hegelich et al., 2002].

Currently achievable laser intensities are not sufficient to accelerate the inertial ions directly. Therefore, laser-ion acceleration is a two-step process. Followed by ionization, electrons (as mediator) absorb energy from laser, create a charge separation field which in turn accelerates the more inertial ions.

2.1.1 Ionization of a Solid Target

The ionization of matter by single photons via the photoelectric effect is only possible for photon energies $\hbar\omega_{ph}$ exceeding the work function (electron binding energy) of that material. Values of the photoelectric work function for metals are typically around 4 to 5 eV [Tipler and Llewellyn, 2003]. They are hence larger than e.g. photon energies from a Ti:sapphire laser ($\lambda_L = 800\,\text{nm}$), where $\hbar\omega_L = 1.55\,\text{eV}$.

Nevertheless, at high laser intensities ($I_L > 10^{10}\,\text{W}\,\text{cm}^{-2}$) it is likely that electrons absorb several low-frequency photons, resulting in an energy larger than the work function [Gibbon, 2005]. This ionization mechanism is therefore called *multiphoton ionization*.

With laser intensities I_L slowly approaching the atomic intensity I_a,

$$I_a = \frac{\epsilon_0 c E_a^2}{2} \tag{2.1}$$

which is the intensity where the laser field equals the electric field strength of the atom E_a, the Coulomb field that binds the electrons to their nuclei is strongly distorted by the laser field. The speed of light in vacuum and the vacuum permittivity are denoted by c and ϵ_0, respectively. The Coulomb potential, $V_C(x) = -\frac{1}{4\pi\epsilon_0}\frac{Ze^2}{|x|}$ at position x, modified by the strong electric field of the laser $V_L(x) = -eE_L x$, results in an effective potential that can be written as

$$V(x) = -\frac{1}{4\pi\epsilon_0}\frac{Ze^2}{|x|} - eE_L x \ , \tag{2.2}$$

where e is the elementary charge. Thus, the potential barrier is lowered by $eE_L x$, and electrons may quantum-mechanically tunnel through the barrier with a finite probability. This mechanism is called *tunnel ionization*. A useful measure for the transit between multiphoton ionization to tunneling ionization is the Keldysh parameter [Keldysh, 1965]

$$\gamma_K = \omega_L \sqrt{\frac{2V_{ion}}{I_0}} \approx \sqrt{\frac{V_{ion}}{\Phi_{pond}}} \ , \tag{2.3}$$

where

$$\Phi_{pond} = \frac{e^2 E_L^2}{4 m_e \omega_L^2} \propto I_L \lambda_L^2 \tag{2.4}$$

is the ponderomotive potential of the laser field, which is the cycle-averaged kinetic energy of an oscillating free electron. Here, m_e and ω_L are the electron mass and the laser frequency, respectively, and V_{ion} is the ionization potential of the electronic state. For large laser intensities I_L and long wavelengths λ_L, $\gamma_K < 1$ and tunneling dominates, while multiphoton ionization applies for $\gamma_K > 1$.

With further increase of the intensity, the barrier falls below V_{ion} and electrons can escape without tunneling. This mechanism is referred to as *barrier suppression ionization*. Once enough electrons have been released from their atoms, *collisional ionization* becomes predominant compared to the aforementioned field ionization processes [Gibbon, 2005].

2.1.2 Absorption of the Laser Pulse in the Plasma

For describing the absorption of the laser pulse in a plasma, it is convenient to introduce the dimensionless parameter

$$a_0 = \frac{e|\vec{E}_0|}{m_e c \omega_L} = \sqrt{\frac{I_0}{I_1}} \tag{2.5}$$

with

$$I_1 = 1.37 \times 10^{18} \, \mathrm{W\,cm^{-2}} \left(\mu m \, \lambda_L^{-1} \right)^2 \tag{2.6}$$

I_0 and E_0 are the laser peak intensity and the electric field, respectively. For circular polarization, the value of I_1 is twice as large.

For $a_0 > 1$, i.e., at $\lambda_L = 800 \, \mathrm{nm}$ and for laser intensities $I_0 > 1.71 \times 10^{18} \, \mathrm{W\,cm^{-2}}$, a considerable number of plasma electrons is accelerated up to relativistic energies. The plasma is hence called *relativistic plasma* and is typically considered collisionless [Daido et al., 2012; Pegoraro et al., 2005].

In contemporary laser-ion acceleration experiments, the energy of the laser field cannot be directly transferred to the ions. Instead, the particles with the largest charge-to-mass ratio, i.e. electrons, are accelerated first and give rise to charge separation fields responsible for the ion acceleration. This can be easily seen when regarding a_0 and I_1 for ions, which can be done by replacing m_e by the ion mass m_{ion}. In order to obtain $a_{ion} > 1$, an irradiance of $I_{ion} \approx 5 \times 10^{24} \, \mathrm{W\,cm^{-2}} \left(\mu m \, \lambda_L^{-1} \right)^2$ would be required for protons, which is

far beyond currently achievable laser intensities [Daido et al., 2012].

When deriving the equation of motion from the Lorentz force for single electrons in a plane electromagnetic wave, it can be seen that electrons only move during the laser-electron interaction. Hence, electrons would not gain any net kinetic energy in this simple picture. However, in a dense plasma, this *Woodward theorem* does not apply and electrons can gain considerable momentum. As already mentioned, the light electrons are pushed forward, while the heavier ions respond much slower. This results in a transverse oscillation of the electron density n_e with the plasma frequency ω_P

$$\omega_P = \sqrt{\frac{n_e e^2}{\epsilon \gamma m_e}} \ , \tag{2.7}$$

where ϵ denotes the dielectric constant of the plasma and $\gamma = 1/\sqrt{1 - \frac{v^2}{c^2}}$ is the relativistic Lorentz factor. That way, charge-separation fields are created between the displaced electrons and the remaining ions.

From the dispersion relation for electromagnetic waves in a collisionless plasma [Swanson, 2012],

$$c^2 k^2 = \omega_L^2 - \omega_P^2 \ , \tag{2.8}$$

it is evident that the electromagnetic wave can only propagate for plasma frequencies $\omega_P < \omega_L$. Plasmas with densities below the *critical density n_{crit}*,

$$n_{crit} = \frac{\epsilon_0 \gamma m_e \omega_L^2}{e^2} \approx 1.1 \times 10^{21} \gamma \left(\frac{\lambda_L}{\mathrm{\mu m}} \right)^{-2} \mathrm{cm}^{-3} \ , \tag{2.9}$$

are thus called *underdense plasmas*, whereas plasma densities $n_e > n_{crit}$ are referred to as *overdense plasmas*. In case of fully ionized solid targets, plasma densities are larger than the critical density for optical wavelengths.

It is worth mentioning the different mechanisms for laser energy absorption by plasma electrons. At moderate laser intensities ($I\lambda_L^2 \sim 10^{12} - 10^{17} \, \mathrm{W\,\mu m^2\,cm^{-2}}$), i.e. before the peak intensity is reached, absorption is dominated by *inverse bremsstrahlung* and *resonant absorption*. With increasing intensity, *vacuum heating*, *Brunel absorption* or $\vec{j} \times \vec{B}$ *heating* become more and more important for the energy transfer of the laser field to the electrons. For more details, the reader is referred to Daido et al. [2012].

2.1.3 Ion Acceleration

Figure 2.1 illustrates two scenarios of how the ions can gain energy and the influence that the laser contrast has. In the case of high prepulse intensities, plasma expansion and even ion acceleration will already occur before the arrival of the main pulse and the high peak intensity itself is not exploited. Conversely, for high contrast, i.e. low prepulse intensity, the electron cloud remains more compact and the plasma can be pushed by the transferred radiation pressure.
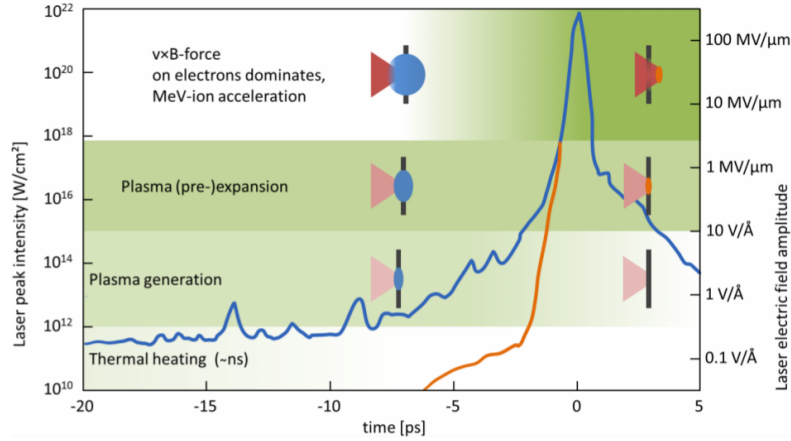
Figure 2.1: Temporal profile of the laser intensity as a function of time relative to the arrival of the main pulse. Different stages of the ion acceleration are sketched schematically. The blue curve corresponds to a typical temporal intensity profile for target normal sheath acceleration (TNSA). For radiation pressure acceleration (RPA), an intensity profile as sketched in orange is required. From Schreiber et al. [2016a].

The here described and more mechanisms for ion acceleration have been proposed and studied both experimentally and in particle-in-cell (PIC) simulations. They are typically relying on the interaction of an ultra intense laser pulse focused on an initially solid density target, which is quickly turned into a plasma according to the previously described ionization processes. The solid target itself can be a metallic or plastic foil of several nm to µm thickness. Note that the relevant acceleration regime strongly depends on both laser and target parameters and borders between different regimes are not sharp [Daido et al., 2012].

In the following, the most prominent and most investigated acceleration mechanism, the *target normal sheath acceleration (TNSA)*, and the regime that becomes of special interest at extremely high laser irradiance, *radiation pressure acceleration (RPA)*, are briefly introduced. A contemporary overview of experimentally obtained ion spectra is given at [ALPA].

Target Normal Sheath Acceleration (TNSA)

The predominant acceleration regime in contemporary laser-ion acceleration experiments is the TNSA mechanism [Macchi et al., 2013]. It was first introduced in 2001 by Wilks et al. [2001] explaining previously obtained experimental results (e.g. Snavely et al. [2000]).

A sketch of the TNSA mechanism is shown in figure 2.2. Briefly, the prepulse or the rising edge of the main pulse rapidly ionizes atoms on the front surface of the target. The resulting front surface plasma is heated by the aforementioned energy absorption processes and the generated *hot electron cloud* with electron temperature T_e (in eV) spreads through the target. While the hot electrons are able to entirely penetrate the overdense region of the target, the foil still remains opaque for the laser pulse itself.

The hot electron cloud then extends out of the target, forming a so-called plasma sheath

(a) Acceleration Mechanisms   (b) TNSA Spectrum
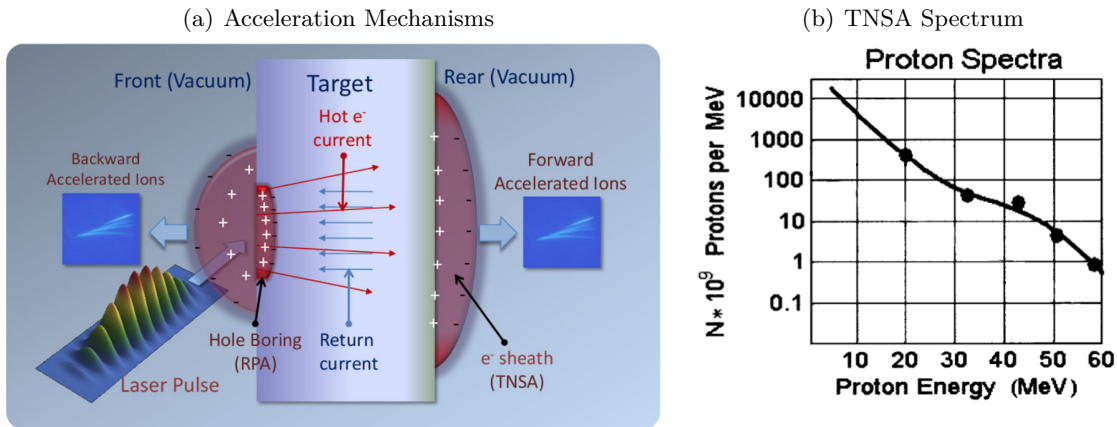
Figure 2.2: In (a), a cartoon showing laser-ion acceleration mechanisms in the interaction of an intense laser pulse with a thick solid target is depicted. From Macchi et al. [2013]. Panel (b) shows the measured proton energy spectrum, obtained in TNSA by irradiating a 100 µm thick solid target by a 423 J and 0.5 ps long laser pulse. Adapted from Snavely et al. [2000].

of several Debye lengths

$$\lambda_D = \sqrt{\frac{T_e}{4\pi n_e e^2}} \ , \tag{2.10}$$

where n_e is the mean hot electron density. This gives rise to a strong electric field which is mainly directed along the normal to the target surface [Macchi et al., 2013]. The initial electric field strength is proportional to the electron temperature [Daido et al., 2012]:

$$E_{\text{sheath},0} = \sqrt{\frac{2}{e}} \frac{T_e}{e\lambda_D} \ . \tag{2.11}$$

Note that in this equation e denotes the electron charge, while e represents Euler's number. Typical values for the quasi-static charge separation fields at the target rear side are in the order of the electric field of the laser, i.e. MeV/µm.

Due to their lowest charge-to-mass ratio among ions, acceleration in this electric field is most effective for protons. Their presence also in metallic targets can be explained by a surface contamination layer of the metal foils (e.g. water, hydrocarbons), which is typically present unless they are removed via target heating prior to the acceleration experiment [Hegelich et al., 2002]. Therefore, protons are the predominant ion species in the TNSA regime, as they take most of the energy from the accelerating field, such that acceleration of heavier ions becomes considerably less efficient under standard experimental conditions.

Proton energy distribution functions from TNSA are typically characterized by their quasi-thermal shape with a maximum cut-off energy E_{max}. Notably early experimental results in this acceleration regime were published by Snavely et al. [2000]. They measured an exponentially decaying proton spectrum with energies up to 58 MeV and 10^9 protons/MeV at E_{max} (see figure 2.2b).

Radiation Pressure Acceleration (RPA)

As an electromagnetic wave carries momentum, it exerts pressure on a surface that absorbs or reflects radiation. In the 1960s, shortly after the presentation of the first laser, a *Nature* article was published discussing the acceleration of an interstellar vehicle by a terrestrial laser via momentum transfer of the laser light to the vehicle [Marx, 1966]. The author expanded on earlier work from the 1920s that considered light-driven satellites or space ships. In the framework of laser-plasma acceleration, Esirkepov et al. [2004] reconsidered this idea as a representation of Veksler's coherent acceleration approach [Veksler, 1957]. For velocities approaching the speed of light, the efficiency of the momentum transfer rises up to almost 100%. Hence, almost the entire energy of the laser pulses could then be converted into kinetic energy of the plasma bunch. Although these considerations may sound like science fiction, the idea of acceleration driven by radiation pressure upon a light sail can be applied to much smaller objects, like thin foil targets.

The *radiation pressure acceleration* regime thus relies on the energy transfer from laser field to particles via radiation pressure. Depending on the target thickness RPA comes in different flavors, for example as *hole boring* and *light sail* acceleration for relatively thick and thin target foils, respectively. An absolute requirement for acceleration in the RPA regime is that electron heating like in TNSA is strongly suppressed. Therefore, an extremely high laser contrast with a very sharp rising edge (see orange curve in figure 2.1) is necessary. Initial theoretical studies have shown that RPA is dominant over the TNSA regime at laser intensities exceeding $10^{23}\,\mathrm{W\,cm^{-2}}$ [Esirkepov et al., 2004]. However, it was realized that by changing the laser polarization from linear to circular, the RPA dominant regime is already accessible at much lower intensities normally incident onto a ultra-thin foil target (see, for instance Henig et al. [2009]).

Under such conditions, the formerly mentioned electron heating processes are strongly suppressed as there is no oscillating component of the Lorentz force. Therefore, less hot electrons are created and consequently a sheath acceleration of ions as in the TNSA regime is strongly suppressed. Instead, the ponderomotive force of the laser piles up a highly dense and spatially confined electron layer. With adequate laser intensity, target thickness and density, an equilibrium of radiation pressure and restoring force due to the generated electrostatic charge-separation field can be obtained. Thus, the irradiated target area propagates as quasi-neutral plasma bunch that can gain energy from the laser field [Henig et al., 2009], similar to the interstellar vehicle mentioned above.

Besides an efficient energy transfer to the ions, a special feature of this RPA regime is that quasi-monoenergetic ion bunches can be obtained. For thick target foils, i.e. in the hole boring regime, the kinetic ion energy reads

$$E_{\mathrm{ion}} = 2m_{\mathrm{ion}}c^2 \frac{B^2}{1+2B} \;, \tag{2.12}$$

with the ion mass m_{ion} and $B = \sqrt{I_L/(\rho c^3)}$, where ρ denotes the mass density of the

plasma [Tikhonchuk, 2010]. Interestingly, equation 2.12 implies that the ion energy is independent of the ion charge. In the light sail regime for thin target foils in the order of a few nm, almost all laser energy may in theory be converted into kinetic energy of the ions once they reach velocities close to c [Daido et al., 2012].

2.1.4 Special Features of Laser-Accelerated Ion Bunches

Due to the unique laser-ion acceleration mechanism, properties of laser-accelerated ion bunches deviate substantially from conventionally accelerated ions from electrostatic accelerators, or radio-frequency driven (synchro-)cyclotrons or synchrotrons. The use of established ion detection and beam monitoring devices, which are e.g. widely available for clinical accelerators, is therefore limited. Especially the high instantaneous flux due to the quasi-instantaneous ion acceleration is a challenge for conventionally used beam monitoring systems. Before the currently most common LION beam characterization methods are presented in section 3.1, the most relevant features of laser-accelerated ion bunches compared to conventionally accelerated ions are summarized. If not explicitly referenced, the presented quantities and characteristics were taken from Daido et al. [2012]; Schreiber et al. [2016a]; Linz and Alonso [2007, 2016].

Beam Intensity

The maximum proton beam current extracted from a typical cyclotron is in the order of µA. This corresponds to an intensity in the order of 10^{12} to 10^{13} protons/s in a nearly continuous beam. In proton beam therapy facilities, the beam current at the treatment site is in the order of nA, hence 10^{10} protons/s.

Bunch charges in laser-ion acceleration are in the nC range, corresponding to $\sim 10^9 - 10^{10}$ protons. However, the remarkable feature is that the duration of the bunch at its origin is in the order of ps. Even relatively far from the source, where the bunch duration notably increases due to the different drift velocity of the polyenergetic ions, the bunch duration is still in the order of few to several tens of ns.

The expected peak ion fluxes during these bunches are thus orders of magnitude larger than compared to any conventionally accelerated ion bunch.

Beam Energy and Energy Spread

Proton energies from conventional accelerators installed in clinical facilities are typically reaching 250 MeV, or 60 MeV in facilities dedicated to uveal melanomas. The energy spread $\Delta E/E$ of beams from such clinical accelerators is in the order of $0.1 - 1.0\%$.

To this date, the highest published proton energy in laser-plasma experiments is 94 MeV [Higginson et al., 2018], differing not too much from proton energies coming from clinical accelerators. The major difference, however, is the energy distribution of laser-accelerated ions. Typical TNSA spectra are of exponentially decaying shape, corresponding to a

beam spread of $\Delta E/E \sim 100\%$. More narrow energy spreads (*quasi-monoenergetic*) have been reported using special targets (for instance Schwoerer et al. [2006]) or by realizing acceleration mechanisms other than TNSA (e.g. Henig et al. [2009]). Moreover, beam shaping devices, such as magnetic quadrupole lenses or solenoids are used to obtain a smaller energy spread. Nevertheless, typical energy spreads of quasi-monoenergetic ion bunches are still within several percent.

Mixed Field

Although synchrotrons are capable to accelerate several different ion species, only one ion type can be accelerated within one cycle.

In contrast, laser-accelerated ion bunches are characterized by their mixed radiation field. Although typically dominated by protons, heavier ions at various different charge states may be co-emitted from the target, depending on the target composition. Furthermore, from the acceleration mechanisms, it is obvious that the ions are accompanied by highly relativistic electrons. Also, photons over a very broad energy range are emitted, ranging from microwave radiation up to x-ray and gamma radiation.

For any electronic system near the laser-plasma interaction, including electronic detection systems, the strong electromagnetic pulse (EMP) in the GHz to THz range is a major obstacle. The origin for the EMP in the GHz range can partially be explained by the discharge of the laser target through the target holder [Poye et al., 2015].

Additionally, the interaction of primary beam particles or x-rays with components within the experimental vacuum chamber, or with the chamber walls themselves, can lead to a strong background of secondary particles, mixing with the actual accelerated ion bunch.

Source Size and Divergence

In laser-ion acceleration, source sizes of the strongly diverging ion beam are in the order of μm. Divergence angles are typically ranging from a few up to a few tens of degrees. Although this property poses a challenge for efficient beam guidance, it is actually advantageous for detection, as it relaxes the high fluxes with increasing distance to the target.

Shot-to-Shot Fluctuations

At conventional accelerators, fluctuations of the emerging beam current are well under control. In contrast, laser-ion acceleration is a complex process with various parameters influencing the quality of the resulting ion bunches. Shot-to-shot fluctuations of laser-accelerated ion bunches are typically in the order of a few up to several tens percent. As an example, in figure 2.3, the proton energy spectra of 85 consecutive laser shots at LEX Photonics are shown, indicating the strong fluctuations in the particle number and maximum cut-off energies.
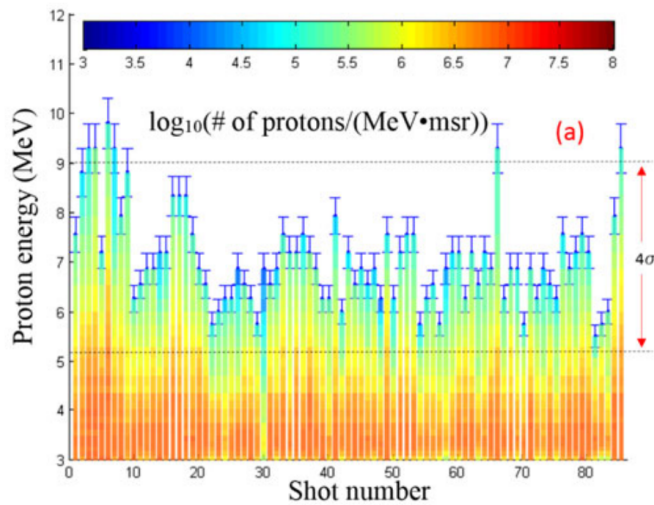
Figure 2.3: Proton energy spectra of 85 consecutive laser shots at LEX Photonics, measured by a magnetic spectrometer. The shot-to-shot fluctuation in the maximum energy was 27%. From Gao et al. [2017].

2.2 Interaction of Ionizing Radiation with Matter

Any kind of radiation which is capable to ionize matter it is interacting with is commonly denoted by *ionizing radiation*. This term therefore includes electromagnetic radiation (gamma rays, x-rays and partly ultra-violet radiation), charged particles (protons, ions, electrons, positrons or muons) and neutral particles (neutrons or neutral pions). The energy transfer of ionizing radiation to the absorber material is fundamental for e.g. treatment of cancerous tissue and radiographic imaging, as well as for detection.

In the following, the most important interaction mechanisms of photons, ions and electrons for the energy ranges of interest are briefly described. Interactions of neutrons with matter are not further described here, as such interactions are not relevant for the scope of this project. A more elaborate description on this topic can be found in dedicated text books (e.g. Leo [1994], Attix [1986], Knoll [2010]), the Review of Particle Physics by the Particle Data Group [Patrignani et al., 2016] or in the review article for proton therapy by Newhauser and Zhang [2015].

2.2.1 Photon Interaction

A wide range of possible mechanisms of photons interacting with matter exists. Their relevance is typically depending on the photon energy and the target material. In figure 2.4, the cross-section of photons in carbon for the most important interaction processes are plotted as a function of photon energy. The underlying mechanisms are briefly listed in the following.
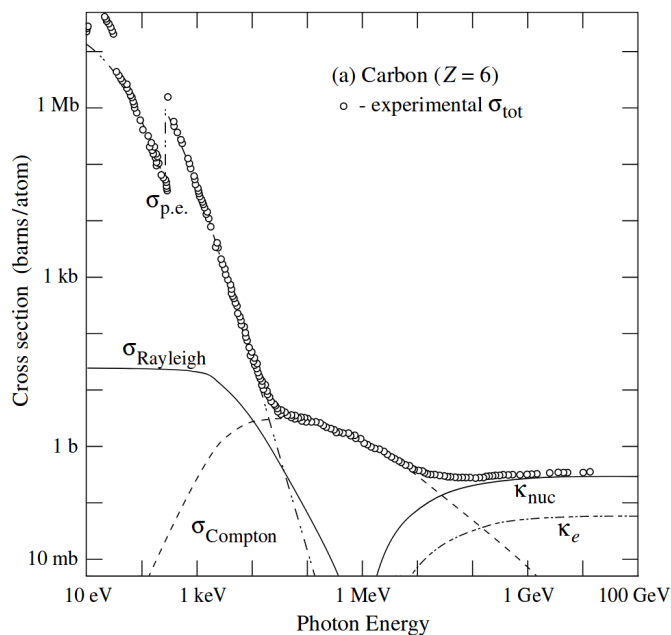
Figure 2.4: Photon interaction cross-sections as a function of energy in carbon. From Patrignani et al. [2016].

Photoelectric Absorption

Photoelectric absorption, $\sigma_{p.e.}$, is by far the most dominant interaction process at low photon energies. The photon interacts with a shell electron of a target atom and is absorbed under emission of an energetic photoelectron. The energy of this ejected electron equals the photon energy $E_\gamma = h\nu$, minus the binding energy E_b of the electron in its original shell. Obviously, that implies that the photon energy exceeds the binding energy. The photo-induced vacancies are filled by capture of a free electron or rearrangement of electrons from higher shells, which results in the emission of characteristic x-ray photons or Auger electrons that are usually re-absorbed close to their origin. The cross-section for the photoelectric effect shows some characteristic discontinuities in the low-energy region, the so-called absorption edges. These edges correspond to the binding energies of electrons within certain shells and are characteristic for the respective material. The probability for the occurrence of the photoelectric effect is approximately proportional to $Z^n/E_\gamma^{3.5}$, with the exponent n varying between 4 and 5. As the photon is entirely absorbed in this interaction, the photoelectric effect is the basis for x-ray absorption imaging.

Rayleigh Scattering

Rayleigh scattering, $\sigma_{Rayleigh}$, is an elastic scattering process, relevant for low photon energies and most pronounced in high-Z absorber materials. Photons interact coherently with all electrons of an absorber atom without any net transfer of energy and absorber atoms are neither ionized, nor excited. With increasing photon energy, the deflection angle

of the photons with respect to their original direction decreases.

Compton Scattering

In Compton scattering, $\sigma_{Compton}$, the incident photon is inelastically scattered at a weakly bounded electron of the absorber material. Part of its energy $E_\gamma = h\nu$ is transferred to an emitted recoil electron, such that the emitted photon after the interaction has an energy

$$h\nu' = h\nu \left(1 + \frac{h\nu}{E_0}(1 - \cos\theta) \right)^{-1} \; , \tag{2.13}$$

where $E_0 = 511\,\text{keV}$ is the rest mass of the electron times c^2, and θ is the deflection angle with respect to the original photon direction. Compton scattering is the dominant interaction process for photon energies around $1\,\text{MeV}$ and its probability increases linearly with Z.

Pair Production

If the photon energy exceeds twice the rest energy of an electron ($E_\gamma > 1.022\,\text{MeV}$), pair production ($\kappa_{nuc}$) is energetically possible. Due to momentum conservation, the spontaneous transformation of a photon into an electron-positron pair is only possible in the vicinity of an absorber nucleus. Triplet production (κ_e) in the vicinity of an electron is energetically possible for photon energies higher than four times the electron rest energy. The energy of the photon exceeding twice the rest energy of an electron (or four times for triplet production) is converted into kinetic energy of electron and positron. Pair production becomes the dominant interaction process starting from photon energies exceeding the threshold energy by around $1\,\text{MeV}$ and is more important for high-Z absorbers.

Photonuclear Interaction

High energetic photons may also be absorbed by a target nucleus under the emission of protons, neutrons or heavier nuclear fragments. However, due to its low probability, these photonuclear interactions ($\sigma_{p.n.}$) do not play an important role in the context of this project and are therefore not described further.

Total Photon Attenuation Coefficient

All the aforementioned attenuation probabilities can be combined to the so-called *linear attenuation coefficient*

$$\mu = \sigma_{p.e.} + \sigma_{Compton} + \kappa_{nuc} + \kappa_e + \sigma_{p.n.} \tag{2.14}$$

or equivalently, the mass attenuation coefficient, which is simply the linear attenuation coefficient divided by the mass density of the absorber material, μ/ρ. The linear attenua-
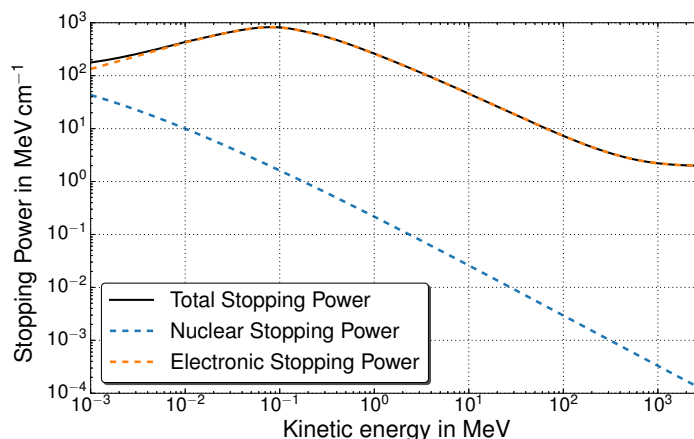
Figure 2.5: Electronic, nuclear and total stopping power of protons in water, data was taken from NIST PSTAR [Berger et al., 2005]. The total energy loss rate is highly dominated by the electronic stopping power. Nuclear stopping power is negligible except for very low kinetic energies.

tion coefficient is thus the probability that a photon is removed from an incident beam per unit path length. At a depth x inside an absorber, the number of transmitted photons, or rather the transmitted intensity is hence given by

$$I(x) = I_0 e^{-\mu x}, \tag{2.15}$$

where I_0 is the initial intensity.

2.2.2 Heavy Charged Particle Interaction

On their passage through matter, heavy charged particles interact with atomic electrons and nucleons, resulting in loss of kinetic energy and a change in their trajectory.

Energy Loss

The mean energy loss rate of heavy charged particles per unit path length, also denoted by *linear stopping power*, is defined by

$$S = -\frac{\mathrm{d}E}{\mathrm{d}x} \ . \tag{2.16}$$

The stopping power is often also expressed as *mass stopping power*, by dividing eq. 2.16 by the mass density of the absorbing material ρ such that the energy loss rate is independent of the material density. It is worthwhile to mention that the mass stopping power does not differ a lot for a large variety of absorber materials [Leo, 1994].

Over a wide range of kinetic energies, the energy loss of ions is dominated by frequent inelastic Coulomb interactions with atomic shell electrons (see figure 2.5). This gives rise to a quasi-continuous energy loss along their path, while the change in their trajectory is neg-

ligible since their rest mass is large compared to the electron mass [Newhauser and Zhang, 2015]. The resulting mean energy loss rate, also denoted by *electronic stopping power*, is described by the *Bethe-Bloch formula* [Bethe, 1930; Leo, 1994], which is valid for energies larger than $\sim 1\,\text{MeV/u}$:

$$-\frac{\mathrm{d}E}{\mathrm{d}x} = 2\pi n_e r_e^2 m_e c^2 \frac{z^2}{\beta^2} \left[\ln \left(\frac{2m_e c^2 \beta^2 W_{\max}}{I^2(1-\beta^2)} \right) - 2\beta^2 - \delta - 2\frac{C}{Z} \right] , \qquad (2.17)$$

where $n_e = N_A \rho \frac{Z}{A}$ is the electron density of the absorber material with Avogadro's number N_A, mass density ρ, atomic number Z and atomic mass number A of the target material. The classical electron radius and the electron rest mass are denoted by r_e and m_e, while z and β are the charge and the velocity of the projectile scaled by the speed of light c, respectively. I is the ionization potential of the medium, whereas $W_{\max}$ is the maximum possible energy transfer in a single collision with a free electron. This formulation of the Bethe-Bloch formula includes two correction terms, namely the density effect correction δ, which is important at high projectile energies, and the shell correction C, important at low energies. Both correction terms also depend on the material properties of the absorber.

Studying dependencies in eq. 2.17, a strong dependence of the energy loss on the ion charge can be found, while the mass of the projectile has no influence. Hence, for the same velocity, the stopping power of an α-particle is four times the energy loss rate of a proton. Furthermore, it can be seen that in a wide energy range the stopping power increases with decreasing projectile velocity via $1/\beta^2$. At low energies ($\lesssim 0.1\,\text{MeV/u}$), the energy loss rate becomes smaller again due to recombination processes between projectile ions and electrons from target atoms. The ion charge z in eq. 2.17 reduces to an effective charge z_{eff}, which can be described by the semi-empirical formula [Barkas and Evans, 1963]:

$$z_{\text{eff}} = z \left(1 - \exp(-125\beta z^{-\frac{2}{3}}) \right) . \qquad (2.18)$$

Thus, the strong $1/\beta^2$-dependence in eq. 2.17 combined with the decreasing effective charge of eq. 2.18 at low energies yields a depth distribution of the energy deposition in the target material which is governed by an almost constant plateau, followed by a sharp rise and fall at the end of the ion range. The resulting curve (shown for water in figure 2.6) is commonly denoted as *Bragg curve*, and the high peak is the so-called *Bragg peak* (BP). This well-defined maximum of energy deposition at the end of the particle's range is the basis for ion beam therapy in cancer treatment.

Range and Energy Straggling

An important quantity related to the interaction of ions with matter is their range R, which is defined as the expected value of the path length of the particle until it comes to rest [Attix, 1986]. For convenience, an approximation that assumes a continuous energy loss instead of multiple discrete energy losses, called continuous slowing down approximation
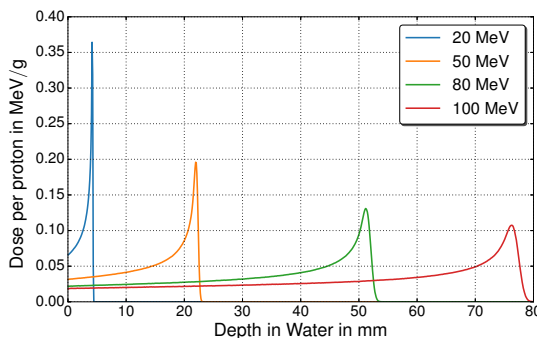
Figure 2.6: Integrated depth-dose curves of monoenergetic proton beams in water, according to FLUKA MC simulations. The Bragg peak width increases with higher beam energy due to energy straggling.

(CSDA), is used to express this range. Differences between the actual range R and the CSDA-range R_{CSDA} are negligible [Attix, 1986]. For an initial kinetic energy E_{in}, the mean range can be calculated by

$$R(E_{in}) \simeq R_{\mathrm{CSDA}}(E_{in}) = \int_0^{E_{in}} \left(\frac{\mathrm{d}E}{\mathrm{d}x}\right)^{-1} \mathrm{d}E \ . \tag{2.19}$$

For proton energies of interest for radiotherapy and for this study, a linear relationship can be found between the logarithm of the range and the logarithm of the energy. The particle range can therefore be calculated using a simple power law,

$$R(E) = \alpha E^p \ , \tag{2.20}$$

with a material-dependent constant α, which is approximately proportional to the square root of the target's effective atomic mass, $\sqrt{A_{\mathrm{eff}}}$ [Bortfeld, 1997]. The two parameters α and p are usually obtained empirically by fitting eq. 2.20 to measured or tabulated range and corresponding energy values.

Up to this point, a smooth and continuous energy loss of ions in the target material was assumed. However, the number of collisions experienced by an individual ion, as well as the energy transferred within each interaction is governed by statistical fluctuations. The summation of all the small variations in energy loss give rise to to the so-called *range straggling*, or *energy straggling*, which is the reason for the increased Bragg peak width as compared to purely analytical calculations using only the average energy loss given by eq. 2.17. Therefore, range straggling for purely monoenergetic ion beams is more pronounced for higher energies and the resulting Bragg peak width hence increases with the initial kinetic energy. Bragg curves of protons with different kinetic energies are shown in figure 2.6.

For a thick absorber, the range straggling can be well described by a Gaussian probability distribution function [Bohr, 1915]. Its variance is proportional to the inverse of the projectile mass [Schardt et al., 2010], hence for the same initial energy spread, the Bragg

peak width of protons is larger than for heavier ions. For thinner targets, the assumption that the central limit theorem holds is not valid anymore, as the number of individual collisions is small. The energy straggling can then be described by the theories of Landau [1944] and Vavilov [1957].

Lateral Scattering

Elastic scattering of projectile ions in the repulsive Coulomb field of target nuclei results in lateral deflection with respect to their original trajectory. The energy loss within such interaction can be considered negligible. Single elastic Coulomb scattering events are well described by Rutherford scattering [Rutherford, 1911]. An ion penetrating a thicker target will experience numerous Coulomb scattering events, changing its trajectory.
An analytical solution to deal with *multiple Coulomb scattering* (MCS) was derived by Molière [1948], which is valid until close to the stopping of the ion [Gottschalk, 2010]. Neglecting single large-angle scattering events ($> 10°$), the angular distribution of a large number of single scattering events can be described by the Highland formula [Highland, 1975; Lynch and Dahl, 1991]

$$\theta_0 = \frac{13.6\,\text{MeV}}{\beta cp} z \sqrt{\frac{x}{X_0}} \left[1 + 0.038 \ln \left(\frac{x}{X_0} \right) \right] \ , \qquad (2.21)$$

assuming a Gaussian distribution with the standard deviation θ_0, being the root mean square (rms) angle in a plane. Here, βc and p are the incident particle velocity and momentum, respectively, and x/X_0 is the absorber thickness divided by the material dependent radiation length. From eq. 2.21 follows that the scattering angle increases with decreasing ion energy.
However, Highland's approximation assumes that the scattering medium is sufficiently thick such that multiple scattering events occur, but thin enough that the projectile energy does not decrease a lot. A generalized Highland formula and a detailed discussion on scattering of protons in the energy range relevant for radiotherapy can be found in Gottschalk [2010].

Nuclear Reactions

Less frequent, but of non-negligible impact are non-elastic nuclear reactions of projectile particles with target nuclei, provided their kinetic energy is sufficient to overcome the Coulomb barrier of the target nucleus. Note that these nuclear reactions have nothing to do with the nuclear stopping power shown in figure 2.5, which is caused by projectiles interacting with the electromagnetic field of the the target nuclei.
Due to such nuclear interactions, the initial ion fluence Φ_0 decreases with increasing depth in the absorber material, x, via

$$\Phi(x) = \Phi_0 \, e^{-N\sigma_R x} \ , \qquad (2.22)$$
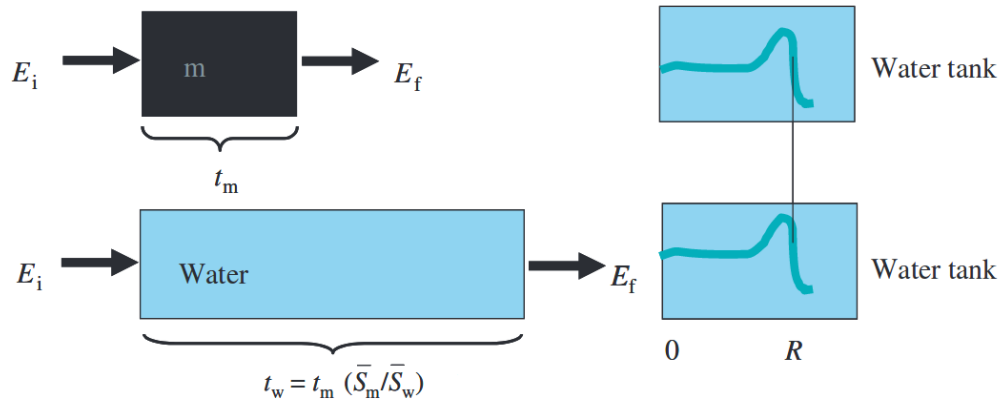
Figure 2.7: Schematic illustration of the WET concept. Adapted from Zhang and Newhauser [2009].

where N is the nuclear density of the medium and σ_R is the total reaction cross section for nucleus-nucleus collisions.

Part of the reaction products may be β^+-emitters. The emitted positrons annihilate within few mm under emission of two $511\,\mathrm{keV}$ photons. These photons can be detected and used for range verification in ion beam therapy [Parodi et al., 2007; Würl, 2016] or as diagnostic for laser-accelerated ions (see 3.1.1).

Quantities of Interest for Ion Imaging and Radiation Therapy

In the last part of this brief overview of heavy charged particles' interaction with matter, quantities and concepts important for radiotherapy and ion imaging are introduced.

The probably most important quantity in radiotherapy in general is the macroscopic quantity *absorbed dose D*. It is defined as the average energy deposition by ionizing radiation to an absorber per unit mass:

$$D = \frac{\mathrm{d}\epsilon}{\mathrm{d}m} \ , \tag{2.23}$$

commonly expressed in Gray ($1\,\mathrm{Gy} = 1\,\mathrm{J/kg}$). Typical doses in radiotherapy are $\sim 2\,\mathrm{Gy}$ per treatment fraction and 30 to $50\,\mathrm{mGy}$ for an x-ray CT scan of a head [Mettler et al., 2008; Johnson et al., 2015].

The radiological thickness of a material in ion beam therapy is usually expressed by its *water-equivalent thickness* (WET) [Zhang and Newhauser, 2009]. The concept can easily be explained by figure 2.7. An ion beam with certain energy E_i penetrates a slab of material with thickness t_m, loses some of its energy according to the material-specific mean stopping power $\overline{S_m}$, and exits the slab with a residual kinetic energy E_f. The WET of that slab is then the thickness of water t_w that an ion beam with the same initial energy E_i has to traverse such that it exits with the same residual energy E_f:

$$\mathrm{WET} \equiv t_w = t_m \frac{\overline{S_m}}{\overline{S_w}} \ . \tag{2.24}$$

The mean stopping power can be calculated by $\overline{S} = \int_E S \mathrm{d}E / \int_E \mathrm{d}E$ [1].
For radiologically thin targets[2], eq. 2.24 can be approximated by

$$\text{WET} = t_m \frac{S_m(E_i)}{S_w(E_i)} \ , \tag{2.25}$$

whereas for thick targets it is more convenient to express the WET by the ion range [Zhang and Newhauser, 2009]:

$$\text{WET} \approx t_m \frac{R_w(E_i)}{R_m(E_i)} \ . \tag{2.26}$$

Occasionally, also the unit-less quantity water equivalent ratio (WER) is used, being the ratio of t_w to t_m. While the WER is almost independent of the kinetic energy for most radiobiologically relevant materials, for radiologically thick absorbers consisting of high-Z material, the WER is far from being constant. Due to its use in the clinical environment and since the WET concept generally holds for tissue materials, it is also convenient to be used as quantitative measure for the radiography studies performed within the framework of this thesis.

Another related quantity frequently used in ion imaging is the *water-equivalent path length* (WEPL). It is defined as the path integral of the object's *relative stopping power* (RSP) along the trajectory l of an ion within that object:

$$\text{WEPL} = \int_l \text{RSP} \ \mathrm{d}l' = \int_l \frac{S_m(E)}{S_w(E)} \ \mathrm{d}l' \ . \tag{2.27}$$

Phenomenologically, it can be understood as the length of an ion path in water, that would result in the observed energy loss [Johnson et al., 2015]. In literature, some ambiguities of the terms WET and WEPL exist and the two terms are sometimes used to express the same quantity. Evidently, according to eq. 2.25 and eq. 2.27, the ratio of WET over WEPL approaches unity for very thin objects.

2.2.3 Electron Interactions

For the sake of completeness, this section is dedicated to the interaction of fast electrons with matter. Since their mass is equal to the mass of the atomic electrons, elastic scattering in nuclear and electronic collisions is much more pronounced than for heavy charged particles. This results in a zig-zag motion of the energetic electrons in the absorber

---

[1]Note that depending on literature, S_m and S_w may also be defined as the *mass* stopping power, such that eq. 2.24 also explicitly includes the ratio of the mass densities ρ_m/ρ_w and would become WET $= t_m(\rho_m/\rho_w)(\overline{S_m}/\overline{S_w})$. However, this latter definition is *not* used throughout this thesis.

[2]In this context, an absorber is considered thin, when the ion beam only loses a small fraction of its initial kinetic energy. In a radiologically thick target, the energy loss of the ions is large. Whether an absorber is thick or thin depends on the initial kinetic energy of the ions, the material properties and, of course, the geometrical thickness [Zhang and Newhauser, 2009].

material.

While energy loss of ions in the energy range of interest for this thesis is dominated by inelastic Coulomb interactions with atomic electrons, *radiative losses* in addition to the *collisional losses* contribute to the total linear stopping power of fast electrons in an absorber:

$$\frac{\mathrm{d}E}{\mathrm{d}x} = \left(\frac{\mathrm{d}E}{\mathrm{d}x}\right)_{col} + \left(\frac{\mathrm{d}E}{\mathrm{d}x}\right)_{rad} \ . \tag{2.28}$$

For the collisional energy loss, an expression similar to the Bethe-Bloch equation (eq. 2.17) can be derived by dividing the first moment of the Møller cross section by $\mathrm{d}x$. In case the incident particles are positrons, a similar derivation based on the Bhabha cross section is possible [Patrignani et al., 2016].

Deflections of the electrons along their trajectory is equivalent to an acceleration. Therefore, the electrons must radiate energy in form of bremsstrahlung. Radiative stopping power is proportional to $EZ(Z+1)$, hence radiative losses increase with increasing kinetic energy of the electrons and become especially important for high-Z absorber materials. The ratio between the two contributions is approximately given by [Knoll, 2010]:

$$\frac{(\mathrm{d}E/\mathrm{d}x)_{rad}}{(\mathrm{d}E/\mathrm{d}x)_{col}} \approx \frac{EZ}{700\,\mathrm{MeV}} \ . \tag{2.29}$$

2.3 Signal Generation in Semiconductor Detectors

Since a substantial part of the experimental work performed in the framework of this thesis is based on the use of silicon detectors, it is worthwhile to give a short introduction to semiconductor detectors and how the signal to be measured is generated. A deeper insight on this topic is given in various text books (e.g. Spieler [2005], Lutz [2007] or Knoll [2010]).

2.3.1 Properties of Semiconductors

Semiconductor materials are characterized by their crystalline structure with numerous atoms arranged in a periodic lattice. Silicon and germanium, the most commonly used semiconductor materials for radiation detectors, crystallize in a diamond lattice with a lattice constant a of 5.43 Å and 5.65 Å, respectively [Spieler, 2005]. Each atom within the lattice shares its four valence electrons with the four nearest neighboring atoms, forming covalent bonds.

For a temperature $T = 0\,\mathrm{K}$, all valence electrons are bound in their respective lattice. With increasing temperature, some thermal energy is shared by the electrons in the crystal in terms of thermal vibrations. Such energy can be sufficient to break the covalent bond between two lattice atoms, creating a free electron that leaves behind a vacancy, the so-called *hole*. The remaining hole can then be filled by a nearby electron, thus both the electron and the hole can travel freely within the lattice and are available for conduction.

Describing this process in terms of the band model, the electron is lifted from the *valence band* into the energetically higher *conduction band*, which is separated from the former by the *bandgap* or *forbidden gap*. Typical widths of this forbidden gap in materials used for radiation detectors are ranging between $0.7\,\text{eV}$ for germanium and $5.5\,\text{eV}$ for diamond [Spieler, 2005]. In conductors, valence and conduction band can either be overlapping or the conduction band is already partially filled [Lutz, 2007].

In an intrinsic semiconductor, no impurities are contained such that electrons (and holes) in the conduction band can only be thermally generated (in absence of ionizing radiation). The probability that a certain energy state in the conduction band is filled is given by the Fermi-Dirac distribution

$$f_e(E) = \frac{1}{\exp\left(\frac{E-E_F}{k_B T}\right) + 1} \ , \tag{2.30}$$

with the absolute temperature T and the Fermi energy E_F, which is the energy for which the occupation probability $f_e(E_F) = 0.5$. Correspondingly, the probability that a hole state is empty, reads

$$f_h(E) = 1 - f_e(E) = \frac{1}{\exp\left(\frac{E_F-E}{k_B T}\right) + 1} \ . \tag{2.31}$$

At room temperature ($T \approx 300\,\text{K}$), the thermal energy is $k_B T = 26\,\text{meV}$. According to eq. 2.30 and for the Fermi level in the middle of the bandgap, the probability that an electron occupies a state in the conduction band in silicon (bandgap energy $E_g = 1.12\,\text{eV}$) is 4×10^{-10}. Nevertheless, the intrinsic carrier density at this temperature is $n_i = 1.45 \times 10^{10}\,\text{cm}^{-3}$, given the high density of states [Spieler, 2005].

From eq. 2.30 it is also clear that conductivity of a semiconductor with a fixed bandgap energy strongly depends on the absolute temperature. Cooling the semiconductor to $0\,°\text{C}$ reduces the intrinsic carrier density to $n_i = 1.3 \times 10^9\,\text{cm}^{-3}$.

In the absence of an electric field, electrons and holes randomly diffuse according to their thermal motion and may ultimately recombine with other holes and electrons. Thus, an equilibrium between charge carrier creation and recombination is established. The mean kinetic energy of these charge carriers is $\frac{3}{2}k_B T$, such that at room temperature their mean velocity is of the order of $10^7\,\text{cm}\,\text{s}^{-1}$.

When applying an electric field to the semiconductor material, the random thermal movement is superimposed by a net average drift parallel or anti-parallel to the electric field, with opposite direction for electrons and holes. Since the charge carriers also interact with the crystal lattice via excitation of lattice vibrations (phonons), the carriers are not continuously accelerated in the electric field but they drift with constant velocity in an equilibrium between acceleration and scattering. Thus, the drift velocity of electrons and holes, v_e and v_h, only depends on the electric field $\vec{E}$

$$v_{e/h} = \mu_{e/h}|\vec{E}| \ , \tag{2.32}$$

with the temperature- and material-dependent mobility $\mu \propto \frac{1}{k_B T}$ [Spieler, 2005]. For silicon at $T = 300\,\mathrm{K}$, the mobilities of electrons and holes are $1350\,\mathrm{cm^2\,V^{-1}\,s^{-1}}$ and $480\,\mathrm{cm^2\,V^{-1}\,s^{-1}}$, respectively [Knoll, 2010].

When a voltage is applied across a slab of a semiconductor with thickness d and surface area A, both the electrons and the holes contribute to the resulting current

$$I = I_e + I_h = An_i e(v_e + v_h) = An_i e \frac{V}{d}(\mu_e + \mu_h) \ . \tag{2.33}$$

The theoretical value of the intrinsic resistivity $\rho = (en_i(\mu_e + \mu_h))^{-1}$ of silicon at room temperature is hence $2.3 \times 10^5\,\Omega\,\mathrm{cm}$ [Knoll, 2010]. In reality, this intrinsic resistivity can not be achieved due to residual impurities in the silicon lattice.

2.3.2 Creation of a pn-Junction

By targeted introduction of impurities into the pure intrinsic semiconductor material, its resistivity (or conductivity) can be changed. The process of introducing a small amount of impurities in a controlled manner is called *doping*. Depending on the number of valence electrons of the introduced impurity atom, the doped material is referred to as n-type or p-type material. A special notation was introduced for thin layers of semiconductor materials with very high impurity concentrations. Such heavily doped materials are commonly denoted by n^+ and p^+ for n-type and p-type material, respectively.

n-Type Doping

In *n-type doping*, one silicon atom in the lattice is replaced by an atom from the fifth group in the periodic table (e.g. P, As, Sb). As a result, the fifth valence electron of the dopant cannot form a covalent bond. The so-called *donor* electron is still lightly bound to the impurity atom, but the bound level (*donor level*) is only in the order of 0.01 eV below the conduction band. The energy gap is hence sufficiently small such that the probability of thermal excitation to the conduction band is large. Therefore, a large fraction of all donor impurities is ionized.

The concentration of impurities N_d is generally large ($\sim 10^{12} - 10^{18}\,\mathrm{cm^{-3}}$) compared to the intrinsic carrier density n_i. Thus, the carrier density in an n-type semiconductor is dominated by the contribution from the dopants. Of course, this influences the equilibrium between electrons and holes in a way that the number of conduction electrons is much greater and the number of holes is much smaller than in the undoped semiconductor. Hence, electrical conductivity is dominated by the flow of electrons. Electrons in n-type materials are therefore called *majority carriers*, while holes are the *minority carriers*.

p-Type Doping

Introducing atoms from the third group of the periodic table (e.g. B, Al, Ga, In) into the semiconductor lattice is called *p-type doping*. The impurity embedded in the lattice has one valence electron less than the surrounding silicon atoms, leaving an unpaired covalent bond. The impurity atom, also called *acceptor* impurity, thus "borrows" an electron from neighboring atoms to fill its covalent bond. However, this electron is slightly less attached to it than other valence electrons due to the lower charge of the nucleus. This gives rise to a bound state close to the valence band (*acceptor level*), separated by an energy gap in the order of 0.01 eV. Due to this small gap, most of the vacancies created by the impurities are filled by thermally excited electrons from other covalent bonds, leaving behind holes in the valence band.

Analogue to the n-type semiconductor, the concentration of acceptor impurities N_a is generally large compared to the intrinsic hole concentration, such that the carrier density in a p-type semiconductor is again dominated by the concentration of acceptors. Therefore, in p-type material, the majority carriers dictating the electrical conductivity are holes.

The pn-Junction

When joining together n-type and p-type semiconductors, a *pn-junction* is obtained. While initially, both the n-type and p-type regions are electrically neutral, the density of electrons is much higher in the n-type region. Due to thermal diffusion, the charge carriers move across the junction. However, a net diffusion of conduction electrons from the n-type to the p-type material exists, where they combine with holes. Thus, they leave behind a net positive charge in the n-region. Accordingly, a net negative charge builds up in the p-region due to a net diffusion of holes to the n-region. These two space charge regions give rise to an electric field which limits further net diffusion. A region (nearly) free of mobile charge carriers is created between the two space charge regions, the so-called *depletion region* with the depletion width w_d.

Isolated p-type and n-type materials show a difference in their Fermi level E_F. While for an intrinsic semiconductor, the Fermi level is in the middle of the bandgap, donor impurities shift the Fermi level closer to the conduction band and acceptor impurities to the valence band. The *built-in potential*, V_{bi}, of a pn-junction is the potential difference between the p- and the n-region and thus corresponds to the difference between their two Fermi levels (see figure 2.8 top) [Spieler, 2005]:

$$V_{bi} = E_{Fn} - E_{Fp} = \frac{k_B T}{e} \log\left(\frac{N_a N_d}{n_i^2}\right) \; . \tag{2.34}$$

For example, doping concentrations of $N_a = 10^{16}\,\mathrm{cm}^{-3}$ and $N_d = 10^{12}\,\mathrm{cm}^{-3}$ for respective acceptor and donor concentrations in silicon at room temperature result in a built-in potential of $V_{bi} = 0.46\,\mathrm{V}$ [Lutz, 2007].
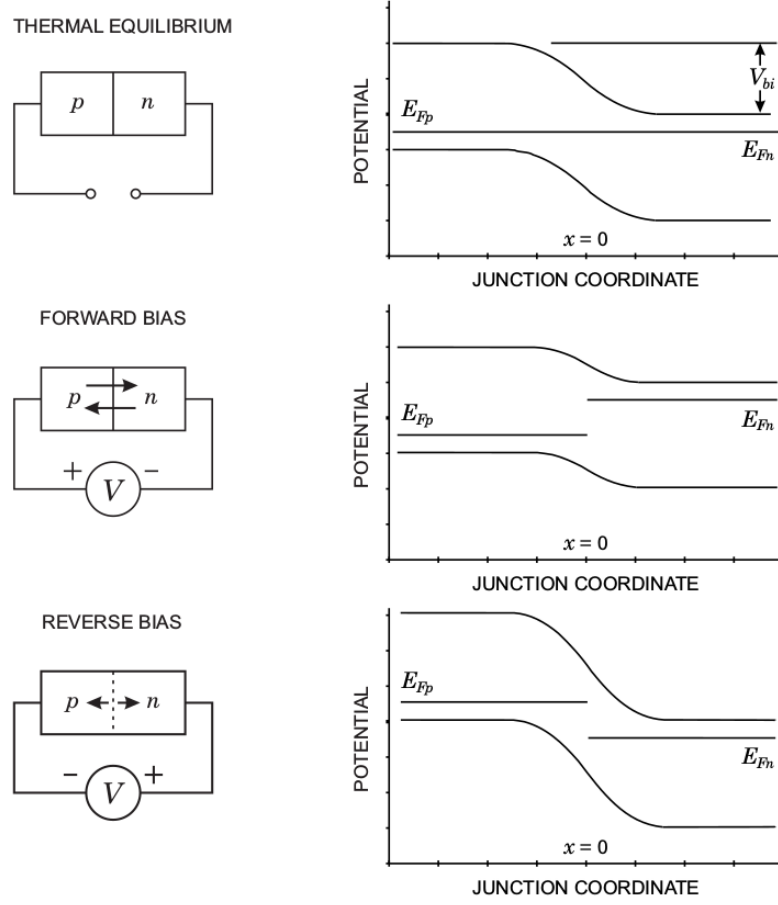
Figure 2.8: The pn-junction and the resulting potential as a function of junction coordinate for thermal equilibrium (top), forward bias (middle) and reverse bias (bottom). E_{Fp} and E_{Fn} denote the Fermi level of p-type and n-type semiconductor material, respectively. From Spieler [2005].

Thermal equilibrium no longer holds, when an external potential is applied to the pn-junction. A positive potential on the p-region and a negative potential on the n-region reduces the the built-in potential barrier and current flow between both regions increases (*forward bias*). An opposite polarity increases the potential barrier and with it the width of the depletion region (*reverse bias*). Both scenarios are shown schematically in figure 2.8.

The *Shockley equation* describes the current-voltage characteristic of a diode under forward and reverse bias (derived in Spieler [2005]):

$$I = I_n + I_p = I_0 \left(\exp\left(\frac{e \cdot V}{k_B T}\right) - 1 \right) \tag{2.35}$$

with

$$I_0 = e n_i^2 \left(\frac{D_n}{N_a L_n} + \frac{D_p}{N_d L_p} \right) . \tag{2.36}$$

$D_{n,p}$ and $L_{n,p}$ are the diffusion constant and diffusion length for electrons and holes, respectively. When a reverse bias voltage is applied, the contribution of the exponential
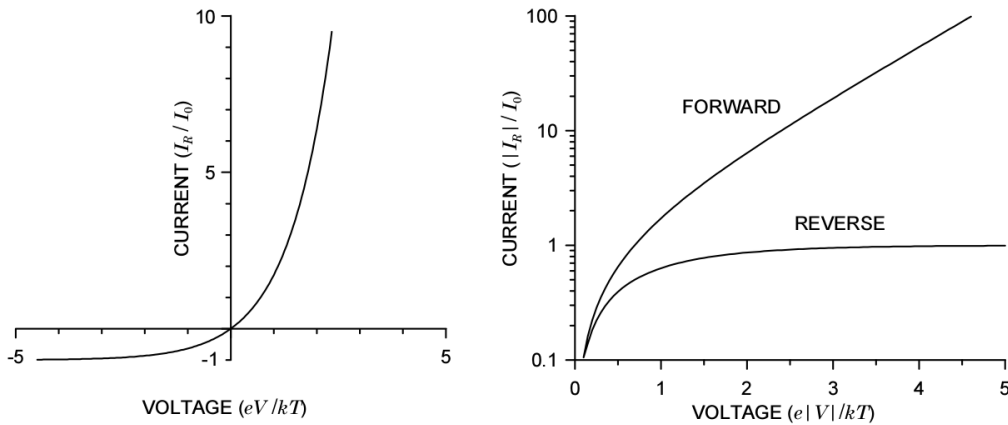
Figure 2.9: Current as a function of voltage of a semiconductor diode. From Spieler [2005].

term in eq. 2.35 reduces with increasing bias voltage until the reverse saturation current $I = I_0$ is reached. In a forward biased diode, the exponential term dominates and current flow rapidly increases with applied bias voltage. The current-voltage characteristic of a semiconductor diode is shown in figure 2.9. Impurities and defects in the crystal lattice strongly affect the reverse saturation current and can increase it by orders of magnitude [Spieler, 2005].

Semiconductor radiation detectors and photodiodes usually contain reverse-biased pn-junctions. The positively and negatively charged n-type and p-type regions, separated by the depleted region free of charge carriers, form a capacitor with capacity

$$C = \epsilon\epsilon_0 \frac{A}{w_d} \ . \tag{2.37}$$

A is the junction area and ϵ the dielectric material constant, which is 11.68 for silicon. As already mentioned previously, the width of the depletion region w_d depends on the built-in voltage V_{bi} and the applied reverse bias V_b according to

$$w_d = \sqrt{\frac{2\epsilon\epsilon_0 (N_a + N_d)}{e N_a N_d}(V_{bi} + V_b)} \ . \tag{2.38}$$

By increasing the applied reverse bias voltage, the width of the depletion region can be increased until virtually the entire thickness of the pn-junction is depleted. In this case, one speaks of *full depletion*, which is the preferable configuration for radiation detectors, as only ionization in the depleted regions of a detector leads to charge carrier separation and thus a measurable signal. Increasing the depleted regions hence results in an increased sensitive volume. In partially depleted detectors, the electric field drops to zero at the edge of the depletion region, which results in slower drift velocities of the charge carriers in the low-field regions and to recombination. Hence, timing properties and charge collection efficiency of fully depleted detectors are superior [Knoll, 2010].

However, increasing the reverse bias further will eventually result in an electrical break-

down of the diode. This can be a liberation of the electrons from the valence to the conduction band due to the strong electric field (*Zener breakdown).* Also, charge carriers accelerated by the electric field may gain sufficient energy to break up covalent bonds in the lattice upon collisions, resulting in additional electron-hole pairs (*avalanche breakdown*) [Lutz, 2007]. Obviously, reaching this breakdown level is not desirable for semiconductor detectors operating in proportional mode, in contrast to e.g. SiPMs (silicon photomultipliers).

2.3.3 Signal Formation in Semiconductor Detectors

Incident radiation in the sensitive volume of a semiconductor detector creates electron-hole pairs, similar to the creation of an electron-ion pair in a gas-filled ionization chamber. Due to the electric field, these radiation-induced charge carriers drift parallel to it, resulting in a measurable signal current.

Depending on the nature of radiation, the shape of the radiation-generated charge cloud differs. For near-infrared, visible and ultra-violet light, generally one single electron-hole pair is created per photon. Given the limited penetration depth of light in silicon, this happens close to the detector surface for visible and ultra-violet light, while the relatively longer penetration depth of near-infrared light can result in charge-carrier creation at slightly larger depths, provided the photon energy is still larger than the bandgap ($E_g = 1.12\,\text{eV}$ for Si).

The higher energetic x-rays can produce several electron-hole pairs within a very localized spatial region. From the average energy required to create a pair of charge-carriers, the number of generated pairs can be estimated.

Charged particles passing through a semiconductor produce many electron-hole pairs along their tracks. The ionization density increases with the penetration depth according to eq. 2.17, resulting in a pronounced maximum at the end of their range inside the detector. Neutrons and high-energetic photons can also produce signal in a semiconductor detector by generation of charged secondaries. However, the probability for this to happen is rather small. Thus, for their detection, silicon detectors are typically combined with other materials (e.g. scintillators).

Ideally, the number of generated electron-hole pairs is proportional to the energy deposited inside the semiconductor detector. For high-energy quanta, the energy to produce an electron-hole pair in silicon at room temperature is $E_i = 3.6\,\text{eV}$. Thus, it is about a factor of 10 smaller than the amount of energy required to create an electron-ion pair in a gas-filled detector. The relative statistical fluctuations in the number of created charge carriers is therefore reduced, as their total number is by a factor of 10 larger. This factor influences the limiting energy resolution of a detector. Remarkably, the observed statistical fluctuations are even smaller than expected according to a Poisson model. The so-called *Fano factor F* was introduced to relate the observed variance to the variance predicted by the Poisson model. The intrinsic energy resolution of semiconductor detector is hence

given by [Spieler, 2005]

$$\Delta E_{FWHM} = 2.35 \cdot E_i \sqrt{F N_Q} \, , \tag{2.39}$$

where N_Q is the number of created charge carrier pairs, which is the total deposited energy divided by E_i.

Due to thermal excitation, a small amount of current is always present. This is commonly referred to as *dark current* or *leakage current*. By cooling the detector, leakage current can be drastically reduced. Leakage current can also be increased by lattice defects, which will be further addressed in the following.

2.3.4 Radiation Damage

The performance of a semiconductor detector strongly depends on the near perfection of the crystal lattice. Any defects can lead to trapping of charge carriers and incomplete charge collection [Knoll, 2010]. Non-ionizing energy transfer to the lattice atoms by incident radiation can lead to irreversible changes and a degradation of the detector.

Basically, one can discriminate between two types of radiation damage mechanisms [Spieler, 2005]:

- In *displacement damage*, an incident particle or photon that is able to deposit an energy of about $25\,\text{eV}$ to a silicon atom, can displace it from its lattice site. This can result in the formation of mid-gap states within the bandgap between valence and conduction band. This additional level facilitates the emission and capture process of charge carriers. In reverse-biased diodes, this leads to an increased leakage current. Additional states close to the edge of the bandgap increase the probability of trapping, i.e. charge carriers may be temporally captured. The measured signal is hence reduced, but as trapped charge carriers are released after some time, this results in an additional source of noise. Furthermore, displacement damage can result in a change of the doping characteristics which modifies the electrical properties of the semiconductor material and can result in *type inversion*, i.e. the n-type region appears p-like.

- The second type of radiation damage is called *ionization damage*. Electron-hole pairs are not only generated in the semiconductor, but also by energy absorption in insulating oxide layers. The liberated charge carriers diffuse or drift until they are trapped somewhere, causing unintended charge concentration and hence parasitic electric fields. This mechanism is independent of the type of radiation but increases with increased energy deposition.

State-of-the-Art

This chapter sets the experimental and computational studies performed within the framework of this thesis in context to the state-of-the-art in the respective fields. An overview of currently existing and commonly used diagnostic instruments for the characterization of laser-accelerated ion bunches is given in section 3.1. Advantages and drawbacks of the individual techniques are highlighted, indicating the need for further developments. In section 3.2, different approaches for proton radiography from conventional and laser-driven accelerators are presented.

3.1 Characterization of Laser-Accelerated Ion Bunches

Due to the unique features of laser-accelerated ion bunches summarized in section 2.1.4, combined with the harsh environmental conditions (high vacuum, EMP), the diagnostics of such bunches is a challenging task. Various different diagnostic devices are often used in parallel, as no single detection system provides the ultimate capability to give unambiguous, accurate and precise measurement of the entire outcome of the laser-plasma interaction. This section is intended to give a brief overview of detection systems that are commonly used for characterization of laser-accelerated particle bunches. Within this overview, diagnostic instruments are sub-divided into *offline* and *online* detection systems, defined by the time it takes to obtain the relevant information after the experiment. Thus, online refers to diagnostics that is suitable for moderately high repetition rate ($\sim 1\,\mathrm{Hz}$) experiments. Although interesting properties of the laser-plasma interaction and therefore predictions of accelerated ions can be performed indirectly by probing the laser-induced plasma itself, this overview is only dedicated to the direct detection and characterization of ions.

Typically, both offline and online detection systems are coupled to a certain energy-selection, or rather energy-dispersion system, which is based on the energy and charge-to-mass ratio dependent deflection of charged particles in a magnetic and/or electric field. Besides the obvious advantage that discrimination between different particle species and

energies is possible in this configuration, the detector itself is also less exposed to unwanted background radiation. Further information on commonly used diagnostic devices for laser-accelerated particles can be also found in e.g. Bolton et al. [2014] and Daido et al. [2012].

3.1.1 Offline Detectors

In single-shot laser-ion experiments mainly offline detection systems are used. They are typically based on a (transient) change of some detector material properties, which can be used for delayed beam characterization, partly after some processing and scanning. Their biggest advantage compared to online detection systems is their insensitivity to the strong EMP accompanying the laser-plasma interaction.

Nuclear Track Detectors (CR-39)

A simple but powerful method to obtain the absolute number of laser-accelerated ions is the use of solid state nuclear track detectors like CR-39. It is a transparent plastic polymer (polyallyl-diglycol-carbonate - PADC) and is commercially available in various sizes and thicknesses. If the energy deposition of a charged particle exceeds a material dependent threshold value, the particle creates a track of broken covalent bonds inside the polymer. By etching the irradiated CR-39 track detector in a hot NaOH solution, particle tracks can be revealed due to different etching rates of tracks and undamaged bulk region [Séguin et al., 2003]. It hence results in several µm-sized pits at the surface of the etched nuclear track detector. Using a microscope, the individual pits can then be counted, providing the absolute number of ions that hit the detector.

For spectrometric measurements, several layers of CR-39 are arranged in a stack. Since the penetration depth of ions inside the plastic polymer depends on their initial kinetic energy, an absolute ion energy distribution can be obtained based on the knowledge of the energy loss within each layer. The stack therefore stores the depth distribution, which can be deconvolved for obtaining the energy distribution.

A major advantage regarding the mixed radiation field produced in laser-ion acceleration experiments is that CR-39 is practically insensitive to electrons, x-rays or visible light and allows identification of single ions. Depending on the ion species and energy, as well as on the etching time, an outstanding spatial resolution down to a few µm can be achieved [Daido et al., 2012]. On the other hand, several hours of etching, scanning and pit counting are required to obtain the final ion distribution function. Moreover, at high fluxes ($\gtrsim 10^8$ particles/cm^2) or for long etching times, the individual tracks start to overlap, resulting in saturation and artifacts [Gaillard et al., 2007].
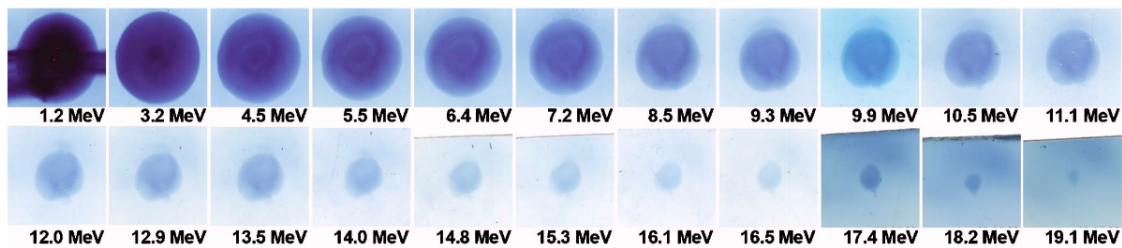
Figure 3.1: RCF stack after exposure to a laser-accelerated proton bunch at the TRIDENT laser at the Los Alamos National Laboratory (LANL). The energies below the films indicate the proton energies, for which the Bragg peak lies inside the respective film layer. From Nürnberg et al. [2009].

Radiochromic Films (RCF)

Being comparably inexpensive, radiochromic films (RCF) are widely used as diagnostic device for laser-accelerated ion bunches. They are blueish or yellowish plastic films of some 100 μm thickness. The active layer of RCFs, which is sandwiched between two plastic substrates, is composed of organic monomers. Exposure of the constituents of the active layer to ionizing radiation leads to polymerization, which results in a significantly increased optical absorption. The color of the darkening depends on the absorption spectrum of the polymers.

The advantage of RCFs as compared to CR-39 is their simple handling, as they are self-developing. Film coloring appears within milli-seconds after irradiation. However further non-negligible darkening occurs within the next hours. Therefore, when scanning the films for spectral analysis it is recommended to wait two days after exposure [Bolton et al., 2014].

RCFs can be read out by scanning them with conventional color flat-bed CCD[1] scanners. The measured quantity is the optical density (OD), which is the negative decade logarithm of the intensity I transmitted light through the exposed film, divided by the light intensity without film I_0:

$$OD = -\log(I/I_0) \ . \tag{3.1}$$

The OD can be calibrated against dose deposition in the film at a conventional accelerator. However, a strong dependence of the film response on the scanning orientation has been reported [Butson et al., 2006] and should therefore be taken into account wherever an accurate dose measurement is required. Furthermore, the high linear energy transfer (LET) of low-energetic protons and heavy ions results in a considerable under-response *(quenching effects)* of the film that needs to be accounted for [Kirby et al., 2010].

Similar to the CR-39, it is often convenient to arrange RCFs in a stack to obtain spectrometric information of the ion bunch. Lower energetic protons are stopped within the first layers, while protons with higher energies reach the more downstream layers. The

---

[1]Charge-Coupled Device

proton energy spectrum can then be reconstructed from the measured dose deposition [Nürnberg et al., 2009]. An example of an RCF stack after irradiation is shown in figure 3.1.

Like nuclear track detectors, RCFs provide an excellent spatial resolution of some µm and different film types are available, that cover dose deposition over a large dynamic range (1 mGy up to 400 Gy) [Bolton et al., 2014]. However, single particle detection is not possible using RCFs. Also, RCFs are sensitive to any kind of ionizing radiation, including x-rays and ultra-violet light.

Image Plates (IP)

Image plates (IP) are re-usable, two-dimensional position-sensitive detectors based on photo-stimulated luminescence (PSL). The active material is a photostimulable phosphor (BaFBr:Eu^{2+}) screen. Upon exposure to ionizing radiation, electrons are promoted from the Eu^{2+} ions to the conduction band, from where they are trapped at meta-stable F^{+}-centers [Takahashi et al., 1984]. The trapped electrons can again be liberated to the conduction band by scanning the surface of the IP with e.g. a He-Ne laser ($\lambda = 633\,\text{nm}$). From there, they return to the Eu^{3+} ions resulting in excited Eu^{2+*} ions that de-excite under emission of UV light, hence PSL. The emitted light is read by a photo-multiplier tube (PMT) and converted to an electric signal, which (neglecting fading effects) is proportional to the emitted UV light, and hence, to the deposited energy.

Equivalently, by exposing the IP to intense light for at least 15 minutes, the stored information on the IP can be entirely erased. IPs can hence be used several times, which is a major advantage compared to RCFs or CR-39.

The spatial resolution of IPs is in the sub-100 µm range and is determined by the scanner. Like RCFs, IPs are not sensitive to single particles but to any kind of ionizing radiation. They are of special interest for detection of laser-accelerated ions due to the possibility to store energy deposition over a high dynamic range [Paterson et al., 2008].

Nuclear Activation Diagnostic

When using the aforementioned offline detectors (except for CR-39) without additional magnetic and electric fields, it is practically impossible to disentangle the contribution coming from different sources of ionizing radiation from the measured signal. An interesting approach to overcome this problem is based on the measurement of nuclear activation induced by ions with energies exceeding the threshold energy for nuclear reactions ($\sim$ several MeV) [Santala et al., 2001; Offermann et al., 2010]. By choosing a proper target material, β^{+}-emitters can be produced by proton- or carbon-induced nuclear reactions. The activation can then be measured by detection of the two resulting 511 keV annihilation photons. However, this approach is only rarely used, and the capability to resolve spectral details is rather limited [Santala et al., 2001].

3.1.2 Online Detectors

For beam characterization of laser-accelerated ion bunches beyond single-shot experiments, the use of offline detectors is rather impractical. Diagnostic devices giving (nearly) immediate feedback on the ion energy spectrum on a shot-to-shot basis, ideally including spatial information, are therefore an absolute requirement for emerging applications of laser-accelerated ions at (moderately) high repetition rate laser systems.

Micro-Channel Plate (MCP)

A Micro-Channel Plate (MCP) is a two-dimensional matrix of several thousands to millions miniature electron multipliers [Wiza, 1979]. Each of these channels is a glass capillary with diameter of some μm [Bolton et al., 2014]. The channels are typically tiled at a small angle ($\sim 8°$) with respect to the input surface of the MCP. Incident ionizing radiation within a channel produces secondary electrons when colliding with the channel wall. These electrons drift in the applied electric field towards the output electrode, generating multiple further secondary electrons in subsequent collisions with the channel wall. Depending on the channel wall material and the electric field, electron amplification within one channel can be in the order of 10^4, and by stacking multiple MCPs together (*Chevron stack*), multiplication factors as high as 10^7 can be obtained [Wiza, 1979]. MCPs are typically coupled to a phosphor screen, converting electrons to visible light, which can be detected by a CCD camera system.

The spatial resolution that can be obtained using MCPs is approximately the diameter of the capillaries. They are highly sensitive to any kind of ionizing radiation, limiting their use in mixed particle fields to a combined detection system with magnetic or electric fields (see section 3.1.3). Of course, quantitative analysis of an ion distribution requires adequate calibration relating the CCD camera signal to ion number [Prasad et al., 2010].

Scintillator-based Detectors

Scintillators are materials emitting (visible) light subsequent to energy deposition by ionizing radiation. This scintillation light can be detected by e.g. photomultipliers, photodiodes or CCD cameras, giving spatial information on the amount of energy deposited within the scintillator. The range of scintillating materials comprises both inorganic crystals, e.g. NaI(Tl), and organic liquids and plastics. For diagnostic of laser-accelerated ions, mainly the latter type of scintillators is used. A detailed description of the scintillation mechanism can be found in Knoll [2010] and Birks [1964].

In an ideal scintillator, the light yield scales linearly with the energy loss of the ionizing particle. However, this is not true for organic scintillators, where the light output for high-LET particles is lower than for low-LET particles. Therefore, a proper calibration for relevant particle species and energies is mandatory to obtain the absolute ion yield. Of course, this calibration must also include the associated readout system. Moreover, care

has to be taken when using plastic scintillators for diagnostics of laser-accelerated ions, as radiation damage can cause a significant decrease in light yield, whereas some recovery of the damage over a certain time after exposure was observed [Knoll, 2010].

Scintillators are sensitive to any kind of ionizing radiation and the detected light therefore comprises contributions from ions, high-energetic electrons and x-rays. However, it is possible to disentangle the ion contribution for large distances between target and scintillator. If a gated CCD camera is used and both camera and scintillator provide a sufficiently short response time, the initial scintillation light generated by electrons and x-rays can be gated out and only the scintillation light from the delayed ions contributes to the measured signal [Green et al., 2011].

Pixel Detectors

Semiconductor pixel detectors are widely used for x-ray or particle detection, ranging from medical imaging to high-energy physics. Their basic principle has been thoroughly described in section 2.3.

A detailed study on the usability of such detectors for direct detection of laser-accelerated ions can be found in Reinhardt [2012], where a CCD imaging sensor (*Kappa DX-4*), the large-area CMOS sensor *RadEye* and the hybrid pixel detector *Timepix* were tested. The latter two detectors were also used in the framework of this thesis and will be further described in section 4.2.

While all three detectors have shown capable to detect single protons and to withstand the EMP generated in the laser-plasma interaction, only the RadEye sensor was able to detect a $20\,\text{MeV}$ proton flux of up to $10^7\,\text{protons}\,\text{cm}^{-2}\,\text{ns}^{-1}$ without saturation and with linear response [Reinhardt, 2012; Reinhardt et al., 2013]. A general issue of silicon sensors in detection of heavy charged particles is radiation-induced damage of the crystal lattice. This causes an increased leakage current and hence decreased energy resolution. Tests with the RadEye detector have shown that an exposure to $6 \times 10^{10}\,\text{protons}\,\text{cm}^{-2}$ resulted in a loss in dynamic range of 50% [Reinhardt et al., 2013].

Like the two other presented online detection methods, semiconductor pixel detectors are sensitive to all kind of ionizing radiation. Discrimination between different particle species is hence not possible for the RadEye detector. This, however, is possible for the Timepix detector when exposed to a low particle flux (see section 4.2.2).

3.1.3 Advanced Detection Systems

Frequently, the previously described detectors (offline and online) are not used as standalone detection systems, but they are combined with magnetic or electric fields, enabling a better discrimination between different types of ionizing radiation and particle species. Besides, also entirely different detection systems have been proposed and tested for diagnostics of laser-accelerated ion bunches, relying on the localized heating induced by the
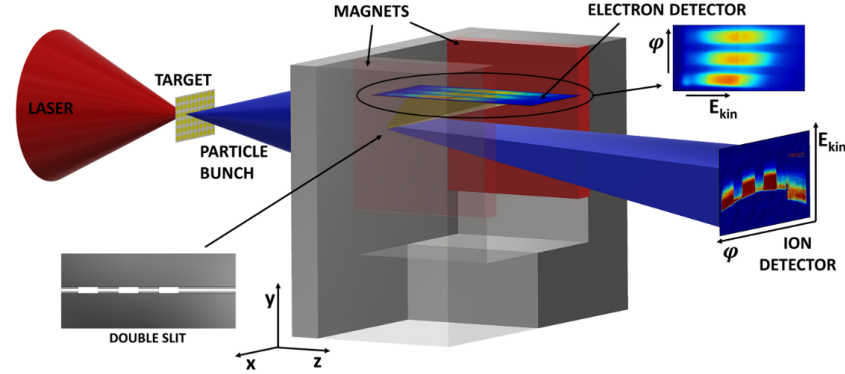
Figure 3.2: Sketch of the wide-angle spectrometer for combined ion and electron spectrum measurement. The particle bunch (indicated in blue) enters the magnetic spectrometer through a *double slit* (see magnification). Large-area pixel detectors are placed on top of the dipole magnet to detect electrons, as well as in forward direction for ion detection. From Lindner et al. [2018].

energy deposition of heavy charged particles in a water tank, or on the time-of-flight difference of ions with different kinetic energies, as compared to x-rays and ultra-relativistic electrons.

Magnetic Spectrometer

In order to obtain ion spectra with high energy resolution, the energy-dependent dispersion of ions in a magnetic field can be exploited, combined with one of the previously described detectors. Laser-accelerated particles enter a set of (permanent) dipole magnets through a thin entrance slit or pinhole. According to their opposite charge, electrons and ions are deflected in the magnetic field in different directions, while the deflection angle depends only on their momentum. The energy range that can be resolved is determined by the magnetic field strength, the distance between magnetic field and detector, as well as by the size of the detector in the dimension of the deflection. The energy resolution is mainly determined by the width of the aperture and the spatial resolution of the detector. Particle energy calibration can be obtained by adding thin layers of absorbing materials directly in front of the detector, providing unambiguous stopping edges corresponding to certain ion energies [Chen et al., 2008].

Wide-angle spectrometers (WASPs), i.e. a set of dipole magnets with a long entrance slit and a sufficiently large gap between the two dipole magnets, are used to obtain also one-dimensional angular distribution of the ion energy spectrum. A WASP with energy resolution better than 10% at $50\,\mathrm{MeV}$/nucleon ions and an acceptance angle of 30° was presented by Jung et al. [2011a]. For detection of the deflected ions, a layer of CR-39 followed by an IP with a distance of $32\,\mathrm{cm}$ to the magnet is used in this setup. The two-layer design of the detector allows to distinguish between protons and C^{6+} ions, as for the same momentum, the range of protons is significantly longer than for carbon ions. Replacing offline detectors by e.g. large-area pixel detectors transforms magnetic spectrom-

eters into an online diagnostic device. An online WASP, which is capable to measure both ion and electron spectra has been recently presented [Lindner et al., 2018]. It is based on the RadEye pixel detectors and a dedicated double-slit configuration at the aperture of the magnetic field (see figure 3.2). This spectrometer was used as standard diagnostic device in experiments performed at the Laboratory for Extreme Photonics (LEX Photonics).

Since the magnetic deflection alone is not sufficient for separating ions with different charge-to-mass ratios and for a wide energy distribution, magnetic spectrometers are best suited for experiments where protons are the dominant ion species. However, with increasing proton energies, high magnetic fields and large distances between magnetic field and detector are required to maintain a reasonable energy resolution. This makes magnetic spectrometers bulky and hence rather impractical for diagnostics of high-energy protons. Moreover, using this diagnostic device simultaneously to an application is limited, as the initial particle bunch is almost entirely lost. Nevertheless, for some applications the magnetic deflection can be useful to obtain a quasi-monoenergetic proton distribution at a certain position and without x-ray background [Bin et al., 2012].

Thomson Parabola Spectrometer

A full spectrometric characterization of mixed ion fields is not possible when relying only on magnetic deflection. A common method to overcome this problem is based on the mass-spectrometer invented more than a century ago, the Thomson parabola spectrometer [Thomson, 1910]. It is based on a combination of electric and magnetic field, where the two parallel fields are perpendicular to the propagation of the ion beam. A small pinhole at the entrance of the spectrometer collimates and defines the size of the incoming beam. The deflection of ions in both fields results in characteristic parabolic traces in the detector plane. Different charge-to-mass ratios of ions with various charge states result in spatially separated parabolas. The position along each parabolic trace depends on the kinetic energy of the particle. Higher energy particles are less deflected and hence closer to the zero point, which is defined as the point in the detection plane that would correspond to an undeflected beam. The resolution of Thomson spectrometers is mainly determined by the size of the entrance pinhole and the drift length between the distal end of magnetic and electric field and detection plane, as well as their field strengths.

Thomson spectrometers are a valuable tool for spectrometry in mixed ion fields, especially if the detector is sensitive to single particles. They are widely used in the community for quantitative analysis of laser-accelerated ion bunches. Although both offline and online detectors can be used, current setups mainly employ online detectors such as plastic scintillators [Miao-Hua et al., 2011] or MCPs [Prasad et al., 2010; Cirrone et al., 2014].

Since the deflection depends on the charge-to-mass ratio and not on the ion mass alone, ions with the same ratio are detected within the same parabolic trace. Moreover, different traces can only hardly be resolved in the vicinity of the zero point, i.e. for high particle energies. Also, the pinhole prohibits to obtain any spatial information on the laser-accelerated

ion beam. An overview of recent developments to overcome these limitations is given in Alejo et al. [2016].

Thomson spectrometers are rather complex devices compared to simple magnetic spectrometers due to the necessity to bring high-voltage into the experimental vacuum chamber. In order to obtain a reasonable resolution, such diagnostic devices become rather bulky. The total size of a Thomson spectrometer can easily be in the order of $1\,m$ [Jung et al., 2011b]. Similar to magnetic spectrometers, beam characterization in parallel to experiments using the laser-accelerated ion beam may only be possible in very limited cases.

Online Scintillator Stack

The idea to characterize an ion energy spectrum via its energy loss in a stack of RCFs or CR-39 may also be transferred to an online diagnostic device. This can be achieved by detecting scintillation light from a stack of (plastic) scintillators.

Green et al. [2011] presented a two-dimensional ion beam profile monitor, based on three layers of different plastic scintillators. Each scintillator emits light in a different wavelength range, with the scintillator emitting at the longest wavelength being the first layer. Due to stopping of low-energetic ions in the upper layers, the spectrum of the emitted light contains information on the particle energy. A camera lens behind the scintillator stack couples the light into a fiber optic bundle, guiding the light to an intensified CCD camera. Since the light is guided to the camera located outside of the experimental chamber, radiation damage and distortion due to the EMP are minimized. Moreover, this makes the entire setup quite compact. However, the use of only three scintillating layers results in a rather coarse energy resolution.

A stack of ten $350\,\mu m$ thin plastic scintillators, covered by $13\,\mu m$ thin light-tight black plastic foils to avoid optical cross-talk between the layers was proposed by Metzkes et al. [2012]. The light emission at the upper edge of each scintillating layer was guided to a CCD camera for read-out. This setup allows an energy resolution below $1.5\,MeV$ for proton energies above $12\,MeV$. The last scintillation layer corresponds to a proton energy of $18.3\,MeV$. While the scintillator part of this setup is quite compact, the directly attached housing for the CCD camera still makes the entire device rather big.

Instead of various layers, a more recently proposed setup of the same group makes use of a dedicated absorber matrix prior to only one plastic scintillator [Metzkes et al., 2016]. This matrix consists of 60 macro-pixels with 9 different aluminum absorber thicknesses each. The spatial resolution is hence given by the size of the macro pixels and the energy resolution is determined by the aluminum thickness. Both quantities can be varied by changing the absorber matrix. The scintillation light is detected by a CCD camera, looking at the scintillator from the back via a mirror. Moreover, a hole in the center of the absorber matrix allows the diagnostic device to be used together with an additional Thomson parabola. Similarly, the central part of the beam could also be used for applications.

Despite its quite small footprint, the height of the device (32 cm) might be impractical for some applications.

One attempt to build a compact online scintillator stack, based on a CMOS pixel detector is shown in Englbrecht et al. [2018]. The prototype device consists of a stack of nine layers of radiation hard polysiloxane scintillators [Dalla Palma et al., 2015] on teflon support structures. The thickness of polysiloxane and teflon layers was $\sim 150\,\mu m$ each. The polysiloxane layers are mounted perpendicularly to and are optically coupled to a large-area pixelated CMOS sensor (RadEye1, see section 4.2.3 for details on the detector). The light-sensitive CMOS sensor then detects the radiation-induced scintillation light. To avoid optical cross-talk of adjacent layers, the polysiloxane layers were covered with a thin foil of aluminized Mylar foil. The number of scintillating layers is then a direct measure for the range, and hence for the kinetic energy of the particles. Given that the light yield scales (almost) linearly with the energy deposition, the entire spectrum could then be reconstructed, similarly as for the offline RCF stacks. However, several shortcomings due to problems in the manufacturing have been encountered for this prototype spectrometer, namely a non-uniform coupling of the layers to the CMOS sensor and a non-homogeneous thickness of the layers. Accurate and precise spectrometry is hence not possible with this first prototype, whereas further developments and improvements in the design could potentially result in a reliable spectral diagnostic device for laser-accelerated ion bunches. The limited spatial resolution can be enhanced by the use of a second CMOS sensor coupled to the other edge of the polysiloxane layers.

Ion-Bunch Energy Acoustic Tracing (I-BEAT)

Dose deposition of a monoenergetic ion bunch of short duration in a water volume results in a localized slight temperature increase, which is strongly correlated to the Bragg peak and scales with the number of ions in that bunch. As this heating happens on time scales much shorter than the propagation of sound waves in water ($\sim 1.5\,mm\,\mu s^{-1}$ [Kinsler et al., 2000]), the sudden temperature rise results in a pressure wave, the so-called ionoacoustic effect. This pressure wave can be detected using dedicated ultrasound transducers and allows for a direct measurement of the Bragg peak position inside the water volume [Bowen, 1982; Assmann et al., 2015]. Key requirements for such measurements are short bunch duration and large number of ions, which are fulfilled by the high fluxes obtained in laser-ion acceleration experiments.

The ion-bunch energy acoustic tracing (I-BEAT) was very recently proposed and is based on analyzing the pressure wave, generated by the dose deposition of such ion bunches in a small water volume [Haffa et al., 2018]. Its schematic layout is shown in figure 3.3. A MHz ultrasound transducer is used to detect the pressure wave generated inside a small water volume. The use of an iterative reconstruction algorithm allows to fully retrieve the initial ion energy distribution.

Due to the slow propagation of sound waves in water compared to the speed of light, the
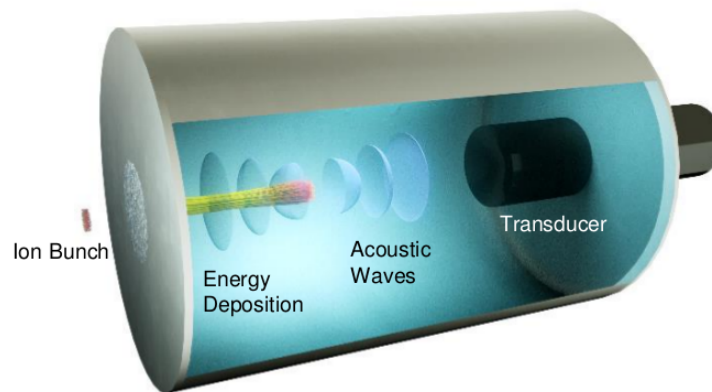
Figure 3.3: Schematic layout of the I-BEAT detection system. The laser-accelerated ion bunch enters a small water volume from the left, deposits its energy in the water, generating an acoustic wave. This pressure wave is measured by an ultrasound transducer. From Haffa et al. [2018].

measured signal is not affected by distortions caused by the EMP. On the other hand, it is still sufficiently fast, allowing high repetition rate experiments, provided that the time it takes for spectrum reconstruction is low. As the detecting medium is water, saturation and radiation damage is practically no concern. This diagnostic device has several promising features for characterization of laser-accelerated ion bunches and may also be used for e.g. some biological irradiation experiments. However, it is not suitable as beam monitoring device in general, since the measurement requires the complete absorption of the ion bunch. Moreover, a spectrum reconstruction discriminating different ion species and charge states without further magnetic or electric field seems complicated, given that the measured sound wave is the result of the total dose deposition within the water volume.

Time-of-Flight (TOF)

A convenient approach to obtain online spectral information of ion bunches is by exploiting the time-of-flight (TOF) difference of ions with different kinetic energies. Detailed considerations on TOF spectrometry are subject of this thesis and will be presented in chapter 6.

First detector systems for beam characterization of laser-accelerated particle beams based on the TOF method were already used more than a decade ago. In principle, any kind of online detector can be used for TOF spectrometry, provided the response time of detector and readout electronics are sufficiently fast for the expected energy- and drift-space-dependent time differences.

Krása et al. [2005, 2008] used a Faraday cup to measure the total current of slow copper and carbon ions emitted from a Cu-plasma produced by a 308 nm excimer laser and a carbon plasma produced by a Nd:YAG laser, respectively. From the measured current signal, they deconvolved the abundance of ions at different charge states and their respective velocity distribution, based on the use of shifted Maxwell-Boltzmann functions. A

similar study was also published for gold ions [Picciotto et al., 2006], where the authors could identify 8 current peaks corresponding to ion groups with different charge states and mean velocities. As TOF differences in their studies are about 2 to 3 orders of magnitude higher than expected for (near-)relativistic protons and the assumption of having Maxwell-Boltzmann velocity distributions does not hold for laser-accelerated protons in general, their technique is not relevant for the study presented in this thesis.

The first reported spectrometric measurement of laser-accelerated protons was based on a 0.2 mm thin plastic scintillator coupled to a photomultiplier tube (PMT) [Nakamura et al., 2006; Yogo et al., 2007]. The current signal was then recorded by a high-speed oscilloscope. In their two presented setups, the drift space between target and detector, which is essential for the obtainable energy resolution, was 2.1 m and 1.4 m, respectively. Proton energies in their reported experiments were below 1.4 MeV and were thus entirely stopped inside the plastic scintillator. The detection efficiency of the scintillator was calibrated using monoenergetic protons in the energy range between 1 MeV and 2.5 MeV from a Van de Graaf accelerator. The PMT current signal was converted to a proton energy distribution dividing it by the energy-dependent detection efficiency. Their results were compared to measurements using a Thomson parabola spectrometer. Reasonably good agreement between the two measurement techniques was observed in the high-energy part of the spectra, i.e. close to the cut-off energy. Although not further discussed, considerable discrepancies could be seen in the low-energy part of the spectra. Two reasons could be responsible for this discrepancy. First, the scintillator response was calibrated for energies above 1 MeV, whereas especially at low proton energies, quenching effects in plastic scintillators are most pronounced. Second, according to their description on how they obtained the proton energy spectrum, they did not take into account the signal prolongation caused by the finite time response of the PMT and scintillator.

A similar setup based on a thicker plastic scintillator and a PMT was proposed by Choi et al. [2009]. The distance between target and scintillator was 1.65 m. A central hole inside the scintillator and the subsequent reflecting mirror allows the central part of the laser-accelerated ion bunch to enter a Thomson parabola spectrometer with CR-39 detectors. An absolute calibration of the TOF spectrometer could hence be obtained by correlating the current signal from the PMT to the simultaneously obtained Thomson spectrometer data. Quenching effects in the plastic scintillator are therefore inherently taken into account. This method is viable, as long as the spectral distribution is rather independent from the angle with respect to the central beam axis. However, calibration and measurements were only performed for relatively low energetic protons (< 1.6 MeV) and the temporal response of the scintillator and PMT were not taken into account. Given the relatively large transit time spread of PMTs, the usability of this scintillator-based setup for higher energetic protons remains to be shown. Improvement could probably be achieved by using faster silicon photo-multipliers (SiPM).

Fukuda et al. [2009] used an MCP at a distance of almost 1 m from a cluster gas target

to detect Helium, Carbon and Oxygen ions with kinetic energies up to 20 MeV/nucleon. However, their measured TOF signal only served as rather coarse cross-check of their spectrum measured using a stack of CR-39 nuclear track detectors, and no effort was made to deconvolve the contribution of different ion species.

Margarone et al. [2011] compared measured TOF signals of different laser-accelerated ion species from various foils, using a Faraday cup, a silicon carbide (SiC) detector and a single-crystal diamond detector. Proton energies up to 2 MeV were reported. Among the advantages of SiC and diamond detectors is their high efficiency and radiation hardness. A long list of publications exists, mostly from the same group, where SiC detectors were used for TOF measurement of laser-accelerated ions, e.g. Cutroneo et al. [2013], Torrisi et al. [2016] or Cannavò et al. [2016]. The TOF signals shown in their publications were either deconvolved using Coulomb-Boltzmann shifted functions [Torrisi, 2016] showing contributions of different ions at different charge states, or qualitatively by calculating the kinetic energy corresponding to the TOF of encountered peaks. Hence, no quantitative spectral information was retrieved. A closer look at their published results also reveals that such qualitative analysis or analysis based on assumed velocity distributions should be done with great caution. Oscillations in the TOF signal are attributed to ion signal, whereas their periodic appearance could also indicate a severe high-frequency cut-off in the measured current signal. Also, in these presented publications, the temporal response function of the detector is not taken into account. The necessity to include the response function for spectrometry can easily be seen, when comparing the decay of the measured TOF signals to fits obtained based only on the Coulomb-Boltzmann shifted functions.

SiC and diamond detectors in TOF configuration are also considered as one diagnostic device at the ELIMAIA (ELI Multidisciplinary Applications of Laser-Ion Acceleration) beamline of the ELI (Extreme Light Infrastructure) in Prague. Installed at a distance of 2 m and 9 m from the laser-target interaction, good energy resolution can be expected also for proton energies approaching the 100 MeV level [Milluzzo et al., 2017b,a; Scuderi et al., 2017].

Fast diamond detectors are also a diagnostic device at the PHELIX laser (Petawatt High Energy Laser of Ion eXperiments) at the GSI (Gesellschaft für Schwerionenforschung) Helmholtz center in Darmstadt, Germany [Busold et al., 2013, 2014, 2015]. Via phase focusing of the emerging polyenergetic proton bunches, the temporal divergent bunch is re-compressed to a bunch length below 0.5 ns (FWHM) at a distance of 6 m from the target. In this configuration, the diamond detector is used to determine the final bunch duration.

However, the published spectra of laser-accelerated ion bunches obtained using the TOF method are typically given in arbitrary units and/or are based on initial assumptions on the velocity distribution of different ions at different charge states. Such assumptions may only be valid in a very limited number of laser-ion acceleration experiments. Moreover, the temporal response function of the detection system was not explicitly taken into account

in these publications, which may result in incorrect spectrum reconstruction for proton energies in the (near-)relativistic energy range and for TOF distances in the order of up to some meters. Last but not least, except for the setup based on the plastic scintillator with a hole, the presented methods are destructive diagnostic devices. Hence, the monitored beam cannot simultaneously be used for other applications. Therefore, the development of a TOF spectrometer with a dedicated reconstruction scheme addressing the aforementioned shortcomings is one major goal of this thesis.

3.2 Proton Radiography

The possibility to use protons for medical imaging had already been pointed out in the early 1960s by one of the founders of computed tomography (CT), Allan Cormack [Cormack, 1963]. A first radiography using 137 MeV protons was published by Koehler [1968], where the *unusually high contrast* and the *relatively poor spatial resolution* due to multiple Coulomb scattering (MCS) were explicitly pointed out.

A first proton radiography of a dog patient was performed by Schneider et al. [2004] at the proton therapy beamline of the Paul Scherrer Institute (PSI) in Villigen, Switzerland. Two scintillating fiber based hodoscopes before and after the patient were used to detect the location of individual protons at the two sides of the dog [Pemler et al., 1999]. A range telescope, consisting of 59 scintillating plates was used to determine the residual range of the protons after having passed the animal patient. Image reconstruction was performed with a backprojection algorithm, assuming straight proton paths. The authors estimated the imaging dose and found a tremendous dose reduction by a factor of $50 - 100$ as compared to an x-ray radiography, being consistent with previous findings [Kramer et al., 1980]. The irradiation time required to obtain the image was 20 s. Spatial resolution is limited by MCS, but an improvement by using more complex reconstruction algorithms based on curved paths (*most likely path*) is feasible [Williams, 2004].

Several systems for proton radiography at other clinical beamlines, based on single particle tracking, have been reported within the past years (e.g. Bucciantonio et al. [2013]; Presti et al. [2016]) with the main goal of patient positioning verification. By rotating proton source and detector, or more easily by rotating the object to be imaged within the instrument by at least 180°, volumetric imaging (pCT - proton computed tomography) can be achieved. The construction of a pCT system, able to acquire images within a clinically acceptable time is an active field of research. A couple of (close to) working prototype systems already exist, e.g. Saraya et al. [2014]; Johnson et al. [2015]; Taylor et al. [2015]. However, pCT is beyond the scope of this project and is therefore not further discussed.

Counting rate capabilities of such tracking systems are typically in the order of 10^6 particles per second. As particle fluxes from laser-ion acceleration exceed these tracking rates by many orders of magnitude, laser-accelerated proton radiography based on particle tracking or counting is far from being achievable. A detailed description of this approach is therefore

beyond the scope of this thesis. A rather complete introduction to this topic and a general overview also of pCT systems can however be found in a recent review paper [Johnson, 2018].

For laser-accelerated proton radiography, position-sensitive and integrating detection systems are required, similar to the first proton radiographies from the 1960s. A first qualitative proof of principle study for proton radiography, using a pixelated CMOS sensor with a monoenergetic proton beam from a conventional clinical facility was presented in Seco et al. [2013]. The main advantage of an integrating detection system is the tremendous decrease of detector complexity. However, this advantage comes at the price of a reduced spatial resolution.

In the following, different radiography approaches based on the detection of the integrated proton signal at conventional and laser-driven proton accelerators are presented.

3.2.1 Imaging using Energy-Modulated Proton Beams

An approach which is not relying on single proton tracking but using an energy-modulated cone-beam was suggested by Koehler in a private communication in 1994 and was first implemented by Zygmanski et al. [2000]. By adding an energy modulator wheel with variable thickness, rotating about an axis parallel to the proton beam direction, they produced a monotonically decreasing proton signal versus penetration depth in water, similar to typical depth-dose curves generated by x-ray absorption. The signal produced in an x-ray intensifying screen downstream of the object to be imaged was captured using a CCD camera. A calibration for the conversion of signal intensity to WET was performed using various thicknesses of PMMA (Polymethyl methacrylate $(C_5H_8O_2)_n$) sheets. Since not optimized for imaging dose, the total dose delivered to the water-filled, $14\,\mathrm{cm}$ high PMMA tube with a diameter of $9.5\,\mathrm{cm}$ was around $0.57\,\mathrm{Gy}$. The proton stopping power values for various materials obtained with this setup were in better agreement with directly measured stopping power values as compared to the conventional approach, where x-ray CT Hounsfield units are converted to proton stopping power based on Mustafa and Jackson [1983] and Schneider et al. [1996]. MCS limited the spatial resolution of the reconstructed image, but visual contrast between PMMA and water persisted up to about 2 line pairs per cm.

Based on these encouraging first results, subsequent studies have been published aiming to investigate the influence of the shape of the modulated depth-dose curve [Ryu et al., 2008] as well as to compensate for the MCS effect on the pCT measurements, while reducing the imaging dose at the same time by using the sparse-view sampling scheme [Lee et al., 2015]. A comparison of a proton radiography using two different energy-modulated proton beams to an x-ray image is shown in figure 3.4.

Another active field of research using energy-modulated proton beams for radiographic and tomographic imaging is based on time-resolved dose measurement (e.g. Lu [2008]; Gottschalk et al. [2011]; Testa et al. [2013]; Jee et al. [2017]) and is of special interest for
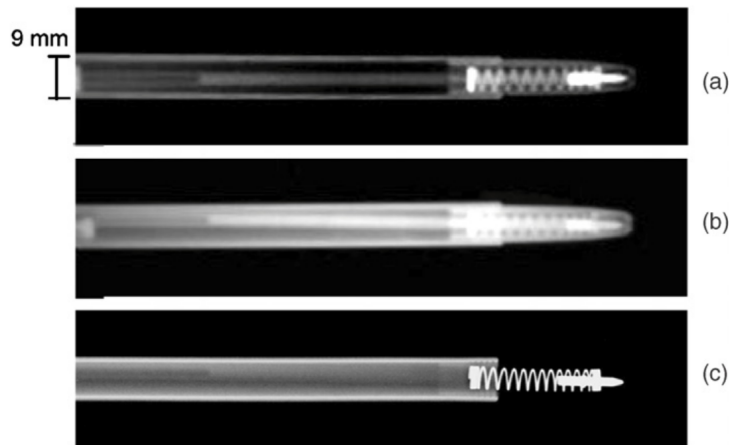
Figure 3.4: Radiographic images of a ballpoint pen with two kinds of modulated proton beam energy distributions (a,b), compared to an x-ray image (c). From Ryu et al. [2008].

proton therapy facilities where passive range modulator wheels are used for the generation of spread-out Bragg peaks (SOBPs). This technique relies on the time dependence of the periodic dose distribution, which is delivered by proton beams passing a range modulator wheel [Testa et al., 2013]. The WEPL of the protons is therefore unambiguously encoded in the measured temporal dose rate function [Jee et al., 2017]. When using a 2D imaging or dosimetric device capable of measuring the dose rate with a sufficient temporal resolution, proton radiographies can quite easily be obtained. Jee et al. [2017] reported an accuracy of the measured relative stopping power values of 2% and an imaging dose of 2.6 mGy for one radiographic image taken within 5 s.

Common to all presented methods in this section is the need for an empirically derived calibration curve. The great advantage of approaches based on energy-modulation is the rather simple setup. Single particle tracking requires sophisticated detectors and fast data acquisition systems for scanning the object in a tolerable time. On the other hand, large-size flat-panel imaging systems with sub-millimeter pixel pitch, as used by Jee et al. [2017], are already commercially available and widely used in clinical routine.

However, the mentioned advantages come at a cost of considerably larger imaging doses as compared to single particle tracking. Also, accounting for the blurring due to MCS is much more challenging since it is impossible to obtain information on the individual particle trajectories.

3.2.2 Laser-Driven Ion Radiography

Radiography using protons accelerated by high-power lasers is becoming increasingly popular. Their unique spatial and temporal properties open up the capability to observe physical phenomena on ns-short time scales. The major interest in the laser-ion acceleration community is the use of such proton bunches for diagnostics of dense plasmas along with electric field distributions inside such plasmas and around the laser-irradiated
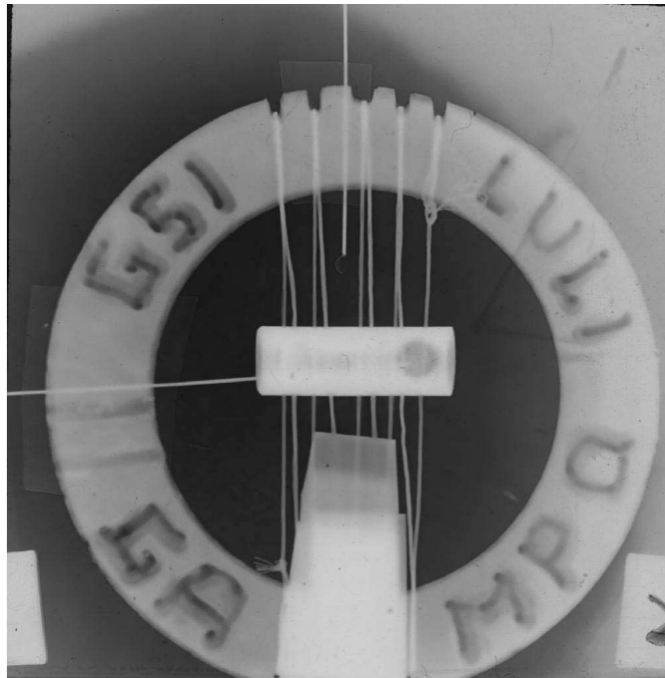
Figure 3.5: Laser-accelerated proton radiography of a relatively thick compound target, composed of a 1 mm thick epoxy ring with engravings of the names of the collaborating institutes, copper wires, a hollow steel cylinder, several thin titanium sheets and a glass hemisphere. From Roth et al. [2002].

targets [Borghesi et al., 2001; Roth et al., 2002]. This kind of radiographic applications is dominated by the use of offline detectors, such as CR-39 or RCFs. Temporal information is obtained by exploiting the polychromaticity of the laser-accelerated ion bunch. Higher energetic protons reach the object to be imaged first and have the largest penetration depth in a stack of offline detectors.

Faenov et al. [2009a,b] used carbon and oxygen ions with energies up to 4 MeV, accelerated by a Ti:sapphire laser system focused onto a CO_2 gas cluster target, for nanostructure diagnostics. By placing the objects to be imaged 14 cm and 16 cm from the laser target and using CR-39 track detectors, they could measure thickness inhomogeneities below 100 nm and resolve small structures with $< 1\,\mu m$ spatial resolution. An absolute requirement for such resolution is, however, that the detectors are placed in direct contact with the back surface of the object.

Choi Chang et al. [2011] compared radiographic images of sub-mm sized objects obtained with laser-accelerated protons and 1.8 MeV protons from a Tandem accelerator. Again, CR-39 was used as detector with the objects directly attached to it to keep scattering-induced image blurring small. Based on their acquired radiographies, they concluded that the use of a polyenergetic proton beam is superior to the use of a monoenergetic proton beam. A spatial resolution of several μm was reported in a follow-up study, with optimized etching conditions of the nuclear track detector [Son et al., 2014].

Roth et al. [2002] were the first presenting a laser-accelerated proton radiographic image of an object beyond the μm scale. The object to be imaged was placed 5 cm behind

the laser-irradiated target and a stack of RCFs was placed closely behind the object. The radiography of their compound target, consisting of a 1 mm thick epoxy ring, copper wires, a hollow steel cylinder, several thin titanium sheets and a glass hemisphere is shown in figure 3.5. Note that the image corresponds to one layer of RCF, corresponding to a residual proton energy of 7.5 MeV.

All of the radiographic approaches using laser-accelerated ions rely on the use of offline detectors, making imaging in (nearly) real-time impossible. Furthermore, the presented studies were not aiming to obtain quantitative information from the measured radiographies, but only acknowledged the measured high contrast corresponding to different traversed materials and thicknesses.

With energies of laser-accelerated protons approaching 100 MeV, an entirely new field of applications for proton radiography opens up. Given that the range in water of protons at this energy range is in the order of some cm, laser-driven proton bunches can be used to irradiate and image larger scale objects, like e.g. for biomedical studies of small animals. Obviously, this requires radiographies from which quantitative information can be retrieved, ideally immediately after exposure to the ion bunch. The latter, of course, requires the use of online detection systems. Moreover, imaging in the vicinity of the laser-plasma interaction is not feasible when it comes to in-vivo experiments as this would result in prohibitively large doses and requires bringing the object into high-vacuum.

Instead of the approach described in section 3.2.1, relying on actively or passively modulated monoenergetic proton beams from conventional accelerators like synchrotrons or (synchro-) cyclotrons, the inherent polychromaticity of laser-accelerated ion bunches could be inherently exploited for such imaging purposes. Typical TNSA spectra show an exponentially decaying shape with a beam divergence of a few degrees up to a few tens degrees. This hence results in a monotonically decreasing depth-dose distribution and a transversally broad proton field, without any additional scatterers or absorbers.

Computational Tools & Experimental Materials

In this chapter, tools and materials for the experimental and computational studies carried out in the framework of this thesis are presented. First, in section 4.1 the FLUKA Monte Carlo code, which was used for many purposes within these studies is briefly introduced, highlighting the relevant features and user-routines. Section 4.2 comprises an overview of the detectors that were used for both experimental and simulation studies. Their basic functionality and their fields of application are described. Finally, the ion accelerators and laser systems where experiments were conducted are presented in section 4.3. These are the Munich Tandem accelerator, the ATLAS-300 laser system at LEX Photonics used for ion acceleration and the ZEUS laser system, where detector characterization measurements were carried out.

4.1 FLUKA Monte Carlo Simulations

FLUKA (FLUktuierende KAskade) is a general purpose Monte Carlo (MC) code for the calculation of particle transport and interaction with matter [Ferrari et al., 2005; Böhlen et al., 2014]. Its origins go back to the 1960s, when it was written by Johannes Ranft at CERN with the purpose to design shielding of high energy proton accelerators. Throughout the decades, FLUKA was gradually further developed such that it nowadays covers a huge variety of applications ranging from high energy physics over radiation protection studies to medical physics and radiobiology, just to name a few of the numerous possible applications.

Within the framework of this thesis, simulations were performed with the most recent FLUKA releases available at the time, ranging from the now obsolete version 2011.2b.6 to the current version 2011.2x.2. In all these versions, interactions and transport of about 60 different particles and all kinds of heavy ions in a large energy range can be simulated.

Photons and electrons are supported from 1 keV up to thousands of TeV, hadrons from 1 keV up to 20 TeV and neutrons 20 MeV down to thermal energies.

The simulation input is read from an ASCII file, in which various *commands*, each consisting of one or more particularly formatted lines (*cards*), define beam source properties, the simulation geometry, output quantities to be scored (*detectors*), particle transport energy cutoffs and step sizes, etc. The simulation default `PRECISIOn` was used for all simulations, as it uses predefined particle transport settings relevant for the conducted studies.

Almost any kind of simulation geometry can be handled in FLUKA using combinatorial geometry, based on bodies and regions specified and arranged by the user. Pre-defined and user-defined materials with arbitrary compositions and properties can be assigned to the created regions. For more complex geometries, FLUKA provides the possibility to create so-called *voxel* geometries. Voxels are tiny, equally-sized parallelepipeds arranged in a 3-dimensional grid and different materials can be assigned to the individual voxels. A graphical user interface, *FLAIR* [Vlachoudis, 2009], is available to create and edit FLUKA input files in an easily readable way. It also includes an interactive geometry editor providing immediate debugging information.

In many more advanced scenarios, the ASCII input cards are not sufficient to describe the problem or to record a specific output. Therefore, many `Fortran` user interface routines (*user-routines*) are available and can be modified to adapt simulation input and output and in limited cases even particle transport according to the user's needs. For the simulations presented in this thesis, two user-routines were used:

- `source.f` allows to sample properties of the primary particles from any kind of distribution or from given phase-spaces. The kinetic energy distribution of the primary particles, as well as their spatial distribution and divergence are defined in this user-routine.

- `mgdraw.f` is used to write during simulation runtime additional output into an ASCII file, which is not accessible via the pre-defined FLUKA scoring functionalities. This is of special interest when information on the exact position, kinetic energy or age of every simulated particle at certain locations within the simulation geometry is required.

The user-routines are activated in the simulation input file by their corresponding cards and are compiled and linked to the FLUKA library, using the event generator DPMJET-3 [Roesler et al., 2001], when creating the executable.

4.2 Detectors

Four different types of silicon detectors were used within the experimental part of this work, namely two prototype microdosimeters, the hybrid pixel detector Timepix and the

(a) Schematic layout

(b) Photograph
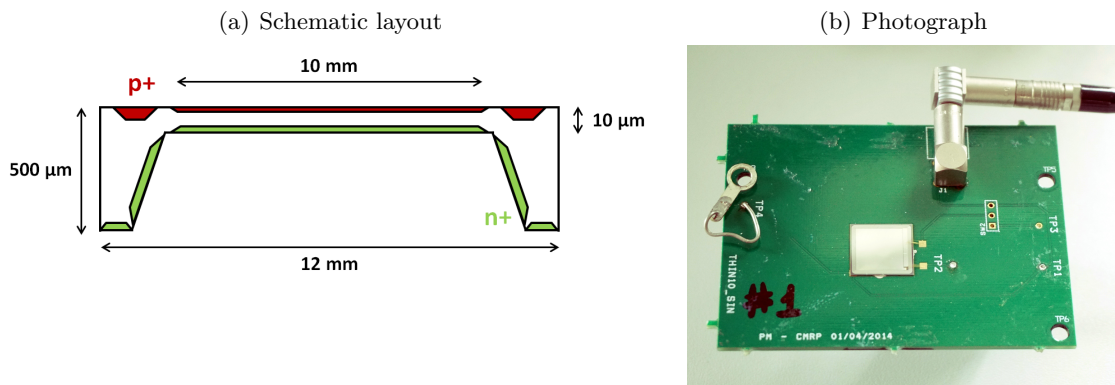
Figure 4.1: Ultra-thin silicon detector. In (a), the layout is sketched schematically. Sizes are not to scale. The detector mounted on the printed circuit board (PCB) is shown in (b).

commercially available CMOS sensor RadEye1. In this section, their main characteristics and functionalities are presented.

4.2.1 Microdosimeters

The first detector types to be presented are silicon microdosimeters developed by the Centre for Medical Radiation Physics (CMRP) of the University of Wollongong, Australia. As microdosimetry aims to measure the microscopic pattern of energy deposition by ionizing radiation, the sensitive volume (SV) of such silicon detectors needs to be micron-sized, i.e., comparable to the dimensions of biological cells [Rossi and Zaider, 1996]. A small SV typically also results in a fast detector response and low energy loss of protons traversing it. This gives rise to the possibility to use this kind of detectors as transmission time-of-flight detectors for the characterization of laser-accelerated ion bunches, where fast response and little interaction with the bunch is desired.

Ultra-Thin Silicon Detector

The ultra-thin silicon detector, shown in figure 4.1, is a planar detector on an n-type substrate. Its peculiarity is the $10 \times 10 \, \text{mm}^2$ large active area having a total geometrical thickness of only $10 \, \mu\text{m}$.
The fabrication process is similar to the production of conventional planar sensors, but with a thickness reduction of the active area, while the surrounding frame remains at the original substrate thickness of $500 \, \mu\text{m}$ for better mechanical stability. High uniformity of the active area's overall thickness is achieved by chemical wet etching using Tetramethylammonium hydroxide (TMAH) [Povoli et al., 2015].
Due to its relatively large active area with very low geometrical thickness, this detector has high potential to be used in transmission with only minimal beam perturbation. However, its planar architecture with large area and low thickness results in a rather large capacity, which can easily be seen from eq. 2.37. This translates into inferior timing properties and
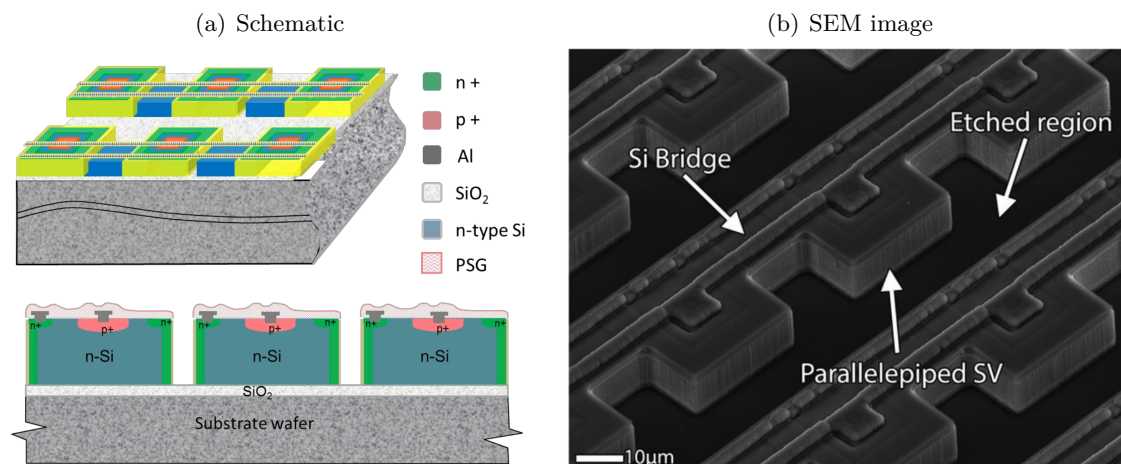
Figure 4.2: BridgeV2 microdosimeter. A schematic 3D view and cross-section of the microdosimeter is shown in (a). From Tran [2014]. In the scanning electron microscope (SEM) image in (b), some of the 3D SVs and the connecting bridges can be seen. From Tran et al. [2015a].

prevents its use in TOF spectrometry of laser-accelerated particle bunches as shown in this thesis project [Würl et al., 2017].

Nevertheless, due to its low geometrical thickness and with proper characterization and readout, the thin detector can be used in transmission prior to any experimental setup to provide online information on the total charge per proton bunch or for triggering a data acquisition system. In the experiments presented in section 6.2.1, the ultra-thin detector was used in transmission mode as trigger and to monitor beam current fluctuations.

Bridge Microdosimeter

To overcome the angular dependence of the ultra-thin detector to incident radiation, research activities at the CMRP are also directed towards fully free-standing 3D SVs. Since this requires rather complex fabrication procedures, the so-called Bridge microdosimeter was developed as an intermediate step. The silicon surrounding the SVs was etched, whereas thin silicon *bridges* between adjacent SVs were left to support the aluminum tracks [Tran, 2014; Tran et al., 2015b,a].

The silicon-on-insulator (SOI) microdosimeter consists of 4248 3D SVs with size $30 \times 30 \times 10 \,\mu m^3$, fabricated on a high resistivity n-SOI active layer and a low resistivity supporting wafer. Thus, in total it covers an area of $4.1 \times 3.6 \,mm^2$ [Tran et al., 2015a]. The square p-n junction structure in each SV was produced by ion implantation and the entire device is covered by layers of phosphorus silicon glass and SiO_2 [Tran et al., 2015b]. The Bridge microdosimeter is segmented into three parts such that capacitance and reverse current of each segment can be reduced. Within each segment, *even* and *odd* pixel rows are read out independently [Tran, 2014]. A schematic view of the design and a scanning electron microscope image of a part of the microdosimeter are shown in figure 4.2.

(a) Test Adapter   (b) Passive Adapter   (c) Active Adapter
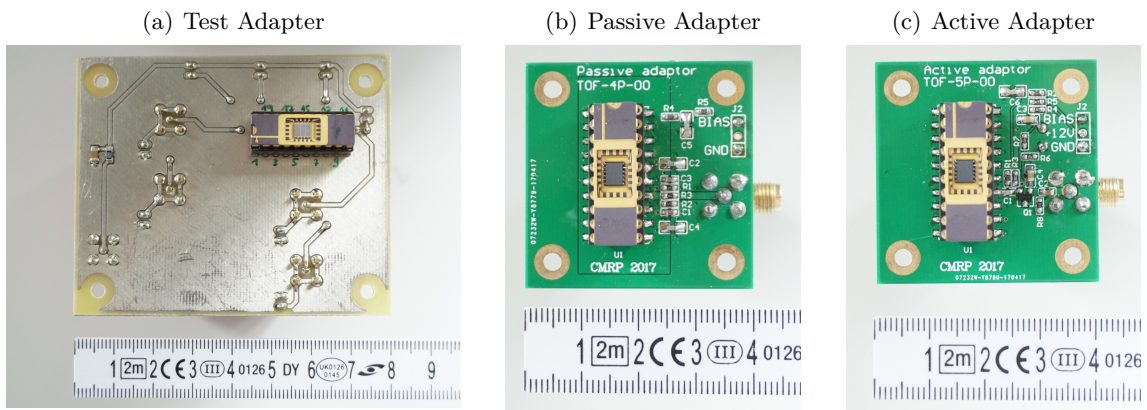
Figure 4.3: Adapters for Bridge microdosimeters with the detectors mounted.

Two versions of this novel microdosimeter were used within this study. In the first version, *BridgeV1*, a 5 µm thick silicon layer was accidentally left surrounding the SVs due to incomplete etching [Tran et al., 2015b]. This shortcoming was solved in the second version, *BridgeV2*, where the surrounding silicon was fully etched down to the SiO_2 layer, providing a well-defined geometry as in the design (figure 4.2a) [Tran et al., 2015a].

For both generations of Bridge microdosimeters, a charge collection efficiency of almost 100% under the core p^+ region of the SVs was found even without bias voltage, while a uniform charge collection in the entire SVs could only be observed for BridgeV2. Charge collection was also detected in the thin bridge regions connecting the SVs [Tran et al., 2015a].

The microdosimeters are mounted on a standard dual in-line (DIL) package in a way that n^+ and p^+ contacts of each of the six arrays can be accessed. Three custom-made circuit boards, shown in figure 4.3, were used as interface between the microdosimeters on the DIL package and the data acquisition system, as well as to provide the external bias voltage to the detector:

- The **Test Adaptor** was the first prototype circuit board to be used. It was given this name, because up to four arrays of the segment could be individually addressed for testing, using jumpers on the backside of the circuit board. Reverse bias voltage is supplied to the n^+ bulk via an RC Filter. Arrays that are not reverse biased and connected to the output are left floating. The current signals of the SV arrays are fed directly to an SMA mount adapter without matching the $50\,\Omega$ load of the readout device. This adapter was used together with the BridgeV1 microdosimeters for detector characterization and for TOF spectrometry of laser-accelerated protons at the ATLAS-300 laser system, presented in chapters 5 and 6, respectively. However, the improper load matching, the jumpers and the not-optimized arrangement of the components and transmission lines on the circuit board resulted in suboptimal performance regarding the pick-up of high-frequency noise.

- Due to the first adaptor's high sensitivity to electronic noise, the **Passive Adaptor** was developed. Only one array of SVs can be read out at a time, while the remaining arrays are connected together and to the bias supply to minimize noise and series resistance. Bias voltage is connected to the n^+ bulk of the detector via a two-stage noise suppression filter. The microdosimeter sources current into a low-ohmic load via two parallel resistances. The current is attenuated by an additional resistance to match the $50\,\Omega$ load of the readout device. The adapter delivers about $5\,mV$ per $1\,mA$ of detected current. Since this circuit board was developed after the shutdown of the ATLAS-300 laser system, it was only used for detector characterization purposes presented in chapter 5 and its actual performance in TOF spectrometry remains to be investigated in future experiments.

- For lower output current of the detector, the **Active Adaptor** was developed. Again, only one array can be read out at a time, while the other arrays are grounded. Bias voltage is supplied to the output (p^+) of the connected SV array. The detected current is fed into a transistor amplifier stage with about $6\,\Omega$ input impedance via a decoupling capacitor. A cable matching resistor is used to achieve the correct output impedance of $50\,\Omega$. Due to the additional amplification stage, the active adapter delivers about $25\,mV$ per $1\,mA$ of detected current. Detector tests and TOF spectrometry experiments at the Tandem accelerator (chapters 5 and 6, respectively) were performed using this circuit board, due to the lower proton fluxes as compared to experiments at a laser-driven ion source.

4.2.2 Timepix

The hybrid pixel device Timepix [Llopart et al., 2007] is based on its predecessor, the position-sensitive single photon counting ASIC chip Medipix2 [Llopart et al., 2002; Llopart and Campbell, 2003], which was developed at CERN by the Medipix2 Collaboration. The device consists of a semiconductor *sensor chip*, which is bump-bonded to the Timepix *readout chip*. Several sensor materials (e.g. Si, CdTe, GaAs) at different thicknesses are available, allowing for various different applications and radiation energies. The n-type semiconductor sensor chip has a single common back-side electrode and a front-side matrix of electrodes (pixels) [Granja et al., 2007]. The sensitive area of the sensor contains an array of 256×256 square pixels with pitch $55\,\mu m$, resulting in a total active area of $1.4 \times 1.4\,cm^2$. Each pixel of the Timepix readout chip contains a preamplifier, a discriminator and a digital 14-bit counter and can be operated independently in one of the following three operation modes [Llopart et al., 2007]:

- **Event counting mode** or **Medipix mode**: The counter increments by 1 for each event above threshold and hence counts the number of incoming particles.

- **Time-over-threshold (TOT) mode**: As long as the input charge from the pream-

(a)
(b)
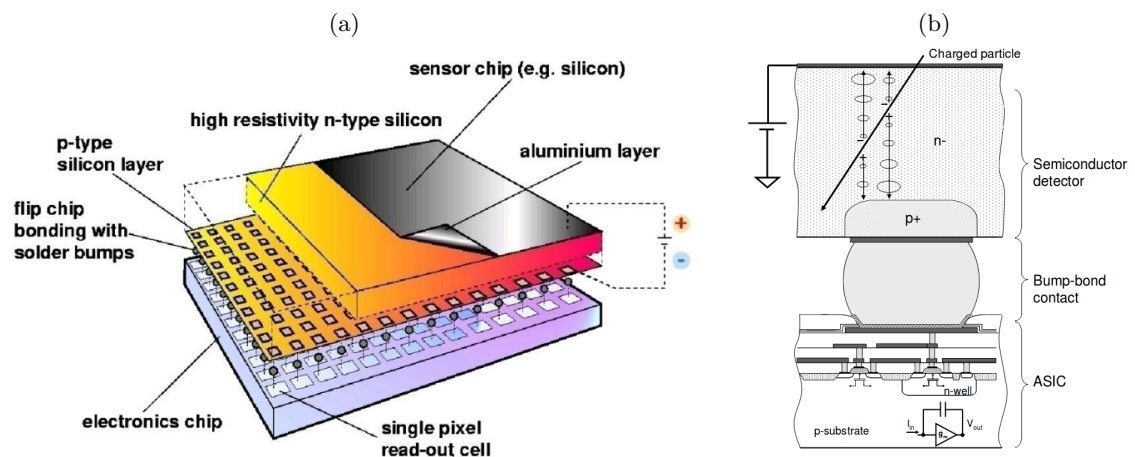
Figure 4.4: Schematic layout of the Timepix detector. In (a), the entire detector is shown schematically, including the sensor chip (reddish), bump-bonded to the read-out chip (bluish). A magnification showing the layout of one pixel is shown in (b). Both figures were taken from Campbell [2012].

plifier output is over threshold, the counter increments continuously. It is therefore a measure for the energy deposition in the sensitive volume.

- **Arrival time mode**: From the moment the discriminator is activated, the counter is incremented until the global shutter signal is set high and thus measures the time of the particle detection.

In any case, the counter is stopped when reaching the overflow limit of $11\,810$ counts [Llopart et al., 2007].

During charge collection, the charge cloud created by single incident ionizing particles inside the sensor chip expands, resulting in the so-called *charge sharing effect*. This is mainly due to electrostatic repulsion and charge diffusion and becomes observable in the charge collection by several adjacent pixels, also called *clusters* [Jakůbek, 2009]. The diffusion of the initial charge cloud perpendicular to the electric field lines and thus the maximum signal height and the size of the clusters can be influenced by changing the applied bias voltage. Higher bias voltage leads to shorter charge collection times and thus results in smaller clusters with a larger peak signal [Kroupa et al., 2014]. Although not related to charge sharing effects, the motion of charged particles within the sensor chip can also affects the size and the shape of the cluster. By analyzing the shape, different particle types can therefore easily be distinguished (see figure 4.5).

Timepix detectors have already been used in a broad field of applications, including radiography and tomography using x-rays, heavy charged particles and neutrons (e.g. Jakůbek [2009]; Gehrke et al. [2018]). Within the framework of this thesis, a simplistic model of this detector is implemented for a MC simulation study regarding its feasibility for laser-accelerated proton radiography (chapter 8). Furthermore, the detector is used in an experimental study exploring edge-on spectrometry of polyenergetic proton sources
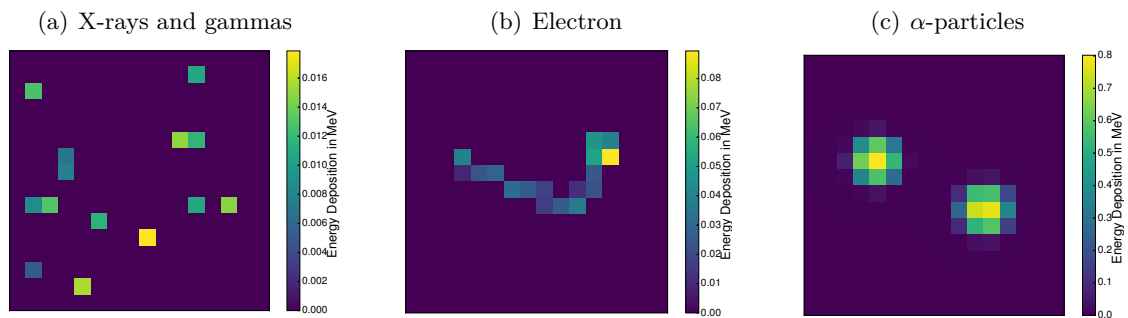
Figure 4.5: Example of Timepix clusters of x-rays and gammas (a), one electron (b) and two α-particles (c).

(chapter 7).

The Timepix detector used within this project consists of a $500\,\mu m$ thick silicon sensor chip. The USB readout interface FITPix [Kraus et al., 2011], developed in the Institute of Experimental and Applied Physics (IEAP) of the Czech Technical University (CTU) in Prague, is used for control of the Timepix device and provides a bias voltage up to $100\,V$ to the sensor. Measured data are acquired and visualized on a PC using the software package Pixelman [Turecek et al., 2011].

4.2.3 RadEye1

The RadEye1 detector is a high-resolution, large area CMOS imaging detector developed by the *Rad-icon Imaging Corp, USA*[1], for digital x-ray radiography. Targeted applications include e.g. mammography, bone densitometry and dental imaging, as well as industrial inspection [Graeve and Weckler, 2001; Reinhardt, 2012]. Making use of the highly developed and widely available CMOS manufacturing infrastructure, the sensors are available at relatively low prices of less than $2\,k\!\in$ per unit.

The detector itself consists of a two-dimensional array of 512×1024 photodiodes along with CMOS structures for readout at a $48\,\mu m$ spacing. Hence, it is covering a total active area of $24.6 \times 49.2\,mm^2$. Multiple sensor modules can be tiled together at three sides, leaving only a gap of less than $100\,\mu m$ between the active areas of two adjacent sensors [Graeve and Weckler, 2001]. Thus, even active areas of $10 \times 5\,cm^2$ can easily be achieved. Each pixel has a fill factor of more than 80%. Both the depletion width and the thickness of the SiO_2 passivation layer on the sensor surface are about $2\,\mu m$ thick [Reinhardt, 2012]. For the abovementioned applications, usually a scintillator screen (e.g. Gd_2O_2S) is directly coupled to the detector to convert the incident x-rays to visible light [Graeve and Weckler, 2001]. However, no scintillation layer is required when aiming for direct detection of protons or heavier ions.

---

[1]now part of the *Teledyne DALSA Inc., Canada*

Figure 4.6: Remote RadEye detector system using four sensor modules. From Reinhardt [2012].

In the *Remote RadEye* configuration, the detector system has proven to be capable withstanding the harsh conditions in the proximity of laser-plasma interactions. It is fully operational and remotely controllable in vacuum, is insensitive to the strong electromagnetic pulse when using proper shielding and has shown radiation hardness up to 6×10^{10} protons cm^{-2}. Moreover, it has proven to be capable of detecting ions over a wide range from single ions up to 10^7 protons cm^{-2} ns^{-1} without non-linearity effects [Reinhardt et al., 2011, 2013].

The Remote RadEye system (shown in figure 4.6) as it was used for some experiments presented in this thesis (sections 6.2.1 and 8.6) and for online diagnostic of laser-accelerated ions at LEX Photonics consists of a *Pleora iPort PT1000* as frame grabber with a *GigE-Vision Ethernet interface* for remote control. An in-house software solution is used to control the PT1000 to provide pulse sequences for readout and reset to the connected sensor modules and to display and store the acquired image frames [Englbrecht et al., 2017].

Besides its experimental use and similar to the Timepix detector, the RadEye1 detector is modeled in the Monte Carlo study presented in chapter 8 as an imaging detector.

4.3 Lasers and Ion Sources

4.3.1 The Munich Tandem Accelerator

Despite the motivation of this work to characterize and use laser-accelerated proton bunches for radiography, most of the experimental work presented hereafter was performed at the MLL Tandem Van-de-Graaf accelerator [Assmann et al., 1974] due to its well reproducible beam characteristics. The electrostatic particle accelerator, located at

the research campus in Garching (near Munich), was built in the late 1960s and became operational in 1970. The following sections present its basic functionality and important features relevant to the reported experiments, along with the methods used to manipulate the continuous and monoenergetic beam as well as to characterize it.

Ion Acceleration

Negatively charged ions are extracted from one out of four different sources and pre-accelerated by a potential of 80 to 150 keV, before they enter within the evacuated beamline a 25 m long pressure tank filled with insulating gas. Depending on the ion source, DC proton beam currents up to 100 µA can be injected into the tank. The ions are accelerated towards the positively charged *terminal*, which is located in the center of the tank and has an adjustable potential of up to about 12 MV. A *stripper foil* in the terminal is used to remove electrons from the negative ions such that the now positively charged ions are further accelerated by the same electrostatic field towards the ground at the other side of the tank. Due to the dual-use of the same accelerating voltage, which gives rise to the name *Tandem*, proton energies up to almost 24 MeV can be obtained. However, for the experiments carried out in the framework of this thesis, only proton energies from 17 to 20 MeV were used. An energy precision of $\frac{\mathrm{d}E}{E} \approx 10^{-4}$ at the experiment can be reached thanks to an 90° analyzing magnet with a bending radius of 1.667 m and a maximum field of 1.6 T [Dollinger and Faestermann, 2018].

Beam Guidance and Diagnostic

After the analyzing magnet, the proton beam is guided through the beamline vacuum ($p \sim 10^{-7}$ mbar) to the experiment via a switching magnet and several quadrupole lenses and steerer magnets. The beam current can be reduced down to 3×10^{-8} of its initial value using three optional attenuators (two providing an attenuation of 1/1000 and one of 1/33) upstream of the switching magnet, which can be inserted individually or combined. Each attenuator is a 50 µm thin tungsten foil with a matrix of laser-drilled holes. The holes are arranged such that the desired fraction of protons can pass through them. The other protons lose some of their kinetic energy and are hence stronger deflected by the switching magnet, preventing them to reach the experiment.

Directly prior to the end of the beamline at the experimental site, a quartz scintillator crystal can be driven into the beam. The crystal is monitored by an ethernet camera via a mirror, giving optical feedback regarding the beam spot position and shape. In addition to that, two CsI crystals mounted on a servomotor which is controlled by a Raspberry Pi single-board computer are included in the actual experimental setup. Both crystals can be flipped into the beam individually. Thus, the beam position at the location of interest, as well as unwanted steering of the beam caused by quadrupole lenses or dipole magnets in the beamline can be detected from the back using a telescope with camera aligned on

(a) Tandem Accelerator

(b) Experimental Vacuum Chamber
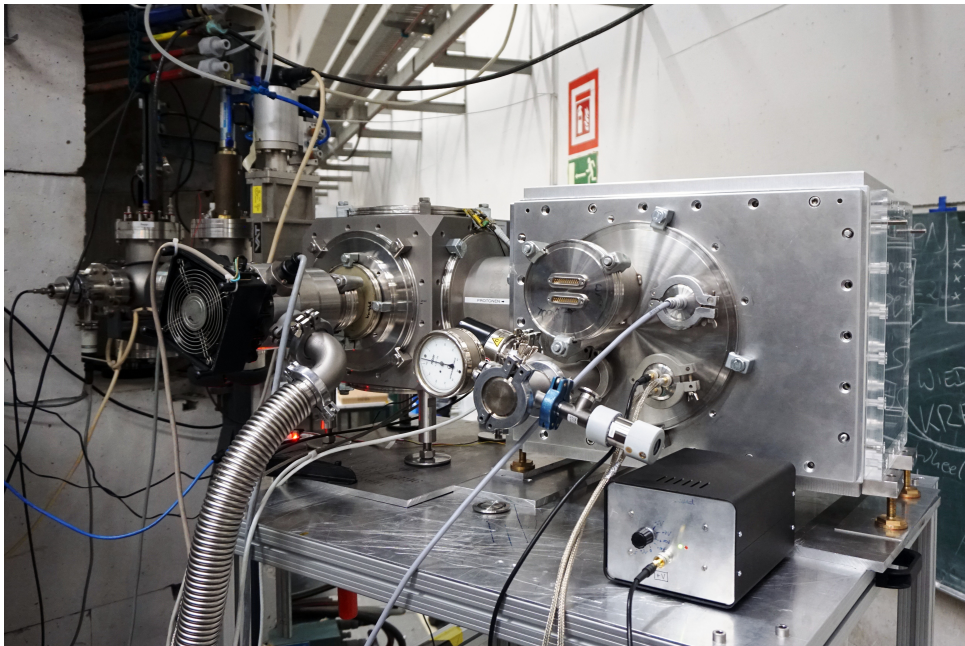
Figure 4.7: The Munich Tandem Accelerator. The pressure tank housing the Tandem accelerator can be seen in (a). In (b), the vacuum chamber, which is flange-mounted to the I-40° beamline is shown. The chamber was used for the experiments performed within the framework of this thesis.

the nominal beam axis.

The proton beam current is checked by Faraday cups (FC) at various locations along the entire beamline. Current values given in this work are the ones measured by the last FC before the experiment, around 20 cm upstream of the quartz crystal.

Generation and Measurement of ns-short Proton Bunches

For the time-of-flight experiments presented in chapter 6, ideally sub-ns short and highly intense proton bunches at a rather low repetition rate are required to mimic the conditions given in laser-ion acceleration. At the Munich Tandem accelerator, pulsed proton beams with a temporal width around 1 ns can be obtained using the built-in chopper and buncher system [Rohrer et al., 1984], located at the low-energy side upstream of the Tandem.

The delay of the 5 MHz electromagnetic field of the buncher with respect to the 5 MHz chopper frequency, as well as the amplitude of the bunching field need to be optimized in order to obtain the shortest possible proton pulses. A mobile measurement setup [Freiwang, 2014], based on a plastic scintillator coupled to a photomultiplier tube (PMT), is used to give immediate feedback of the temporal structure of the bunch, which is required for the optimization of the bunch duration.

The scintillator on the PMT is typically placed under a small angle ($\lesssim 10°$) with respect to the beam axis in vicinity of the vacuum window, or any other thin foil, to detect single scattered protons. The time difference between the arrival of these protons and the following stop signal of the beam chopper is converted to an amplitude by a Time-to-Amplitude Converter (TAC) and is then digitized and stored in a Multi Channel Analyzer (MCA) for further data analysis. Detecting a large number of single protons within individual bunches then results in a histogram showing proton counts versus time difference to the stop signal of the chopper pulse. If the MCA is well calibrated, this yields the temporal structure of the proton bunches.

However, sub-ns measurement accuracy is not achievable with this measurement setup. The reason for this is the jitter of the stop signal of the chopper frequency, which is in the order of 1 ns. Furthermore, it is important to keep the distance between scintillator and scatter foil and the angle with respect to the beam axis small. With increasing angle, the energy distribution of the scattered protons broadens. The broader energy distribution then translates into a longer time interval in which the scattered protons reach the scintillator. Hence, the measured bunch duration would appear longer than it actually is.

Generation of Polyenergetic Proton Bunches using Passive Degraders

In order to obtain polyenergetic proton bunches from the almost perfectly monoenergetic 20 MeV Tandem beam, different energy degraders were designed and produced. One type of degraders was designed to quickly obtain lower proton energies without the need for

a time-consuming change of the acceleration potential. Additionally, range straggling inside the absorber results in an increased energy spread $\left(\frac{\mathrm{d}E}{E}\right)$ of the quasi-monoenergetic bunches. The other type of absorber aimed for producing an energy distribution resembling the typical exponentially decaying TNSA spectrum (see section 2.1). In general, an exponential energy spectrum can be achieved, if different parts of the initially monoenergetic proton beam pass through different absorber thicknesses, where the largest fraction of protons needs to penetrate the thickest absorber and only a small fraction traverses the thinnest (or no) absorber.

The overall requirements for these degraders are listed in the following:

- **Passive absorbers**. Since the energy distribution of ns-short, single proton bunches should be measured in the experiments presented in chapter 6, the use of active beam modulation as commonly done in some clinical facilities to produce spread-out Bragg peaks is not possible here. Therefore, energy degradation needs to be static such that each monoenergetic proton bunch results in a polyenergetic bunch with (nearly) equal energy distribution.

- **Position invariance**. The beam spot size at the Tandem accelerator is around 1 to 2 mm (FWHM) and its position may vary within an area of comparable size. Therefore, the area of the degrader has to be larger than the beam spot size and the position variation of the spot. For the degrader aiming to produce a polyenergetic proton spectrum, an additional constraint arises from the first requirement. Any absorbing sub-structure must be sufficiently small, i.e. smaller than the beam spot size, and must repeat over the entire degrader area.

- **Vacuum compatibility**. Experimental measurements were performed in vacuum. Hence, the absorbers need to vacuum compatible, meaning that they should have low out-gasing and their properties should not change in vacuum.

- **Radiation hardness** and **low activation**. An obvious requirement when irradiating with protons is that the absorber material does not change its properties with accumulated radiation dose. Furthermore, a low level of proton-induced activation of the material or at least short half-lives of the produced radio-isotopes is desired for time-efficient experimental work.

Achieving such small structures as required for position invariance is difficult when using conventional manufacturing techniques. Therefore, the energy degraders were produced using PolyJet 3D-printing technique. The selected material was the rigid transparent photopolymer AR-M2. Its outgasing properties in vacuum were not studied in detail, however test vacuum pumping has shown that high vacuum ($\sim 10^{-6}$ mbar) could be achieved easily even with a large sample of that material inside the pumped volume. Also its radiation hardness has shown to be sufficient for the performed irradiation. Only a

(a) Photograph (b) Expected Energy Spectrum
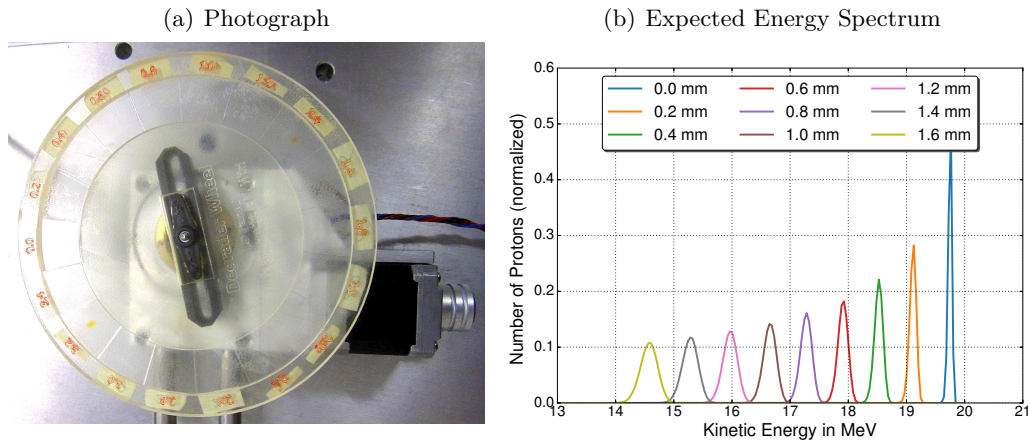
Figure 4.8: Energy degrader wheel for generating monoenergetic proton bunches at the Tandem accelerator with decreased energy and an increased energy spread. In (a), the wheel mounted on a vacuum compatible motorized rotation stage is shown. The expected energy distributions of 20 MeV protons after a 50 μm Kapton foil, the ultra-thin silicon detector and different absorber thicknesses are plotted in (b), according to FLUKA MC simulations.

slight yellowish staining was observed after extensive irradiation with 20 MeV protons. The 3D-printing resolution is specified to be finer than for many other materials ($39 \times 61 \times 15$ μm in x, y and z dimensions) [Waheed et al., 2016]. However, low printing accuracy had been reported in Kamei et al. [2015].

The first energy degrader produced for the studies performed in the context of this work is a round slice, 5 mm thick and with a diameter of 16 cm. This *wheel* has 18 equally spaced 4.2 cm^2 large segments close to its outer edges, each covering 20°. Every segment has a different thickness ranging from 0 mm to 3.4 mm in steps of 0.2 mm. The wheel was mounted on a vacuum compatible motorized rotation stage such that the desired absorber thickness could be remotely placed in the proton beam path. Figure 4.8 shows a photograph of the mounted absorber wheel and the FLUKA MC simulated energy distribution after some of the absorber thicknesses and the additional material (50 μm Kapton and the ultra-thin silicon detector, described in section 4.2.1) in the beam path when performing the experiments.

Since the areas of the degrading segments are large compared to the beam spot size at the Tandem accelerator and a thickness variation below $\sigma = 8$ μm was measured using a micrometer screw, position invariance of the absorber wheel can be stated. The overall thickness difference as compared to the design thickness was found to be below 20 μm for every segment and was taken into account in the data evaluation.

The density of the absorbing plastic was determined in a straight-forward way by accurately measuring the geometrical dimensions and the weight of a 3D-printed sample cuboid of the same material. The obtained density $\rho_{\text{absorber}} = (1.094 \pm 0.005)\,\text{g cm}^{-3}$ was in excellent agreement with the weight of the entire absorber wheel divided by its volume according to the CAD-drawing used as input for the 3D-printer.

(a) 3D CAD Drawing (Cut)

(b) Photography and Microscopic Image

(c) 1D Profile

(d) Expected Energy Spectrum
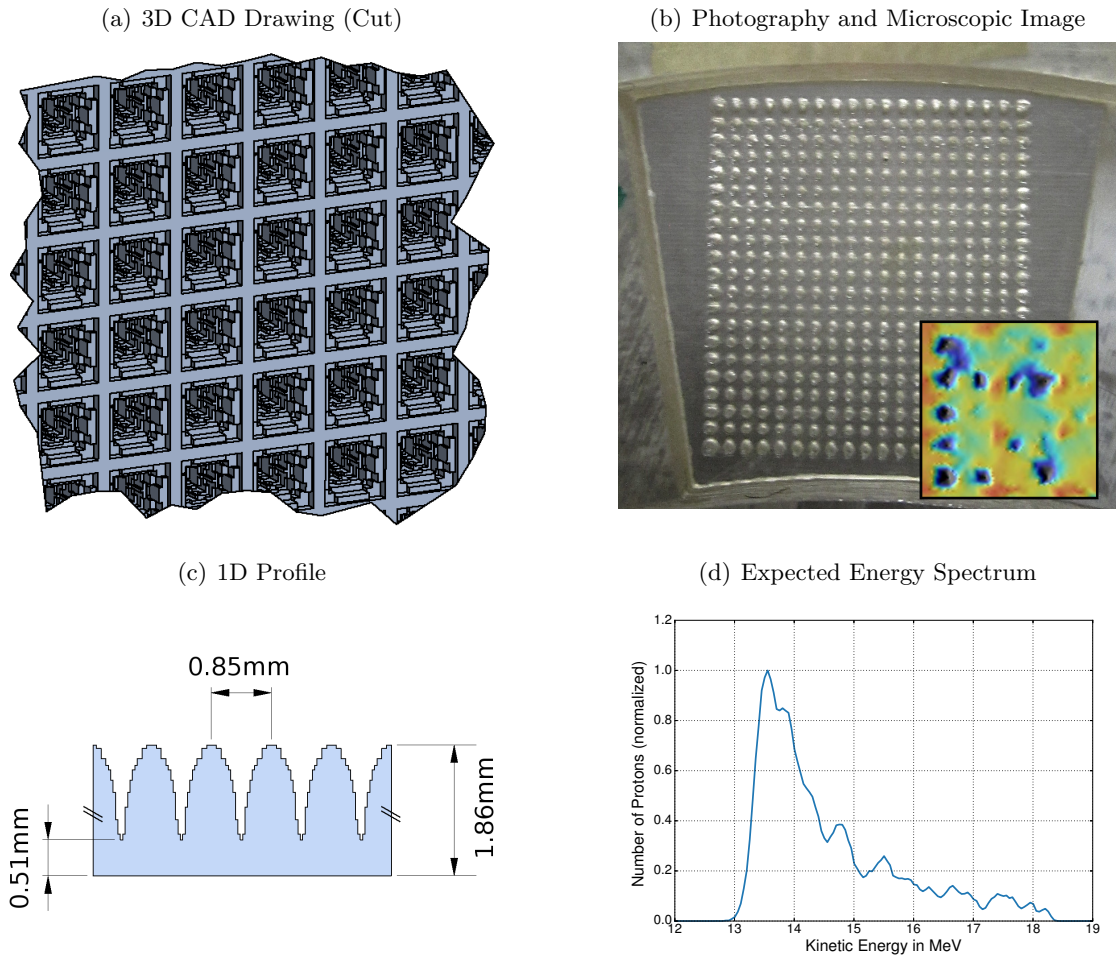
Figure 4.9: Passive energy degrader for generating a polyenergetic proton distribution at the Tandem accelerator. An excerpt of the CAD-drawing used as input for the 3D-printer is displayed in (a). In (b), a photograph of the actual printed degrader is shown together with a confocal microscope image of 5×5 pits. A profile through the pits is sketched in (c). The expected energy distributions of 20 MeV protons after a 50 μm Kapton foil, the ultra-thin silicon detector and the designed absorber, as calculated using a FLUKA MC simulation, is shown in (d).

The second passive absorber was designed and optimized in a trial-and-error method using FLUKA MC simulations to produce an exponential-like energy distribution starting from a lower cut-off energy of around 13 MeV. It consists of a 1.86 mm thin 3D-printed plastic slab of the same lateral dimensions as the segments of the wheel, such that it can be mounted in the 0 mm segment or on top of any other segment. A matrix of 19×21 small pits with convex surfaces, each 1.35 mm deep and spaced by 0.85 mm is used to obtain the broad energy distribution. Figure 4.9a shows a cut of the CAD-drawing with several pits, as it was used as input for the 3D-printer. A 1D profile through the absorber with the corresponding distances is sketched in figure 4.9c. In figure 4.9b, a photograph of the printed absorber is shown together with a confocal microscopic image of 5×5 pits in the inset. It can be clearly seen that the actual printed absorber deviates from its design due to the already mentioned limited printing accuracy. The expected energy distribution

according to the design was calculated in FLUKA and is plotted in figure 4.9d.

It has to be stressed that due to the inaccurate printing of the absorber, the actual energy distribution obviously deviates from the design spectrum. Therefore, measurements using a magnetic spectrometer were performed for comparison (see section 6.2.1). Within these measurements shown thereafter, it turned out that despite the apparently large inaccuracies, the resulting energy spectrum showed only a moderate dependence on the position where the beam spot impinged upon the absorber. Thus, the initial requirements are sufficiently fulfill.

4.3.2 Ion Acceleration at the ATLAS-300 Laser

Until its shut-down for relocation and energy upgrade in December 2016, the ATLAS-300 *(Advanced Titanium-Sapphire Laser)* was a Ti:sapphire laser system situated in the Laboratory for Extreme Photonics (LEX Photonics) at the Garching research campus. The table-top laser system is shown in figure 4.10a. Operating at a repetition rate of up to 5 Hz, it delivered 2 J on target within a pulse duration of 20 to 30 fs (FWHM) and with a central wavelength of 800 nm.

After pulse compression, the laser was guided through a vacuum pipe system below a double floor into the radiation protection *cave*, where a mirror brought the beam into the $0.8 \times 1.0 \times 2.0 \, \text{m}^3$ large *LION* (laser-ion acceleration) vacuum chamber (figure 4.10b). Here, the laser pulses were focused by a 90° off-axis parabolic mirror down to a spot size of 2.7 µm, resulting in a peak intensity of $3.3 \times 10^{20} \, \text{W cm}^{-2}$ [Gao et al., 2017].

An automated foil-target positioning system, based on a motorized target wheel and a hexapod with six degrees of freedom, was used to position thin $(10 \, \text{nm} - 5 \, \text{µm})$ target foils into the laser focus at a 0.5 Hz rate [Gao et al., 2017]. Typically, gold and polymer foils were used in the experiments at LEX Photonics. For the TOF spectrometry experiments presented in section 6.2.2, 600 nm thin plastic foils were used. The target positioning system is shown in figure 4.10c.

The common diagnostic system for characterizing laser-accelerated ions at LEX Photonics was a wide-angle magnetic spectrometer, described in section 3.1 and Lindner et al. [2018]. Proton energies up to almost 12 MeV have been detected, however only ~ 8 MeV protons had been accelerated on a regular basis.

A movable doublet of permanent magnetic quadrupoles (PMQs) could be used optionally to focus the laser-accelerated ion bunches to a target-focus-distance of interest in the range of 0.4 to 1.5 m. Since both, the focal position and the kinetic energy of the focused ion beam depend on the position of the PMQs, this doublet could be used to generate quasi-monoenergetic foci for *design energies* ranging from 6 to 10 MeV [Rösch et al., 2017].

(a) ATLAS-300 laser system

(b) Experimental setup for laser-ion acceleration
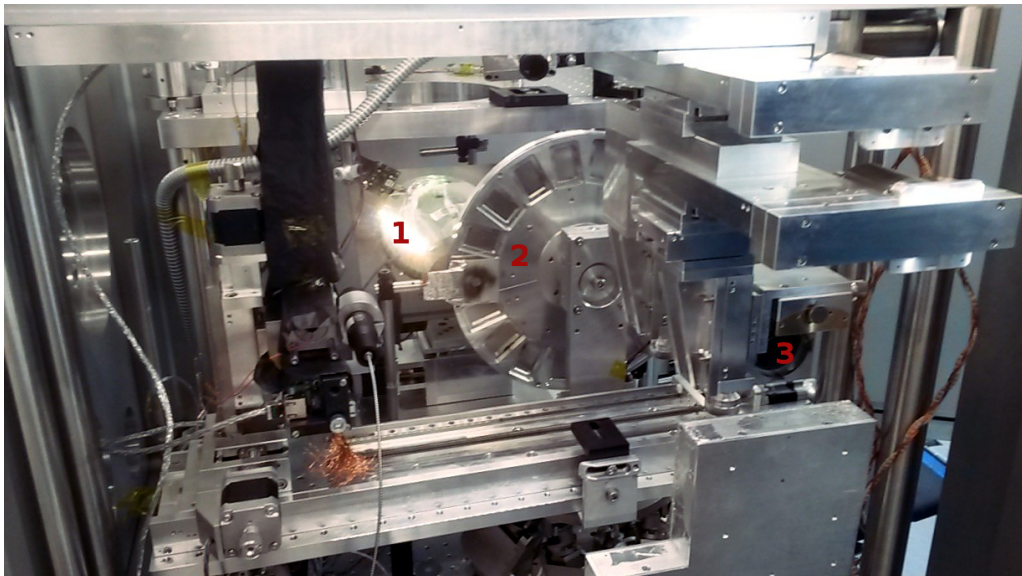
Figure 4.10: Photographs of the experimental setup for laser-ion-acceleration at LEX Photonics. The table-top laser system is shown in (a). From Schreiber et al. [2016b]. The inside of the vacuum chamber used for laser-ion acceleration can be seen in (b). The laser pulses coming from the top are focused by an off-axis parabola (1) onto a thin target foil mounted on a motorized target positioning wheel (2). A pair of permanent magnetic quadrupoles (3) can optionally be used to focus the divergent laser-accelerated ion bunches.

4.3.3 The ZEUS Laser

The ZEUS laser is a femtosecond Ti:sapphire laser system based on the commercial *Cent-Aurus X* laser *(Amplitude Technologies, France)*. End of 2017, it was set up at CALA as a small training laser system. With its two separate pulse compressors, it is well suited to perform pump-probe experiments at modest beam intensities.

It has a central wavelength of 800 nm and runs at a repetition rate of 10 Hz, providing pulse energies of 10 mJ in its probe arm and up to 250 mJ in its pump arm. After temporal stretching, the seed pulse is amplified in a regenerative amplifier and in one or two multi-

pass amplifiers for the probe and the pump pulse, respectively, before it is compressed to a pulse duration of 40 fs.

For a reduction of the pulse energy, which was necessary for the experiments presented in chapter 5, the multipass amplifier was pumped with reduced pump energy. This resulted in an energy around 0.3 to 0.5 mJ. As a result of the reduced pump energy, the amplifier was not saturated, leading to an increase of the ASE level.

Detector Characterization for Time-of-Flight Spectrometry

Essential detector properties required for TOF spectrometry of laser-accelerated ions are fast timing properties, signal linearity over several orders of magnitude and high radiation hardness. The timing properties of a detector are typically expressed by the rise time and the fall time of the detected current signal. Since the TOF of protons in the energy range of interest ($E_{\text{kin}} \sim 10 - 100\,\text{MeV}$) is in the order of $\sim 10 - 20\,\text{ns}$ per meter drift, sub-ns rise times of detector and associated electronics are desirable for high-resolution spectrum reconstruction. Fall times of the detector are not as crucial, however long decay times might lead to incorrect energy reconstruction in the lower part of the spectrum due to blurring of the signal.

Since laser-accelerated proton energy spectra typically have an exponentially decaying shape and the energy deposition inside a thin[1] SV of a detector decreases with increasing kinetic energy, the amplitude of the measured signal may span over several orders of magnitude. An ideal detector would hence be sensitive to single high-energetic protons, as well as to a large number of low-energy ions. Moreover, good radiation hardness of a detector exposed to laser-accelerated ions is required, due to the tremendous proton fluxes generated in this acceleration mechanism.

Within this chapter, the suitability of the Bridge microdosimeters for TOF spectrometry of laser-accelerated ion bunches, based on the aforementioned detector properties, is investigated experimentally. The timing properties are determined by measuring the detector response (function) to an ultra-short ($\ll 1\,\text{ps}$) near-infrared laser pulse and extracting the rise and fall times, respectively[2]. By changing the intensity of the incident light pulse

---

[1]thinner than the residual range of the protons in the material of the SV

[2]Similar measurements had been previously performed for the ultra-thin silicon detector (sec. 4.2.1) and the BridgeV1 detector in a slightly different experimental setup. The results have been published in: M Würl *et al* 2017 *J. Phys.: Conf. Ser.* **777** 012018

over a wide range, non-linearities of the detection system can be found and described properly. The radiation hardness of the detector is estimated in this section by reverse leakage current measurements before and after exposure to α particles.

In section 5.1, the two experimental setups used for this study are described. The findings are presented in section 5.2 and discussed in section 5.3. A conclusion on the suitability of the Bridge microdosimeters for TOF spectrometry, as well as future perspectives are given in section 5.4.

5.1 Materials & Methods

5.1.1 Detector Response Measurements

The response (function) of the Bridge microdosimeters and associated electronics, described in section 4.2.1, is determined at the ZEUS laser system, which is delivering ultra-short ($\ll 1\,\mathrm{ps}$) near-infrared laser pulses with a central wavelength of $800\,\mathrm{nm}$. The refractive index of silicon and the absorption coefficient at this wavelength are $n = 3.669$ and $\alpha_{800\,\mathrm{nm}} = 827.10\,\mathrm{cm}^{-1}$, respectively [Polyanskiy; Schinke et al., 2015]. According to the Beer-Lambert law for uniform attenuation and taking into account the surface reflectance at normal incidence, the transmitted light after $10\,\mathrm{\mu m}$ silicon is about 20% of the initial flux. Therefore, electron-hole pairs contributing to the measured signal are created within the entire sensitive volume and the near-infrared laser pulse can be considered as a good surrogate for irradiation with heavy charged particles.

The laser pulse energy after pulse compression was some hundreds of $\mathrm{\mu J}$ and was then further reduced by additional absorptive filters. However, the interest of this study was only in the relative change of light intensity rather than absolute pulse energy. Therefore, no effort was made in accurately determining the pulse energy that actually impinged the SV of the microdosimeters.

The measurement setup installed on an optical table is shown in figure 5.1. The laser pulses, coming from the left hand side are attenuated by an absorptive filter before reaching a 50/50 beam splitter. The straight arm of the laser pulse impinges the microdosimeter under investigation. The microdosimeter was reverse biased using an adjustable voltage source. The reflected arm is detected by a commercial photodiode *(DET10A/M, Thorlabs, USA)* which was used as a reference and trigger. Additional absorptive filters are attached to the photodiode, assuring that the signal measured by it is not corrupted by saturation effects.

In order to achieve fast response, low load resistance ($R_{\mathrm{load}} \leq 50\,\Omega$) of a broadband readout device is required. Therefore, $50\,\Omega$ DC input coupling of a $4\,\mathrm{GHz}$ oscilloscope *(WaveRunner 640Zi, Teledyne LeCroy, USA)* was used for both the photodiode and the detector. The oscilloscope provides a sampling rate of $20\,\mathrm{GS\,s}^{-1}$ and a signal rise time of about $100\,\mathrm{ps}$. Besides a fast oscilloscope, proper choice of cables is necessary in order
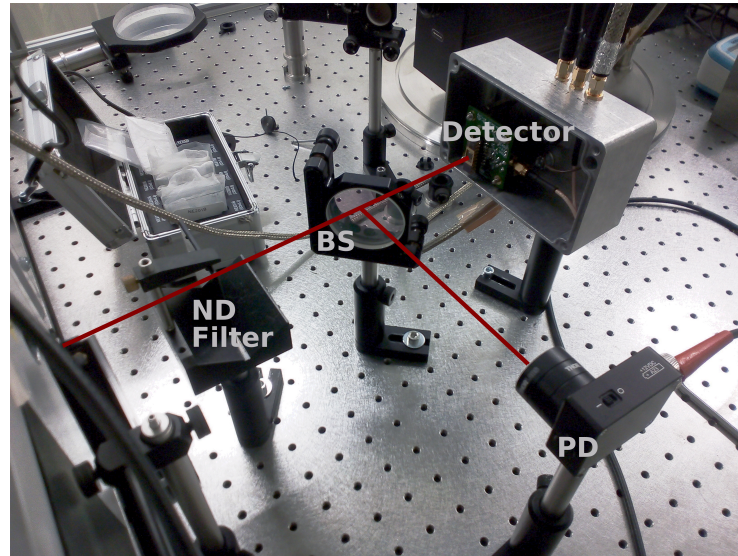
Figure 5.1: Experimental setup for measuring the detector response. The laser pulses (red line) are coming from the left and are attenuated by variable ND filters before reaching a 50/50 beam splitter (BS). One part of the light is measured by a commercial photodiode (PD), the other part is reaching the detector of interest.
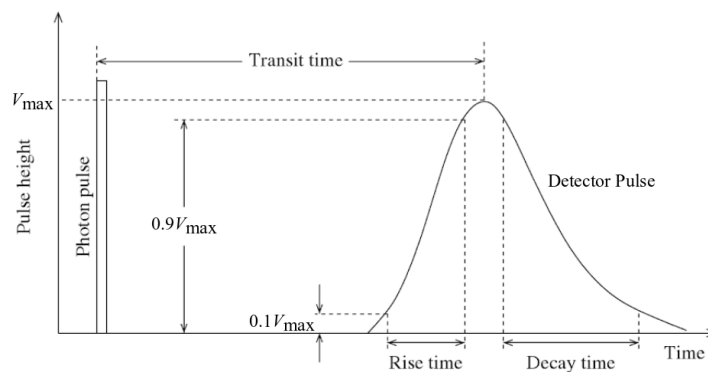
Figure 5.2: Schematic representation of the time response of a detector to an ultra-short incident light pulse. Adapted from Ahmed [2014].

to not degenerate the signal. High-frequency compatible SMA (SubMiniature version A) coaxial cables were used to connect the microdosimeters to the input of the oscilloscope. The same types and lengths of cables were used as in the TOF spectrometry experiments presented in chapter 6, including the SMA vacuum-feedthrough required when operating the detector in vacuum.

A few hundred response curves for every detector, reverse biased at several different voltages ranging from 0 to 10 V, were recorded. During post-processing, response curves where the signal recorded by the photodiode indicates an instability of the laser in terms of light output or is affected by low-frequency noise are sorted out. The remaining traces were used for evaluation and to create the average detector response function for a given set of detector, signal amplitude and bias voltage.

In figure 5.2, the response of a detector to an incident ultra-short light pulse is shown

Table 5.1: Optical density (OD) and measured transmission T of absorptive filters used to measure the detector response to ultra-short near-infrared laser light pulses. OD and its uncertainty ΔOD are specified by the vendor for visible light. The transmissions given in the third column were measured with a photodiode and normalized to the highest transmission ($T/T_{\max}$). Their uncertainty, $\Delta(T/T_{\max})$, is the standard deviation of the respective measured transmissions T, divided by $T_{\max}$.

OD	ΔOD	$T/T_{\max}$	$\Delta(T/T_{\max})$
4.0	0.20	100.00%	11.91%
4.5	0.23	40.07%	4.91%
5.0	0.26	14.60%	1.17%
6.0	0.30	1.28%	0.14%
6.5	0.33	0.53%	0.05%

schematically. The rise and the fall times are defined as the time for the measured current to rise or fall from 10% to 90% or from 90% to 10% of the peak value, respectively. Thus, the timing properties of the detection system can be obtained in a straight-forward manner from the obtained response curves. Since not relevant for subsequent experiments, the transit time indicated in figure 5.2 is not further considered.

5.1.2 Energy Linearity Measurements

For the Bridge microdosimeter seated on the passive adapter[3], a series of detector response curves is acquired as described in the previous paragraph. In order to study the linearity of the detector with incident light intensity, the ND filter prior to the beam splitter is exchanged by filters with different absorption values or complemented by further filters to enhance the absorption.

The nominal light transmission (T) is related to the optical density (OD) via

$$T = 10^{-OD} \ . \tag{5.1}$$

Since the optical density values of these filters are specified for visible light and are given with rather large uncertainties, the actual light transmission of the filters was cross-calibrated using the photodiode. In order not to anticipate linearity of the photodiode over a wide range, the additional absorptive filters prior to the photodiode were adjusted in a way that the peak amplitude measured by it was low ($< 100\,\mathrm{mV}$). A comparison of the photodiode signal with and without the additional photodiode filter was performed at an intermediate global absorption filter, where both filtered and unfiltered photodiode signal amplitude were between $5\,\mathrm{mV}$ and $100\,\mathrm{mV}$. The obtained transmission for the additional photodiode filter was hence measured to be 5.35%.

The measured light transmission for the global filter configurations used in the experiments

---

[3]No measurements were performed using the active adapter, since its amplification stage was only designed for small input currents.

is given in table 5.1. The values are normalized to the maximum transmission obtained using the filter with the lowest OD.

5.1.3   Radiation Damage Measurements

The long-term behavior of the leakage current of a detector can be used to detect the radiation damage the detector has suffered [Knoll, 2010]. An I-V characterization of the individual SV-arrays of the BridgeV2 microdosimeter before and after exposure to a mixed nuclide α source, consisting of ^{239}Pu, ^{241}Am and ^{244}Cm, was carried out. Their dominant α energies are within 5.16 and 5.80 MeV. [Kinsey et al., 1996]. A dedicated FLUKA MC simulation was set up to estimate the fraction of emitted α particles that actually reached the SVs of the microdosimeter. Taking into account the actual activity of the source and the exposure time, the total number of α particles reaching the SV was calculated to be $N_\alpha = 5 \times 10^7$ [Brumer, 2017].

A picoammeter *(Picoammeter 6485, Keithley, USA)* was used to measure the dark current of the Bridge microdosimeter for each array of SVs before and after exposure to the mixed nuclide α source. A tunable DC bias voltage supply was connected to the n$^+$ electrode of the SV array to be measured. The p$^+$ electrode was connected to the picoammeter where the dark current was then read for different bias voltages. Since the Bridge microdosimeter is sensitive to visible light, the setup was shielded from ambient light during measurement. The leakage current was measured at room temperature.

5.2   Results

5.2.1   Detector Response

Normalized detector response curves for the two versions of Bridge microdosimeters on the three adapters are shown in figure 5.3a for a filter setting $OD = 6.0$. To allow better comparison, the three curves are shifted in time such that their peaks are centered at $t = 0$. A fast rise of the signal is common to all three response curves, while the decay of the signal is longer for the BridgeV1 microdosimeter on the test adapter.

The undulations in the decaying slope of all response curves are striking, since typically a decaying shape as shown schematically in figure 5.2 would be expected.

Neglecting these oscillations and analyzing the falling slope of the measured response curves reveals a further interesting characteristic (figure 5.3b). The common model of an exponential decaying signal is not properly describing the observations, but rather the sum of two exponential functions fits the falling slope. The first, *fast*, component can be attributed to signal generated in the pixels where efficient and fast charge collection is present due to the large electric field. Electron-hole pairs created in the silicon forming the bridges between adjacent pixels also contribute to the measured signal. Field strengths inside this part of the detector are much lower, resulting in a slower charge collection and
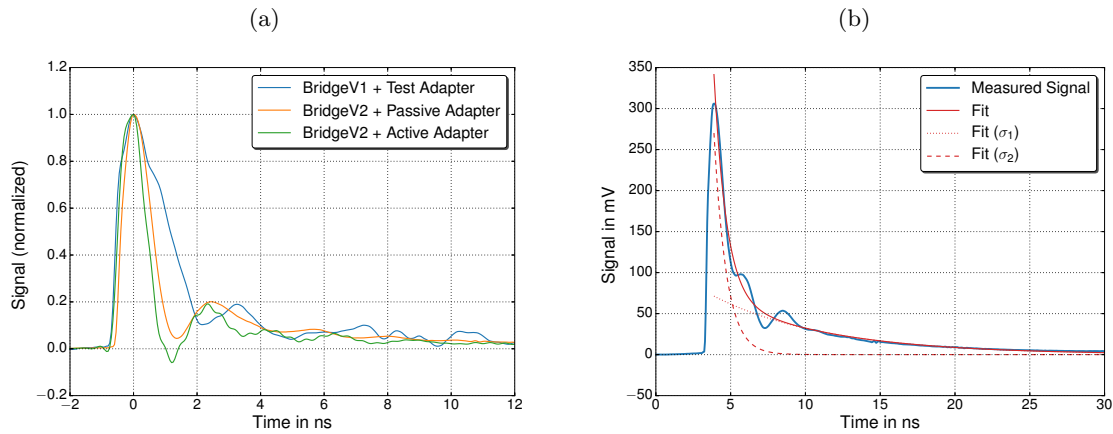
Figure 5.3: Measured detector response functions of the Bridge microdosimeters to an ultra-short near-infrared laser pulse. The detectors were reverse biased at $7\,\text{V}$. In (a), the normalized response curves, measured for $OD = 6$, are compared for three different detector/adapter settings. In (b), a double exponential decay function (red, solid) was fitted to the response of the BridgeV2 detector on the passive adapter (blue), measured with $OD = 5$. The red dashed and red dotted lines show the fast and the slow component of the decaying signal, respectively.

hence longer decay times of the signal. This is referred to as the *slow* component of the signal decay.

Prior to the pronounced peak of all response curves, a shallow signal rise expanding over about $3\,\text{ns}$ can be seen. As this rising pedestal is also observed in response curves measured with the photodiode, it is not connected to the response of the microdosimeters but is due to actual light emitted prior to the main laser pulse. It can be attributed to the ASE of the gain medium of the ZEUS laser system, which was mentioned in section 4.3.3. In order to obtain the actual detector response function, this rising pedestal needs to be subtracted.

5.2.2 Timing Properties

From the individual detector response curves, rise times t_{rise} and fall times t_{fall} were deduced. The results are summarized in table 5.2. Since the active adapter was developed for low output current, only one measurement at low light intensity was performed. Due to the oscillations in the the decaying slope, t_{fall} were extracted from double exponentially decaying fits to the individual signal curves.

Sub-ns response with rise times around $0.4\,\text{ns}$ to $0.5\,\text{ns}$ have been measured for both microdosimeter versions and all three adapters when applying a reverse bias of $7\,\text{V}$, with slightly better performance of the BridgeV2 detector. Since the rise time of the detection system is the square-root of the quadratic sum of the rise time of its components, the rise time of the amplification stage was calculated to be $t_{\text{rise,amp}} = (0.29 \pm 0.07)\,\text{ns}$.

For low current signal measurements, the signal decay time is around $3\,\text{ns}$ for the test adapter and the passive adapter, while it is a factor of 3 times shorter for the active adapter. This can be explained by the additional signal shaping caused by the amplifier.

Table 5.2: Timing properties of the Bridge microdosimeters for different detector and adapter combinations. The detectors were reverse biased at 7 V. The filter settings and the measured average signal amplitudes are given in the second and third column, respectively. The rise and fall times are the mean values obtained from 400 individual response curves, their listed uncertainties are the corresponding standard deviations.

Detector & Adapter	OD	$V_{\mathrm{max}}/\mathrm{mV}$	$t_{\mathrm{rise}}/\mathrm{ns}$	$t_{\mathrm{fall}}/\mathrm{ns}$
BridgeV2 & Passive	4.0	877	0.45 ± 0.02	14.32 ± 0.60
	4.5	563	0.42 ± 0.02	9.48 ± 0.40
	5.0	307	0.38 ± 0.01	6.27 ± 0.17
	6.0	43	0.38 ± 0.02	2.96 ± 0.17
	6.5	18	0.38 ± 0.03	2.69 ± 0.29
BridgeV2 & Active	6.0	167	0.48 ± 0.10	1.03 ± 0.10
BridgeV1 & Test	4.0	1768	0.50 ± 0.02	36.05 ± 4.16
	6.0	60	0.47 ± 0.03	3.12 ± 0.11

(a) Rise Time　　　　　　　　　　　　　(b) Fall Time
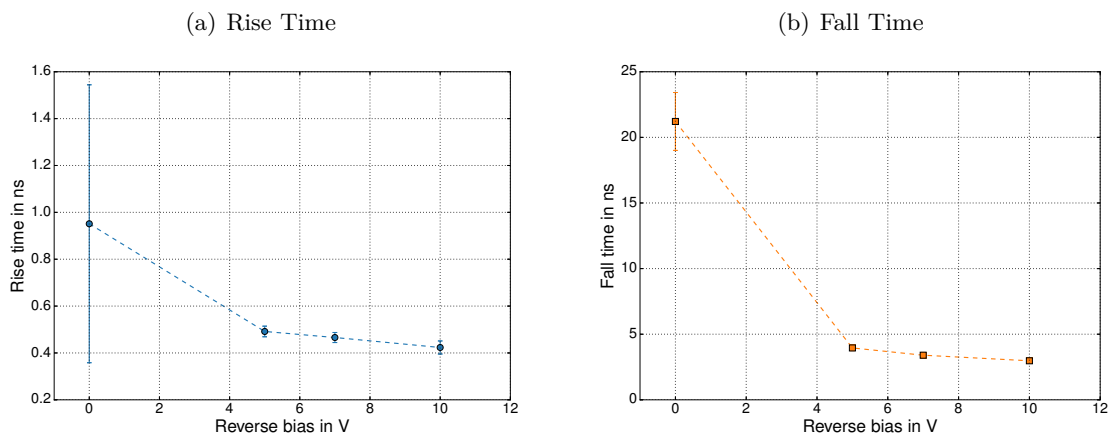
Figure 5.4: Rise times (a) and fall times (b) of the BridgeV1 microdosimeter mounted on the test adapter as a function of reverse bias voltage. The errorbars indicate the standard deviation of the individual measurements. Dashed lines are introduced to guide the eye. The relatively large errorbars at zero bias are attributed to the low signal to noise ratio.

It is worthwhile mentioning that the fall time is dominated by the fast components of the signal decay, while for a signal decay down to the, e.g. 5%-level, the slow component of the falling slope would contribute mostly (see figure 5.3b). Increasing the light intensity in the response measurements leads to an increased fall time, while the rise time barely changes. This observation will be further investigated in the following section.

Obviously, timing properties of the detector depend on the electric field in the active detector volume and hence on the applied reverse bias voltage. In figure 5.4, the dependence of t_{rise} and t_{fall} on the bias voltage are shown for the BridgeV1 microdosimeter on the test adapter. With no bias applied, charge collection is rather slow, resulting in a rise time of almost 1 ns and a fall time exceeding 20 ns. In this case, fast and slow component of the decaying slope are hardly separable. On the other hand, timing properties are not
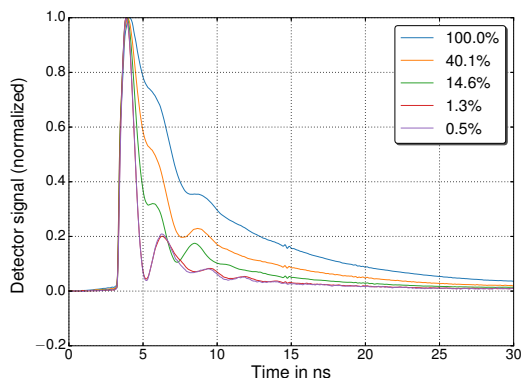
Figure 5.5: Normalized detector response functions of the BridgeV2 detector on the passive adapter, measured for different incident light intensities. The percentages in the legend refer to the relative transmission values summarized in table 5.1.

improving a lot when increasing the reverse bias from $5\,\mathrm{V}$ to $10\,\mathrm{V}$. These results show that bias voltages in this range are large enough to minimize the detector capacitance and allow for a fast charge collection.

Note that the different signal amplitude V_{max} given in table 5.2 for the same OD mainly arises from positioning uncertainties of the detector with respect to the laser beam spot when changing the adapter. A comparison of the signal amplitude for the same OD can hence not be used to judge signal losses or amplifications in the adapters.

5.2.3 Energy Linearity

The results presented in table 5.2 for the BridgeV2 microdosimeter on the passive adapter show that starting from a certain signal amplitude, the fall time strongly depends on the light intensity which generated the signal. This can clearly be seen in figure 5.5, where normalized response curves of the BridgeV2 detector on the passive adapter for a large range of input light power are displayed. For signal amplitudes of $18\,\mathrm{mV}$ and $43\,\mathrm{mV}$, the measured response functions are practically identical. Increasing the light power by one order of magnitude leads to a small deformation of the falling slope of the response curve, while a further increase results in considerably different signal shapes. Also, the undulations previously described become less pronounced with higher signal currents.

When plotting the integrated charge of the response curves versus the incident light power, a perfectly linear dependence is found (see figure 5.6a). This finding hence demonstrates that in the investigated range of incident light power, the total collection of charge carriers generated by the laser pulses is not affected. However, non-linearity effects are encountered when considering only the amplitude of the response curves, as shown in figure 5.6b. This is consistent with the observed longer decay times. The same behavior was found for the test adapter, while for the active adapter no measurements with such high light intensity were performed.

(a) Integrated charge

(b) Signal amplitude
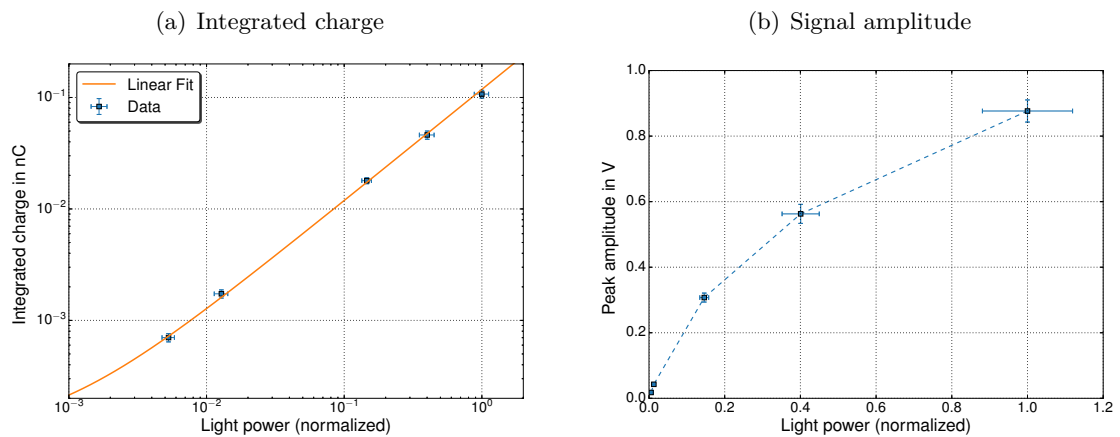
Figure 5.6: Energy linearity measurement of the BridgeV2 microdosimeter on the passive adapter. In the logarithmic plot in a), the integrated charge of the measured response is plotted in blue against the incident light intensity in arbitrary units. The orange line is a linear fit to the data points. In b), the amplitude of the response curve is shown. Errorbars in the y-dimension indicate the standard deviation of the individual response curves, errorbars in x-dimensions refer to the values of $\Delta T / T_{\max}$ given in table 5.1. The dashed line is introduced to guide the eye.
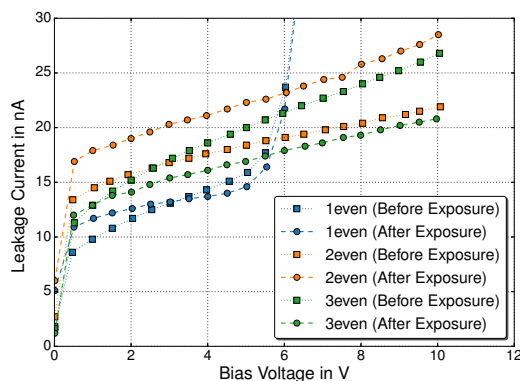
Figure 5.7: I-V characterization of three SV arrays of a BridgeV2 detector for radiation damage study. The colors indicate the different arrays. Circles connected by dotted lines correspond to the leakage current before exposure to α particles. Squares connected by dashed lines correspond to the measured leakage current after exposure. Lines are to guide the eye.

5.2.4 Radiation Damage

In figure 5.7, the reverse leakage current is shown for three pixel rows (1even, 2even and 3even; see section 4.2.1) of the BridgeV2 microdosimeter before and after exposure to about 5×10^7 α particles, which corresponds to a fluence of $\Phi_\alpha = 10^9 \, \mathrm{cm}^{-2}$.

A slight increase of leakage current of $\sim 4 \, \mathrm{nA}$ was observed for the 2even array of the microdosimeter. However, no significant change can be seen for the 1even array, while the leakage current even appears to be lower after exposure for the 3even array.

It is therefore likely that the measured differences before and after exposure only reflect uncertainties in the measurement setup and cannot be correlated with the exposure to ionizing radiation. Contributions to the uncertainty could be e.g. some residual ambient

light at the setup despite the shielding, or, since the temperature was not actively sta-bilized, small temperature differences. The latter would affect both the detector and the picoammeter.

The sudden leakage current increase for the 1even array for bias voltages exceeding 5 V is independent of the accumulated exposure to ionizing radiation and indicates approaching break-down of this SV array. Arrays showing this kind of behavior were therefore not used in experiments presented in chapter 6. These findings also show the importance of leakage current measurements prior to the detector usage.

5.3   Discussion

5.3.1   Oscillations in the Response Functions

An unexpected observation when measuring the detector response to ultra-short near-infrared light pulses is the oscillating behavior of the decaying slope of all response curves, with a frequency around 400 MHz to 500 MHz.

The most straight-forward explanation for this phenomenon would be unwanted reflections in the signal path. Yet, based on the length of the cables used in the experiments and given that the oscillation frequency does not change with different cable length, reflections cannot explain such undulations. Also, pickup of HF noise can be excluded since these oscillations are closely correlated to the amplitude of the signal and their magnitude is decaying rapidly with time.

Since frequency and magnitude of the undulations do not differ substantially for the three different adapter boards, it is likely that they originate either from a high-frequency cutoff in the signal path, or, more likely, from parasitic inductance of the detector leads and the DIL socket. Although more detailed investigations may help to find the origin of these oscillations and may reveal strategies to suppress them in a future coupling of the detector to the adapter board, this study is beyond the scope of the presented work. These effects are not of concern for the targeted activities in TOF spectrometry, as they are encountered both in the response and the measured TOF signals (see e.g. section 6.3.1).

5.3.2   Non-linearity Effects

Ideally, both the amplitude and the integrated charge of the detector signal should scale linearly with the amount of incident radiation or, in the presented case, with the intensity of the incident near-infrared laser pulse. Although this linear relation could be nicely reproduced for the integrated charge, indicating that the collection efficiency of produced charge carriers remains constant over more than two orders of magnitude, this was not found to be true for the signal amplitude. Rather, for both detector versions on passive and test adapter, non-linearity was observed starting at light intensities corresponding to a signal amplitude between 50 mV and 300 mV. According to the characteristics of

the passive adapter (see section 4.2.1), this translates to photocurrents between 10 mA to 60 mA.

This effect might be explained by a plasma-like cloud created by the large density of electron-hole pairs inside the depleted detector region. This cloud then shields its interior from the electric field, which is responsible for fast charge collection (see eq. 2.32). Hence, only the outer part of this cloud is subject to the influence of the electric field and drifts towards the electrodes, resulting in a slow erosion of the plasma-like cloud until all charge carriers are collected [Taroni and Zanarini, 1969a]. Obviously, this affects the shape, as well as the time characteristic of the measured current pulses.

In the late 1960s, these plasma-like effects resulting in longer charge collection times than theoretically expected have been observed for strongly ionizing particles in solid state detectors with a sufficiently low electric field inside its depletion region, e.g. [Alberigi-Quaranta et al., 1968; Taroni and Zanarini, 1969a,b]. It is thoroughly plausible that such a large and instantaneous near-infrared photon fluence as in the presented experiments, which is capable to penetrate the entire depletion width, can give rise to a similar ionized region in the SVs of the Bridge microdosimeters.

The reduced charge collection time in the high-intensity exposure thus leads to a current source spanning over a longer time and hence the undulations observed for low-intensity measurements begin to blur. Similarly, the decaying slope of the high-intensity detector signal can be rather well described by a single exponential decay function.

For the targeted application in TOF spectrometry, these non-linearity effects need to be considered in order to avoid a bias of the reconstructed proton energy distribution (see section 6.3.3).

5.3.3 Radiation Hardness

According to the I-V characterization presented in section 5.2.4, no radiation damage could be observed for the Bridge microdosimeter up to an integrated α particle fluence of $\Phi_\alpha = 10^9\,\mathrm{cm}^{-2}$.

Nevertheless, a significant increase of leakage current by more than a factor of 2 has been observed for one BridgeV1 microdosimeter which was excessively used in TOF experiments with laser-accelerated particle bunches in the experiments presented in section 6.3.3. These I-V curves are not shown here, as the number of ionizing particles to which the detector was exposed can only be estimated very vaguely and therefore does not allow for quantitative conclusions. But since the number of detected ion bunches is in the order of thousands and the by far largest fraction of protons stopped inside the detectors' SVs, relatively good performance in terms of radiation hardness can be anticipated.

However, given the encountered degradation after the extensive exposure at LEX Photonics, a continuous monitoring of the leakage current, e.g. on a daily basis, would be strongly recommended when used for high repetition-rate laser-plasma experiments as foreseen at CALA. That way, radiation damages can be detected at an early stage and the detector
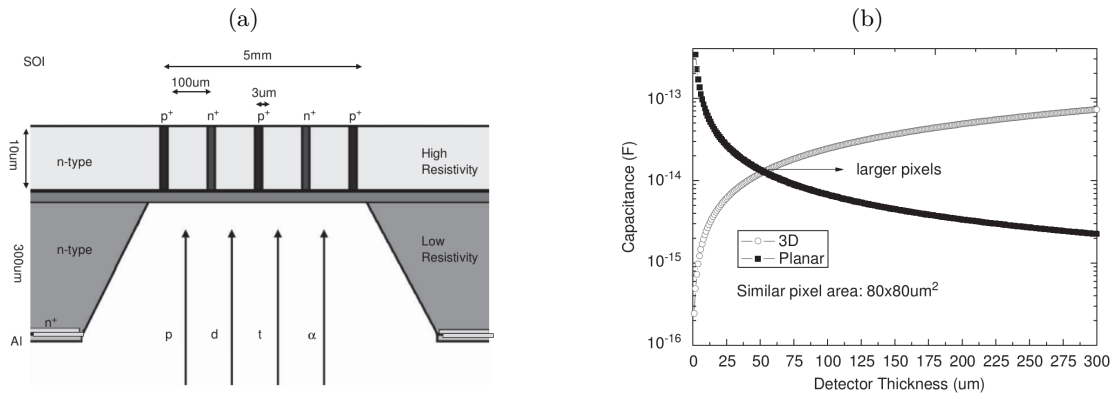
Figure 5.8: In a), a schematic layout of the U3DTHIN detector is shown. Sizes are not to scale. The dependence of capacitance on the detector thickness is shown in b) for planar (black) and 3D (gray) detector fabrication technique. Both pictures are taken from Pellegrini et al. [2009].

can be replaced to avoid errors in reconstructed ion spectra.

5.4 Conclusion & Outlook

Detector response curves to ultra-short, near-infrared laser light pulses were measured for the Bridge microdosimeters at different detector bias voltages. Based on signal rise times below 0.5 ns, both versions of the Bridge microdosimeter provide a sufficiently fast response for use in TOF spectrometry of laser-accelerated ions.

Furthermore, no significant radiation damage in terms of I-V-characteristic could be detected after exposure to an α particle fluence of $\Phi_\alpha = 10^9 \, \mathrm{cm}^{-2}$. In order to obtain more reliable data on the radiation hardness of this detector, a detailed radiation damage study including measurement of the charge collection before and after exposure would be beneficial. Moreover, data on leakage current obtained under well-controlled climatic conditions after irradiation with a wider range of particle fluences and with different particle species would be desirable in future.

The charge collected by the BridgeV2 microdosimeter has shown to be linear with the incident light power, while the response function starts to change at a signal amplitude between 50 mV and 300 mV. The considerable increase of the decay time at high signal amplitudes, most likely caused by a plasma-like charge carrier cloud, has to be taken into account when using the detector over a wide dynamic range.

In summary, despite some minor drawbacks, the Bridge microdosimeters exhibit promising properties for application in TOF spectrometry. They have been therefore used in the TOF experiments presented in chapter 6.

For an ideal experimental setup using laser-accelerated ions for e.g. biomedical applications, the detector should be used to monitor the ion spectra in transmission and, most importantly, in a non-destructive way. That means, the total geometrical thickness of the detector needs to be small, such that the energy loss of the incoming ion bunches in

it remains low. This can be achieved by etching the substrate wafer as it was done for the planar ultra-thin detector (see section 4.2.1), which however shows insufficient timing properties.

A promising candidate for transmission TOF spectrometry might be the U3DTHIN detector [Pellegrini et al., 2009; Tran et al., 2014]. This detector is shown schematically in figure 5.8a. It has a geometrical thickness comparable to the planar ultra-thin detector, but its n^+ and p^+ electrodes are arranged as a matrix of small 3D columns inside the n-type active silicon layer. Due to the 3D detector fabrication, a tremendous reduction of capacitance can be obtained for small detector thicknesses as compared to planar detectors (see figure 5.8b). This reduced capacitance translates into faster timing properties, i.e. sub-ns rise times should be easily achievable. Future detector tests with the U3DTHIN detector investigating its suitability for transmission TOF spectrometry are therefore foreseen in the near future.

Time-of-Flight Spectrometry

The time-of-flight difference of protons with different kinetic energies can be exploited to determine their initial energy. Within this chapter, an approach to determine the energy distribution of ultra-short proton bunches, as obtained in laser-ion acceleration, is presented and evaluated based on experimental measurements performed at the Munich Tandem accelerator and at LEX Photonics[1].

In section 6.1, fundamental considerations of TOF spectrometry based on extracting the spectral information from the pile-up signal of a polyenergetic bunch inside a detector are sketched and explained. The experimental setups for measurements performed at the Tandem accelerator and at LEX Photonics are shown in sections 6.2.1 and 6.2.2, respectively. The method to reconstruct energy spectra from the measured TOF signals is presented in section 6.2.3. Results for both types of experiments are shown in section 6.3, together with an attempt to determine the bunch duration at the Tandem accelerator by means of deconvolution of the detector response from the measured TOF signal. This section is followed by a detailed discussion of the uncertainties of the presented results and the challenges of TOF spectrometry in mixed ion fields and in presence of electromagnetic pulses, which are both typical for laser-ion acceleration. Finally, a conclusion and future perspectives are given in section 6.5.

6.1   Introduction

When measuring the TOF signal of short and highly intense particle beams like laser-accelerated proton bunches, the detector is exposed to a continuous irradiation starting from the highest energetic protons until the slowest ions that can still enter the SV of the detector. Due to the high fluxes exceeding $10^9 \, \mathrm{cm}^{-2} \, \mathrm{ns}^{-1}$, it is not possible to distinguish individual particles, hence the measured signal is the pile-up of numerous individual events.

---

[1]Part of the methods and results presented in this chapter have been submitted as:
M Würl *et al* 2018 *Rev. Sci. Instrum.*
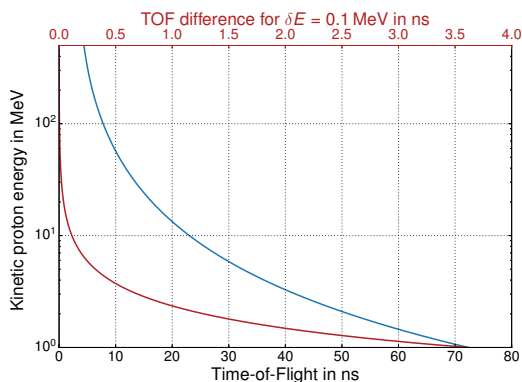
Figure 6.1: Kinetic proton energy versus time-of-flight (blue) for a drift space of $1\,\mathrm{m}$, calculated according to eq. 6.1. In red (upper x-axis), the TOF difference corresponding to a difference in kinetic energy of $\delta E = 0.1\,\mathrm{MeV}$ is plotted.

In other words, the cumulative signal of all particles is recorded.

Resolving the signal components generated by individual particles by means of deconvolution or pulse fitting, like performed in e.g. Marrone et al. [2002] and Belli et al. [2008], becomes virtually impossible. However, a deconvolution approach would become feasible, if the continuous ion bunch was considered as consisting of many short particle *packages*, where each package contains all particles arriving at the detector within a certain time interval Δt.

After discretizing the continuous signal, which is inherently done by digitizing the analogue detector signal, the measured signal can thus be treated as a superposition of many signals, each generated by one proton package with a bunch duration of the digitizer's sampling width. Protons corresponding to one package are then protons arriving at the detector within the time window $\left[t_{\mathrm{TOF}} - \frac{\Delta t}{2}, t_{\mathrm{TOF}} + \frac{\Delta t}{2}\right)$, where t_{TOF} is the time sampling point, relative to the particles' starting time $t = 0$.

Given a drift length d and assuring that at $t = 0$ all particles start to drift simultaneously, every time sampling point t_{TOF} can be translated to a kinetic energy according to

$$E_{\mathrm{kin}}(t_{\mathrm{TOF}}) = \left(\frac{1}{\sqrt{1 - \left(\frac{d}{c t_{\mathrm{TOF}}}\right)^2}} - 1 \right) \cdot m_p c^2 \ , \tag{6.1}$$

where c and m_p are the speed of light and the proton rest mass, respectively. The functional behavior, as well as the time difference corresponding to a difference in kinetic energy of $\delta E = 0.1\,\mathrm{MeV}$ are plotted in figure 6.1 for a drift space of $1\,\mathrm{m}$.

In case of LIONs, the starting time t_0 can be obtained from the electromagnetic radiation and ultra-relativistic electrons that are co-emitted from the plasma and are detected at $t_{\gamma,\mathrm{e}} = d/c$. However, when additional beam shaping and transport elements are included prior to the detector, it may be beneficial to additionally use an external trigger. This could be for instance a fast photodiode detecting a fraction of the laser pulse used for the

acceleration, transmitted through one of the mirrors in the laser beamline. Of course, this external trigger has to be thoroughly synchronized with the actual arrival of the laser pulse at the laser-plasma interaction point. In figure 6.2, the idea how the cumulated signal is generated in case of LION bunches is schematically visualized at different time steps.

Ion velocities in contemporary LION experiments are typically in the (near-)relativistic range, reaching values up to $\sim 0.4c$. Having a reasonable drift space of up to a few meters, this translates to times in the order of some nanoseconds. Following the aforementioned example plotted in figure 6.1, resolving a difference in kinetic energy of 0.1 MeV for 20 MeV protons and a drift space of 1 m would require a detection system that is capable of measuring a time difference of 40 ps. This example stresses the importance of fast detectors and successive electronics, as previously discussed in chapter 5. It is furthermore important to properly take into account the response function of the detector and electronics when reconstructing an energy spectrum from measured TOF signals. Of course, the choice of suitable cables with low damping at high frequencies is crucial for TOF spectrometry to maintain the original shape of the rising edge of the detected current signal as good as possible.

6.2 Materials & Methods

6.2.1 TOF Spectrometry at the Tandem Accelerator

In order to test the performance of TOF spectrometry using the BridgeV2 microdosimeter under well-controlled and reproducible conditions, a set of measurements was performed at the Munich Tandem accelerator using a chopped and bunched proton beam (see section 4.3.1 for details). The kinetic energy of the protons before entering the experimental setup was 20 MeV. The average beam current, measured using the last FC upstream of the experiment was (0.8 ± 0.2) nA. According to scintillator measurements of the bunched beam, the proton bunch duration was around 1 ns (see section 6.3.2 for details). From the 5 MHz chopper frequency, the bunch repetition rate was reduced down to 9765 bunches per second, resulting in an average of $(5.1 \pm 1.3) \times 10^5$ protons per bunch.

Experimental Setup

A schematic overview of the experimental setup is shown in figure 6.3. To avoid additional energy loss of the protons within their drift space, the entire experiment was performed in vacuum. The main vacuum chamber was separated from the beamline vacuum by a 50 μm thin Kapton foil. This separation has two advantages for the conducted experiments. First, measurements could already be started before reaching the high vacuum of the beamline $(p_{BL} \sim 1 \times 10^{-7}$ mbar), provided that the vacuum inside the chamber is sufficiently low such that interactions of protons with the remaining gas is negligible. Second, the Kapton foil acted as an additional scatterer, resulting in a slightly larger beam spot size and
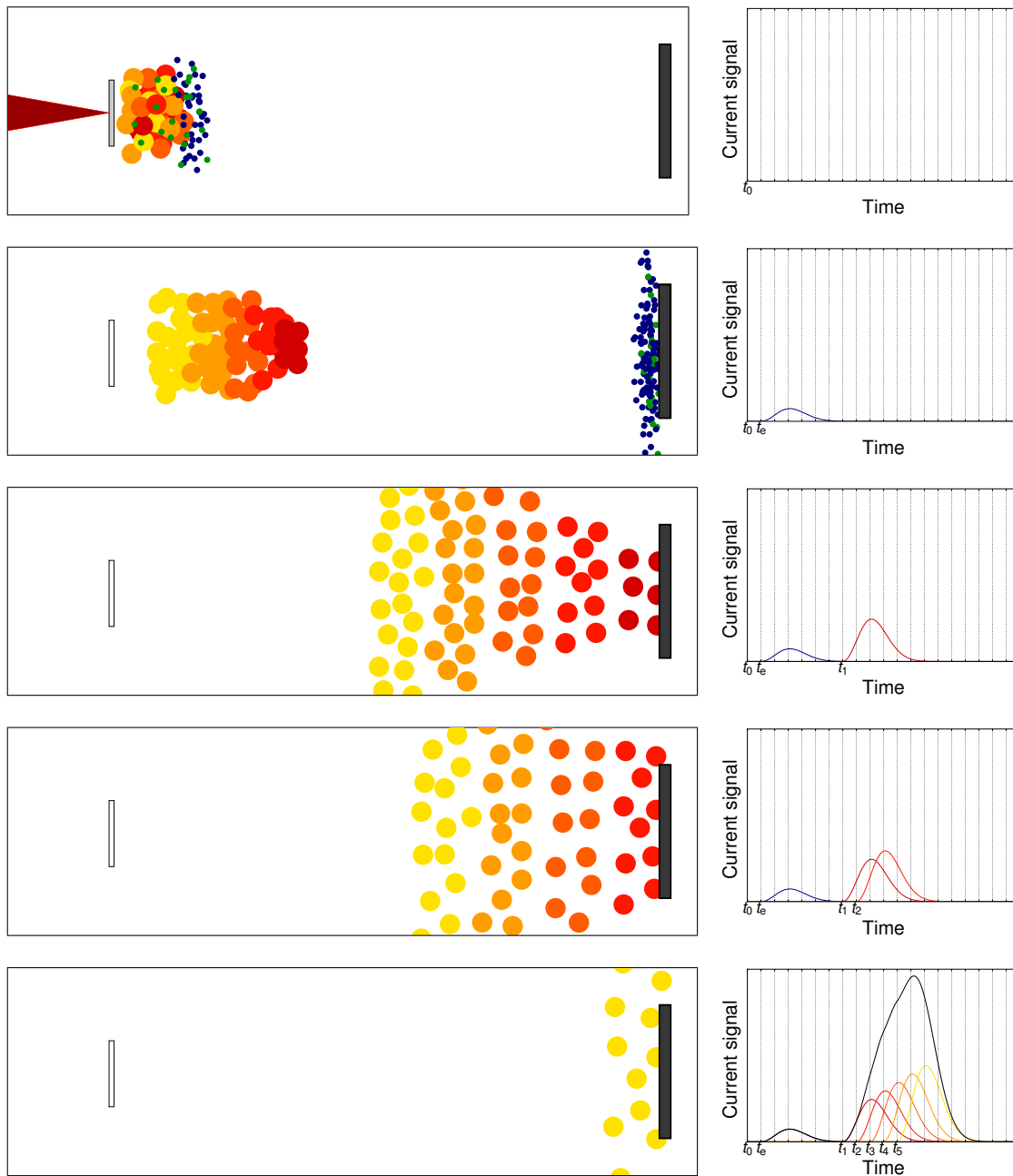
Figure 6.2: Schematic illustration of TOF spectrometry of laser-accelerated ion bunches. Each line corresponds to a certain time sampling point of the readout device. At t_0, the laser focus hits the target and ions, electrons and electromagnetic radiation is emitted from it quasi instantaneously (as compared to time scales relevant for electronic detectors). After $t_e \approx d/c$, with the drift space d and the speed-of-light c, photons and highly relativistic electrons reach the detector creating the signal shown in blue. Step by step, the fastest ions, followed by the slower ions reach the detector, deposit some energy inside its SV giving rise to current signals shown by reddish to yellow colors. The black curve in the last image corresponds to the actually measured detector signal, which is the pile-up of all individual proton *packages*.

producing large-angle scattered protons that can be detected by the plastic scintillator coupled to the PMT used for measuring and monitoring the temporal bunch profile during experiments.
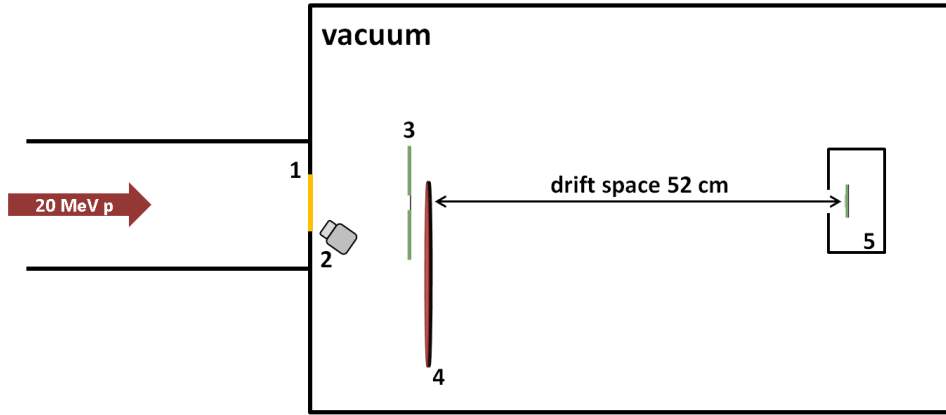
Figure 6.3: Schematic overview of the experimental setup for TOF spectrometry at the Tandem accelerator. The ns-short, 20 MeV proton bunches are coming from the left, passing through a 50 µm thin Kapton foil (1). A plastic scintillator coupled to a photomultiplier tube (2) detects large-angle scattered protons from the foil. The proton bunches pass the ultra-thin silicon detector (3), a motorized wheel with different absorbers mounted (4) and drift 52 cm through vacuum until they reach the BridgeV2 TOF detector in an aluminum housing (5).

The scintillator and PMT, connected to the data acquisition system explained in section 4.3.1, were located close to the Kapton foil at an angle of $\sim 10°$ with respect to the proton beam direction. The distance between scintillator and Kapton foil was kept as short as reasonably achievable. Since this method is not sufficiently accurate to obtain sub-ns information on the temporal structure of the proton bunch, it was only used as a diagnostic tool for optimizing the settings of the buncher in order to obtain the shortest possible proton bunches. Moreover, data was acquired during the entire measurement campaign to verify that the temporal structure of the bunches remained constant throughout all experiments.

The proton bunches passed through the ultra-thin silicon detector and different passive energy absorbers, further described in sections 4.2.1 and 4.3.1, respectively. After a drift space of 52 cm, the proton bunches were detected by the BridgeV2 microdosimeter, mounted on the active circuit board (see section 4.2.1) inside an aluminum housing to reduce high frequency noise. The detector was reverse biased with 7 V and only one array of SVs was read out to reduce capacitance and hence improve its timing properties.

The amplified output of the BridgeV2 microdosimeter was connected to the 50 Ω DC input of a 4 GHz oscilloscope *(WaveRunner 640Zi, Teledyne LeCroy, USA)* with a sampling rate of $20\,\mathrm{GS\,s^{-1}}$ via a floating SMA vacuum feed-through and using high frequency compatible SMA coaxial cables. Similarly, the current signal of the ultra-thin silicon detector was connected to the oscilloscope. It was used for triggering and to define the start time $t = 0$ of the TOF signal. According to FLUKA MC simulations, the mean energy loss of 20 MeV protons inside the detector after having passed the Kapton foil is 48 keV, such that the total mean energy loss before entering the passive absorbers amounts to 239 keV.

The steering of the proton beam was checked using two scintillator crystals mounted on servomotors, while the aluminum enclosure housing the BridgeV2 microdosimeter was

outside the beam. Additionally, the actual beam spot size and lateral position at the distal location of the Bridge detector was measured using an EBT-3 film with an absorber thickness of 200 µm. The film was scanned in landscape orientation using an Epson Expression 11000XL photo scanner *(EPSON Deutschland GmbH, Meerbusch, Germany)* and the corresponding beam spot size was determined to be 12 mm FWHM. However, due to Coulomb scattering, the spot size strongly changes with different absorber thicknesses.

Spectrum Determination using a Magnetic Spectrometer

For comparison, the spectra of the proton bunches were measured using a magnetic spectrometer, similar to the one described in Lindner et al. [2018]. After the passive energy degraders, the scattered protons were collimated by a 30 µm thin slit between two 1 cm thick aluminum blocks, before they entered a $L = 9$ cm long dipole magnet ($B = 600$ mT). Due to the Lorentz-force, protons were deflected in the magnetic field perpendicular to the proton beam direction according to their kinetic energy. After a drift space in vacuum of $d = 34$ cm, they are detected by the Remote RadEye detector system (see section 4.2.3). The vertical offset $\Delta h\left(E_{\mathrm{kin}}\right)$ with respect to the slit height depends on the kinetic energy of the proton, E_{kin} and can be calculated by

$$\Delta h\left(E_{\mathrm{kin}}\right) = R\left(E_{\mathrm{kin}}\right) - \sqrt{R\left(E_{\mathrm{kin}}\right)^2 - L^2} + \frac{d \cdot L}{R\left(E_{\mathrm{kin}}\right)\sqrt{1 - \left(\frac{L}{R(E_{\mathrm{kin}})}\right)^2}} \ , \qquad (6.2)$$

where $R = \frac{mv}{B}$ is the radius of a proton with momentum mv in the magnetic field B. Isoenergy curves were then drawn in the detector plane and with them, the signal in each pixel was converted to a proton number according to Lindner et al. [2018].

The slit configuration used in this setup translates to a full acceptance angle of the spectrometer of 6 mrad, resulting in a slight smearing of the signal in the detector plane and hence a broadening of the measured energy spectrum. The broadening of the signal was reduced by deconvolving the response from the acquired raw image using Richardson-Lucy deconvolution.

FLUKA MC simulations

The experiments were complemented by FLUKA MC simulations with a detailed model of the experimental geometry including the relevant dimensions and distances. Simulations were performed for several purposes. First, the average energy loss inside the SV of the Bridge microdosimeter, which is required to generate the system matrix presented in section 6.2.3, was calculated. Moreover, the TOF difference between the thin detector and the position of the absorber was computed to determine the actual starting time t_0, which is at the position of the energy modulation. Last but not least, the simulation results served as a reference for comparison to the reconstructed energy spectra.

The BridgeV2 microdosimeter was modeled similar to Tran et al. [2017], but the number of SVs was reduced since only one of the arrays was read out in the experiments.

As material for the 3D-printed plastic absorbers of unknown chemical composition, PMMA was used with adjusted material properties. Its density was set to $\rho_{\text{absorber}} = 1.094\,\text{g cm}^{-3}$, which was obtained experimentally (see section 4.3.1). The other adjusted material property was the ionization potential I_p, which cannot be measured directly. Hence, the water-equivalent thickness of the material was determined by ionoacoustic measurements of a 20 MeV proton beam in water [Lehrack, 2018]. Using that method, the ratio of water thickness d_w and material thickness d_m was determined to be $d_w/d_m = 1.096$. In a trial-and-error process, I_p was modified in the simulation input until the correct ratio of range in water and range in absorber material was obtained for $I_p = 59.0\,\text{eV}$.

The initial proton energy distribution from the Tandem accelerator was 20 MeV with an energy spread of 0.1% FWHM. A spot size of the proton beam of 2 mm FWHM and a divergence of 5 mrad were chosen, matching best the experimental spot size measurements using the EBT-3 film.

Since in the actual experiment the microdosimeter was not perfectly aligned on the beam axis, a 2 mm horizontal shift of the detector with respect to the beam axis was also included in the simulation geometry.

6.2.2 TOF Spectrometry of Laser-Accelerated Proton Bunches at LEX Photonics

Until the shut-down of the ATLAS-300 laser system in December 2016, a number of beamtimes aiming to establish TOF spectrometry for laser-accelerated ion bunches were conducted using the BridgeV1 microdosimeter mounted on the in-house made test adapter. It was reverse biased with 7 V and two arrays of SVs were read out simultaneously and independently. Like in the experiments at the Tandem accelerator, the current output of the detector was connected to the 50 Ω DC input of the oscilloscope using the same floating SMA vacuum feedthrough and cables.

The detector on the test adapter was mounted in a closed aluminum housing with one small hole at the front surface above the sensitive area of the detector *(entrance hole)* and one hole at its side, where SMA coaxial cables for signal and bias supply were guided through. A thin aluminum foil was used to cover the entrance hole to make the housing light-tight and to absorb low-energy protons. Moreover, the aluminum box served to suppress high frequency noise by the EMP.

There were basically two kinds of TOF measurements performed at LEX Photonics, which can be classified by the way the laser-accelerated ion bunch is handled. In the simplest case, the highly divergent laser-accelerated ion bunches propagate from the target foil in an unperturbated way, reaching an online wide-angle magnetic spectrometer (WASP; described in section 3.1) used for ion and electron diagnostics. In this configuration, the aluminum box housing the Bridge detector was placed right next to the entrance slit of the
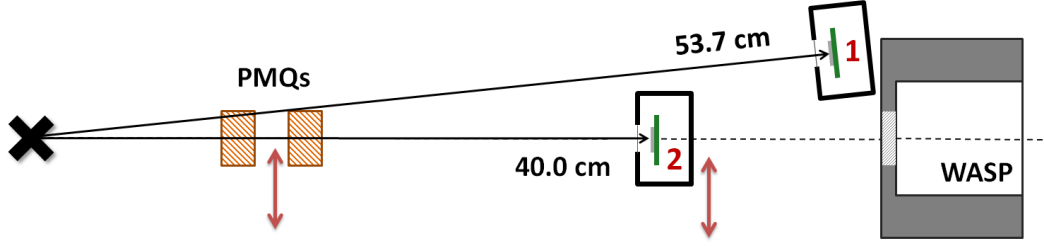
Figure 6.4: Schematic overview of the experimental setup for TOF spectrometry at LEX Photonics (top view, lengths not to scale). The proton source is marked by the black cross. In setup 1, the Bridge microdosimeter mounted inside and aluminum box is placed right next to the entrance slit of the WASP, such that spectra can be measured simultaneously with both diagnostic devices. The distance to the source is 53.7 cm. In setup 2, a pair of PMQs is used to focus the divergent particle beam. The Bridge microdosimeter was placed in the focal point for 6 MeV protons, at a distance of 40.0 cm from the source. In this configuration, the entrance slit of the WASP is blocked and no alternative diagnostic device can be run simultaneously.

WASP at a distance to the target of 53.7 cm, resulting in an angle of 8.1° with respect to the laser axis. Therefore, TOF spectrometer and WASP could be operated simultaneously. The thickness of the aluminum foil in these experiments was 30 μm. Thus, the low-energy cut-off of this detection setup was $E_{\text{cut-off}} = 1.6 \,\text{MeV}$.

In the second setup, the initial laser-accelerated ion beam was focused by a doublet of PMQs, further described in section 4.3.2. The positions of the PMQs were adjusted such that they were focusing 6 MeV protons onto the Bridge detector, located at a distance of 40 cm from the target. Since the doublet of PMQs does not eliminate ions outside the design energy but defocuses them, a contribution of other proton energies was still expected to be present. The Bridge detector was mounted on a motorized horizontal stage, such that its active area could be driven into the ion focus for measurements and driven to its stand-by position when the WASP was used for beam diagnostic. In this experimental setup, the thickness of the aluminum foil covering the entrance hole was 90 μm, resulting in a cut-off energy of $E_{\text{cut-off}} = 3.2 \,\text{MeV}$.

6.2.3 Reconstruction of the Proton Energy Distribution

Following the considerations of section 6.1, the digitized TOF signal $S(t)$ can be treated as the superposition of signals $s_i(t)$, each generated by a discrete ion packages arriving at the detector within a certain time bin i:

$$S(t) = \sum_i s_i(t) = \sum_i R(t) * [\, n_i \cdot \langle E_{\text{dep},i} \rangle \cdot \delta\left(t - t_{\text{TOF},i}\right)\,] \ , \tag{6.3}$$

where $R(t)$ is the detector response function, n_i is the number of protons reaching the SV of the detector within the time bin i, $\langle E_{\text{dep},i} \rangle$ is the mean energy deposition per proton of bin i and $\delta\left(t - t_{\text{TOF},i}\right)$ is a delta distribution which is unity when t equals the time-of-flight of bin i, $t_{\text{TOF},i}$. The symbol "$*$" indicates a convolution. Of course, the time bins

in eq. 6.3 can also be exchanged by energy bins according to eq. 6.1.

The energy distribution can therefore be obtained by solving this equation system by means of linear least-squares optimization with the only constraint that the particle number $n_i \geq 0$ $\forall i$. Substituting the response $R(t)$ and $\langle E_{\mathrm{dep},i} \rangle \, \delta \left(t - t_{\mathrm{TOF},i} \right)$ by the system response matrix $\mathcal{A}$, the least-squares problem can be written as

$$\min_{\vec{n}} \| \mathcal{A} \cdot \vec{n} - \vec{S} \| \; , \quad n_i \geq 0 \; \forall i \; . \tag{6.4}$$

The Python package `scipy.optimize` [Jones et al., 2001–] with an adaptation of the Trust Region Reflective algorithm described in Branch et al. [1999], was used to compute the constrained least-squares solution.

Since the inverse problem to be solved is ill-posed and the solution is expected to be rather smooth, Tikhonov regularization was used to penalize overfitting at the cost of an artificial broadening of the reconstructed energy spectrum. The least-squares problem hence becomes

$$\min_{\vec{n}} \left\{ \; \| \mathcal{A} \cdot \vec{n} - \vec{S} \|^2 + \| L_\mu \cdot \vec{n} \|^2 \; \right\} \; , \tag{6.5}$$

with the so-called regularization matrix $L_\mu = \mu \mathbb{I}$, consisting of the regularization parameter $\mu > 0$ and the identity matrix $\mathbb{I}$. In order to find an adequate solution to the inverse problem, a regularization parameter μ suitable for the measured data needs to be determined empirically.

As previously mentioned, the system matrix $\mathcal{A}$ is substitutes the convolution of the response function with $\langle E_{\mathrm{dep},i} \rangle \, \delta \left(t - t_{\mathrm{TOF},i} \right)$. A straightforward way to obtain this response function $R(t)$ of detector and associated electronics is by exposing the detector to an ultra-short ($< 1\,\mathrm{ps}$) laser pulse, given that the used detector is sensitive to the wavelength of the laser light. This was done in the detector characterization measurements presented in section 5.2.1, which were performed using the same cable types and lengths as in the actual TOF experiments.

In contrast to laser-accelerated ion bunches, the initial temporal structure of proton bunches at the Tandem accelerator is not negligible and thus needs to be taken into account when solving eq. 6.5. Therefore, an alternative approach to obtain $R(t)$ was chosen for the generation of the system matrix used for spectrum reconstruction of the TOF signals measured at the Tandem accelerator. Response curves were obtained by irradiating the Bridge microdosimeter with the bunched $20\,\mathrm{MeV}$ proton beams with no absorbing material in the beam path, except for the $50\,\mathrm{\mu m}$ thin Kapton foil and the ultra-thin silicon detector. Hence, the measured response function $R_{\mathrm{Tandem}}^{\mathrm{meas}}(t)$ is already the convolution of the actual detector response $R(t)$ and the initial temporal shape of the short proton bunches $\mathcal{T}(t)$:

$$R_{\mathrm{Tandem}}^{\mathrm{meas}}(t) = R(t) * \mathcal{T}(t) \; . \tag{6.6}$$

The measured response $R_{\mathrm{Tandem}}^{\mathrm{meas}}(t)$ is then divided by the total energy deposition within
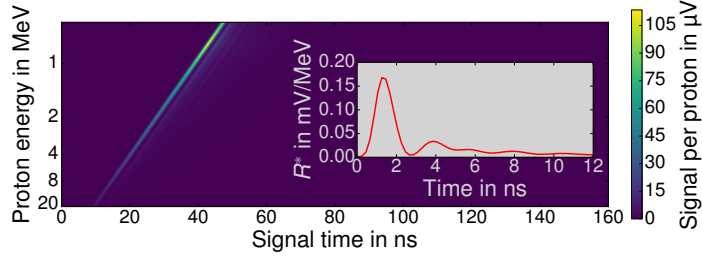
Figure 6.5: Graphical representation of the system response matrix for the Tandem experiments. The color represents the amplitude of the signal. The normalized response $R^*(t)$ is shown in the inset.

the SV of the microdosimeter, according to

$$R^*(t) = \frac{R_{\text{Tandem}}^{\text{meas}}}{N_{\text{p}}^{\text{SV}} \cdot \langle E_{\text{dep}}\left(E_{\text{kin}} = 20\,\text{MeV}\right)\rangle} \ , \tag{6.7}$$

where N_{p}^{SV} is the detected number of protons and $\langle E_{\text{dep}}\left(E_{\text{kin}} = 20\,\text{MeV}\right)\rangle$ is the mean energy deposition within the SV for a proton of the kinetic energy used for the calibration (20 MeV). The detected number of protons N_{p}^{SV} was calculated based on beam current measurements using the FC when recording the response function and the fraction of protons reaching the SVs of the Bridge microdosimeter within one bunch. The latter quantity was estimated using the spot size measurement with the EBT-3 film and dedicated FLUKA MC simulations. Also, the average energy deposition in the detector $\langle E_{\text{dep}}\left(E_{\text{kin}} = 20\,\text{MeV}\right)\rangle$ was computed in these simulations. Hence, the response $R^*(t)$, shown in the inset of figure 6.5, is the detector response corresponding to an energy deposition in the SV of 1 MeV.

A graphical representation of the system response matrix for the TOF measurements at the Tandem accelerator is shown in figure 6.5. The system matrix was created by inserting copies of the normalized response $R^*(t)$ along the second dimension (rows), where each copy is shifted by one sampling point by inserting one zero at the beginning of the response array. The sampling width was set to $\Delta t_{\text{TOF}} = 0.2\,\text{ns}$, i.e. all measured curves were downsampled prior to data evaluation. The copies were scaled in amplitude according to the mean energy deposition inside the SV of protons with the corresponding energies (figure 6.6). These mean energy depositions were calculated in FLUKA MC simulations. Thus, every row in the system matrix corresponds to the signal produced by one average proton reaching the detector's SV within one time bin.

In principle, the system matrix for TOF spectrometry of laser-accelerated ions at LEX Photonics can be created in the same way, except for replacing the measured response function $R_{\text{Tandem}}^{\text{meas}}(t)$ by the response obtained using the ultra-short light pulse[2]. Since the

---

[2]Due to the high signal amplitudes expected in experiments at LEX Photonics, the response corresponding to the largest light intensity was chosen.
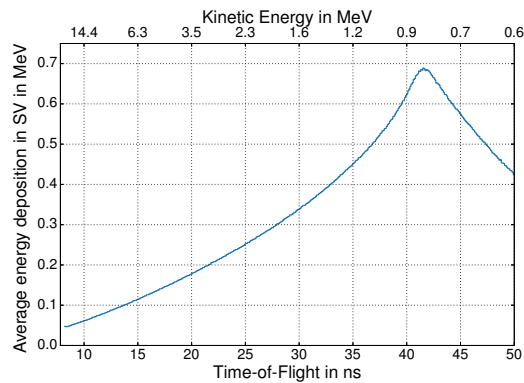
Figure 6.6: Average energy deposition of protons inside the SV of the Bridge microdosimeter, as calculated by FLUKA MC simulations, compared to the kinetic energy and the time-of-flight corresponding to a drift space of 52 cm.

integrated charge of the response signal per MeV energy deposition inside the detector SV is the same, the absolute particle number calibration performed for the Tandem system matrix could also be used for absolute particle calibration of the system matrices for LION spectrometry. However, for the TOF measurements performed at LEX Photonics, the older version of the Bridge microdosimeter, as well as a different adapter were used. Differences in the charge collection have been encountered for the two generations of Bridge microdosimeters both inside the SVs, as well as in between the SVs due to incomplete etching of the surrounding silicon [Tran et al., 2015a]. Yet, the absolute difference had not been quantified. Moreover, the signal that is delivered to the oscilloscope per generated detector current depends on the adapter. Therefore, energy spectra for laser-accelerated ions presented in the following are given in relative units. Nevertheless, for future TOF measurements of laser-accelerated proton bunches using the new BridgeV2 microdosimeter, the performed calibration can be used and reconstructed energy distributions can be given in absolute units.

As previously mentioned, aluminum foil was used in the experiments at LEX Photonics for shielding the Bridge microdosimeter from laser light and low-energy protons. This results in an additional energy loss of the protons inside the 30 μm and 90 μm thin foils before they reach the detector, which also changes the average energy deposition in the SV. For building up the system matrix, this additional energy loss in the thin foils was therefore taken into account.

6.2.4 Deconvolving the Bunch Duration at the Tandem Accelerator

As previously mentioned, the TOF signal acquired to obtain the response function $R_{\mathrm{Tandem}}^{\mathrm{meas}}(t)$ is convolution of the actual detector response function with the initial temporal structure of the bunched proton beam at the Tandem accelerator. $\mathcal{T}(t)$ can therefore be obtained by deconvolving the detector response function, measured using an ultra-short laser pulse in section 5.2.1, from the TOF signal. This deconvolution was done using an
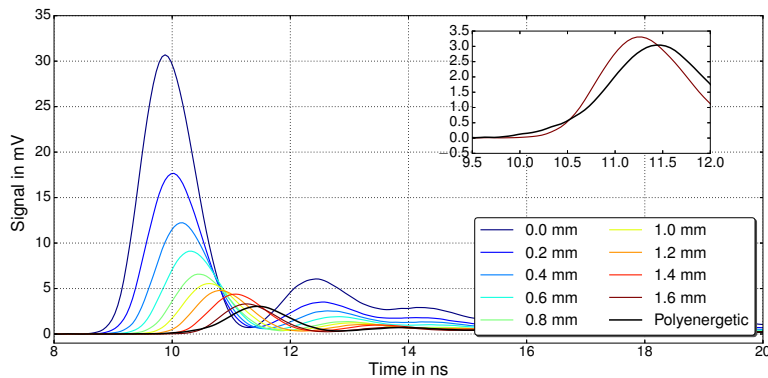
Figure 6.7: Averaged TOF signals for different passive absorbers at the Tandem accelerator. The signal corresponding to zero absorber thickness was taken as response to build the system matrix $\mathcal{A}$. The lower signal amplitude for thicker absorbers is due to increased scattering. In the inset, the rising edges of the detected signals for an absorber thickness of 1.6 mm and the polyenergetic absorber are compared, revealing the different shapes of their rising slopes.

implementation of the Richardson-Lucy deconvolution algorithm.

6.3 Results

6.3.1 TOF Spectrometry at the Tandem Accelerator

TOF signals for (quasi-)monoenergetic proton bunches after having traversed different plastic absorber thicknesses, as well as the polyenergetic proton bunches after the passive energy modulation filter are shown in figure 6.7. Since the amplitude of the signals is rather low, i.e. $V_{max} \lesssim 30\,\text{mV}$, the results were averaged over 500 individual proton bunches. Also, the low amplitudes justify the use of a constant detector response function, as no non-linearity effects had to be expected at these signal levels (see section 5.2.3).

The signals corresponding to the different absorber thicknesses are clearly separated in time. According to FLUKA MC calculations for 20 MeV protons, a difference in absorber thickness of 0.2 mm corresponds to energy differences of around 0.6 to 0.7 MeV for thicknesses up to 1.6 mm (see figure 4.8b). The decrease in signal amplitude towards thicker absorbers is due to the increased scattering, resulting in lower particle fluences at the position of the Bridge microdosimeter.

Comparing the TOF signals generated by monoenergetic bunches after having traversed 1.6 mm plastic and by polyenergetic bunches clearly reveals a difference in their rising edges (see inset of figure 6.7). This difference in signal shape substantiates the plausibility of the approach to obtain spectral information from its rising edges.

For each signal curve, only the very first and highest peak actually arises from protons reaching the microdosimeter. The smaller and broader peaks following the main peak are identical to the undulations observed and discussed in chapter 5. Since these undulations are therefore also included in the system response matrix, the reconstructed spectrum will

not be affected by them.

Reconstructed proton energy distributions from the averaged TOF signal for a monoenergetic spectrum after an absorber thickness of 1.6 mm and for the polyenergetic spectrum are shown in figure 6.8a and c, respectively. They are compared to spectra calculated using FLUKA MC simulations and to the energy distribution reconstructed from measurements with the magnetic spectrometer. The regularization parameter in eq. 6.5 was set to $\mu = 10^{-6}$ as a compromise between artificial broadening of the reconstructed spectrum and overfitting artifacts. The shaded area around the curve corresponding to the magnetic spectrometer in figure 6.8c indicates the variation of the produced energy distribution with the position of the beam spot on the absorber for generating the polyenergetic spectrum. As expected from the microscopic image shown in figure 4.9, complete beam spot position invariance of the resulting spectrum could not be achieved, although the variations are small.

Differences of the reconstructed polyenergetic spectra between simulation and both independent measurements are mainly manifested in the occurrence of two peaks instead of a continuous decaying slope. This differences can be attributed to imperfections in the 3D-printing process that have already been indicated in section 4.3.1. Tiny structures as designed and incorporated in the MC simulation can hardly be achieved. The deepness of the pits and their convex sides, and hence the resulting energy spectrum of the printed absorber differ from its idealized model. Taking the simulated spectrum as the ground truth in the comparison of reconstructed energy spectra therefore has to be done with great caution.

Besides these encountered differences, from a qualitative point of view good agreement in the shape of the spectrum and the energy of its maximum is obtained for all three absorbers and all three methods. In table 6.1, particle numbers and mean kinetic energy are compared between MC simulations and TOF reconstruction. For every absorber used within this study, the agreement of the mean energy of energy distributions from TOF measurements and MC simulations was better than 2%.

Also, the absolute number of particles measured by the Bridge microdosimeter, i.e. the area under the reconstructed spectra in figure 6.8, is in good agreement with MC simulations taking into account the active area of the detector. The encountered differences were typically within 5%. Only for three absorber thicknesses used in the experiments the TOF reconstructed particle number differs by up to 12% from the expected values, which can be explained by beam intensity fluctuations further discussed section 6.4.3.

The energy spread of the reconstructed monoenergetic spectra using the TOF approach is considerably larger than compared to the spread calculated by means of MC simulations. This is mainly due to the regularization and will be discussed further in section 6.4.1. However, this spread is of comparable size as the energy spread from the spectrum obtained with the magnetic spectrometer.

The performance and stability of the reconstruction method was assessed by multiplying

(a) Spectrum (1.6 mm absorber)

(b) TOF signal (1.6 mm absorber)

(c) Spectrum (polyenergetic)

(d) TOF signal (polyenergetic)
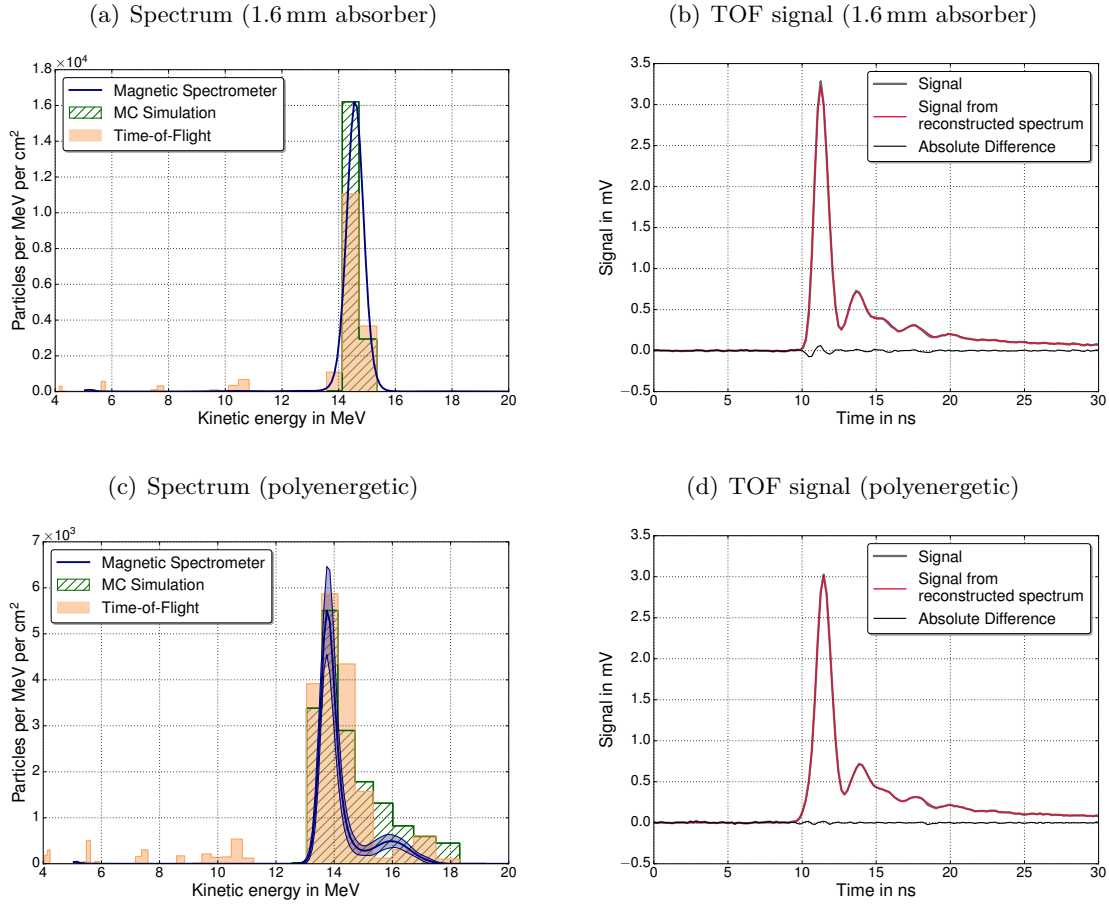
Figure 6.8: Reconstructed proton energy distributions from TOF experiments at the Tandem accelerator. TOF spectra (orange) are shown for the 1.6 mm plastic absorber (a) and the absorber with the matrix of pits with convex sides (c). For comparison, the dashed green area and the blue curves represent the spectra expected from FLUKA MC simulations and measured with the magnetic spectrometer, respectively. The shaded blue area in (c) indicates the spectrum uncertainty due to positioning of the absorber. In (b) and (d), the corresponding averaged TOF signals (thick gray), the reconstructed TOF spectrum multiplied by the system matrix (red) and their absolute differences (black) are shown.

it with the system response matrix $\mathcal{A}$, yielding a TOF signal as expected for such a proton spectrum. Such spectrum is compared to the actual acquired signal in figure 6.8b and d. The good agreement given by relative deviations below 4.6% indicates that the reconstruction itself works properly and that the undulations encountered in the detector response do not affect the reconstruction.

6.3.2 Determination of the Duration of the Bunched Tandem Beam

The deconvolved temporal bunch structure, as well as the original TOF signal are shown in figure 6.9a, where they are compared to the time measurements based on the scintillator detecting protons scattered in the Kapton foil. According to a Gaussian fit to $\mathcal{T}(t)$, the bunch duration is $\tau_{\mathrm{bunch}} = 0.7$ ns (FWHM). In figure 6.9b, the measured TOF signal is compared to $R(t) * \mathcal{T}(t)$. Good agreement can be seen, pointing out the stability of the

Table 6.1: Results obtained from TOF spectrometry at the Tandem accelerator for each passive absorber. In the second column, the peak amplitude of the measured TOF signal is given. The particle number expected from MC simulations and according to the reconstruction are given in columns three and four, while their relative difference is estimated in column five. In columns six, seven and eight, the expected mean energy, the reconstructed mean energy and their relative difference are summarized. For the energy values, spurious events at low kinetic energies were not taken into account for calculating the mean.

Absorber	V_{max}	N_{P}^{exp}	N_{P}^{recon}	$\frac{\Delta N_{\mathrm{P}}}{N_{\mathrm{P}}^{exp}}$	E_{mean}^{exp}	$E_{\mathrm{mean}}^{recon}$	$\frac{\Delta E_{\mathrm{mean}}}{E_{\mathrm{mean}}^{exp}}$
	mV	cm^{-2}	cm^{-2}		MeV	MeV	
$0\,\mu\mathrm{m}$	30.70	104350	108731	4.2%	19.77	19.73	-0.2%
$200\,\mu\mathrm{m}$	17.66	59694	62558	4.8%	18.82	19.18	2.0%
$400\,\mu\mathrm{m}$	12.23	41384	42928	3.7%	18.75	18.46	-1.5%
$600\,\mu\mathrm{m}$	9.10	31765	31525	-0.8%	17.90	17.85	-0.3%
$800\,\mu\mathrm{m}$	6.58	25066	22113	-11.8%	17.12	17.27	0.9%
$1000\,\mu\mathrm{m}$	5.55	20109	18585	-7.6%	16.68	16.65	-0.1%
$1200\,\mu\mathrm{m}$	4.79	16212	15499	-4.4%	15.93	16.00	0.5%
$1400\,\mu\mathrm{m}$	4.38	14195	13925	-1.9%	15.31	15.13	-1.2%
$1600\,\mu\mathrm{m}$	3.31	11438	10091	-11.8%	14.61	14.56	-0.3%
Polyenergetic	3.04	9969	10505	5.4%	14.45	14.19	-1.8%

(a) (b)
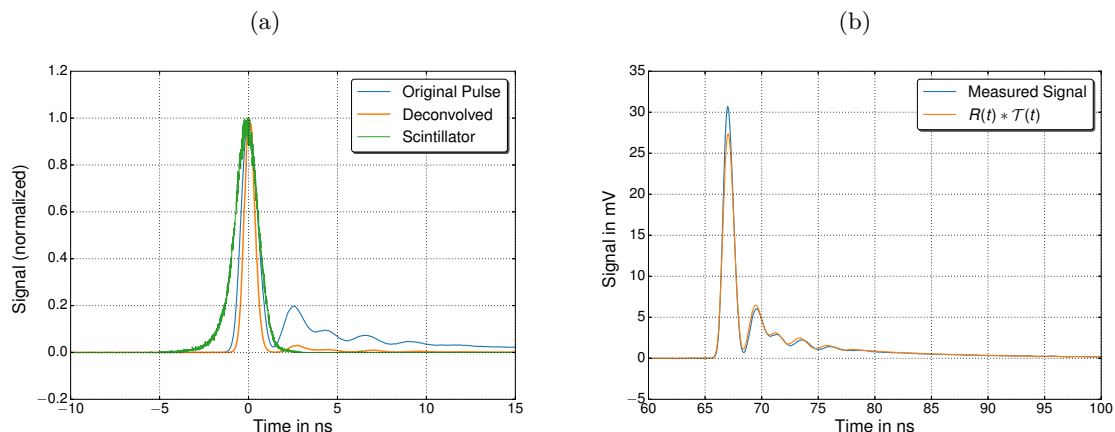
Figure 6.9: Temporal pulse structure of the bunched pulses at the Tandem accelerator. In (a), the bunch structure obtained by deconvolving the detector response (blue) from the measured TOF signal with no absorbers is shown in orange. It is compared to the bunch structure determined with the scintillator detecting large-angle scattered protons (green). For control purposes, the measured signal (blue) is compared to the convolution of the detector response function $R(t)$ with the deconvolved temporal structure $\mathcal{T}(t)$ in (b).

method.

However, the bunch duration obtained with the deconvolution method is clearly shorter than the bunch duration measured with the scintillator and the PMT, which was 1.6 ns (FWHM). The reason for the apparently longer pulse duration measured using the scintillator is due to the jitter of the stop signal of the beam chopper. This jitter is in the order of 1 to 2 ns, which results in a Gaussian smearing of the actual temporal bunch structure since that method relies on the signal of several thousand proton bunches.

(a) TOF Signal

(b) Spectrum
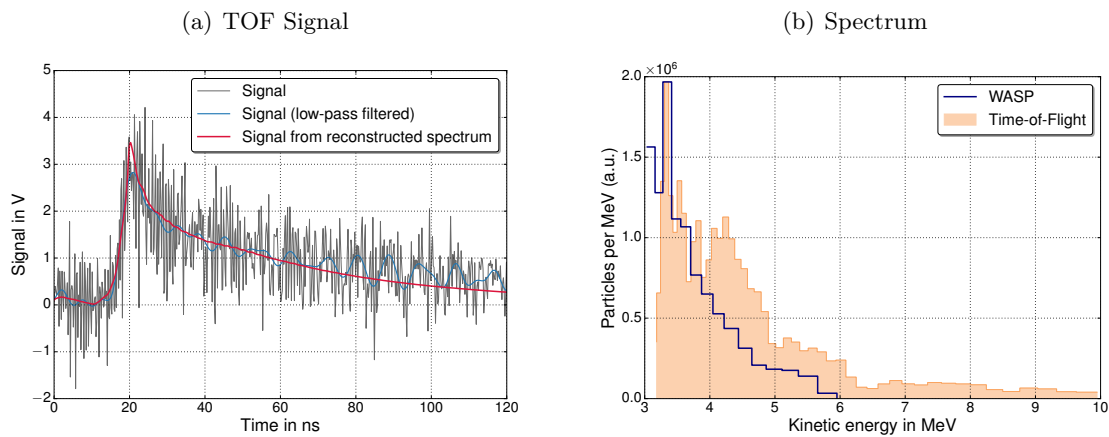
Figure 6.10: Reconstructed proton energy distribution of an unfocused proton bunch at LEX Photonics. The measured TOF signal (gray) and the low-pass filtered signal (blue) are shown in (a). The signal obtained when multiplying the reconstructed spectrum with the response matrix is shown in red. In (b), the reconstructed TOF spectrum (orange) is compared to the spectrum simultaneously measured using the WASP (blue).

6.3.3 TOF Spectrometry of Laser-Accelerated Proton Bunches

In the following, reconstructed proton energy spectra are presented for an unfocused LION bunch, as well as for an ion bunch focused by the doublet of PMQs with a design energy of 6 MeV. Due to the increased high frequency noise, the regularization parameter was set to $\mu = 5 \times 10^{-4}$ to prevent overfitting.

Unfocused Proton Bunch

An example for typical TOF signals obtained at LEX Photonics is shown in figure 6.10a. TOF signals measured at LEX Photonics are dominated by strong high frequency noise. The origin of this noise is the strong electromagnetic pulse (EMP), which is generated in the laser-plasma interaction and which may be picked up by the detector, the adapter board and cables. Despite the obvious disadvantage of this high frequency noise, it can be exploited to determine the starting time for the TOF measurement.

The actual TOF signal can be better visualized by applying a low-pass filter to the data. Note however, that this filtered signal was not used for spectrum reconstruction, as important high frequency components determining the rising edge of the actual signal would otherwise get lost. When looking at the filtered signal, two distinct peaks can be found, separated by several nano-seconds.

The first, smaller peak at 0 ns can be attributed to highly-relativistic electrons, reaching the detector practically at the same time as the electromagnetic pulse. Since this small peak cannot be found in the TOF signals when magnetically focusing the beam (see next section), it can be excluded that it is created by x-rays and gamma rays. This is consistent with the Bridge microdosimeter's relatively low detection efficiency to photons
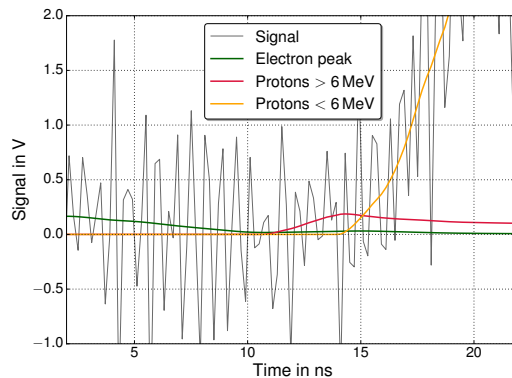
Figure 6.11: Measured TOF signal of an unfocused proton bunch at LEX Photonics (zoomed into the initial part of the rising signal edge). Contributions to the signal by electrons (green) and protons with energies above (red) and below (orange) 6 MeV, obtained when multiplying the reconstructed spectrum with the response matrix, are shown.

with energies above $\sim 10\,\text{keV}$, due to the only $10\,\mu\text{m}$ thin silicon SV.

The second peak encountered at around $20\,\text{ns}$ is the actual ion peak. Due to the high fluxes, signal amplitudes of several V were typically measured. Therefore, the choice of the detector response function for high light intensities, as determined in 5.2.1, is valid for setting up the system matrix.

The proton energy distribution simultaneously measured by the WASP and the spectrum reconstructed from the measured TOF signal are shown in figure 6.10b. Note that due to the missing absolute particle number calibration, the TOF spectrum was scaled to match the WASP spectrum. Despite the differences between 4 and 5 MeV, both spectra are in good agreement and show an exponential shape, which is typical for acceleration in the TNSA regime. According to the TOF spectrum, the highest proton energy in this laser shot was around $9.5\,\text{MeV}$, which is substantially higher than the maximum energy measured by the WASP.

In figure 6.10a, the measured TOF signal is shown together with the signal obtained when multiplying the reconstructed spectrum with the system matrix $\mathcal{A}$. A closer look to the rising edge of the signal is shown in figure 6.11, where the artificial signal generated from the reconstructed spectrum is subdivided into contributions from ultra-relativistic electrons and protons with an energy above and below 6 MeV, respectively. The comparison reveals that the measured signal corresponding to the part of the reconstructed proton spectrum having an energy above 6 MeV is actually dominated by high frequency noise. With the encountered signal-to-noise ratio, the presence of this part of the proton spectrum is therefore rather uncertain.

At the low-energy side of the spectrum, the two measured spectra differ due to the different aluminum foil thickness covering both detectors. In case of the Bridge microdosimeter, this was $90\,\mu\text{m}$, corresponding to a cut-off energy of $3.2\,\text{MeV}$, while the RadEye detectors of the WASP were shielded by a $30\,\mu\text{m}$ thin aluminum foil.

(a) TOF signal

(b) Spectrum
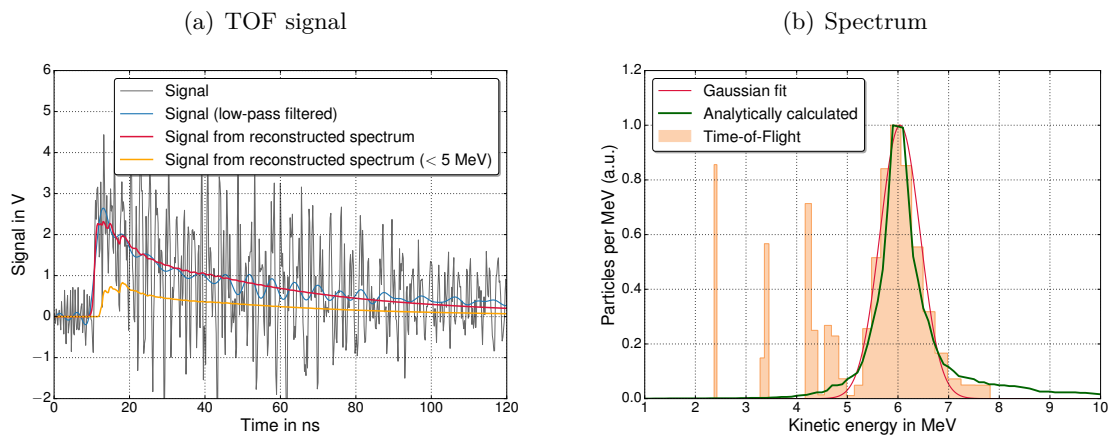
Figure 6.12: Reconstructed proton energy distribution of a focused proton bunch at LEX Photonics. In (a), measured and low-pass filtered signal (gray and blue, respectively) are compared to the signal obtained when multiplying the reconstructed spectrum with the response matrix, shown in red. Contributions to the signal protons with energies below 5 MeV are shown by the orange curve. In (b), the reconstructed TOF spectrum (orange) and a Gaussian fit (red) is compared to the expected energy distribution based on analytical calculations (green).

Focused Proton Bunch

A doublet of PMQs was used to focus 6 MeV protons onto the Bridge microdosimeter, located at a distance of 40 cm from the target position. The measured TOF signal is shown in figure 6.12a. In contrast to the measured signal with no focusing devices, the small peak ahead of the main ion peak is missing. This indicates that the small peak is generated by electrons, as already mentioned previously. Due to their much higher charge-to-mass ratio, electrons are strongly defocused inside the two PMQs, thus only a negligible fraction can reach the Bridge detector.

The reconstructed energy distribution, shown in figure 6.12b, nicely peaks at 6.04 MeV. According to a Gaussian fit of the reconstructed peak, its energy width is 0.93 MeV (FWHM). This is only slightly broader than expected from analytical calculations (+17%), in which the trajectories of protons from a broad energy distribution were traced through the measured magnetic field strengths and the corresponding distances [Rösch, 2018].

Some spurious events can be seen at lower energies. Multiplying the response matrix with the part of the reconstructed spectrum below 5 MeV shows the contribution to the TOF signal (see orange curve in figure 6.12a). From the comparison of this contribution to the measured signal, it can be concluded that these events are most likely fitting artifacts caused by the strong EMP noise.
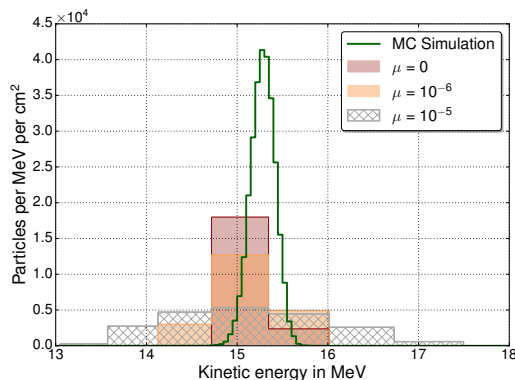
Figure 6.13: Width of the reconstructed energy distribution from TOF measurements at the Tandem accelerator for an absorber thickness of 1.4 mm and for different regularization parameters μ. The MC calculated energy spectrum is shown in green.

6.4 Discussion

6.4.1 Width of the Reconstructed Energy Spectra

For the TOF measurements of quasi-monoenergetic bunches, reconstructed spectra using the TOF approach are in good agreement within 2% with MC simulations and with reconstructed spectra using the magnetic spectrometer, in terms of their mean kinetic energy. The observed differences in the width of the quasi-monoenergetic energy spectra can partially be attributed to the use of Tikhonov regularization when solving the least-squares problem. This regularization was used to enhance the smoothness of the reconstructed spectrum, since a discontinuous spectrum caused by overfitting does not correspond to expectations from such experiments.

A comparison of reconstructed spectra with and without regularization is shown in figure 6.13. The thin energy width of the simulated spectra, which is about 0.46 MeV can only approximately be reproduced when no regularization is used. However, an exact comparison is difficult due to the large energy bin width, caused by the sampling time of 0.2 ns. The impact for different regularization parameters μ can clearly be seen in the increased broadening of the reconstructed spectrum.

6.4.2 Energy Resolution

For a fixed detection and readout system, the achievable energy resolution scales approximately linearly with the distance between proton source and detector. The resolution of the reconstructed spectra presented in this chapter was mainly limited by the relatively short drift spaces between 40.0 and 53.7 cm. Following Nakamura et al. [2006], the energy resolution ΔE_{kin} of the TOF system can be written as

$$\Delta E_{\text{kin}} = \frac{\Delta t(2t_{\text{TOF}} - \Delta t)}{(t_{\text{TOF}} - \Delta t)^2} E_{\text{kin}} \ , \tag{6.8}$$

with the time resolution of the readout system Δt, the TOF of the protons t_{TOF} and the kinetic energy E_{kin}. For example, in case of the focused 6 MeV laser-accelerated proton beam measured at a distance of 40 cm from the source, this would result in an energy resolution of $E_{\text{kin}} = 0.21$ MeV.

In case of the experiments performed at the Tandem accelerator, this short drift length was required because of the large beam divergence due to scattering at the passive absorbers. According to simulations and the FC measurements, the average number of protons that actually reached the SV of one segment of the BridgeV2 microdosimeter per bunch was ranging between ~ 360 and ~ 3800, depending on the absorber thickness. For an absorber thickness of 1.6 mm, the measured amplitude of the signal was around 3 mV. A further increase of drift space from the position in the experiment to e.g. 1 m would have resulted in a more than 70% lower proton fluence and hence, signal amplitude.

For TOF spectrometry of laser-accelerated particles, fluence is not an issue as signal amplitudes of several volts have been obtained at distances around 0.5 m. However, the drift length in the presented experiments was limited by external constraints of the experimental setup. As the target position and the WASP were fixed, only few positions to place the Bridge microdosimeter in forward direction under a small angle with respect to the laser axis were possible. In future experiments at CALA, longer drift spaces in the order of a few meters are foreseen. The possible energy resolution can hence be increased by almost one order of magnitude, while the amplitude of the measured TOF signal will still remain sufficiently high.

Besides larger drift spaces, faster detectors and high-end readout electronics could potentially further increase the energy resolution. Faster detectors can be achieved by reducing their capacitance and are in principle meanwhile available (e.g. U3DTHIN; see section 5.4). Oscilloscopes with a bandwidth that is ten times as large as the bandwidth of the oscilloscope used in this study are commercially available, although to this date, their use might be hindered by the prices of such devices (> 100 k€).

Combining the longer drift space and the in principle available faster detectors and readout can result in an energy resolution gain of about 2 orders of magnitude when measuring in the same range of kinetic energies. When going from the studied proton energy range below 20 MeV to energies in the therapeutically relevant range (< 250 MeV), TOF differences corresponding to an energy difference of $\delta E = 0.1$ MeV decrease by a factor of around 50. With nowadays available equipment and optimized drift spaces, it would hence also be possible to obtain the same energy resolution as presented in this study for proton energies up to 250 MeV.

6.4.3 Uncertainty Estimation for Reconstructed Spectra

From an experimental point-of-view, several sources of uncertainty can contribute to the total uncertainty of the reconstructed particle spectra. Two sources of uncertainty influencing the reconstructed energy spectra are discussed in the following, as well as the

uncertainty of the particle number calibration measurements.

Drift Length Measurement

The first uncertainty is the measurement uncertainty of the drift length. Although in principle this distance can be determined with high accuracy, relatively large errors of a few millimeters may still be expected. The distances at the experimental setup at the Tandem accelerator could be determined within $\pm 2\,$mm. At LEX Photonics, measuring the total drift space was slightly more challenging. A rather conservative estimate of this uncertainty is $\pm 5\,$mm, corresponding to 1.25% of the total drift length for the focused proton bunch. Reconstructing the energy spectrum with this variation in drift space results in a shift of its mean energy by $0.13\,$MeV, or 2.1%. For larger proton energies, this relative uncertainty increases moderately. Needless to say, this uncertainty can be drastically reduced by more accurate length measurements and longer drift spaces.

Determination of the Starting Times

The other source of uncertainty is related to finding the proper starting time $t = 0$. In case of the Tandem measurements, the starting time was given by the ultra-thin detector. Run-time differences between the trigger signal and the TOF signal could be determined by measuring the shift of the signal traces on the oscilloscope for a known proton energy. The starting time could hence be determined with an accuracy better than $0.1\,$ns. For the TOF spectrometry of laser-accelerated protons, the rise of the signal induced by the electromagnetic pulse was used to obtain $t = 0$. However, in some acquired TOF signals it may be difficult to unambiguously determine the exact start of the high frequency oscillations caused by the EMP. In general, finding the starting time with an accuracy better than $\pm 0.2\,$ns should be possible. Nevertheless, the here presented uncertainty estimation will rely on a conservative value of $\Delta t_0 = 0.3\,$ns. Introducing this number into the spectrum reconstruction of the focused LION beam results in a deviation of the reconstructed mean energy of $0.31\,$MeV or 5.2%. With fixed drift space, the relative error rapidly increases with increasing proton energy.

Together with the drift length uncertainty, this adds up to a combined energy uncertainty of 2.4% for the Tandem measurements at energies up to $20\,$MeV and 5.6% for the LION measurements at LEX Photonics at proton energies around $6\,$MeV.

Uncertainty of the Particle Number

The main source of uncertainty in the absolute particle number calibration is the relatively large fluctuation of the beam current during measurements at the Tandem accelerator, which was about 25%. This is also the reason for the encountered discrepancies when comparing the reconstructed particle numbers to expectations from MC simulations, as summarized in table 6.1.

The beam current could not be directly monitored while performing the calibration measurements, but was determined before and after the irradiation using the FC close to the experiment. Although the data used to perform the absolute particle number calibration was averaged over 500 individual bunches within a few seconds, current fluctuations that may extend also over larger time scales can not be entirely averaged out. Yet, observation of the beam current before and after the measurements, as well as of the signal amplitude of the ultra-thin detector, suggest that the remaining uncertainty within the time of the calibration measurements and the TOF measurements was below 10%.

Also, the Bridge microdosimeter was slightly misaligned in the calibration experiment at the Tandem. The accuracy of the measurement of the alignment with respect to the beam axis was about 0.5 mm. Since according to MC simulations, the spot size in the calibration measurements was around 9 mm (FWHM) at the location of the TOF detector, the positioning uncertainty perpendicular to the beam axis translates into an uncertainty of the actual number of protons on the detector of 6.8%.

The statistical fluctuation of the energy deposition inside the SV of the detector may in principle also contribute to this uncertainty. However, its impact is negligible compared to the aforementioned uncertainties, since in general a large number of particles contributes to each reconstructed energy bin.

The combination of those independent uncertainties results in a total uncertainty of the particle number of 12.1% for the Tandem measurements. For the TOF measurements of laser-accelerated ions at LEX Photonics, the older version of the Bridge microdosimeter, as well as a different adapter were used. Therefore, spectra presented for these experiments are given in relative units. A calibration could not be properly performed within this project, since the detector had experienced some severe radiation damage in TOF experiments at LEX Photonics before having the possibility to measure its response at the Tandem accelerator under well-controlled conditions.

6.4.4 Determination of Ion Spectra in Mixed Fields

Although typically dominated by protons, laser-accelerated ion bunches may consist of several different ion species [Daido et al., 2012]. According to FLUKA MC simulations, C^{6+} ions would require kinetic energies above 2.7 MeV/n and 5.7 MeV/n to entirely penetrate the 30 µm and 90 µm thin aluminum foil covering the entrance hole of the Bridge detector box. In the two spectra presented within this chapter, no other ion species than protons was expected to contribute to the measured TOF signal based on the following considerations.

Due to their higher charge-to-mass (q/m) ratio, the acceleration of protons is much more efficient than for heavier ions. Since the high-energy cutoff of protons in the presented spectrum was around 6 MeV, it is very unlikely that carbon ions were accelerated to kinetic energies exceeding 5.7 MeV/n in the same laser-plasma interaction.

In case of the focused particle beam, the absorbing aluminum foil was thinner, such that

carbon ions with kinetic energies above 2.7 MeV/n could potentially contribute to the TOF signal. However, the distances of the PMQs used to focus 6 MeV protons would focus C^{6+} of 1.5 MeV/n onto the same position [Rösch, 2018]. Thus, if there were carbon ions with energies above 2.7 MeV/n, they would have been strongly defocused and their contribution to the TOF signal would have been negligible.

Yet, these considerations are not sufficiently describing the problem in general. If different ion species are present in the laser-accelerated particle bunch and all ions are capable to reach the TOF detector, the signal current generated by the individual species will be overlapping. Hence, without any prior knowledge like the aforementioned beam shaping devices or absorbing foils, it is hardly possible to deconvolve the contribution of each ion species unambiguously. In case no prior knowledge is available, prior assumptions on the typical energy distributions of different ion species might help to get a good estimate of the spectra for each ion species individually.

6.4.5 Electromagnetic Pulse

One of the issues encountered for TOF measurements at LEX Photonics was the dominance of the high frequency oscillations caused by the EMP, as compared to the actual signal generated by the ultra-relativistic electrons or ions.

Interestingly, such a typical EMP signal could also be measured, when no detector was plugged into the DIL socket of the test adapter. This clearly indicates that the adapter itself was responsible for picking up the high frequency noise. This led to the development of better suited adapters aiming for a better performance in terms of immunity to the EMP. However, the improved adapter (passive adapter; presented in section 4.2.1) was developed after the close-down of the ATLAS-300 laser system in December 2016 and its performance could thus not yet be tested.

A qualitative test experiment was therefore performed to judge if better performance can be expected from the new design. Both, the test and the passive adapter, were connected simultaneously to the broadband oscilloscope, which was triggered by the signal generated by the test adapter.

A mobile phone, sending in the GSM and UMTS frequency bands of $f = 0.90$ GHz and $f = 1.98$ GHz, respectively, was used to generated high frequency noise. As it can be seen in figure 6.14, for both frequencies the pick-up of high frequency noise of the new, passive adapter decreased by almost two orders of magnitude as compared to the old, test adapter. Similar EMP reduction is therefore expected in future experiments at CALA.

6.5 Conclusion & Perspectives

In this chapter, a novel approach to obtain absolute spectral information of ultra-short polyenergetic proton bunches was presented. This method is based on the measurement of the pile-up current signal generated in the Bridge microdosimeter by continuous proton
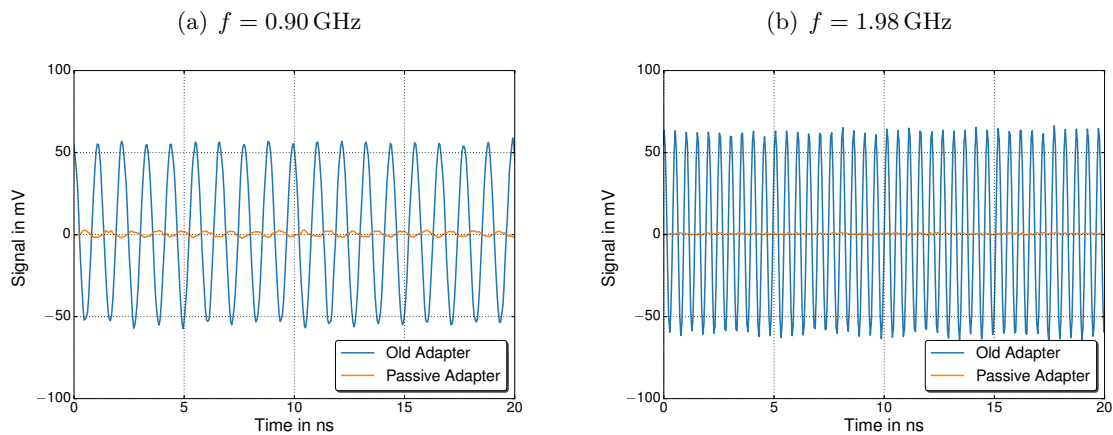
Figure 6.14: Comparison of high frequency noise pick-up of the test adapter (blue) and the newly developed passive adapter (orange). Measured noise is shown for 0.90 GHz and 1.98 GHz in (a) and (b), respectively.

irradiation. Spectra were reconstructed by means of least-squares optimization, exploiting the different arrival times at the detector due to the different kinetic energies of combined sub-packages of the continuous proton bunches. Moreover, the measured detector response function was taken into account to obtain properly reconstructed energy distributions.

Experiments were performed using passively energy-modulated bunched proton beams from the Tandem accelerator, as well as at LEX Photonics, where TOF signals of laser-accelerated proton bunches were measured. In case of the reconstruction of quasi-monoenergetic proton bunches, very promising agreement of the reconstructed and the expected mean energy was obtained within the estimated measurement uncertainties of 2.4% and 5.6% for the Tandem and LION measurements, respectively. For TOF experiments at the Tandem accelerator, the absolute reconstructed proton number agreed with MC based expectations within 12%, which is within the uncertainty caused by beam current fluctuations. On the other hand, no absolute particle numbers could be obtained for the spectrometry of laser-accelerated proton bunches due to different detector configurations as compared to the calibration measurements.

For both laser-accelerated and conventionally accelerated proton bunches, the spectral width of the reconstructed energy distributions of quasi-monoenergetic bunches was found to be larger than expectations, which is caused by the spectral bin width given by the sampling time and the applied regularization in the least-squares optimization. The reconstructed energy distribution of polychromatic proton bunches, however, was found to be in good agreement with measurements using a magnetic spectrometer. Moreover, a method to obtain the pulse duration of proton bunches from the Tandem accelerator, based on deconvolution of the detector response from the measured current signal was presented. The intended sub-ns bunch duration was achieved to emulate the characteristic bunch duration of laser-accelerated protons.

The presence of a strong electromagnetic pulse in the TOF signal of laser-accelerated ions was found to be modestly disturbing the spectrum reconstruction. However, by using a newly developed dedicated interface between the Bridge detector and the readout, this problem can probably be reduced considerably. When reconstructing spectra from a mixed ion source, additional information is required. Up to some extent, such information can feature constraints given by beam shaping devices, like the applied PMQs, or absorbers prior to the detector determining the energy cut-off of different ion species.

When going to higher ion energies, the measurable time-of-flight differences are rapidly decreasing, influencing the achievable spectral resolution. By using larger drift lengths and fastest readout electronics meanwhile available, similar resolution could in principle be achieved for proton energies in the therapeutically relevant energy range up to 250 MeV. Of course, for such high energies, this resolution also requires the use of detectors with sufficiently fast charge collection times even below the timing properties found for the Bridge detector.

Ideally, the detector measuring the TOF signal should be operated online in transmission prior to any experiment. Therefore, the total geometrical thickness of the detector needs to be sufficiently thin to keep the perturbation of the initial ion bunch small. Possible solutions could be a modified version of the Bridge microdosimeter with more segments of SVs spanning over a larger area and in which the supporting wafer is etched to a minimum, similar to the mentioned planar ultra-thin silicon detector. The different segments need to be read out individually to provide spatial information on the ion bunches. Alternatively, the U3DTHIN detector, which has already been proposed in section 5.4, could be a promising choice for transmission TOF spectrometry, despite its lack of spatial information.

Timepix Edge-on Spectrometry

Extensive studies on the usability of the Timepix detector for the detection and character-ization of laser-accelerated protons in *face-on* irradiation are shown in Reinhardt [2012]. Due to the limited dynamic range, observed as a saturation at an incident proton fluence of about 2.5×10^5 protons/cm^2, that PhD study concludes that the Timepix detector system is not suited for diagnostics of laser-accelerated protons.

Nevertheless, the detector capability to detect and distinguish single ions gives rise to certain applications related to laser-ion acceleration, namely where lower particle fluxes are expected. One potential application would be the detection of laser-accelerated helium ions from focusing an intense laser pulse on a supersonic helium gas jet (see appendix A). Also, the Timepix detector could be used as an additional diagnostic instrument to char-acterize laser-accelerated ion bunches far from the laser-plasma interaction, where the fluence drops to an acceptable level due to the intrinsic beam divergence. Similarly, in combination with a dipole magnet deflecting protons with low kinetic energy, the Timepix detector has the potential to detect the relatively low number of high-energy protons close to the cut-off energy.

For such applications, the Timepix detector can be irradiated *edge-on*, i.e., the direction of the incoming protons is parallel to the sensor chip and they hit its edge perpendicularly. In this configuration, the energy deposition of each individual proton along its path inside the sensor chip, as well as the lateral distribution of the bunch along one axis is measured. In other words, it can be used as a silicon-based range telescope with position information in one transversal dimension. Since the signal measured with the Timepix detector scales with the deposited energy and therefore provides more information than in *hit/miss*-measurements, sub-pixel range resolution can be obtained.

In the first section of this chapter, the general concept of Timepix edge-on spectrometry is presented, giving a brief introduction on how the measured signal is composed and how the energy spectrum can be deduced from it. The experimental and computational methods related to this study, ranging from the calibration of the detector to the actual spectrum reconstruction are described in section 7.2. Results are shown and discussed in section 7.3

and section 7.4, respectively, before the chapter is concluded with a brief outlook.

7.1 Concept

When irradiating the sensor chip of the Timepix detector in edge-on configuration with sufficiently low particle fluxes, Bragg curves of individual protons, showing their dE/dx in the sensor chip material at a pixel-size scale and along their entire path length in the detector can be measured (illustrated schematically in figure 7.1). Moreover, the lateral distribution of the incoming proton beams along the sensor chip and hence the beam size and/or inhomogeneities along that axis could easily be detected.

Measurements under very low grazing angles ($\phi \to 0$) have already been shown for protons and heavier ions (e.g. Reinhardt [2012] and Granja et al. [2016]), as well as for fast electrons up to 21 MeV [Granja et al., 2013]. However, these studies were not aiming for a characterization of polyenergetic ion sources like laser-accelerated ion bunches.

The statistical nature of the energy loss of protons in matter also affects their range, resulting in range straggling (discussed in 2.2.2). Obviously, for single proton characterization, this is the limiting factor of the achievable accuracy of the reconstructed initial proton energy.

With increased fluence and consequently overlapping proton tracks, the measured detector signal becomes the superposition of the energy deposition by every individual proton along its entire penetration depth inside the sensor chip. Thus, similar considerations as described for the TOF spectrometry in section 6.2.3 are also applicable to this problem. In this case, for every pixel column i (perpendicular to the irradiated edge), the detector signal S_{ij} in the j-th pixel row (parallel to the edge) can be expressed by

$$S_{ij} = \sum_k n_{ik} \cdot \mathcal{A}_{jk}, \tag{7.1}$$

where n_{ik} is the number of protons within a certain energy bin k in pixel column i and $\mathcal{A}_{jk}$ is the system response matrix, which is given by the average energy deposition of one proton with a kinetic energy k in a pixel of the j-th row.

Thus, for each pixel column i, the proton distribution $\frac{d\vec{n}}{dE}$ can be obtained by solving the linear least-squares problem with bound constraints:

$$\min_{\vec{n}} \|\mathcal{A} \cdot \vec{n} - \vec{S}\|^2 \quad \text{subject to} \quad 0 \leq n_k . \tag{7.2}$$

7.2 Materials & Methods

The functionality and the properties of the Timepix detector used in this study have already been shown in section 4.2.2. In this section, the experimental materials and computational methods for the edge-on spectrometric approach are explained thoroughly.
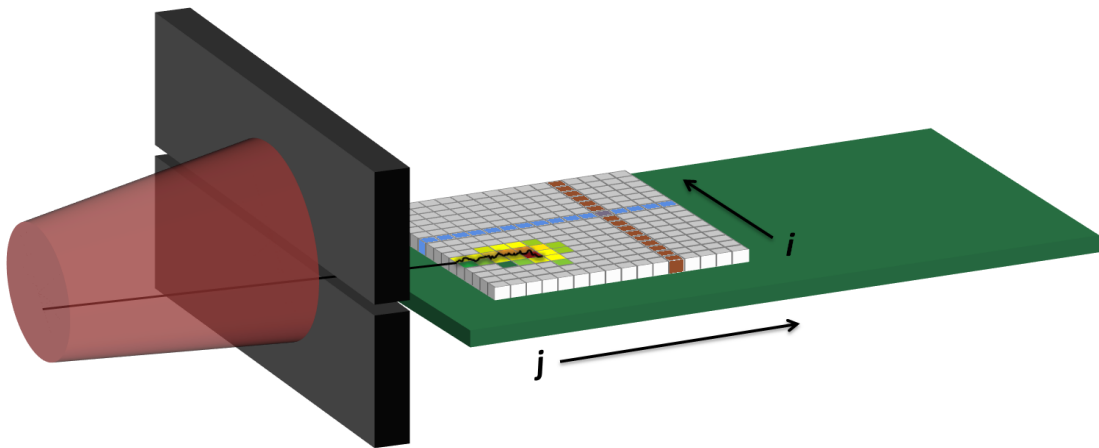
Figure 7.1: Cartoon showing the principle of the Timepix edge-on spectrometry setup. The ion beam coming from the left (red cone) is hitting the collimator (black blocks). The sensor chip of the Timepix detector is shown in gray. Only a small number of protons (indicated by black line) pass through the slit and impinge on the sensor chip's front edge. The individual protons penetrate the sensor chip parallel to its face and are continuously slowed down, giving rise to a detector signal inside the traversed and neighboring pixels which is proportional to the energy deposition (indicated by colors in pixels ranging from green to red). One of the pixel *columns* is colored blue and one pixel *row* is marked in brown to explain the nomenclature used within this chapter.

First, the methodology how to extract clusters from acquired Timepix frames is explained in section 7.2.1. In section 7.2.2 follows the description of the calibration measurements performed to obtain energy deposition values for each individual pixel from the TOT value. Next, the actual experimental setups and the corresponding simulation setups for edge-on irradiation are presented in sections 7.2.3 and 7.2.4, respectively. Since the sensor chip of the Timepix detector used in this study is larger than the readout chip, section 7.2.5 is dedicated to the determination of the extension of the non-overlapping part of sensor and readout chip. Finally, in section 7.2.6 the method to obtain proton energy spectra from both measured or simulated Timepix data is presented.

7.2.1 Cluster Analysis

In face-on irradiation, charge-sharing effects lead to non-zero signal in a cluster of adjacent pixels around the pixel that was hit by the incident particle (see section 4.2.2). Motion of these particles with respect to the sensor surface, like for ions in edge-on irradiation or the erratic motion of electrons, additionally affects size and shape of the clusters. In the following, the term cluster will be used for any group of adjacent pixels with non-zero response.

A routine that identifies and analyzes clusters from an energy-calibrated Timepix acquisition frame (see section 7.2.2) was implemented. In a first step, every frame was median filtered to account for *hot* or *cold* pixels (figure 7.2a). A global threshold of 6 keV per pixel was defined and a mask was created with all pixels of the median filtered frame above that threshold. All objects consisting of adjacent non-zero pixel values (= clusters) were then

(a) Median-filtered frame

(b) Identified clusters
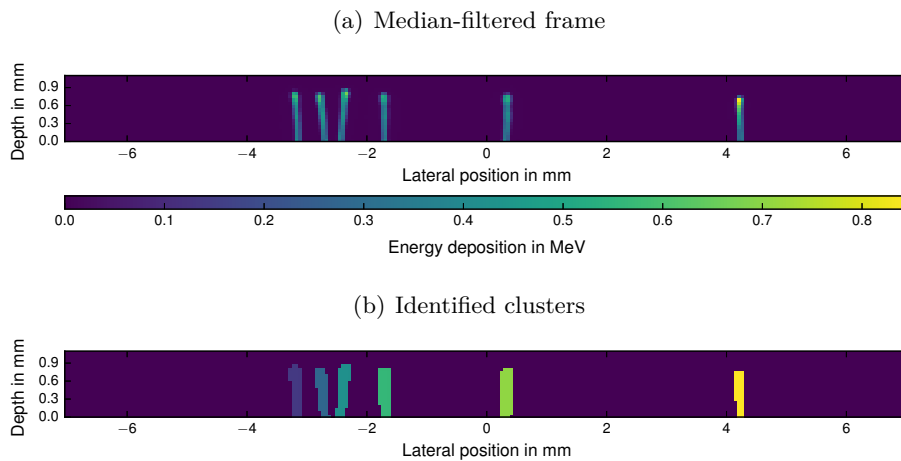
Figure 7.2: Energy-calibrated and median-filtered Timepix frame (a) and corresponding identified clusters (b). The colors in (b) are to distinguish individual tracks. In both images, only the part of the acquisition frame close to the front edge is shown.

identified, labeled and stored (figure 7.2b).

For each identified cluster, the following properties[1] are determined and can be used for analysis and subsequently as cluster selection criteria:

- **Cluster Energy**, or **cluster sum**, is the total deposited energy in a cluster and is calculated by summing the energy values of all pixels belonging to the cluster.

- **Cluster Size** is the number of pixels constituting to the cluster.

- **Track Length** is the extension of the cluster in longitudinal direction.

- **Track Width** is the size of the cluster in transversal direction.

- **Cluster Row** is the longitudinal position of the first cluster pixel. In edge-on irradiation, this value equals 1 for clusters generated by proton tracks.

- **Cluster Column** is the lateral position of the cluster. It is given by the highest pixel value of that cluster along the *cluster row*.

- **Lateral Displacement** is the deviation of the lateral position at the longitudinal peak position from the previously determined *cluster column*.

7.2.2 Energy Calibration of the Timepix Detector

Since every pixel of the Timepix detector is connected to its own analog circuitry and analog-to-digital converter (ADC), an independent energy calibration for each of the 65 536

---

[1]Note that some of these properties are only meaningful when single tracks in edge-on irradiation are studied.
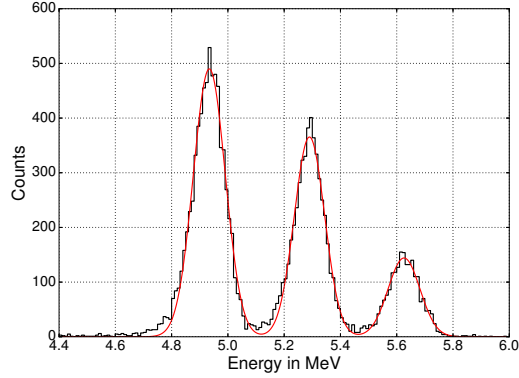
Figure 7.3: Validation of the Timepix energy calibration for higher energies using a mixed α-source. The peaks of the histogram of the cluster energy values (black) were fitted by Gaussian distribution functions (red).

channels is required [Jakůbek et al., 2008]. The TOT to energy calibration measurements were performed at the IEAP of the CTU in Prague, using the same bias voltage (90 V) and readout chip settings as in the subsequent experiments. A detailed description of the energy calibration procedure can be found in Jakůbek [2011].

The calibration curve relating energy deposition E to TOT signal is

$$\text{TOT}(E) = a \cdot E + b - \frac{c}{E - d}\,,\tag{7.3}$$

where a, b, c and d are the fit parameters obtained from the calibration measurements. The last term in eq. 7.3 corresponds to the non-linearity of the detector at very low energies.

A multilayer calibration source, consisting of ^{241}Am and two fluorescent materials (Indium and Iron), was used to irradiate the Timepix detector. The corresponding gamma and characteristic fluorescence x-ray energies are 59.5 keV, 24.1 keV and 6.4 keV. TOT spectra of the three emission lines are acquired for every pixel, taking into account only single pixel clusters. The two higher emission lines correspond to the energy range in which the detector response is linear. The measured TOT distributions were fitted by Gaussian functions and their mean TOT values were extracted. In contrast, the lowest emission line is close to the threshold energy and thus in the non-linear energy range of $\text{TOT}(E)$. Hence, the corresponding measured TOT distribution has the shape of a deformed Gaussian function. Therefore, a combination of a Gaussian function with the inverse of eq. 7.3 was fitted to the TOT response of that emission line, taking into account the two fit parameters obtained from both high-energy emission lines.

Similar to Reinhardt [2012], the quality of the extrapolation of the calibration curve towards higher energies was tested using a mixed α-source consisting of ^{239}Pu, ^{241}Am and ^{244}Cm. Their dominant α energies are 5.16 MeV, 5.49 MeV and 5.80 MeV for the three radionuclides, respectively [Kinsey et al., 1996]. Before entering the sensitive volume of the sensor chip, the α particles have to traverse the thin metallization layer

on the back side of the Timepix sensor chip, which is a $1.2\,\mu m$ thin aluminum layer [X-ray Imaging Europe GmbH, 2018]. According to FLUKA MC simulations, the average residual energies for the respective radionuclides are then $4.95\,MeV$, $5.29\,MeV$ and $5.61\,MeV$.

In the experiment, the total energy of the α particles was determined by calculating the cluster sum after applying the pixel-wise energy calibration to the TOT signal. Three peaks can be distinguished and fitted by Gaussian functions in the measured spectrum (figure 7.3). Their mean energies are $4.93\,MeV$, $5.29\,MeV$ and $5.63\,MeV$, respectively, with standard deviations below $0.06\,MeV$. Since the fitted energies are in excellent agreement with theoretically expected energies, it can be concluded that the energy calibration of the Timepix detector can be extrapolated over almost two orders of magnitude up to energies close to the MeV-range.

7.2.3 Experimental Edge-on Irradiation Setup

All irradiation experiments of the Timepix detector in edge-on configuration were performed in vacuum at the MLL Tandem van-de-Graaf accelerator (section 4.3.1). The Timepix detector and the FITPix readout interface were mounted in a dedicated aluminum box to reduce stray radiation (figure 7.4c). A $150\,\mu m$ thin entrance slit centered with respect to the $500\,\mu m$ thick silicon sensor chip (figure 7.4b) was built using two $5\,mm$ thick aluminum blocks to assure centric and perpendicular incidence of the protons with respect to the front edge of the detector sensor chip. The detector was biased at $90\,V$ and was operated in TOT mode. Signal was converted offline into energy deposition using eq. 7.3.

One experimental session was dedicated to the calibration of the edge-on configuration, while a second experimental session was aiming for spectrometry.

Setup for the Calibration of the Timepix in Edge-on Configuration

A sketch of the experimental setup can be seen in figure 7.4a. In order to calibrate the Timepix edge-on setup, the terminal voltage at the accelerator was varied, such that the kinetic proton energy was changed in $1\,MeV$ steps from $17\,MeV$ to $20\,MeV$. The small experimental vacuum chamber was flange-mounted to the beamline of the accelerator but with a $50\,\mu m$ thin Kapton foil separating the vacuum chamber from the beamline vacuum. The resulting proton energies after the Kapton foil are calculated using FLUKA MC simulations and are listed together with the validation results in table 7.1.

The proton current $I_{\mathrm{p}} = 2\,nA$ was measured using a Faraday cup upstream of the Kapton foil. The current was reduced by the tungsten attenuators (see section 4.3.1) to obtain a flux around $10^4\,protons\,cm^{-2}\,s^{-1}$. With this reduced flux, individual proton tracks could be distinguished in the acquired Timepix frames. The acquisition time per frame was adjusted within 0.1 to $0.5\,s$ assuring an optimal proton number per frame.

(a) Sketch of the experimental setup

(b) Timepix-Box with slit (outside)   (c) Timepix-Box (inside)
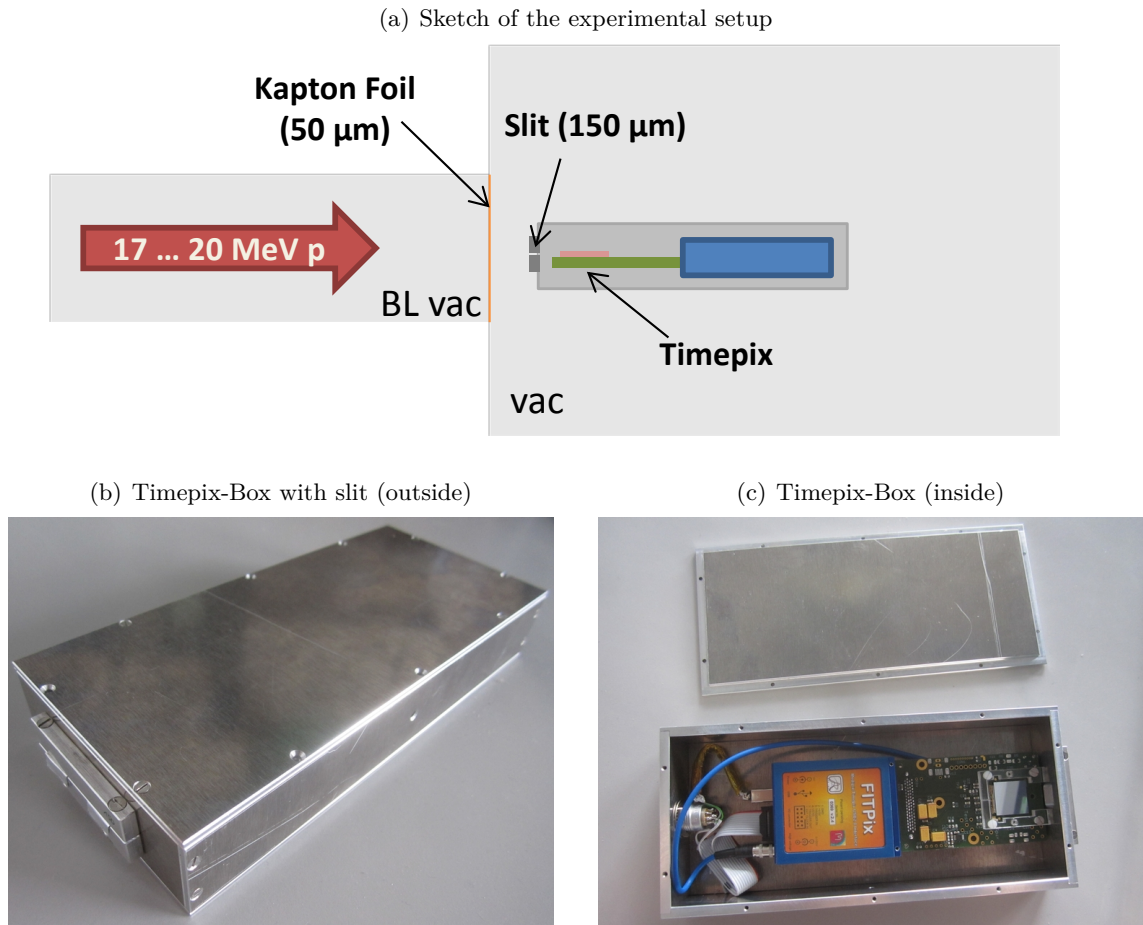
Figure 7.4: A sketch of the experimental setup for Timepix edge-on calibration measurements is shown in (a). The dedicated aluminum box with the 150 µm thin slit between two 5 mm thick aluminum blocks is shown in (b). In (c), the Timepix detector with FITPix interface can be seen.

Setup for Spectrometry in Edge-on Configuration

In the second experimental session, the proton energy from the accelerator was kept constant at 20 MeV. The vacuum chamber housing the Timepix detector was not directly attached to the beamline, so the protons exit the beamline vacuum through a 11.4 µm thin titanium vacuum window, pass an air gap of 9.8 cm before entering the Timepix vacuum chamber through a 50 µm Kapton foil. A similar proton flux and the same acquisition settings were applied as in the calibration experiments.

The non-overlapping part of sensor chip and readout chip (see section 7.2.5) allows to reconstruct protons with energies $E_{\text{kin}} > 16.6$ MeV. According to the expected energy distribution using the polyenergetic modulator described in section 4.3.1, reconstruction of such energy-modulated proton beams is hence not possible in this experimental setup. Therefore, different thin absorbers changing the mean energy and the energy width of the incoming proton bunches of 20 MeV were inserted in the proton path prior to the detector. First, the motorized passive energy degrader wheel described in section 4.3.1 was placed in the air gap close to the Kapton foil. In an additional experiment, a small
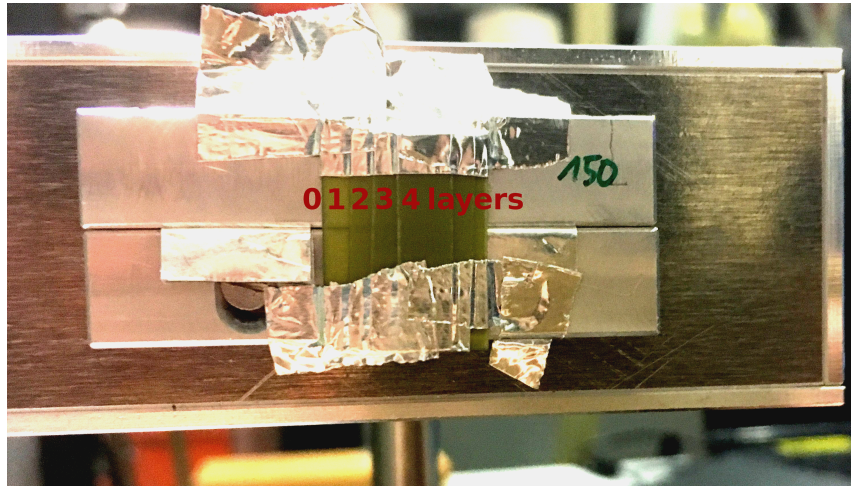
Figure 7.5: Experimental setup for position-resolved spectrometry based on the Timepix edge-on configuration. A sample consisting of 1 to 4 layers of radiochromic films, forming a kind of step phantom, is positioned prior to the entrance slit of the Timepix detector box.

sample consisting of four partially overlapping layers of RCF (EBT-3 films) was prepared and attached to the entrance slit of the detector housing (see figure 7.5) in order to obtain a laterally varying energy distribution.

7.2.4   MC Simulations Setup

FLUKA MC simulations were performed to complement the experimental study, as well as for a MC-based validation of the spectrum reconstruction.

Simulations Complementing the Experiments

Detailed models of the two experimental setups were created in the simulation geometry. The model of the first experimental setup includes a $50\,\mu m$ thin Kapton foil separating beamline vacuum from chamber vacuum, the $150\,\mu m$ thin slit between the two aluminum blocks and a $17.5 \times 17.5 \times 0.5\,mm^3$ homogeneous silicon cuboid on top of a $14 \times 14 \times 1\,mm^3$ silicon cuboid, mimicking the sensor and the readout chip, respectively. A variable offset between the front edge of the sensor chip and the readout chip (*non-overlapping part*) was included since the front edges of the two chips do not overlap (see section 7.2.5 and figure 7.6). Based on the results obtained in the following section, it was finally fixed at $1.62\,mm$. The proton source was modeled as described in section 6.2.1, with a spot size of $2\,mm$ (FWHM) and a divergence angle of $5\,mrad$ (FWHM). The proton energy was varied from 17 to $20\,MeV$ in $1\,MeV$ steps.

In the second simulation geometry, the additional $11.4\,\mu m$ thin titanium foil at the beamline exit, the air gap and the varying plastic thicknesses of the passive absorber wheel are included. The parameters determined in section 4.3.1 and actual geometrical thicknesses of the 3D-printed plastic were used.

In both simulation setups, the simulated detector signal was obtained by scoring the energy deposition inside the silicon sensor chip using a Cartesian energy scorer with $256 \times 256 \times 1$ pixels, each $55 \times 55 \times 500\,\mu m^3$ large. The scorer is arranged such that it is located inside the sensor chip and above the readout chip. Moreover, the energy deposition along the entire sensor chip was scored using a Cartesian energy estimator with no lateral binning but a $1\,\mu m$ fine resolution in beam direction. For each proton entering the overlapping part of sensor and readout chip, the kinetic energy when entering both the sensor chip and the overlapping part was written to an ASCII-file using the `mgdraw.f` user routine. That way, protons not reaching the overlapping part of sensor chip and readout chip and hence not contributing to detectable signal, are not included in the true spectrum.

The maximum step size for the transport of charged particles in the thin foils and the silicon detector was reduced to about one third of the respective region size to ensure proper functionality of the FLUKA energy loss and multiple-scattering algorithm within these small regions.

Simulations for Reconstruction Validation

In order to validate the spectrum reconstruction based on MC data, additional simulations were performed similar to the previously described setup. A first set of simulations was performed with a monoenergetic proton source with energies ranging from 17 to 30 MeV in steps of 1 MeV. For each proton energy, a large number of individual runs was performed with a low number of primary protons per run, resulting in > 1000 individually distinguishable proton tracks for each energy, similar to the acquired frames in the experiments. In a second set of simulations, a larger number of primary particles was used and the initial proton energy was modified. Both, a purely monoenergetic source with kinetic beam energy of 25.3 MeV, and a polyenergetic source with a monotonically decreasing spectrum from 17 to 27 MeV were implemented. In order to generate a simulated signal that laterally extends over a larger part of the detector, the spot size was increased along the axis of the slit such that it was elliptical with spot sizes of 5 mm parallel to the slit and 2 mm perpendicular to it.

7.2.5 Non-Overlapping Part of Sensor and Readout Chip

The area of the silicon sensor chip of the Timepix detector is larger than the connected readout chip, resulting in a non-overlapping part of sensor and readout chip (figure 7.6b). By comparison of the proton range measured using the Timepix detector to corresponding simulated ranges in silicon, the extension of this non-overlapping part was determined.

To this aim, forth-order polynomial functions were fitted to the laterally integrated Bragg peaks of both Timepix and simulation data for the three highest kinetic energies available from experiments. The lowest kinetic energy ($E_{kin} = 17$ MeV) was excluded from the evaluation, since the penetration depth is low and hence no reliable polynomial fit to the

(a) Determination of the dead part

(b) Schematic view
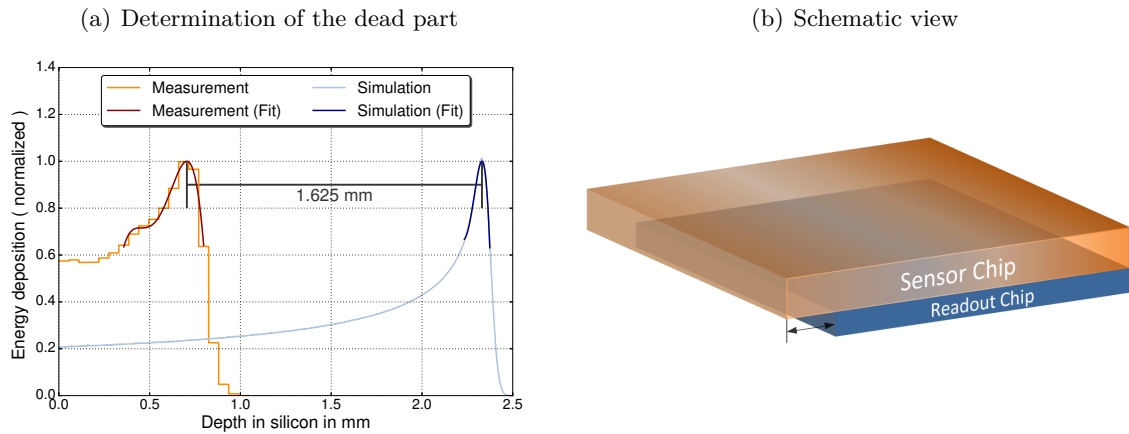
Figure 7.6: Determination of the non-overlapping part of the Timepix sensor and readout chip. In (a), the laterally integrated proton tracks from Timepix measurements (orange) and MC simulations (light blue) are shown for $E_{\mathrm{kin}} = 20\,\mathrm{MeV}$. Forth-order polynomial functions are fitted to the respective peaks (red and dark blue) to determine the peak position with sub-pixel accuracy. The indicated distance is the difference of the two fitted Bragg peak positions. A schematic view of the Timepix detector's non-overlapping sensor and readout chip is shown in (b). The non-overlapping part is indicated by the small arrow.

experimental data was possible.

In figure 7.6a, the range difference is shown for $20\,\mathrm{MeV}$. According to the mean difference of the fitted Bragg peak positions of the three measurements, the length of the non-overlapping part is $z_{\mathrm{no}} = 1.62 \pm 0.01\,\mathrm{mm}$. The given uncertainty includes the standard deviation of the three individually obtained lengths, combined with the thickness uncertainty of the Kapton foil $\left(\frac{\Delta d_{\mathrm{Kap}}}{d_{\mathrm{Kap}}} = 10\%\right)$, which was taken into account in the MC simulations.

Since meaningful track lengths in the measured or simulated data sets need to be larger than 2 pixels in depth, the length of the non-overlapping part translates to a lower cut-off energy of $E_{\mathrm{cut-off}} \sim 16.6\,\mathrm{MeV}$.

7.2.6 Reconstruction of Proton Energy Distributions

As pointed out in section 7.1, the energy distribution of incoming protons can be obtained by solving a linear equation system by means of least-squares optimization. Therefore, a system matrix $\mathcal{A}_{jk}$ containing the detector signal for proton tracks of various energies within the energy range of interest has to be constructed. The procedure of setting up the matrix and solving the equation system is described in the following.

Average Proton Tracks

Two system matrices $\mathcal{A}_{jk}$ were created for reconstructing either MC simulated or measured proton energy distributions. For the reconstruction of simulated data, the matrix $\mathcal{A}^{\mathrm{sim}}$ is based on averaged proton tracks extracted from MC simulations for initial proton energies ranging from $17\,\mathrm{MeV}$ to $30\,\mathrm{MeV}$ in steps of $1\,\mathrm{MeV}$. Due to the lower maximum energy
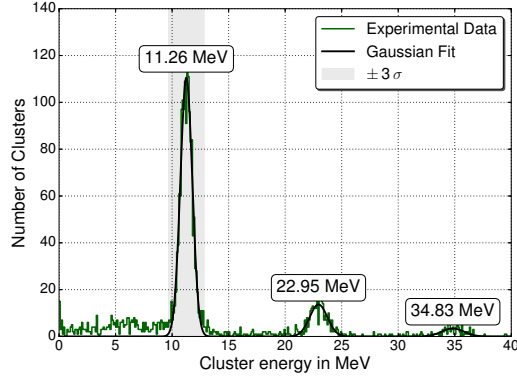
Figure 7.7: Histogram of cluster energies for tracks extracted from experimental Timepix edge-on data for irradiation with 20 MeV. The indicated energies above the observed peaks refer to the mean of Gaussian fits. The gray area indicates the interval of $\pm 3\sigma$ around the fitted mean energy of the first peak.

(a) 2D distribution   (b) Laterally integrated
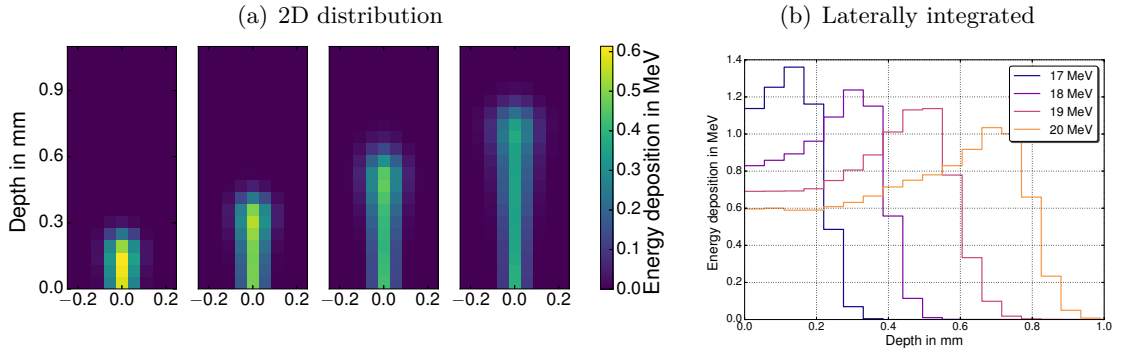
Figure 7.8: Average (model) tracks used to create the experimental system matrix. The 2D distribution of 17, 18, 19 and 20 MeV model tracks is shown in (a), while the laterally integrated tracks are plotted in (b) as a function of depth in the sensor chip.

available at the Tandem accelerator, the experimental system matrix $\mathcal{A}^{\mathrm{exp}}$ is created using measured tracks at kinetic energies of 17, 18, 19 and 20 MeV.

A cluster analysis as described in section 7.2.1 was performed to extract individual proton tracks for every initial proton energy. Only clusters starting at the first pixel row and with a cluster size larger than one pixel were selected for further evaluation. Exemplary, the histogram of the experimentally obtained cluster energies for 20 MeV protons is shown in figure 7.7. Single Gaussian distribution functions were fitted to the obtained peaks in the histogram, corresponding to single tracks and multiple overlapping tracks. The fitted mean energies indicated in the plots are lower than the corresponding initial kinetic energies due to signal loss in the non-overlapping part of sensor chip and readout chip. Yet, the energies are higher than what would be expected if considering only the energy deposition inside the overlapping part. The discrepancy can be explained by the fact that part of the electron-hole pairs created inside the non-overlapping part of the sensor chip contributes to the measured signal in the outermost pixel rows. Since the signal generation was not simulated explicitly, this effect was not observed in the simulated data set.

119

For each kinetic energy, all clusters with an energy deposition within $\pm 3\sigma$ of the mean energy deposition of single protons were selected to account for range straggling in the sensor chip. The accepted energy range is indicated by the gray areas in figure 7.7. The tracks were then averaged, resulting in one *model track* for each kinetic energy (see figure 7.8).

Creation of the System Matrix

To achieve a finer energy resolution than given by the measured or simulated kinetic energies, proton tracks for intermediate energies were interpolated and up to a certain extent, extrapolated for higher and lower proton energies.

First, a forth order polynomial function was fitted to the peak region of each model track and the corresponding Bragg peak positions and heights were extracted. A slightly modified version of eq. 2.20, which accounts for the length of the non-overlapping part of sensor and readout chip, $z_{\mathrm{no}} = 0.162\,\mathrm{cm}$, was fitted to the Bragg peak positions giving a relationship between the kinetic energy E_{kin} and the peak position in silicon, z_{BP}:

$$z_{\mathrm{BP}}[\mathrm{cm}]\,(E_{\mathrm{kin}}) = \alpha \cdot E_{\mathrm{kin}}[\mathrm{MeV}]^p - z_{\mathrm{no}}\,. \tag{7.4}$$

Best agreement was found for the two fit parameters $\alpha = 0.0117$ and $p = 1.772$. In figure 7.9a, experimental and simulated Bragg peak positions and the corresponding fits are shown together with the deviation of the data points from the corresponding fitted values. Similarly, the Bragg peak heights were fitted by a linear functions for experimental and simulated data individually. A linear function has shown to sufficiently describe the fitted peak heights within the energy range of the calibration. Figure 7.9b shows the values for the extracted peak heights and the corresponding fits. The slope of the fit to the experimental data differs from the simulated data due to two effects. First, charge sharing effects are lowering the height of the signal in the Bragg peak region. Second, as previously mentioned, charge carriers created in the non-overlapping part contribute to the measured signal within the outermost pixel rows, resulting in apparently larger Bragg peak heights.

Proton tracks for intermediate energies and energies outside the range of calibration energies were then calculated in steps of $5\,\mathrm{keV}$. This was done in four steps. First, the laterally integrated model tracks were divided by the corresponding fitted Bragg peak height and linearly interpolated on a $1\,\mu\mathrm{m}$ fine depth grid. The interpolated tracks for all model energies were then shifted in depth such that the positions of the Bragg peaks obtained from eq. 7.4 coincide. A weighted mean of all fine model tracks was calculated, where the weights are the inverse of the absolute difference between Bragg peak position of the desired energy and the Bragg peak position of the respective model track energy. Note that the mean was only calculated for depths where the tracks have non-zero energy deposition. The desired proton track was finally obtained by shifting the newly calculated

(a) Bragg peak position   (b) Bragg peak height
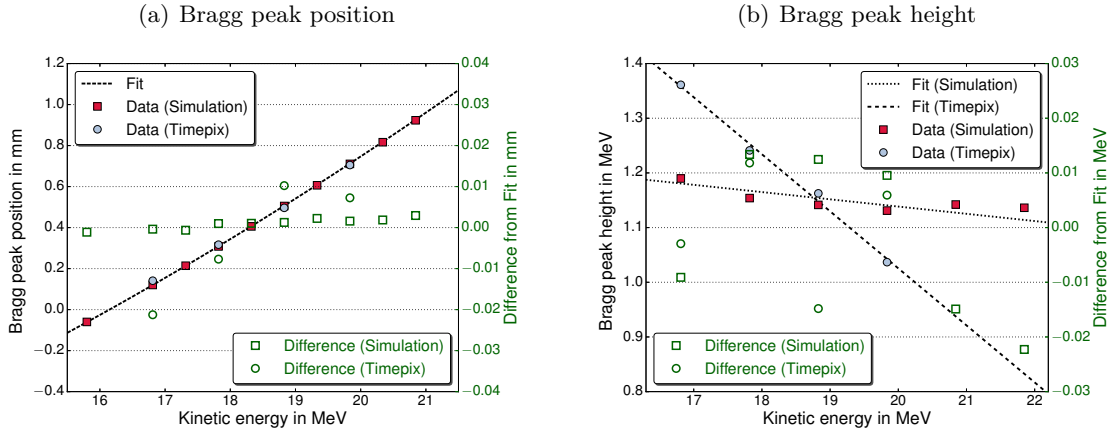
Figure 7.9: Bragg peak position (a) and height (b) as extracted from polynomial fits to experimental (filled circles) and simulated (filled squares) data. Eq. 7.4 was fitted to the Bragg peak positions in (a) and is shown by the dashed black line. The dashed and dotted lines in (b) represent linear fits to the Bragg peak heights of simulated and measured data, respectively. The empty green circles and squares denote the difference between data points and corresponding fitted value (right axis).
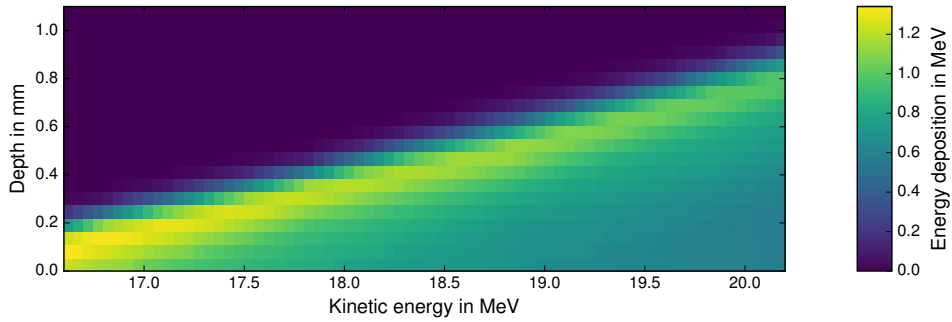
Figure 7.10: A graphical representation of the system matrix $\mathcal{A}^{\text{exp}}$ used for spectrum reconstruction of the experimental data. Every column corresponds to the laterally integrated average detector signal of one proton of a certain energy.

fine tracks back to the corresponding Bragg peak position, resampling the data points to the actual pixel size and multiplying the resulting coarse track by the corresponding Bragg peak height from the linear fit.

Every column of the final system matrix corresponds to the laterally integrated expected energy deposition of a proton with kinetic energy within the respective energy bin of width $\Delta E = 0.1\,\text{MeV}$. Thus, all created tracks with an energy within that bin are averaged and arranged to form the system matrix $\mathcal{A}$. For the experimental data, $\mathcal{A}^{\text{exp}}$ is plotted in figure 7.10.

Solving the Linear Equation System

The linear equation system described in section 7.1 is solved by means of linear least-squares optimization with the only constraint that the particle number $n_k > 0 \ \forall k$. The same algorithm as described in section 6.2.3 was used, including the implementation of

the Tikhonov regularization with regularization parameter μ.

In general, the energy resolution of $\vec{n}$ is given by the longitudinal pixel size. To obtain a finer resolution, i.e. more narrow energy bin widths, the tracks constituting the system matrices $\mathcal{A}$ and the data frames to be reconstructed are both linearly interpolated resulting in a larger set of equations and hence an energy bin width of 100 keV.

The inverse problem can be on the one hand solved discarding the position information and summing up all pixel columns of the Timepix frame prior to the reconstruction. In the following, this is referred to as *1D-reconstruction*. Alternatively, it can be solved for each column independently, maintaining full lateral position resolution at the cost of computational time to solve 256 inverse problems. To achieve almost real-time reconstruction, four adjacent pixel columns were summed together before reconstruction, reducing the number of equation systems to only 64 while the lateral position resolution is still 220 µm. In this *2D-reconstruction*, the combined pixel columns were reconstructed in parallel on all available CPUs, requiring only a few seconds on a typical desktop computer[2].

For either 1D or 2D reconstruction, the total reconstructed proton number N_p, a quantity discussed in the results section, is then simply calculated by

$$N_p = \sum_k n_k \ .\tag{7.5}$$

7.3 Results

7.3.1 Validation of the Spectrum Reconstruction using MC Data

In order to verify and optimize the spectrum reconstruction method, both a monoenergetic (25.3 MeV) and polyenergetic (monotonically decreasing from 17 to 27 MeV) proton distributions generated by means of FLUKA MC simulations are reconstructed. Reconstruction was performed both without and with Tikhonov regularization. For the latter, the regularization parameter μ was varied between 0.01 and 1.0. The resulting reconstructed energy distributions for three regularization settings are compared to the true spectra obtained using the `mgdraw.f` routine in figure 7.11.

Regardless of the regularization, the mean reconstructed energy is in good agreement with the mean true energy in case of the monoenergetic proton bunch. A slight underestimation of up to 0.8% (= 0.19 MeV) is found due to small spurious peaks at lower energies, shifting the mean energy towards lower values. Concerning the absolute proton number, the reconstructed number is 2.7% lower than the actual proton number according to the simulation output. However, this can be explained by the fact that the true proton number refers to the number of protons at an imaginary interface between non-overlapping and overlapping part of the sensor with the readout chip. Hence, for the true spectrum all

---

[2]Intel$^{®}$ Core$^{™}$ i7-3770 (4 cores), 16 GB RAM
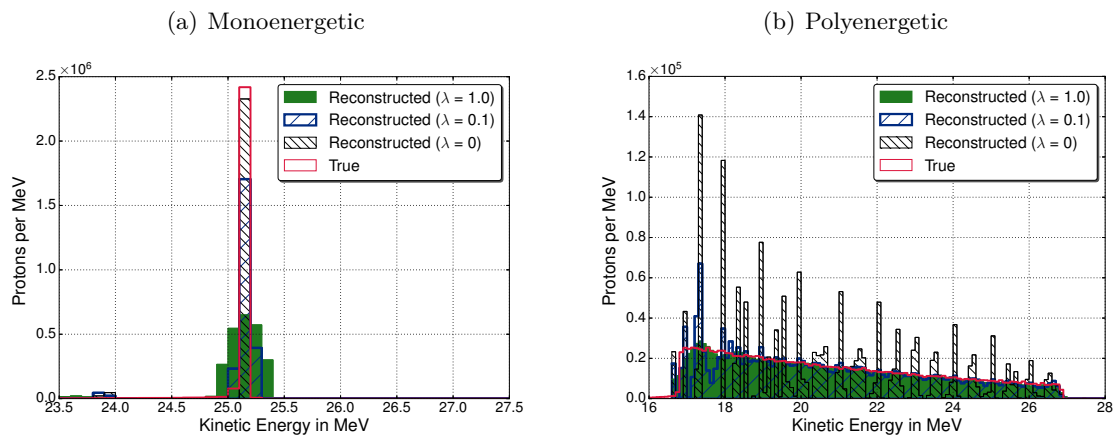
Figure 7.11: Validation of the Timepix edge-on spectrometry reconstruction using MC generated data for a monoenergetic (a) and a polyenergetic (b) proton beams. Reconstruction was performed using Tikhonov regularization with $\mu = 1.0$ (filled green) and $\mu = 0.1$ (blue), as well as without any regularization (black). The true spectra are shown in red.

protons are counted regardless if they are scattered out of the sensor chip right after that interface. As expected, larger regularization parameters result in an additional broadening of the reconstructed energy distribution.

In case of the polyenergetic proton bunch, the importance of a proper choice of the regularization parameter becomes evident. Reconstruction without regularization leads to nonphysical overfitting, i.e. a large overestimation of the proton number in one energy bin and an underestimation in the neighboring energy bins. Best agreement between reconstructed and true spectrum is found for $\mu = 1.0$.

However, since with this parameter the width of the reconstructed monoenergetic spectrum is far too broad, in the following μ was set to 0.1 as a compromise, despite the overfitting artifacts that can be found at energies below 18 MeV. Concerning the total proton number and the mean energy, slightly better agreement was achieved as compared to the monoenergetic proton bunch. For all evaluated regularization settings, the differences are now around 1.6% and 0.3% (< 0.07 MeV), respectively, but the trend of the deviation remains the same.

7.3.2 Reconstruction Validation using Experimental Data

With the regularization parameter set to $\mu = 0.1$, spectrum reconstruction was validated on experimental data with known number of proton tracks and energies. To this aim, artificial frames were created from the individual proton tracks which were selected for the creation of the model track.

The frame containing all 20 MeV tracks and the respective position-sensitive reconstructed energy spectrum is shown in figure 7.12. The lateral shape of the proton beam is nicely reproduced by the reconstructed lateral energy distribution.
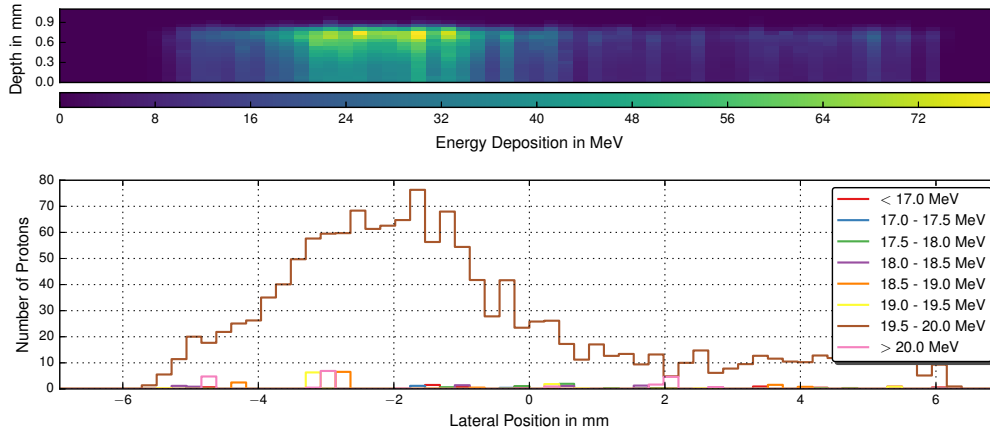
Figure 7.12: Artificial Timepix frame (top) and position-sensitive reconstructed proton energy distribution in absolute particle numbers (bottom). The frame was created using all proton tracks selected for the generation of the 20 MeV model track.

Table 7.1: Validation of the Timepix edge-on spectrum reconstruction method using experimental data. The nominal beam energy, E_{kin}, is given in the first column. In column 2 and 3, the actual mean proton energy according to MC simulations and the number of proton tracks are given. Reconstructed mean energies and proton numbers for 1D and 2D reconstruction are shown as indicated in the header.

E_{kin} / MeV	Expected (MC)		1D reconstruction		2D reconstruction	
	E/MeV	N_p	E/MeV	N_p	E/MeV	N_p
17	16.805	803	16.834	812	16.839	815
18	17.811	948	17.843	953	17.840	956
19	18.818	1518	18.848	1521	18.832	1533
20	19.825	1473	19.860	1478	19.817	1498

In figure 7.13, both the 1D- and the 2D-reconstructed proton energy distributions are compared to the spectra obtained from MC simulations for the four calibration energies. The mean reconstructed energies, as well as the total particle numbers are listed in table 7.1.

Concerning the mean proton energy, excellent agreement was achieved both in the 1D- and the 2D-reconstruction with a maximal deviation of 35 keV, corresponding to relative deviations below 0.2%. Very good agreement was also obtained in the 1D-reconstruction for the particle number ($\Delta N_p < 1.2\%$). In case of the 2D-reconstruction, differences between true and reconstructed particle numbers were slightly increased ($\Delta N_p \leq 1.7\%$).

7.3.3 Statistical Influences

The statistical nature of energy loss inside the sensor material and the related range straggling give rise to an additional uncertainty when reconstructing only a small number of proton tracks. This effect is investigated by dividing 1000 measured proton tracks with

(a) 17 MeV

(b) 18 MeV

(c) 19 MeV
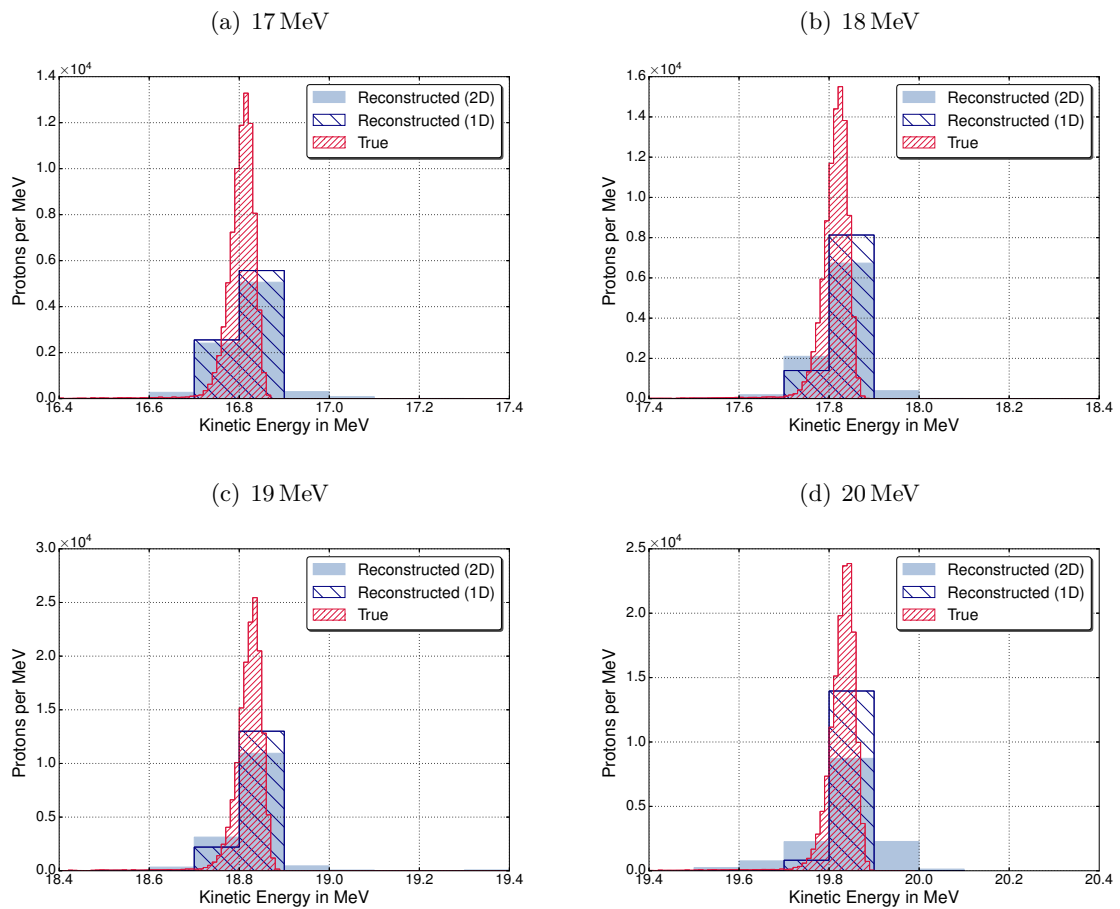
(d) 20 MeV

Figure 7.13: Validation of the Timepix edge-on spectrometry reconstruction using experimental data at proton energies ranging from 17 MeV to 20 MeV. The 2D-reconstructed (filled blue) and the 1D-reconstructed (dashed blue) distributions are compared to the spectrum obtained from MC simulations (red).

$E_{\mathrm{kin}} = 19\,\mathrm{MeV}$ into m frames of N_p proton tracks each, with

$$N_p = [1, 2, 5, 10, 20, 50, 100, 200, 500, 1000]$$

and

$$m = \frac{1000}{N_p} \ .$$

Every frame was then reconstructed individually.

The resulting energy distributions of exemplary reconstructed frames for $N_p = [1, 10, 100]$ are shown in figure 7.14a-c, respectively. In figure 7.14d, the mean reconstructed energy of the individual frames with varying proton numbers are shown, as well as the standard deviation σ_{E}, plotted as a function of proton number per frame. Although σ_{E} drops below 0.1 MeV already for 10 proton tracks per frame, the width of the reconstructed spectra approaches the true spectral width only for $N_p > 100$.

125
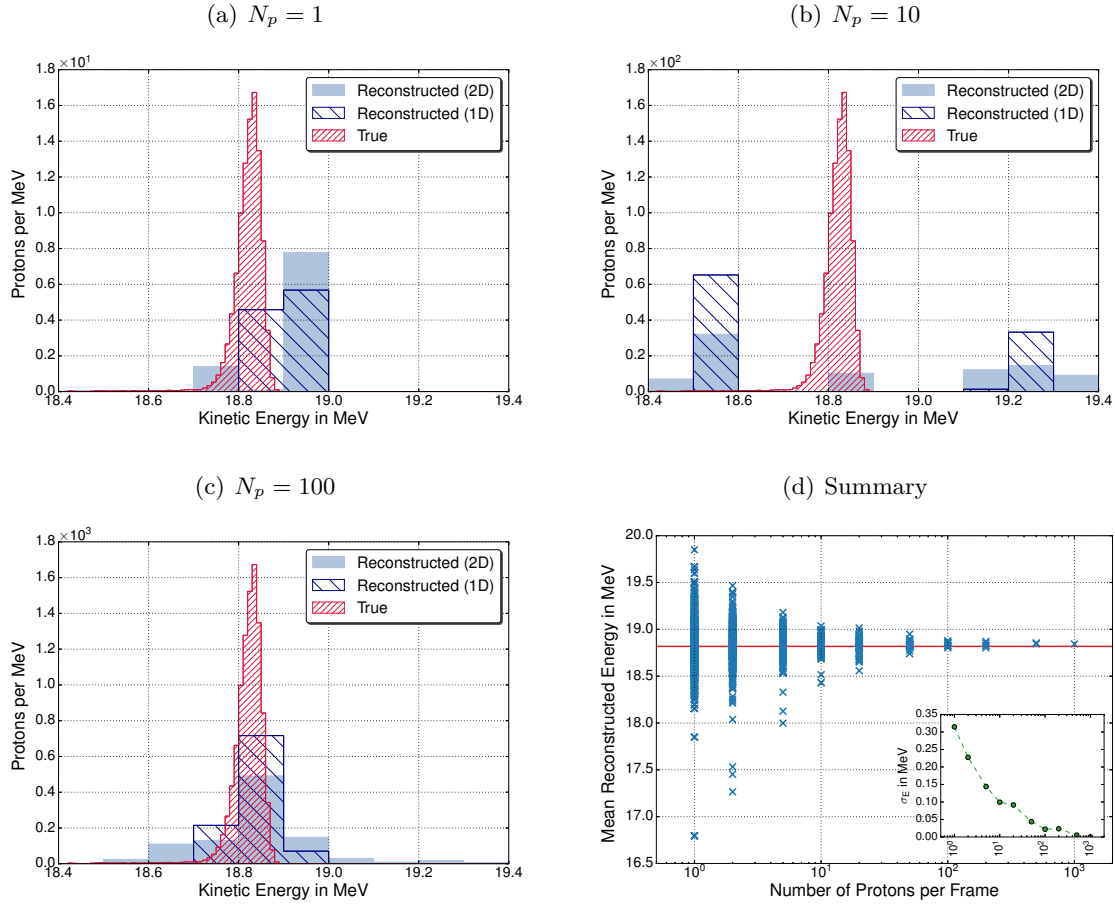
Figure 7.14: Statistical uncertainty of the Timepix edge-on reconstruction. Artificial Timepix image frames consisting of 1, 10 and 100 randomly picked clusters from 19 MeV protons were reconstructed and examples are shown in (a), (b) and (c), respectively. The spectrum expected from MC simulations is shown in red. In (d), the mean reconstructed energy for $m = 1000/N_p$ frames is shown by crosses as a function of different proton numbers per frame. The red line indicates the true mean energy. The standard deviation of the mean reconstructed energy is shown in the inset.

7.3.4   Timepix Edge-On Spectrometry

For a 0.6 mm thin 3D-printed plastic absorber, the reconstructed energy distribution is compared to the distribution calculated using MC simulations in figure 7.15a. Also, calculated energy spectra from simulations are shown, taking into account the uncertainties of the two foil thicknesses ($\pm 10\%$), the length and density of the air gap (± 2 mm and $\pm 0.02 \times 10^{-3}$ g cm^{-3}), as well as the thickness and density of the plastic absorber (± 8 µm and ± 0.005 g cm^{-3}). The three simulated spectra are scaled in height according to N_p obtained from the 1D-reconstruction of the experimental data.

Within the stated geometrical uncertainties used in the MC simulation, very promising agreement of the mean reconstructed energy ($E_{\mathrm{mean}} = 17.61$ MeV) with the mean simulated energy was found ($E_{\mathrm{mean}}^{\mathrm{min}} = 17.60$ MeV; $E_{\mathrm{mean}}^{\mathrm{max}} = 17.73$ MeV).

For control purposes, in figure 7.15b the measured laterally integrated energy deposition

(a) Reconstructed spectrum

(b) Control plot
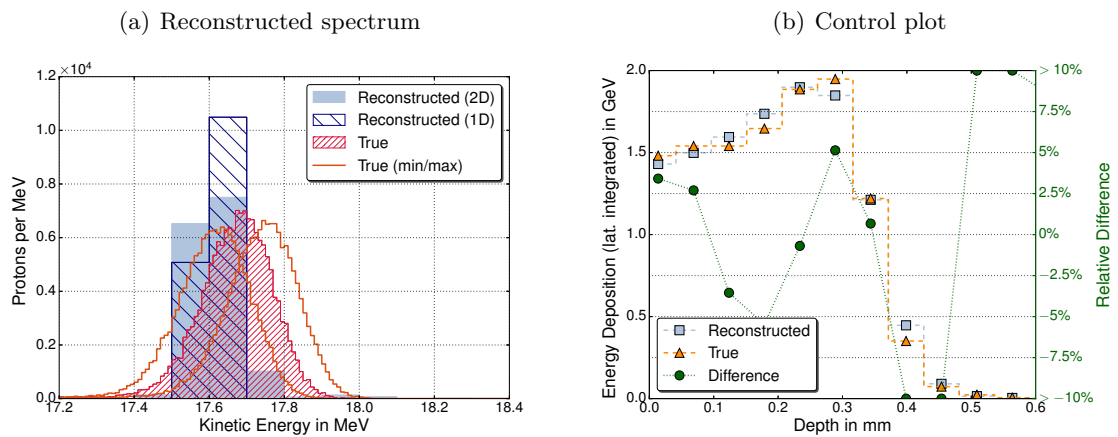
Figure 7.15: Reconstructed energy spectrum after a plastic absorber thickness of 0.6 mm. In (a), the 2D-reconstructed (filled blue) and the 1D-reconstructed (dashed blue) distributions are compared to the spectrum obtained from MC simulations (red) and the MC spectrum with distances adjusted according to measurement uncertainties (orange). For control purpose, in (b) the laterally integrated detector signal (orange) is compared to $\mathcal{A}^{\mathrm{exp}}$ multiplied by the reconstructed, laterally summed particle number (light blue). The difference between two curves is shown in green (right axis).
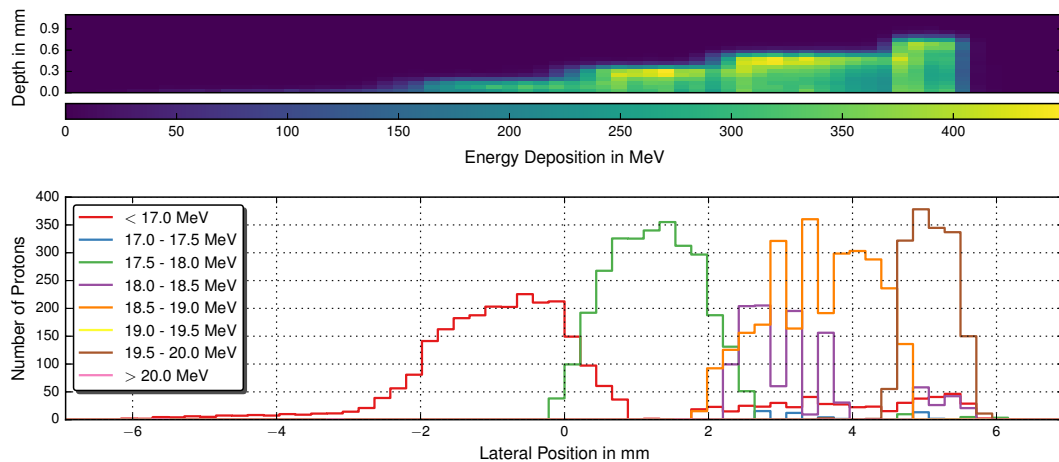
Figure 7.16: Measured Timepix data and reconstructed lateral energy distribution for a sample of 4/3/2/1/0 layers of RCF attached prior to the entrance slit of the aluminum box housing the Timepix detector.

as a function of depth is compared to the energy deposition obtained when multiplying the system matrix $\mathcal{A}^{\mathrm{exp}}$ with the vector representing the reconstructed particle numbers, $\vec{n}$. It can be seen that $\mathcal{A}^{\mathrm{exp}}\vec{n}$ nicely follows the measured signal, with differences mainly below 5% except in the distal fall-off region of the signal.

When replacing the plastic absorber by a sample consisting of up to four layers of RCF, an energy distribution that is varying step-wise over the lateral dimension was created. The measured Timepix data and the reconstructed lateral energy distribution, for better visibility plotted in rather coarse energy steps, is shown in figure 7.16. It can be seen

that the steps that can be discriminated in the original data are nicely reproduced in the reconstructed spectra. The part of the data set corresponding to four layers of EBT-3 film could not be reconstructed correctly, since the proton range after having passed the two vacuum windows, the air gap and four layers is not sufficient to fully penetrate the non-overlapping part of sensor and readout chip. Only a faint glow in the first two pixel rows is visible at that lateral position due to charge carriers created in the non-overlapping part.

7.3.5 Saturation Limit of Timepix Detector in Edge-On Configuration

Since the 14-bit counter of the digital part of each Timepix pixel operated in TOT mode stops at 11 810 counts, the dynamic range theoretically extends up to an energy deposition within each pixel of $\sim 7.35\,\mathrm{MeV}$ before saturation is reached. However, non-linear response of the Timepix front-end electronics to high input charges corresponding to an energy collected by one pixel exceeding $\sim 0.85\,\mathrm{MeV}$ has been observed [Granja et al., 2011; Kroupa et al., 2014, 2017].

Therefore, a coarse estimation of the maximum detectable proton fluence within one acquired frame of the edge-on spectrometry setup was performed, based on a maximum energy deposition of 0.85 MeV per pixel. According to the measured average tracks shown in figure 7.8, the laterally integrated energy deposition in the Bragg peak region of protons entering in edge-on configuration is up to 1.4 MeV for $E_{\mathrm{kin}} \geq 17\,\mathrm{MeV}$.

When assuming a spatially perfectly homogeneous irradiation with 17 MeV protons, this would limit the number of protons per pixel column to 0.6. Given that pixel size and slit width are 55 μm and 150 μm, respectively, the maximum proton fluence before non-linear saturation occurs is

$$\Phi_{\mathrm{sat}} = \frac{0.6}{55\,\mu\mathrm{m} \cdot 150\,\mu\mathrm{m}} \approx 7 \times 10^3\,\mathrm{cm}^{-2} \ . \tag{7.6}$$

7.4 Discussion

7.4.1 Potential and Features of the Timepix edge-on Approach

The here presented spectrometric technique could in principle be considered to be a range telescope or an online and semiconductor-based version of a stack of nuclear track detectors. It is sensitive to single particles and since the measured detector signal scales with the particles energy loss along its path through a pixel row, the penetration depth in silicon can be determined with a sub-pixel range resolution. This is in contrast to a pure *hit/miss*-measurement, where the resolution is determined by discrete steps, i.e. the pixel size in the longitudinal dimension.

Another interesting feature of the Timepix edge-on approach is given by the charge sharing effects, resulting in non-zero signal within the pixels adjacent to the pixels the particle went

through. Although not performed within this study, the lateral position of single incident ions could easily be determined with sub-pixel resolution by fitting a Gaussian distribution function to the pixel values in the first lateral pixel row. According to Jakůbek et al. [2008], spatial resolution in the order of 1 µm could in principle be achieved.

As long as individual tracks can be discriminated, a distinction between different particle species can be performed based on the shape of the cluster. While tracks created by electrons follow an erratic path through the detector's sensor chip and the clusters obtained from x-rays or gammas are point-like, rather straight paths are obtained from ions. Since for the same range in the sensor chip, energy loss along their path is higher for heavier ions than for protons and such tracks may be accompanied by tiny tracks of created delta electrons, a track analysis can be used to distinguish between different ion species.

When the detector signal comprises multiple overlapping tracks, the aforementioned distinction is not possible and a statistical evaluation of the integrated image, as performed within this study, is necessary. The here presented edge-on experiments based on a prior calibration have shown an excellent energy resolution of 0.2% for a number of tracks in the order of 10^3. Also the number of reconstructed particles agrees better than 2% with the true value. However, it needs to be stressed that the experimental validation was performed on an artificially created frame containing only tracks that were also used to generate the model track for each energy.

Although detector properties were not explicitly simulated within this study, a more realistic assessment of the reconstruction capabilities is given by MC simulations. In that case, also protons that undergo nuclear interactions or leave the sensor chip due to scattering contribute to the signal which is then reconstructed. Hence, the discrepancies are slightly increased. Yet, in the simulated energy range, both the reconstructed mean energy and the particle numbers were found in good agreement with the ground truth.

7.4.2 Limitations and Uncertainties

Most of the aforementioned features of the Timepix edge-on spectrometry approach rely on the possibility to distinguish between individual tracks. For large particle fluxes, as typical for laser-accelerated ion bunches, a statistical evaluation of the measured frames, as thoroughly described within this chapter, is required. Applying this spectrum reconstruction method to samples with low track numbers results in an increased uncertainty which has been depicted in figure 7.14. The uncertainty is caused by fluctuations of the actual proton path and energy losses of individual protons, while the reconstruction is based on the average path and energy losses of a relatively large (~ 1000) sample.

Reliable reconstruction performance in terms of kinetic energy was found for track numbers of ~ 100 for the laterally integrated frame. When lateral spectrum information is desired, this number needs to be even higher. With slit dimensions as in the experimental setup, the minimum track number would correspond to a fluence of about $5 \times 10^3 \, \text{protons/cm}^2$. This fluence is only slightly below the determined saturation limit. Hence, the fluence

range in which the statistical uncertainty is low, yet the detector is not saturated is very limited. This hinders the usability of the Timepix detector in edge-on configuration for spectrum characterization of single laser-accelerated ion bunches.

The determined saturation limit of the Timepix detector in edge-on configuration is a factor ~ 30 lower than the saturation level given in Reinhardt [2012]. However, the quoted fluence value of that work was given for 20 MeV protons in face-on irradiation on a 300 μm thin sensor chip. The total energy deposition per proton is hence much lower than in edge-on irradiation performed within this study. Moreover, at a fluence of 2.5×10^5 protons/cm^2, saturation artifacts had already been encountered in these measurements [Reinhardt, 2012].

Moreover, particles that leave the sensor chip due to Coulomb scattering or that experience nuclear interactions are not accounted for in the statistical reconstruction approach. These effects strongly depend on the kinetic energy of the incident particles. While at a kinetic energy of 20 MeV almost 98% of the initial protons penetrating the sensor chip are entirely stopped within it, the number drastically decreases for higher proton energies. At 30 MeV, one fifth of the protons leaves the sensor chip due to scattering. For the highest proton energy that could in principle still stop within the sensor chip (56 MeV), more than two third of the initial protons leave the sensitive volume instead of continuously slowing down until they stop. Note that these MC-based considerations rely on the idealized assumption of normal and centric incidence of the protons with respect to the edge of the sensor chip. Thus, when using a collimator with finite slit extension and a divergent beam, scattering in the collimator itself and non-normal incidence would result in even larger particle losses.

Another uncertainty which is worth being considered is the positioning uncertainty of the device, namely the rotational uncertainty along the axis between front edge and sensor chip plane. A slit width of 150 μm and 5 mm thick collimators correspond to a half acceptance angle of 0.86°. Obviously, alignment with respect to the particle direction would need to be more accurate than that, as otherwise measured tracks would result from ions that have experienced energy loss and scattering by going through a small fraction of the collimator. However, the results obtained within two different experimental sessions indicate that a sufficient reproducibility of positioning the diagnostic device with respect to the beam direction is manageable. Nevertheless, positioning will become even more crucial when using thicker collimators, which would be required when going to higher proton energies.

The non-overlapping part of sensor chip and readout chip constitutes another limitation of this setup. Protons with energies below ~ 16.6 MeV are fully stopped within the non-overlapping part, but still generate a measurable signal within the first pixel rows due to charge-sharing effects. For spectrometry of a proton bunch with a broad energy distribution where the number of low-energetic particle outnumbers the contribution by high-energetic particles, this can pose a severe problem for the reconstruction. The algorithm cannot distinguish whether the signal in the first pixel rows comes from protons that actually reached these pixels or from particles that stopped before. Therefore, recon-

structed proton numbers close to the minimum detectable energy are given with a large uncertainty.

7.5 Conclusion & Outlook

Despite the promising features pointed out for low particle fluxes, as well as the good spectrum reconstruction capabilities for simulations and experimental data summed over many individual frames acquired at low beam current, the usability of the Timepix detector in edge-on configuration in its current setup is debatable for spectrometry of laser-accelerated ion bunches. Most importantly, the tremendous proton fluxes will inevitably result in saturation of the detector. Although it may still be possible to determine the high-energy cutoff of these ion bunches together with their transversal profile, any further spectrometric information is lost. Decreasing the slit width to a level where the number of particles reaching the sensor chip is below the saturation limit would be rather impractical. Furthermore, the non-overlapping part of sensor and readout chip and the total sensitive distal length of the sensor chip of $1.4\,\mathrm{cm}$ limits the use of this diagnostic device to an energy range between $\sim 17 - 56\,\mathrm{MeV}$. Nevertheless, one could still think of possible approaches to circumvent these limitations. They will briefly be presented in the following.

Exclusive Detection of High-Energy Protons

In a first scenario, the Timepix detector in edge-on configuration can be combined with the WASP presented in section 3.1.3 in order to detect the high-energy cut-off of the ion spectrum with high accuracy. In the vicinity of the assumed cut-off energy, the number of protons is so low that it typically lies within the background level of the WASP's detection system, since the energy deposition of high-energetic protons in the thin sensitive layer of the RadEye detector is low. The single particle sensitivity of the Timepix detector can hence be exploited when mounting the device on top of the RadEye detection system. The magnetic deflection at these high energies is low, such that the non-normal incidence with respect to the edge is only a minor effect.

Alternatively, additional absorbers prior to the slit result in a stopping of the low-energy ions, while higher-energy protons can still reach the sensitive detector volume. Due to scattering inside the absorber, the number of protons leaving the absorber such that they are still capable to traverse the collimator is tremendously reduced. However, to what extent the increased scattering in the slit dimension deteriorates the reconstruction performance and the resulting detection efficiency would need to be thoroughly evaluated.

Detection of Scattered Particles

Another approach solving the issue of the non-overlapping part and partially the low saturation relies on the detection of scattered particles instead of the primary beam.

131

(a) Timepix signal (2D)   (b) Laterally integrated Timepix signal
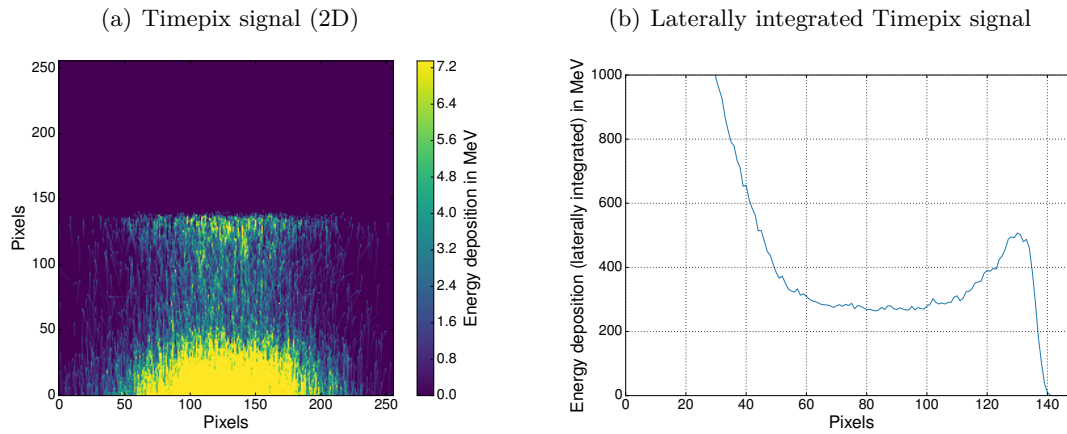
Figure 7.17: Simulated detector signal of the Timepix detector in edge-on configuration detecting scattered protons. 30 MeV protons pass through the 150 μm thin slit between two aluminum collimators and are absorbed in a 0.8 mm thick PMMA slab mounted on top of the sensor chip. In (a), the two-dimensional energy deposition distribution is shown. The maximum of the color scale is set to 7.35 MeV energy deposition per pixel, to account for saturation of the Timepix detector. Very high signal can be found in the beginning of the detector, due to protons scattered in the collimator. In (b), the laterally integrated energy deposition is shown. The Bragg peak in PMMA can nicely be seen.

This idea is based on a study performed by Merchant et al. [2017]. Detection of scattered particles could be achieved by mounting a slab of absorber material (e.g. PMMA) onto the face of the sensor chip and adjusting the slit such that the incoming protons all penetrate the absorber slab. The position of the slab with respect to the sensor chip edge can be chosen such that the non-overlapping part is entirely skipped.

By choosing a proper slab thickness and slit height, the number of protons reaching the sensor chip due to scattering within the absorber slab can be varied. With a large number of incident particles, the Timepix detector will still measure a Bragg curve-like signal, as it can be seen in a preliminary simulation study depicted in figure 7.17. In the shown example, a 30 MeV proton beam passes through a 150 μm thin slit and impinges centrically on a 0.8 mm thick PMMA slab mounted on top of the Timepix sensor chip. The proton fluence at the slit entrance was 6.6×10^6 protons/cm^2.

Other Detectors with Larger Dynamic Range

Of course, the here-presented spectrometric approach can also be applied to other detectors. Merchant et al. [2017] used a miniature multi-strip silicon detector with a strip size of 20 μm × 2 mm and a 375 μm thick sensitive volume to measure the detector response of a 60 MeV proton beam normally incident on the large edges of the strips. Hence the proton beam passes through several strips and the signal within the traversed strips shows a Bragg curve-like shape. Although losing the spatial information with the use of this detector, polyenergetic proton distributions could potentially be deconvolved by the method described in this chapter.

Feasibility Study on Laser-Driven Proton Radiography

In this chapter, a detailed MC simulation study investigating the feasibility of laser-driven proton radiography is presented. After a brief introduction, the relevant methods for the MC study are shown in section 8.2, including the modeling of the proton source, phantoms and detectors, the reconstruction methods and the assessment of the image quality. Two different simulation studies were performed, differing in the detector used for imaging. In section 8.3, the results for proton radiography using a Timepix detector are shown and discussed, while results obtained by using an imaging setup based on the RadEye detector are presented in section 8.4. A summary of the major results is given in section 8.5 before a first proof-of-principle experiment using an energy-modulated proton beam at the Munich Tandem accelerator is shown in the outlook (section 8.6).

8.1   Introduction

Due to the tremendous particle fluxes, the proton radiography method based on single particle tracking or counting, mentioned in section 3.2, is far from being achievable when using laser-driven ion sources. However, a different approach for proton imaging had been proposed by Zygmanski et al. [2000]. This approach is based on passively modulating a monoenergetic proton beam, such that a monotonically decreasing detector signal versus traversed water thickness is obtained.

Such proton depth-dose distributions, similar to x-ray attenuation in water, requires an initial proton energy distribution where the particle number monotonically decreases with increasing kinetic energy. This kind of energy spectrum is naturally obtained in laser-ion acceleration in the TNSA-regime. Hence, the sometimes considered disadvantageous polychromaticity of LION bunches could prove beneficial for imaging purposes.

In experimental studies based on energy-modulation of an initially monoenergetic beam

(e.g. Zygmanski et al. [2000] and Ryu et al. [2008]), the WET of the traversed object is obtained from a previously obtained calibration curve relating the detector signal to water thickness. Due to shot-to-shot fluctuations in the energy spectrum of laser-accelerated ion bunches, a single system calibration is not sufficient anymore. To account for these fluctuations, quantitative imaging requires an accurate spectrometry of each individual particle bunch. Ideally, the used spectrometer should be position-sensitive and used in transmission prior to the object to be imaged, without significantly perturbating the actual proton field. Based on this measured spectrum, the calibration curve then needs to be created on a shot-to-shot basis.

The spectrometer to be used within this simulation study is a hypothetical silicon detector, which is based on the detectors used for TOF spectrometry presented in chapter 6. Since the simulation study is driven by desired applications at the ATLAS laser system, the study is exclusively dedicated to online detection systems capable for rather high repetition rate experiments ($\sim 1 - 10\,\text{Hz}$). Therefore, the two pixelated silicon detectors Timepix and RadEye were chosen.

Furthermore, the imaging setup should be compatible with the general experimental constraints at LEX Photonics and expected at CALA. That implies that additional active or passive beam shaping devices should be avoided, if possible. Also, the dimensions of the objects to be imaged need to be tailored to the expected proton energies. The first part of this study deals with proton energies up to $20\,\text{MeV}$ as accessible at LEX Photonics, while in the second part imaging with a proton energy spectrum up to $100\,\text{MeV}$ as foreseen at CALA is studied.

8.2 Materials & Methods

The simulation study presented in this chapter was entirely performed using the FLUKA MC code, which was described in section 4.1.

8.2.1 Simulation Geometry and Parameters

Proton Source

A proton source was set up using the FLUKA user-routine `source.f`. The source is based on experimentally obtained TNSA spectra [Lindner, 2017], scaled to higher proton energies according to initial expectations (i.e., prior to operation of LEX Photonics) for a $300\,\text{TW}$ laser system. Kinetic energies were therefore sampled from an exponential distribution with a high-energy cut-off E_{cutoff}. The probability density function hence reads

$$N(E_{\text{kin}}) = \begin{cases} 0 & E_{\text{kin}} \leq 0 \\ \lambda \exp(-\lambda E_{\text{kin}}) & 0 < E_{\text{kin}} \leq E_{\text{cutoff}} \\ 0 & E_{\text{kin}} > E_{\text{cutoff}} \end{cases} \tag{8.1}$$
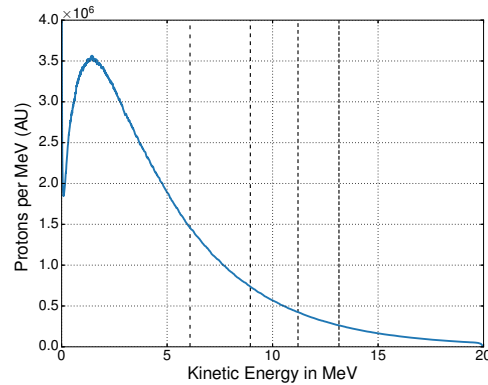
Figure 8.1: Proton energy distribution for the radiography study, scored behind the spectrometer. The dashed vertical lines indicate cut-off energies for WETs of 0.5, 1.0, 1.5 and 2.0 mm, respectively.

with $\lambda = 0.25\,\mathrm{MeV}^{-1}$ and $E_{\mathrm{cutoff}} = 20\,\mathrm{MeV}$ for the low-energy simulations and $\lambda = 0.05\,\mathrm{MeV}^{-1}$ and $E_{\mathrm{cutoff}} = 100\,\mathrm{MeV}$ for higher energies. The expected values of the energy distributions are hence $3.84\,\mathrm{MeV}$ and $19.19\,\mathrm{MeV}$ for the two respective energy ranges. The resulting low-energy spectrum after having passed the spectrometer, which is explained in the following, is shown in figure 8.1.

The typical, few-µm small source size was approximated by a point source. If not stated differently, the divergence of the proton bunches was sampled from a Gaussian distribution with a full divergence angle of $\theta = 5°$ (FWHM). This is a rather modest divergence angle, as typical divergence angles in experiments can easily exceed 10°. Since a spatially homogeneous proton fluence is beneficial for imaging purposes, this small divergence angle approaches the worst case for potential experiments. Furthermore, the energy distribution of the protons was assumed to be independent of the angle with respect to the central beam axis.

Phantoms

Two phantoms, consisting of PMMA, water and different biological materials were created in the simulation geometry. Material properties (density and WER) are listed in table 8.1. For proton energies below $20\,\mathrm{MeV}$, the geometrical thickness of the phantoms was ranging between $0.3\,\mathrm{mm}$ and $2.0\,\mathrm{mm}$. The phantom thickness for high proton energies was ranging between 20 and $23\,\mathrm{mm}$. In either case, a sufficiently large number of protons is expected to entirely penetrate the phantom and reach the imaging detector.

The two phantom types (shown schematically in figure 8.2) are presented in the following.

- The thin **step phantom** consists of a $20 \times 20\,\mathrm{mm}^2$ large and $300\,\mathrm{µm}$ thin PMMA slab with 6 steps. Each step, except the first and the last step, is $2\,\mathrm{mm}$ wide and $60\,\mathrm{µm}$ high. Hence, the geometrical thickness of the last step is $660\,\mathrm{µm}$. For higher proton energies, the slab thickness was $20\,\mathrm{mm}$. The number of steps was reduced to

135

(a) Step Phantom

(b) Insert Phantom
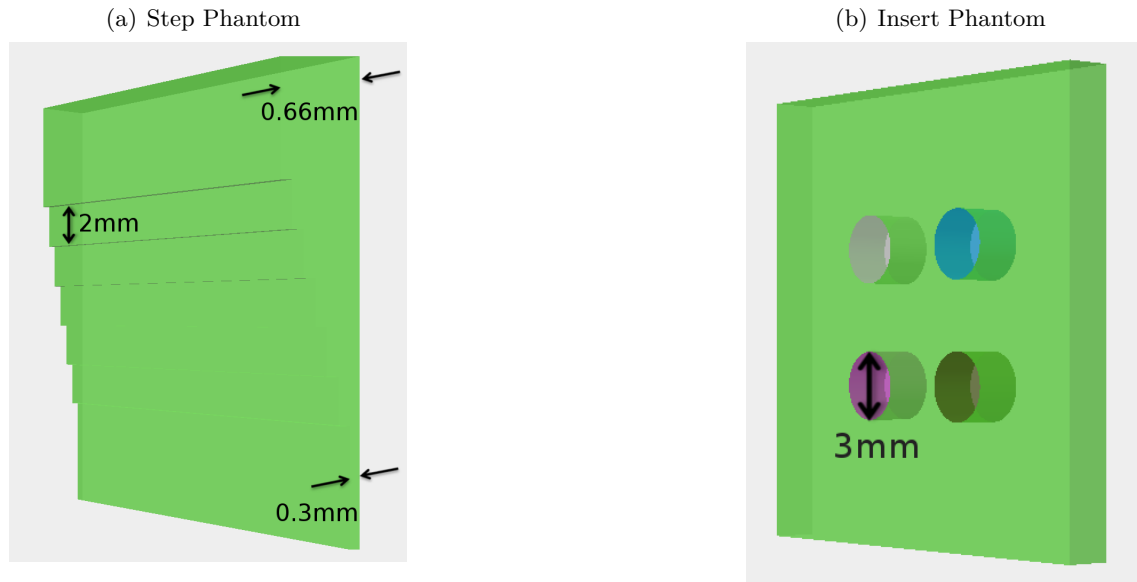
Figure 8.2: Illustration of the two phantoms used in the radiography study for proton energies below 20 MeV. PMMA is shown in light green. Adipose tissue, water, skeletal muscle and compact bone are shown in gray, blue, dark green and purple, respectively. Sizes in the step phantom are not to scale for the sake of better visibility.

Table 8.1: Properties of phantom materials used in the radiography study. The WER of the respective materials was determined based on FLUKA MC simulations, according to the thick target approximation using eq. 2.26. WER values were determined for two energy ranges, corresponding to the energy ranges of interest for this study ($5\,\mathrm{MeV} \leq E_{\mathrm{kin}} \leq 20\,\mathrm{MeV}$) and ($50\,\mathrm{MeV} \leq E_{\mathrm{kin}} \leq 100\,\mathrm{MeV}$). The given values with uncertainties correspond to the WER interval for the respective energy ranges.

Material	Density [$\mathrm{g\,cm^{-3}}$]	WER $E_{\mathrm{kin}} \leq 20\,\mathrm{MeV}$	WER $E_{\mathrm{kin}} \leq 100\,\mathrm{MeV}$
Water	1.00	1	1
PMMA	1.19	1.158 ± 0.001	1.159 ± 0.001
Adipose Tissue	0.92	0.958 ± 0.004	0.949 ± 0.002
Compact Bone	1.85	1.643 ± 0.018	1.682 ± 0.004
Skeletal Muscle	1.04	1.027 ± 0.001	1.030 ± 0.001

3, each 5 mm wide and 1 mm high. The thin and thick step phantoms were used to determine the spatial resolution of the resulting images.

- The **insert phantom** is a $20 \times 20 \, mm^2$ large PMMA slab. Its thickness varied from 0.5 mm to 2.0 mm for the low energy simulation study and was set to 20 mm for the high energy simulations. It has four cylindrical inserts, each with a diameter of 3 mm and spanning over the entire phantom along the proton beam direction. The insert materials are skeletal muscle, compact bone, adipose tissue and water.

Detectors for Spectrum Determination and Imaging

The spatially resolved proton energy distribution was determined in transmission upstream of the phantom using the TOF approach described in chapter 6. To this aim, a thin and pixelated semiconductor-based spectrometer is modeled by a $2 \times 2 \, cm^2$ large and 20 μm thin silicon cuboid, of which only the central area of $1.6 \times 1.6 \, cm^2$ and a thickness of 10 μm are considered as the detector SV. For each proton entering the SV of the spectrometer, arrival time and lateral position, as well as energy deposition inside the SV was stored in list-mode using the FLUKA user-routine `mgdraw.f`.

After runtime, the list-mode data was binned according to position and arrival time at the detector. The spatial bin width, which corresponds to the pixel size of the spectrometer, was set to $2 \times 2 \, mm^2$. The temporal bin width was $\Delta t = 0.05 \, ns$, corresponding to the sampling time of a virtual read-out electronics. The artificial spectrometer signal in each pixel is then created by summing the energy deposition of all protons reaching that pixel within each corresponding time bin. In contrast to the TOF experiments presented in chapter 6, the response of the spectrometer is assumed to be instantaneous, hence no response function was taken into account.

Depending on the setup, two different position-sensitive detectors placed after the object were modeled in the MC simulations, namely the hybrid pixel detector Timepix (section 4.2.2) and the CMOS based detector system RadEye (section 4.2.3). Energy deposition was scored in the SV of the detectors using a Cartesian scorer with bin sizes corresponding to the pixel size of the respective detector. In case of the Timepix detector, this corresponds to a matrix of 256×256 square pixels with a pixel pitch of 55 μm and a thickness of 500 μm. The resulting energy deposition maps were Gaussian filtered to approximate charge-sharing effects (see section 4.2.2). For the RadEye detector, the scoring grid was 1024×512 square pixels with a size of $48 \times 48 \times 2 \, \mu m^3$ each. A 2 μm thin SiO_2 passivation layer on top of the silicon layer was also included in the simulation geometry. Due to the thin sensitive thickness, charge-sharing effects do not play any role for the RadEye detector and were hence not accounted for.
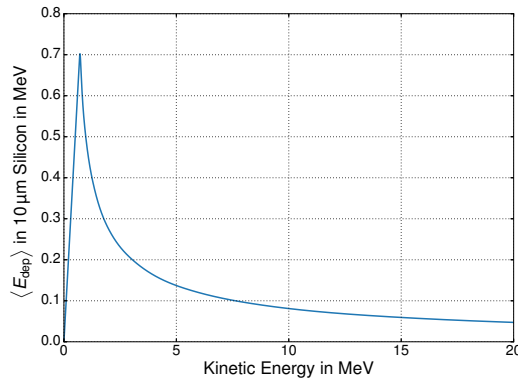
Figure 8.3: Mean energy deposition of protons in $10\,\mu\mathrm{m}$ silicon as a function of kinetic energy, according to FLUKA MC simulations. For kinetic energies below the energy corresponding to the peak, protons are entirely stopped within the silicon volume.

8.2.2   Reconstruction Methods

Reconstruction of the Proton Spectrum

The output of each pixel of the simulated spectrometer is an array containing the signal, i.e., the total energy deposition inside that pixel, and the corresponding time array. With the signal array $\vec{S}(t)$ having n entries, the time array can be expressed either by the central time of each bin, $\vec{t}_{\mathrm{mid}}$ of size n, or by the $n+1$ bin edges, $\vec{t}_{\mathrm{edge}}$.

Both time arrays were then converted into the corresponding kinetic proton energies according to eq. 6.1, resulting in $\vec{\mathcal{E}}_{\mathrm{mid}}$ and $\vec{\mathcal{E}}_{\mathrm{edge}}$, respectively. The calligraphic letter $\mathcal{E}$ was chosen for the energy bins of the spectrometer to avoid confusion with energy deposition. In order to obtain the number of protons within each energy bin i, $N_{\mathrm{p},i}$, the simulated spectrometer signal S_i was divided by the corresponding average energy deposition of protons within the $d = 10\,\mu\mathrm{m}$ thin silicon SV, $\langle E_{\mathrm{dep},i}(d)\rangle$. This average energy deposition was taken from a MC based look-up table, which is plotted in figure 8.3.

In a final step, the resulting spectrum was corrected for the actual energy losses inside the total thickness of the spectrometer ($d = 20\,\mu\mathrm{m}$ silicon), which have been neglected up to this point. This was done by shifting all energy bin edges $\mathcal{E}_{\mathrm{edge},i}$ (and the central energies of each bin, $\vec{\mathcal{E}}_{\mathrm{mid}}$) towards lower energies. The energy dependent shift, calculated by

$$\mathcal{E}_{\mathrm{shift},i}(\mathcal{E}_{\mathrm{edge},i}) = \langle E_{\mathrm{dep}}(\mathcal{E}_{\mathrm{edge},i}; d)\rangle \ ,$$

was also taken from a MC-based look-up table. Bins with final edge energies $\mathcal{E}_{\mathrm{edge},i} \leq 0$ were deleted.

Although the described procedure is relying on several assumptions, especially that the actual energy deposition is close to the average energy deposition $\langle E_{\mathrm{dep}}(\mathcal{E}_{\mathrm{mid},i}; d)\rangle$, the performance of the reconstruction has shown to be sufficient. A comparison of the reconstructed and true energy distributions is shown in figure 8.4. Differences between the
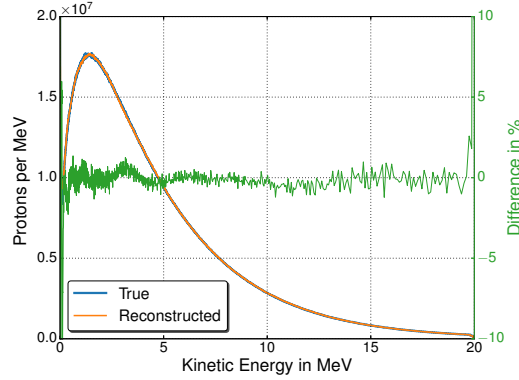
Figure 8.4: Comparison of the true proton energy distribution after the transmission spectrometer (blue) with the reconstructed spectrum (orange). The relative difference between both distributions is shown in green (right axis).

reconstructed proton energy distribution and the actual spectrum recorded behind the spectrometer are typically below 1%, except for very low and high energy bins. However, in the energy range where the highest contribution to the signal in the imaging detector is expected (5 MeV to 15 MeV for the low-energy study), the agreement between reconstructed and true spectrum is very good. The encountered fluctuations are due to statistical fluctuations in the energy deposition inside the detector SV and their impact on the WET reconstruction is assumed to be small.

WET Reconstruction

WET reconstruction in this simulation study is based on the decaying shape of the polyenergetic proton spectrum, resulting in a monotonically decreasing signal in the imaging detector with increasing WET of the traversed object. In other words, the larger the energy deposition inside the SV of the imaging detector, the smaller the WET of the traversed object.

When energy-modulating a proton beam from a conventional accelerator as described in section 3.2.1 with a fixed modulation pattern, the resulting energy distribution function will remain constant. In these cases, the WET can be obtained based on a calibration of the detector signal which is performed once for each modulation pattern. Due to typical shot-to-shot fluctuations in the energy distribution of laser-accelerated protons, this single calibration is not sufficient for accurate WET reconstruction. Therefore, a conversion curve relating the signal in the imaging detector to the WET of the traversed object needs to be done for every single proton bunch individually.

For both imaging detectors used in this study, a look-up table was created relating the expected energy loss of one proton of a certain energy inside the SV of the imaging detector pixel to the traversed WET. This average energy loss, $\langle E_{\text{dep}}(\text{SV}, E_{\text{kin}}, \text{WET}) \rangle$, was calculated only once, using a large set of FLUKA MC simulations scoring the energy deposition inside the respective imaging detector after a block of water. The thickness

(a) Timepix $\langle E_{\mathrm{dep}}(500\,\mu\mathrm{m}\ \mathrm{Si};E_{\mathrm{kin}};\mathrm{WET})\rangle$

(b) RadEye $\langle E_{\mathrm{dep}}(2\,\mu\mathrm{m}\ \mathrm{Si};E_{\mathrm{kin}};\mathrm{WET})\rangle$

(c) Timepix (Energy deposition vs. WET)

(d) RadEye (Energy deposition vs. WET)

(e) Timepix (Energy deposition vs. E_{kin})

(f) RadEye (Energy deposition vs. E_{kin})
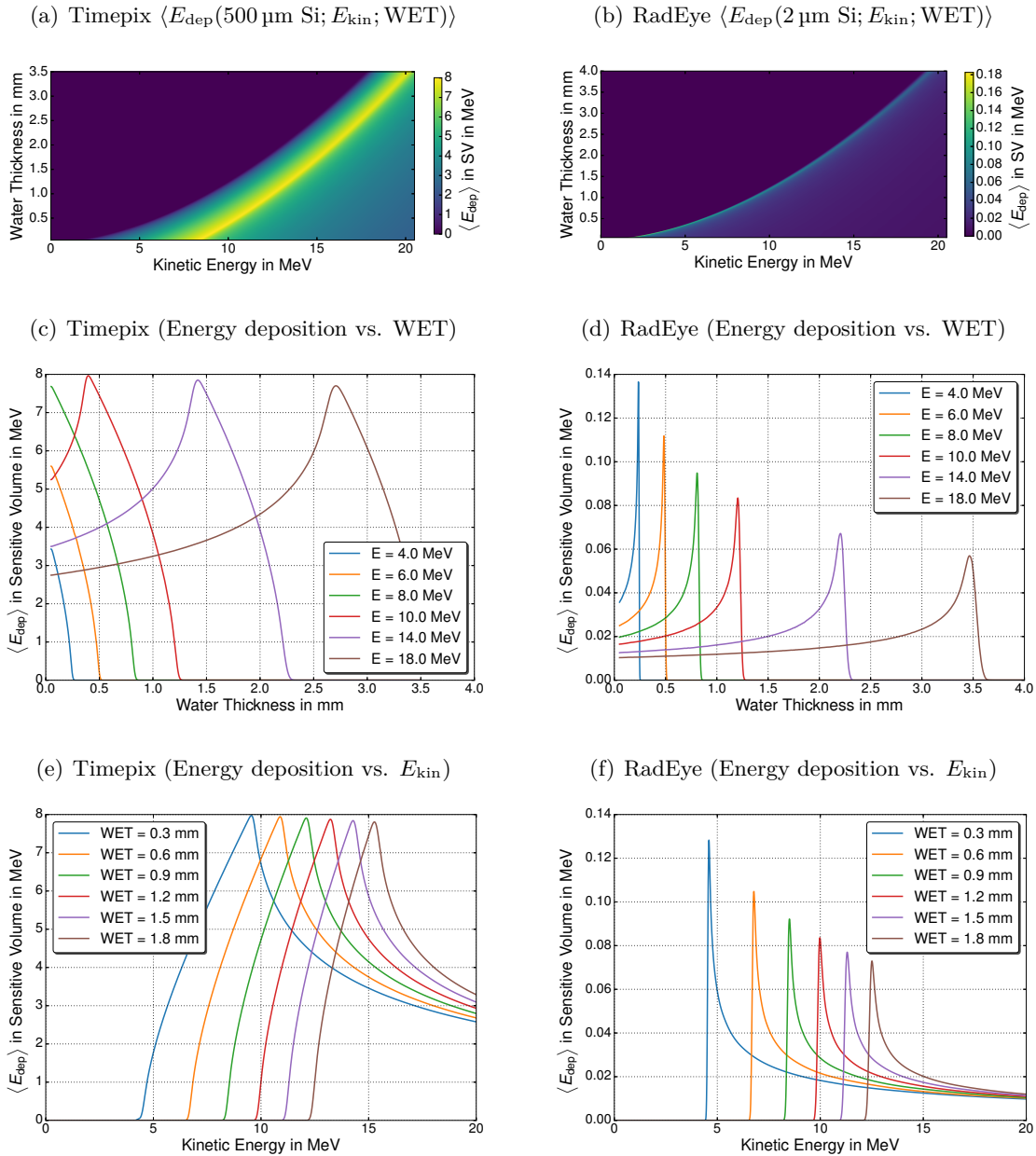
Figure 8.5: Graphical representation of the look-up table for WET reconstruction. It is relating the expected energy loss $\langle E_{\mathrm{dep}}(500\,\mu\mathrm{m}\ \mathrm{Si};E_{\mathrm{kin}};\mathrm{WET})\rangle$ and $\langle E_{\mathrm{dep}}(2\,\mu\mathrm{m}\ \mathrm{Si};E_{\mathrm{kin}};\mathrm{WET})\rangle$ inside SVs of the Timepix (a,c,e) and the RadEye detector pixels (b,d,f) to the proton energy E_{kin} and the WET. Horizontal profiles for a selection of proton energies (c,d), as well as vertical profiles for different water thicknesses (e,f) are shown for the two respective detectors.

of the water block, as well as the initial kinetic energy was varied within this set of simulations. To obtain a finer resolution of the look-up table, a cubic spline fit was performed on the simulation results. A graphical representation of the two look-up tables is shown in figure 8.5.

If the fluence is not spatially homogeneous along the entire detector surface, the conversion curve relating detector signal to WET is not only changing with each proton bunch, but

it may also differ for individual pixels of the imaging detector. Hence, for each pixel, such conversion curve was created analytically prior to the WET reconstruction. First, the number of protons and the energy spectrum that would be expected to reach each detector pixel in an open field configuration, was calculated. The computation is based on the previously reconstructed spectrum, the geometrical size of the pixels and the divergent beam, taking into account the distances from source to spectrometer and from source to imaging detector, which will be given in sections 8.3.1 and 8.4.1 for the two respective setups. Then, the formerly described look-up table was used to create the conversion curve for each pixel of the imaging detector.

The WET of the respective pixel is then the point of the conversion curve, where the detector signal is closest to this curve. One example of this conversion curve with the reconstructed WET value can be found later in this chapter for actual simulation data (see figure 8.16d).

Since the look-up table data was generated from the energy-deposition inside the imaging detector after having traversed a block of water, scattering and fluence reduction due to nuclear effects are inherently taken into account. However, the conversion curves are calculated based on the average energy deposition. Since the total number of protons per image detector pixel is actually relatively small, statistical effects in the energy deposition are not accounted for and can result in fluctuations of the reconstructed WET values. They are partially suppressed by median-filtering the conversion curve and the final WET image as shown in the results section.

8.2.3 Assessment of the Image Quality

Density/WET Resolution

Two quantities were used to judge the density resolution of the reconstructed WET distributions. First, the *mean WET* of defined regions-of-interest (ROIs) was calculated. Each ROI includes only one certain material or one step thickness. Comparing this quantity to the true WET value gives an estimate of the general accuracy of the reconstructed image on a larger scale. Since the interfaces between two materials or two steps are largely affected by multiple Coulomb scattering, a margin between the interfaces and the ROIs was introduced. Pixels closer than 0.3 mm to these interfaces were hence excluded from the ROIs.

On a pixel scale, the accuracy was quantified by calculating the root-mean-square error (*RMSE*):

$$\mathrm{RMSE} = \sqrt{\frac{\sum_i^n (\mathrm{WET}_{\mathrm{recon}}^i - \mathrm{WET}_{\mathrm{true}}^i)^2}{n}} \ . \tag{8.2}$$

This was done for the entire object (*global RMSE*), as well as taking into account only pixels from given ROIs. The normalized RMSE, *NRMSE*, is obtained for the ROIs by

dividing the RMSE by the true WET, while the *global NRMSE* is here defined as

$$\mathrm{NRMSE}_{\mathrm{glob}} = \frac{\mathrm{RMSE}}{d} \tag{8.3}$$

with the geometrical phantom thickness d.

Spatial Resolution

For assessing the spatial resolution of the reconstructed WET images, an approach similar to the one described in detail in Seco et al. [2013] was used.

A sigmoidal curve, described by

$$f(x) = a_1 + \frac{a_2}{1 + \exp\left(-\frac{x - a_3}{a_4}\right)} \tag{8.4}$$

was fitted to the WET values arranged on a line perpendicular to the interface between two adjacent steps of the step phantom. The fit parameter a_1 is the starting value of the sigmoidal curve, hence the WET of the thinner step. The sum $a_1 + a_2$ is the ending value, i.e. the WET of the thicker step. The remaining fit parameters a_3 and a_4 correspond to the position and the width of the inflection. To minimize the impact of fluctuations, the mean of the WET image along the axis parallel to the step interfaces was calculated prior to the fitting procedure.

The spatial distance between the 25%- and the 75%-value of the sigmoidal fit was then taken as the FWHM of a Gaussian line-spread function (LSF). A Gaussian was chosen, since this function properly describes the LSF in proton radiography [Seco et al., 2013]. The optical transfer function (OTF) was then calculated by normalizing the discrete Fourier transform of the LSF, and the modulation transfer function (MTF) was finally obtained by taking the magnitude of the OTF. The 10% value of the MTF, $\mathrm{MTF}_{10\%}$, is expressed in line-pairs per mm ($\mathrm{lp\,mm}^{-1}$) and was used to characterize the spatial resolution.

This calculation was done for all interfaces between adjacent steps and the spatial resolution values given hereafter refer to the mean and its standard deviation.

8.3   Simulation Setup using the Timepix Detector

8.3.1   Overview

For the first simulation study, the entire setup based on the Timepix detector was placed in vacuum. The source-spectrometer-distance was set to 1 m. If not stated differently, the other distances between the thin TOF spectrometer and the phantom, as well as between phantom and imaging detector were 5 mm. A cartoon illustrating the simulation geometry is given in figure 8.6. All results shown within this section refer to the low-energy proton
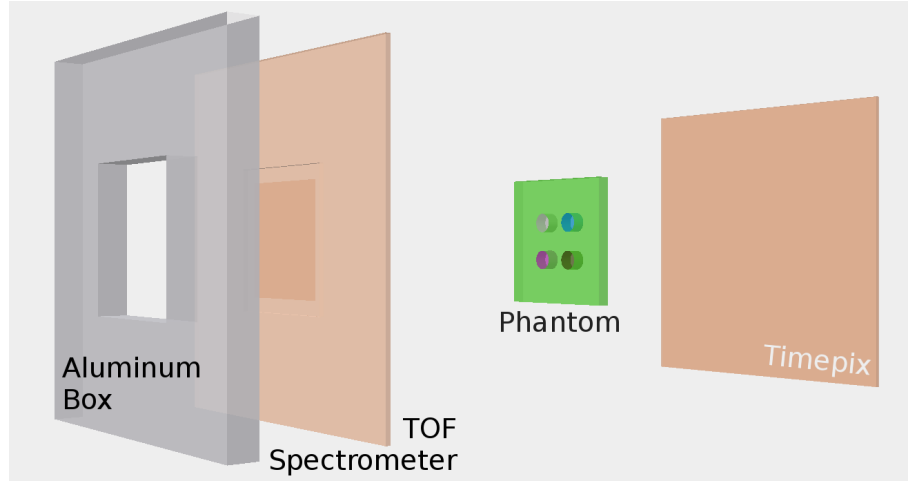
Figure 8.6: Illustration of the simulation geometry for the imaging setup using the Detector detector. The proton bunch is coming from the left, passing the hole inside an aluminum box (gray), the TOF spectrometer (orange) and the phantom with four cylindric inserts before being detected by the RadEye detector (dark green and orange). Distances between objects were enhanced for illustration purposes and are hence not to scale.

(a) 2D WET distribution   (b) 1D WET profile
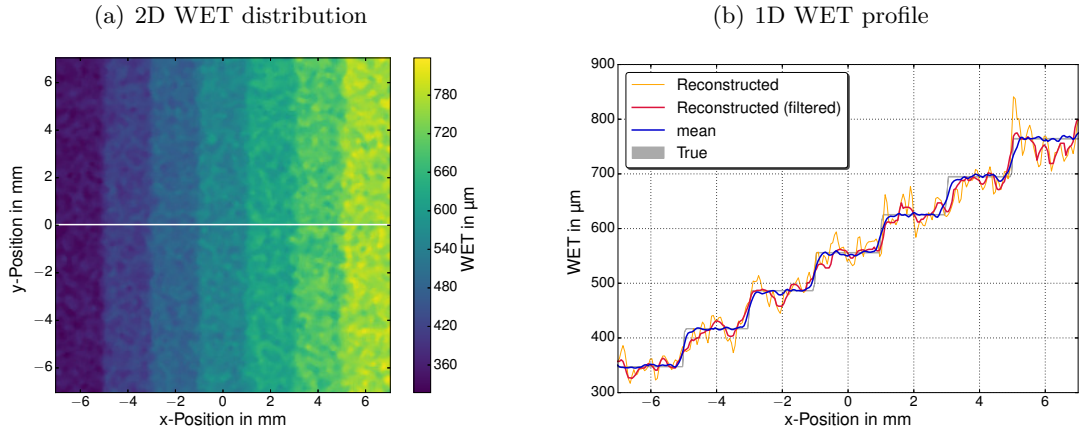
Figure 8.7: Reconstructed WET of the step phantom in the Timepix radiography setup for 10^9 primaries. The 2D distribution is shown in (a). The white horizontal line marks the locations of the 1D profile, which is shown in orange (not-filtered) and red (median filtered) in (b). They are compared to the average WET along the axis (blue) and the true WET (gray).

spectrum ($E_{\text{kin}} \leq 20\,\text{MeV}$) and phantom thicknesses up to $2\,\text{mm}$.

8.3.2 Results

Reconstructed WET distributions

The WET was calculated pixel-per-pixel for the thin step phantom and insert phantoms of various thicknesses up to $2\,\text{mm}$ for a primary proton number of 10^9, distributed according to the energy spectrum shown in figure 8.1 and explained in section 8.2.1.

2D WET distributions and 1D profiles of the step phantom and the $0.5\,\text{mm}$ thick insert

143

(a) 2D WET distribution

(b) 1D WET profile

(c) 1D WET profile

(d) Depth dose profile
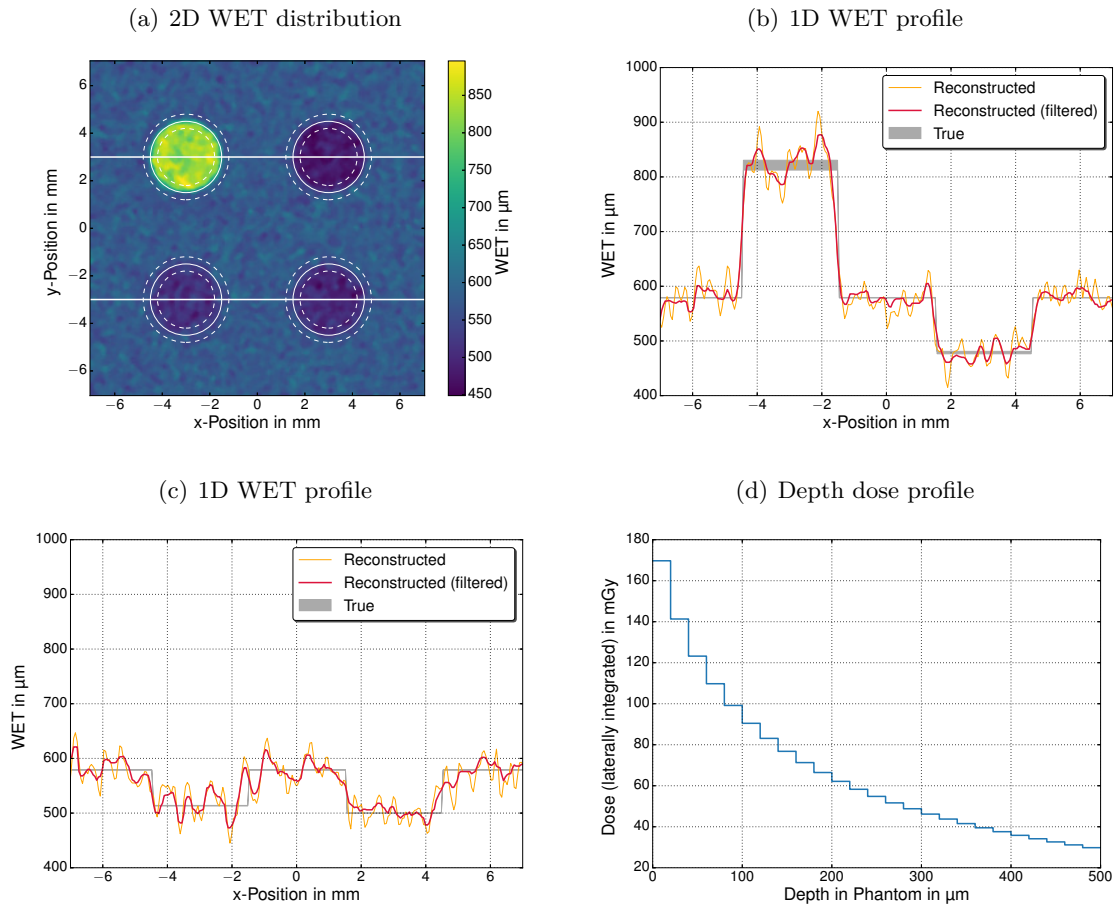
Figure 8.8: Reconstructed WET of the insert phantom in the Timepix radiography setup for 10^9 primaries. The 2D distribution is shown in (a). Insert positions and the borders of the ROIs are indicated by the solid and dashed white circles, respectively. The white horizontal lines mark the locations of the two 1D profiles shown in orange (not-filtered) and red (median filtered) in (b) and (c). They are compared to the true WET (gray). In (d), the laterally integrated depth-dose distribution inside the phantom is shown.

phantom are shown in figures 8.7 and 8.8, respectively. To quantify the WET resolution, ROIs including only one material or one step thickness were defined (see e.g. white dashed circles in figure 8.8a). For both phantom types and all phantom thicknesses up to 2 mm, the mean WET within each ROI was found in very good agreement with the corresponding true value. The largest encountered difference was 0.7%.

For all phantoms investigated within this part of the study, the NRMSE within each ROI was ranging between 1.8% and 3.4%. For the entire phantom, the global RMSE was 17.0 µm and 18.5 µm for the step phantom and the 0.5 mm thin insert phantom, respectively. With increasing thickness of the insert phantom up to 2.0 mm, the global NRMSE slightly increases from initially 3.7% up to 4.2%. This can be attributed to the larger impact of MCS in the thicker phantom.
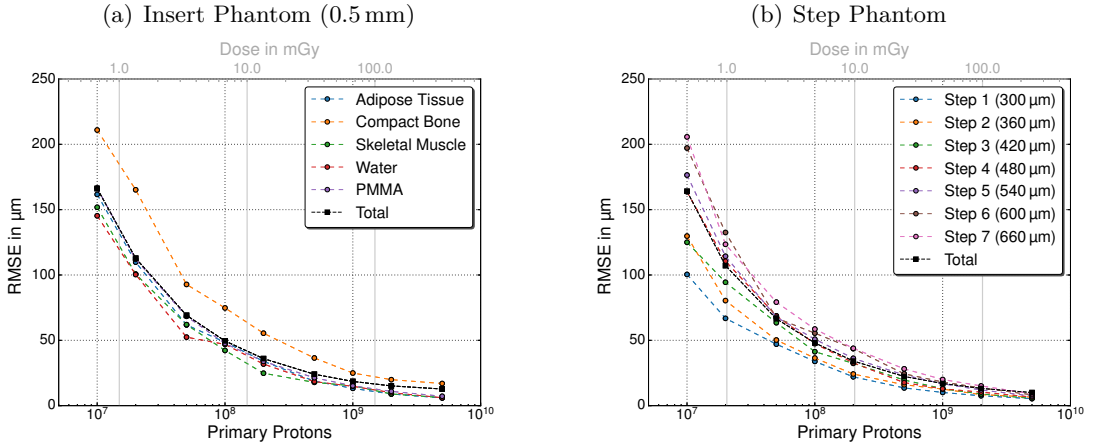
Figure 8.9: Assessment of the image quality versus primary protons for the Timepix radiography setup for the 0.5 mm thin insert phantom (a) and the thin step phantom (b). The RMSE of the reconstructed WET of the total object (black) and the different materials or step sizes (colors) are plotted as a function of primary particle number (lower axis) and the corresponding dose to the phantom (upper axis). The dashed lines are to guide the eye.

Proton Number and Imaging Dose

Due to the divergence of the source ($\theta = 5°$), only 4.5% of the primary protons reach the $4\,\text{cm}^2$ large area of the 1 m distant spectrometer. Absorption of low-energy protons and scattering in the spectrometer further reduce the fluence such that only 3.3% of the initial protons impinge the phantom. The actual proton number contributing to the signal in the imaging detector ($1.4 \times 1.4\,\text{cm}^2$ active area) depends on the thickness of the object. For the insert phantom and a primary proton number of 10^9, the mean fluence at the imaging detector was ranging between 2.6×10^5 and $2.0 \times 10^6\,\text{protons/cm}^2$ for a phantom thickness of 2.0 and 0.5 mm, respectively. Hence, for these two thicknesses, only 0.05% and 0.40% of the primary protons contribute to the signal used for imaging, corresponding to a mean proton number of $\sim 7 - 61$ protons per Timepix detector pixel.

The high absorption and energy losses inside the phantom give rise to the excellent WET resolution reported in the previous subsection. However, this comes at the price of rather high radiation dose in the object to be imaged. The total dose in the phantom ranges between 67 mGy and 25 mGy per 10^9 primary particles for the two aforementioned phantom thicknesses, respectively. Due to the exponential shape of the spectrum and the resulting depth-dose distribution (see figure 8.8d), the total imaging dose decreases with larger phantom thickness, while the dose close to the front surface remains constant.

For the same spectral distribution and phantom, a reduction of the primary proton number results in a deterioration of the image quality, expressed by larger RMSE values. This dependency is shown for the thinnest insert phantom and the thin step phantom in figure 8.9 for primary numbers ranging from 10^7 to 5×10^9.

Reconstructed WET images of the thin step phantom are shown in figure 8.10 for 10^8 and 5×10^9 primary protons. Although still very noisy, adjacent steps can already be visually

(a) 2D WET distribution for 10^8 protons
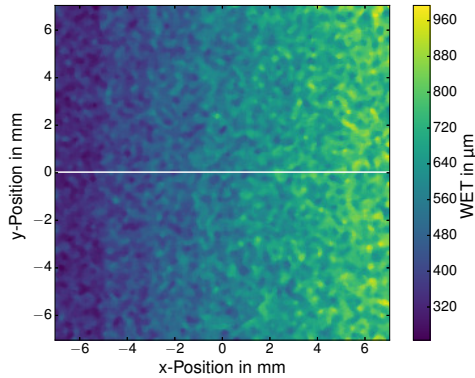
(b) 1D WET profile for 10^8 protons
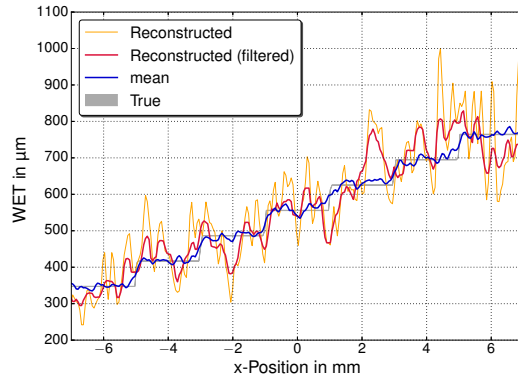
(c) 2D WET distribution for 5×10^9 protons
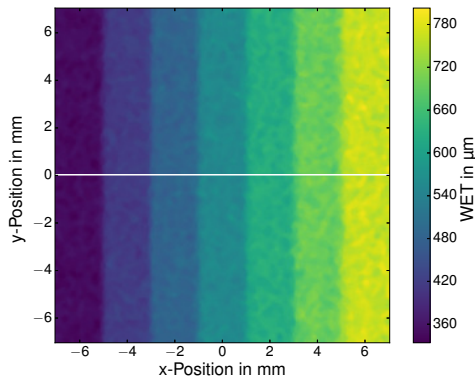
(d) 1D WET profile for 5×10^9 protons
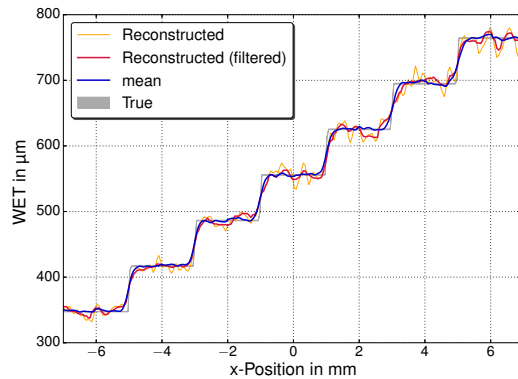
Figure 8.10: Reconstructed WET of the step phantom in the Timepix radiography setup for different number of primary particles. Reconstructed 2D WET distributions and 1D WET profiles for the step phantom are shown in (a,b) and (c,d) for 10^8 and 5×10^9 primaries, respectively. Colors in (b,d) are the same as in figure 8.7.

distinguished at about 10^8 primaries, which corresponds to a fluence at the imaging detector of 2.2×10^5 protons/cm^2 and an imaging dose of $4.9\,\text{mGy}$. The corresponding RMSEs of the individual steps, as well as the global RMSE divided by the mean step thickness is lower than 10%. However, for quantitatively reliable WET images with NRMSEs below or around 3%, at least 10 times higher fluence, and consequently imaging dose, is required.

Spatial Resolution

Spatial resolution in proton imaging is mainly limited by multiple Coulomb scattering of protons inside the phantom, which is most pronounced for low energies. This introduces a blurring of the image, which evidently depends on the thickness of the phantom and the distance between phantom and imaging device. To study this effect, the distances between spectrometer and phantom and between phantom and detector were varied from $1\,\text{mm}$ to $20\,\text{mm}$, while keeping the number of primary particles fixed at 10^9.

Reconstructed WET distributions are shown in figure 8.11 for the smallest and the largest
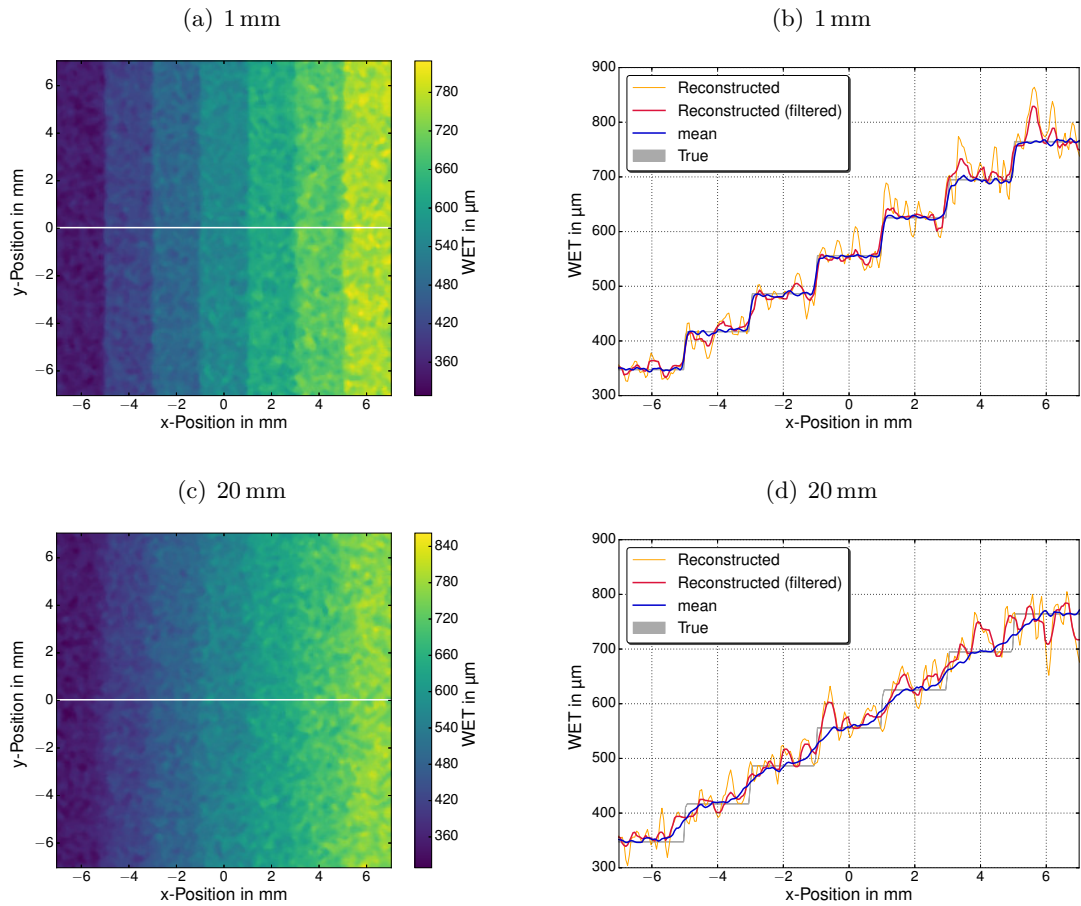
Figure 8.11: Determination of the spatial resolution in the Timepix radiography setup for different phantom-detector-distances. 2D WET distributions (a,c) and 1D profiles (b,d) are shown for a distance of 1 mm and 20 mm in (a,b) and (c,d), respectively. Colors are the same as in figure 8.7.

distances. At a distance of 1 mm, the edges of the step phantom are very well preserved. With increasing distances, blurring of the image becomes more and more pronounced. Nevertheless, the 2 mm wide steps can still be visually distinguished at a distance of 20 mm.

Exemplary for the quantitative analysis, the sigmoidal fit to the last step at distances of 5 mm is shown in figure 8.12a, where also the 25%- and 75%-values (FWHM of the LSF) are indicated. The obtained MTFs for all simulated distances are plotted in figure 8.12b. The faint areas around the MTFs indicate the uncertainty in terms of standard deviation, arising from fits to all interfaces between adjacent steps.

An excellent spatial resolution of $(10.3 \pm 2.3)\,\mathrm{lp\,mm^{-1}}$ was found at the smallest distance of 1 mm. The spatial resolution drops quickly, as shown in figure 8.13. Yet, sub-mm resolution was found for all simulated distances. At a distance of 5 mm, which could be a reasonable distance for experimental imaging of such small samples, the spatial resolution is $(5.0 \pm 0.7)\,\mathrm{lp\,mm^{-1}}$.

(a) Sigmoidal Fit   (b) Modulation Transfer Function
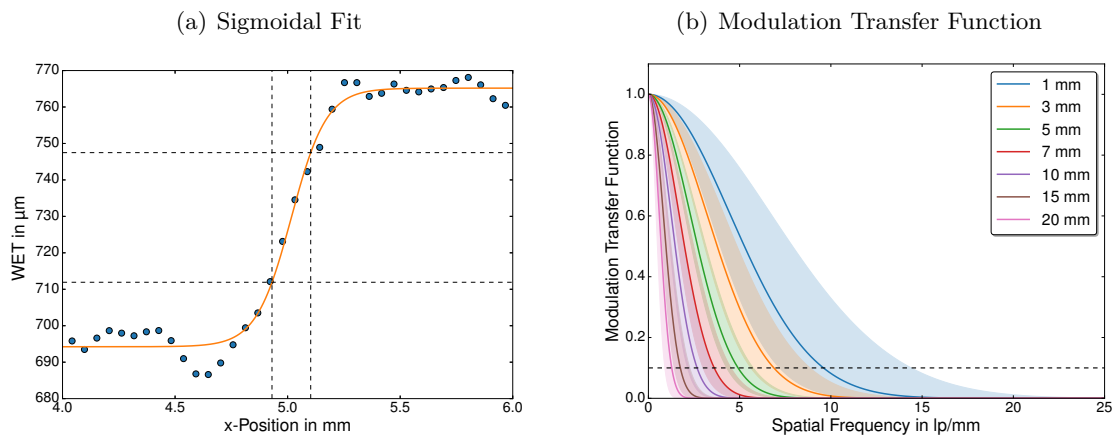
Figure 8.12: Determination of the spatial resolution of proton radiography for the Timepix imaging setup. In (a), the laterally averaged WET values at the interface of the two thickest steps at a detector distance of 5 mm are shown (blue circles) with the corresponding sigmoidal fit. The dashed lines indicate positions and the heights of the 25%- and 75%-value of the sigmoidal curve. The calculated MTFs for all seven investigated distances are shown in (b). The shaded areas around the central lines indicate the standard deviation of the MTFs.
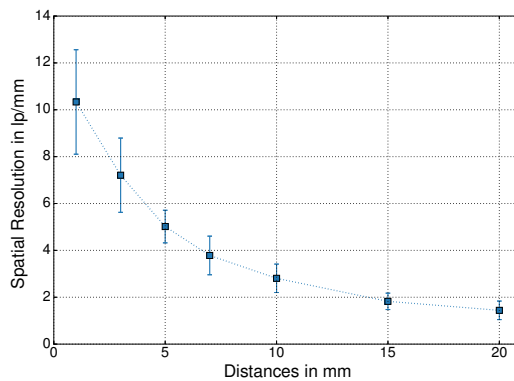
Figure 8.13: Spatial resolution of proton radiography using the Timepix imaging setup for various phantom-detector distances. The dotted line is to guide the eye.

Influence of the Spectrometer Resolution

The accuracy of the reconstructed proton energy distribution is one the major sources of uncertainty for the WET determination. The temporal resolution of the TOF spectrometer directly affects the energy resolution of the resulting spectrum. Furthermore, if the proton field at the phantom location is not homogeneous along the transversal dimensions, the spatial variation of the spectrum has to be measured as well, i.e., pixelation of the TOF spectrometer may be necessary.

The lateral fluence distribution in the phantom plane is shown in figure 8.14 for different beam divergence angles at a source-to-phantom distance of 1 m. In case of large divergence angles ($> 8°$), the spatial proton distribution within a $2 \times 2\,cm^2$ large plane at the phantom location can be considered rather uniform with deviations from the mean fluence smaller
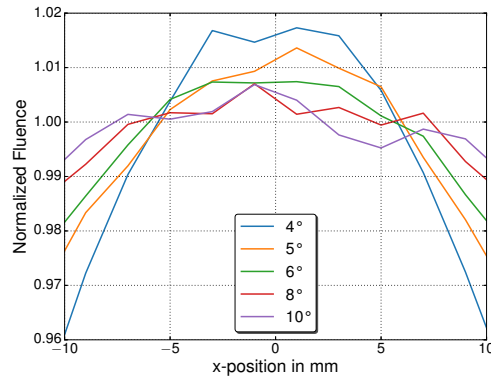
Figure 8.14: Lateral proton fluence distribution in the phantom plane, given for different beam divergence angles.

(a) WET profile for 1 mm pixel size

(b) WET profile for 8 mm pixel size

(c) WET profile along the central step

(d) Difference reconstructed WET / True WET
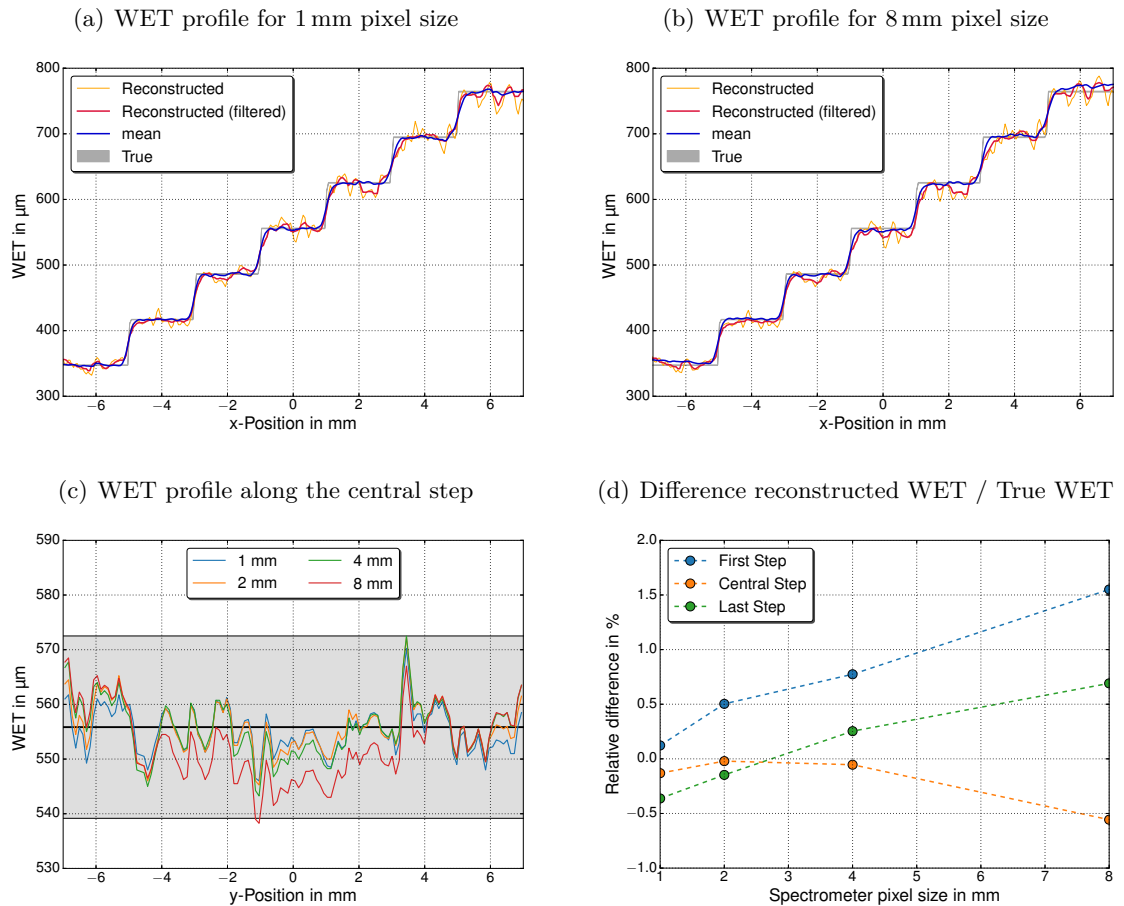
Figure 8.15: Influence of the spectrometer pixel size on the image quality in terms of reconstructed WET for the Timepix imaging setup. In (a) and (b), WET profiles of the step phantom for spectrometer pixel sizes of 1 mm and 8 mm are shown, respectively. Colors are the same as in figure 8.7. The WET profile along the central step is shown in (c) for different spectrometer pixel sizes. The gray area indicates ±3% of the true WET, which is marked by the central black line. In (d), the absolute difference between reconstructed and true WET is plotted versus the spectrometer pixel size for three different steps.

than 1%[1]. For lower beam divergence, smaller source-to-phantom distances and/or a larger field-of-view (FOV), fluence variations along the FOV of several percent have to be expected. Since these variations directly affect the WET calculation, especially at the center and the edges of the FOV, this would result in wrong WET values unless the spectrum is determined spatially resolved.

Therefore, the influence of spectrometer pixel size and the sampling time on the resulting WET resolution was studied in order to determine hardware requirements of the TOF spectrometer for potential imaging applications.

The resulting effect caused by a non-homogeneous proton field on the reconstructed WET distribution was determined for a proton beam with divergence angle of 5°, by gradually increasing the pixel size of the spectrometer from $1\,\text{mm}$ to $16\,\text{mm}$. Practically no difference between a pixel size of $8 \times 8\,\text{mm}^2$ and no pixelation ($\widehat{=} 16 \times 16\,\text{mm}^2$ pixel size) was found due to the point symmetry of the simulated proton beam and the symmetric spectrometer pixel arrangement.

WET profiles for pixel sizes of $1 \times 1\,\text{mm}^2$ and $8 \times 8\,\text{mm}^2$ are shown in figure 8.15(a) and (b), respectively. In figure 8.15(c), the WET profile along the central step of the step phantom for different pixel sizes is compared to the true WET. Only minor differences for the WET profile can be seen at pixel sizes $\leq 4 \times 4\,\text{mm}^2$. For large pixel sizes ($\geq 8 \times 8\,\text{mm}^2$), an underestimation in the center of -1.5% and an overestimation at the edges of the FOV of $+2.6\%$ was found. The relative differences between the mean reconstructed WET of the thinnest, the central and the thickest steps and the corresponding true WET for different spectrometer pixel sizes are summarized in figure 8.15(d).

Increasing the temporal bin width, which consequently leads to a decrease of the energy resolution of the retrieved energy spectrum, results in a systematic overestimation of the WET. However, an increase by a factor of 4, resulting in a sampling time of $0.2\,\text{ns}$, shows only moderate changes ($+1.8\%$) for TOF distance, energy range and phantom thickness used in this study. Increasing the sampling time further to $0.5\,\text{ns}$ then leads to a WET overestimation of up to 4.1%. A reduction of the sampling time from the initial value of $0.05\,\text{ns}$ down to $0.01\,\text{ns}$ did not reveal any benefit in the reconstructed image.

8.3.3 Discussion

Image Quality and Imaging Dose

For a primary proton number of 10^9 in the studied configuration, the mean reconstructed WET within each ROI was found in excellent agreement with the WET values given in table 8.1. The reported relatively low RMSE values within each ROI indicate a quite high precision, despite the small pixels size of $55\,\mu\text{m}$ and the therefore low particle fluence at the

---

[1]Note that in this simulation study the energy distribution is assumed to be laterally constant within the entire divergent beam.

detector, ranging from 7 to 61 protons per pixel, depending on the phantom thickness and material. Larger NRMSE values were encountered when increasing the phantom thickness. One reason for this trend is the increased scattering inside the phantom. This results in less sharp edges of the reconstructed WET at the interfaces between two materials. The second reason is due to the reduced WET contrast in the flatter regions of the conversion curve relating energy deposition inside the detector to the water equivalent thickness. Small statistical fluctuations in the energy deposition in the detector pixels hence result in larger fluctuations in the reconstructed WET as compared to the steep regions of this conversion curve.

Images of such density resolution require a rather high dose deposition of some tens of mGy inside the object to be imaged. Especially the entrance dose at the front surface of the phantom is prohibitively large (see figure 8.8d). Above all, in biomedical applications low imaging doses are usually desired. In the current setup, a further expansion from radiographic to tomographic imaging, where several projections are needed, might therefore only be an option for objects that are insensitive to radiation dose.

Nevertheless, dose reduction down to biologically acceptable values while still maintaining a decent image quality might be possible. The high dose is a result of the exponential-like energy spectrum of the laser-driven ion source. In order to entirely penetrate a 0.5 mm thick water phantom, proton energies $\gtrsim 6\,\text{MeV}$ are required. However, more than two third of the protons from the input spectrum have a kinetic energy below 6 MeV and will therefore not contribute to the signal for reconstruction. Removing all protons with kinetic energies lower than 5 MeV before reaching the spectrometer would hence lead to a dose reduction by almost 50%, while the image quality would not be affected at all. This beam hardening could be achieved either actively by a magnetic chicane or passively by additional absorbing material prior to the phantom. Of course, the latter approach will also impact the image quality due to scattering inside the absorber.

In applications where reduced image quality is acceptable, proton fluence and hence the dose can easily be reduced by a factor of 10. The resulting RMSE is within 10%, thus moderate density or thickness differences in the object can still be detected. The most reliable method to reduce the fluence in an experiment at a laser-driven ion source would be to shift the imaging device further away from the source. Comparable doses as reported by Jee et al. [2017] for time-resolved dose measurement (see section 3.2) could hence be realistic for a similar quality of the radiographs, taken with one single laser-accelerated proton bunch.

The spatial resolution of proton radiography is mainly limited by MCS inside the object, as also discussed in Zygmanski et al. [2000]. Distances between phantom and imaging detector should therefore be as small as reasonably achievable. A good compromise between spatial resolution and experimental applicability for the here presented imaging of thin phantoms with macroscopic inhomogeneities might be a distance of 5 mm. This distance still allows to resolve structures as small as 0.2 mm.

Considerations for the Spectrometer Resolution

The divergence of the proton beam gives rise to a non-uniform proton field at the phantom. At a distance of $1\,\mathrm{m}$ and a full beam divergence angle $\theta = 5°$, this results in a fluence variation of up to 2.5% within a $2 \times 2\,\mathrm{cm}^2$ plane. Although the assumption of a constant fluence within this area gives rise to an only modest additional error in the reconstructed WET values ($< 3\%$), more accurate results are obtained if the spectrometer itself is pixelated. The required pixel size strongly depends on the beam divergence angle and the geometry of the setup, namely the desired FOV and the source-to-phantom distance. For divergence angles down to $\theta \approx 5°$, a distance of source to imaging setup of $1\,\mathrm{m}$ and a FOV of the same size as the sensitive area of the Timepix detector, a pixel size of $4 \times 4\,\mathrm{mm}^2$ is sufficient to keep the impact of the non-uniform proton field low. With a FOV of the size of the Timepix detector, this would hence result in 16 channels for which the TOF signal has to be acquired and converted to an energy spectrum independently. Alternatively, the use of a strip detector as transmission TOF spectrometer could prove beneficial, if the fluence distribution is cylindrically symmetric. The latter approach would tremendously reduce the number of channels to be read out and evaluated. Also, the spatial fluence distribution could potentially be determined by an additional detection system that does not interfere with the imaging setup. If acquired that way, the fluence variation in the FOV can easily be corrected for in the WET reconstruction.

For the setup and the energy range presented in this study, a temporal resolution of the TOF spectrometer of $0.2\,\mathrm{ns}$ appears to be sufficient for WET reconstruction with both precision and accuracy better than 5%. Neglecting effects of spatial inhomogeneities in the proton field, this result would also be applicable to a reduction of the drift space from $1\,\mathrm{m}$ down to $0.25\,\mathrm{m}$ when keeping the temporal resolution at $0.05\,\mathrm{ns}$. Equivalently, increasing the drift space to $4\,\mathrm{m}$ loosens the requirements in the data acquisition system in a way that a sampling time of $0.2\,\mathrm{ns}$ would be sufficient for a precision and accuracy better than 3%. It has to be stressed, though, that in this MC study the detector response was assumed to be instantaneous and the finite detector response was hence not taken into account.

Limitations of this Setup and Possible Solutions

Despite the promising results in terms of spatial and density resolution, an experimental imaging setup using a laser-driven proton source and based on the Timepix detector hardly seems feasible. Up to this point, the detector was assumed to have an unlimited dynamic range which obviously is not the case for a real detector. The Timepix detector on which the simulation is based saturates at $\sim 7.35\,\mathrm{MeV}$ energy deposition inside each detector pixel, for the current threshold settings. As already discussed in section 7.3.5, linear response of the detector only holds until $\sim 0.85\,\mathrm{MeV}$. For a broad proton energy distribution as expected in this study, this corresponds to a fluence at the detector of $\Phi_{\mathrm{sat}} \sim 4 \times 10^4\,\mathrm{cm}^{-2}$, or $5 \times 10^3\,\mathrm{cm}^{-2}$ taking into account the threshold for linear response.

A potential solution to circumvent saturation of the detector even for the thinnest insert phantom could be to assure a maximum fluence of $\Phi \sim 2 \times 10^5 \, \mathrm{cm}^{-2}$ at the spectrometer by further increasing the distance to the proton source. This would reduce the proton fluence per shot at the cost that around 50 proton bunches and thus, laser shots, would be required for one radiography with a NRMSE below 3%. Of course, this would result in a prohibitively long time required for imaging.

Although not studied here, a non-negligible signal in the Timepix detector, caused by energy deposition by electrons and x-rays which are also produced in the laser-plasma interaction, has to expected due to the detector relatively thick SV. On the one hand, this will most likely decrease the image quality. On the other hand, the electrons and x-rays, but also heavier ions which due to their higher energy loss than protons for the same velocity cannot entirely penetrate the phantom, will notably increase the dose deposition inside the object. However, this problem could potentially be avoided or at least minimized by active beamline elements like the previously mentioned magnetic chicane.

Furthermore, the lateral energy distribution is assumed to be constant in this study. According to experimental studies, the higher energy components are situated closer to the central beam axis [Snavely et al., 2000]. The previously drawn conclusions on the spectrometer pixel size may therefore not be entirely reliable. Also, if additional active beamline elements are included in an experimental setup, the lateral energy and fluence distribution at the imaging setup might have larger variations. It is therefore crucial to either have a reliable model of the proton bunch at the location of the phantom, or to determine the spectrum with a fine spectrometer pixel size.

Moreover, the simulation setup was entirely placed in vacuum. Since imaging of biological samples usually needs to be conducted in air, the proton beam has to pass an additional vacuum window before reaching the imaging setup. The effects of imaging in air will be addressed in the following section with a different setup.

8.4 Simulation Setup using the RadEye Detector

8.4.1 Overview

Since the major shortcoming of the first simulation setup is the low proton fluence required to avoid saturation of the relatively thick Timepix detector, the latter was replaced by the thinner CMOS based detector RadEye in the following study. All other objects, distances and dimensions are the same as in the previous study.

The RadEye detector has already been extensively and successfully used for characterization of laser-accelerated ions and electrons [Reinhardt et al., 2013; Lindner et al., 2018] and has proven to withstand the harsh environment in the proximity of laser-plasma experiments. The dynamic range of this detector is 4096 ADU. According to previous calibration measurements resulting in a conversion of (1.09 ± 0.12) ADU/keV [Reinhardt,

153

2012], this corresponds to a maximum energy deposition in the SV of one pixel of around $(3.76 \pm 0.42)\,\text{MeV}$. Another advantage of the RadEye is the larger detector area of $5 \times 2.5\,\text{cm}^2$ and the possibility to further enlarge the detection surface by linking several sensor modules on three possible sides. However, this advantage was not exploited in the present study as the size of the spectrometer was kept the same as in the previous setup. Nevertheless, enlarging the area of spectrometer, phantoms and imaging detector could be adapted in a straightforward manner, provided that the lateral proton fluence distribution is monitored. No considerable changes have to be expected in the obtained image resolution.

For many applications, bringing the object of interest into vacuum is not feasible. Therefore, in a second part of this section, the above described simulation geometry was modified in order to mimic a potential experimental setup in air. Therefore, a $50\,\mu\text{m}$ thin Kapton foil was added $1\,\text{cm}$ upstream of the spectrometer as vacuum window. The vacuum surrounding the phantom and the detector behind the Kapton window was replaced in the simulation geometry by dry air with a density of $1.2 \times 10^{-3}\,\text{g cm}^{-3}$. The additional energy loss in the Kapton foil and the air gap between foil and spectrometer were subtracted from the energy bins in the spectrum reconstruction, as described in section 8.2.1.

In the third part of this study, the extension of this radiographic setup to higher proton energies up to $100\,\text{MeV}$, as expected at CALA after the energy upgrade of the ATLAS laser, is briefly studied. While the air gaps between Kapton window and spectrometer, spectrometer and phantom, as well as between phantom and RadEye detector were not modified, the distance between proton source and spectrometer was increased to $3\,\text{m}$. This distance is also realistic for potential experiments and results in a still acceptable energy resolution of the reconstructed proton spectrum when keeping the time binning of the spectrometer fixed at $0.05\,\text{ns}$. The look-up tables required for spectrum reconstruction, incorporating energy losses in $10\,\mu\text{m}$ silicon, $50\,\mu\text{m}$ Kapton and $10\,\text{mm}$ air were extended, featuring proton energies up to $100\,\text{MeV}$. Similarly, also the look-up table containing $\langle E_{\text{dep}}(2\,\mu\text{m Si}; E_{\text{kin}}; \text{WET})\rangle$, as shown in figure 8.5(b,d,f), was enlarged to include energies up to $100\,\text{MeV}$ and water thicknesses up to $40\,\text{mm}$. Again, the additional vacuum window and air upstream of the spectrometer were taken into account in the spectrum reconstruction.

8.4.2   Results

Part of the results obtained in section 8.3.2 are also valid for this modified setup and are therefore not explicitly shown and discussed hereafter. In particular, these results refer to the dependence of the spatial resolution on the phantom-detector-distance, as well as the impact of both spatial and temporal resolution of the spectrometer on the image quality. In the following, results are presented which are specific to the three new considered setups and scenarios.

(a) 2D WET distribution

(b) 1D WET profile

(c) 1D WET profile
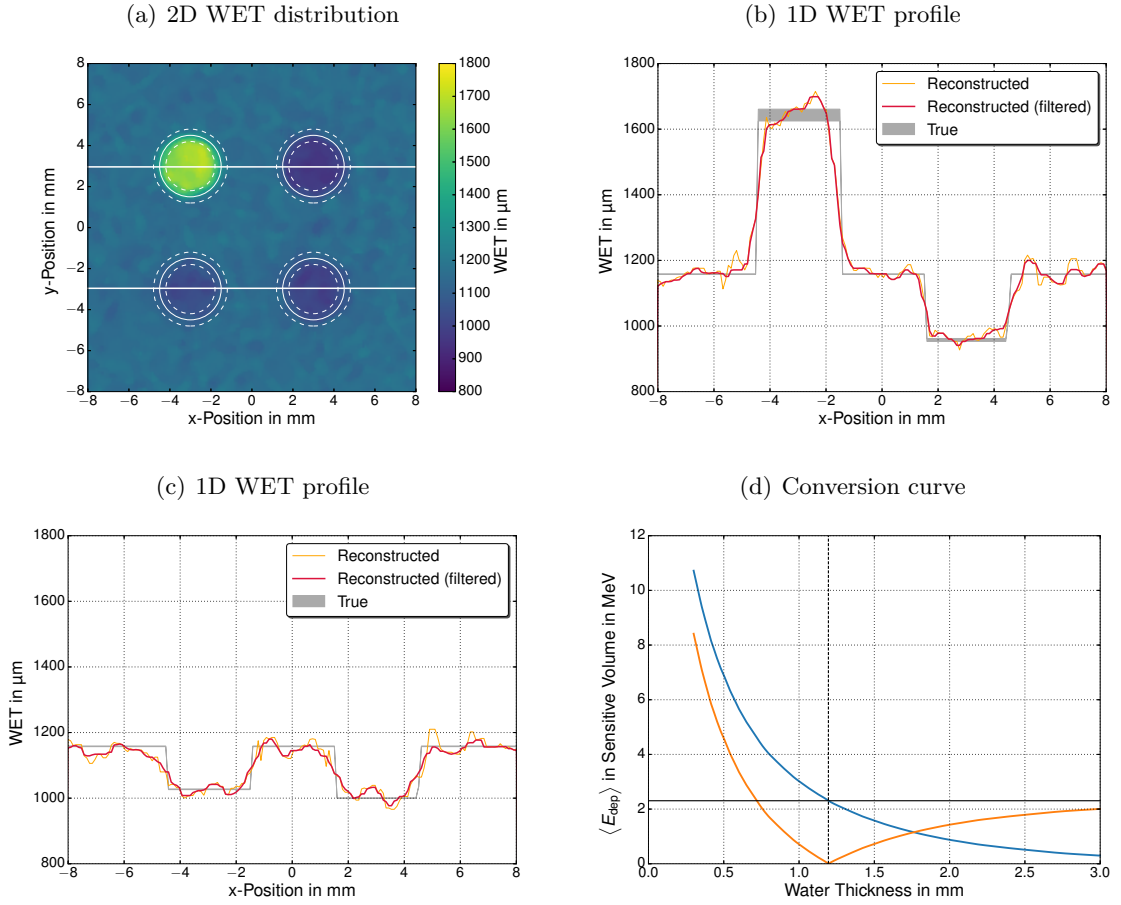
(d) Conversion curve

Figure 8.16: Reconstructed WET of the insert phantom in the RadEye radiography setup for 10^9 primaries. The 2D distribution is shown in (a), 1D profiles are plotted in (b) and (c). Line colors in (a-c) have the same meaning as in figure 8.8. In (d), the conversion curve from energy deposition inside one exemplary RadEye pixel to the corresponding WET value is shown (blue). The simulated energy deposition within that pixel is shown by the horizontal, black line. The absolute difference between both curves is shown in orange. The minimum of the orange line corresponds to the obtained WET, indicated by the vertical dashed line.

WET Reconstruction in Vacuum

Depending on the traversed material, the mean number of protons per detector pixel at a primary proton number of 10^9 and the 1 mm thick insert phantom ranged between 11 and 27, corresponding to a fluence of $4.8 \times 10^5 - 1.2 \times 10^6$ protons/cm^2. With only 2 μm sensitive thickness, statistical fluctuations in the energy deposition within each pixel of the RadEye detector are large. For this reason, as well as for computational reasons, 2×2 adjacent pixels were combined to one macro-pixel with a pixel size of 96×96 μm^2. Thus, about 44 to 108 protons per 10^9 primaries contribute to the signal in one macro-pixel of the RadEye detector. Moreover, a median filter was applied to the energy deposition in the detector prior to WET reconstruction in order to further minimize the effect of statistical fluctuations. The energy deposition within the imaging detector was below the saturation limit of the RadEye detector for all primary particle numbers and phantoms

155
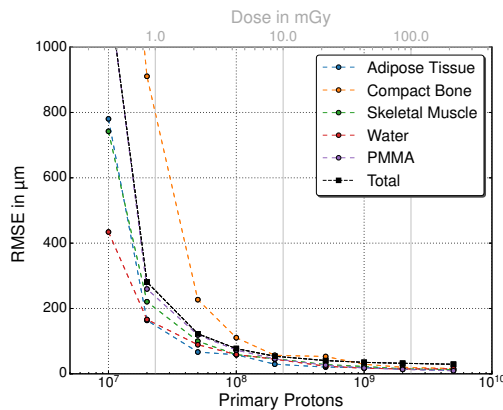
Figure 8.17: Assessment of the image quality as a function of imaging dose for the RadEye radiography setup for the 1 mm thin insert phantom in vacuum. The RMSE of the reconstructed WET of the total object (black) and the different materials (colors) are plotted versus the number of primary particles (lower axis) and the corresponding dose (upper axis). The dashed lines are to guide the eye.

investigated in this study.

The reconstructed 2D WET distribution with two 1D profiles is shown in figure 8.16a-c for 10^9 primary protons. Within all five ROIs, the average reconstructed WET differs by less than 1.5% from the true WET and the NRMSE is below 3%. The global NRMSE for a FOV the size of the spectrometer was found to be 3.5%.

Since there are no additional absorbers prior to the phantom as compared to the first setup, the dose deposition remains the same ($D = 43 \, \text{mGy}$ for the 1 mm thick insert phantom). A further decrease in the primary particle number results in rapidly increasing RMSE values and differences between the average reconstructed WETs and true WETs, which can be seen in figure 8.17. At 10^8 primaries, the reconstructed WET differs by up to 4.4% from the true WET and the NRMSE approaches 7%.

WET Reconstruction in Air

The additional tabulated energy losses inside the Kapton foil and the air gap between foil and spectrometer introduce a further source of uncertainty to the spectrum reconstruction (see figure 8.18a). However, these differences are most pronounced at proton energies below 5 MeV, which for the phantom thickness used in this study do not contribute to the signal in the imaging detector.

The proton number is kept at 10^9 primaries, given that no excess of the detector dynamic range and a satisfactory density resolution can be expected.

When taking into account the 10 µm WET of the additional 1 cm air between spectrometer and RadEye detector, the difference between the mean reconstructed WET and the true WET is still well below 1.5% for the five respective materials. Also the RMSE values for the ROIs ($< 3\%$), as well as the global NRMSE (3.4%) are hardly affected by the additional Kapton foil and air. Moreover, no significant difference in the spatial resolution was found between the setup in vacuum ((2.4 ± 0.5) lp mm^{-1}) and in air ((2.4 ± 0.3) lp mm^{-1}).
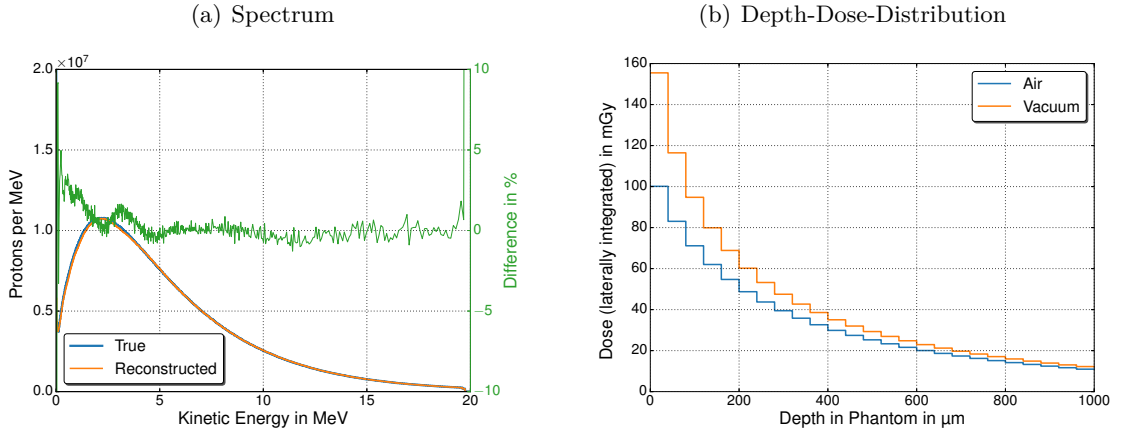
Figure 8.18: Reconstructed energy spectrum and depth-dose distribution for the RadEye radiography setup in air. In (a), the reconstructed proton energy distribution is compared to the true proton spectrum, similar as in figure 8.4. The depth-dose distribution inside the phantom is compared in (b) between the air-filled radiography setup (blue) and the setup in vacuum (orange).

In contrast, the additional material in the beam path results in a hardening of the incoming spectrum. This reduces the imaging dose by more than 20%, as compared to the imaging setup in vacuum. Depth-dose curves for the 1 mm thin insert phantom are shown for the vacuum and the air-filled setup in figure 8.18b.

Radiography at Higher Proton Energies (CALA)

When going to proton energies up to 100 MeV, corresponding to expectations for laser-ion acceleration experiments that will be performed at CALA, thicker phantoms become more relevant. Simulations of the imaging setup in air were performed with 10^{10} exponentially distributed primary protons. The mean proton number reaching the detector macro-pixels was then ranging between 40 and 110, depending on the traversed material. The numbers are hence comparable to the fluence at the detector obtained in the vacuum simulation setup at lower proton energies. Nevertheless, radiation dose delivered to the phantom was reduced down to 13.7 mGy.

The reconstructed WET distribution and the energy spectrum are shown in figure 8.19. Although the different inserts can clearly be distinguished, an increased blurring of the image is evident. This is due to the larger impact of scattering within the phantom as compared to the thinner phantoms previously investigated. The spatial resolution at high energies, determined using a 2.0 to 2.3 cm thick step phantom, was found to be $(1.9 \pm 0.6)\,\mathrm{lp\,mm^{-1}}$ for a distance between phantom and RadEye of 5 mm. Therefore, the margin defining the ROIs was increased to 0.5 mm.

The global RMSE was 0.86 mm, corresponding to 4.2% of the geometrical phantom thickness, while the NRMSE values within the ROIs were found to be small $(1.8\% - 2.3\%)$. Although still sufficiently low, the largest NRMSE was found for the bone insert. This can easily be explained by the increased scattering, lowering the reconstructed WET of

(a) 2D WET distribution

(b) 1D WET profile

(c) 1D WET profile

(d) Proton energy distribution
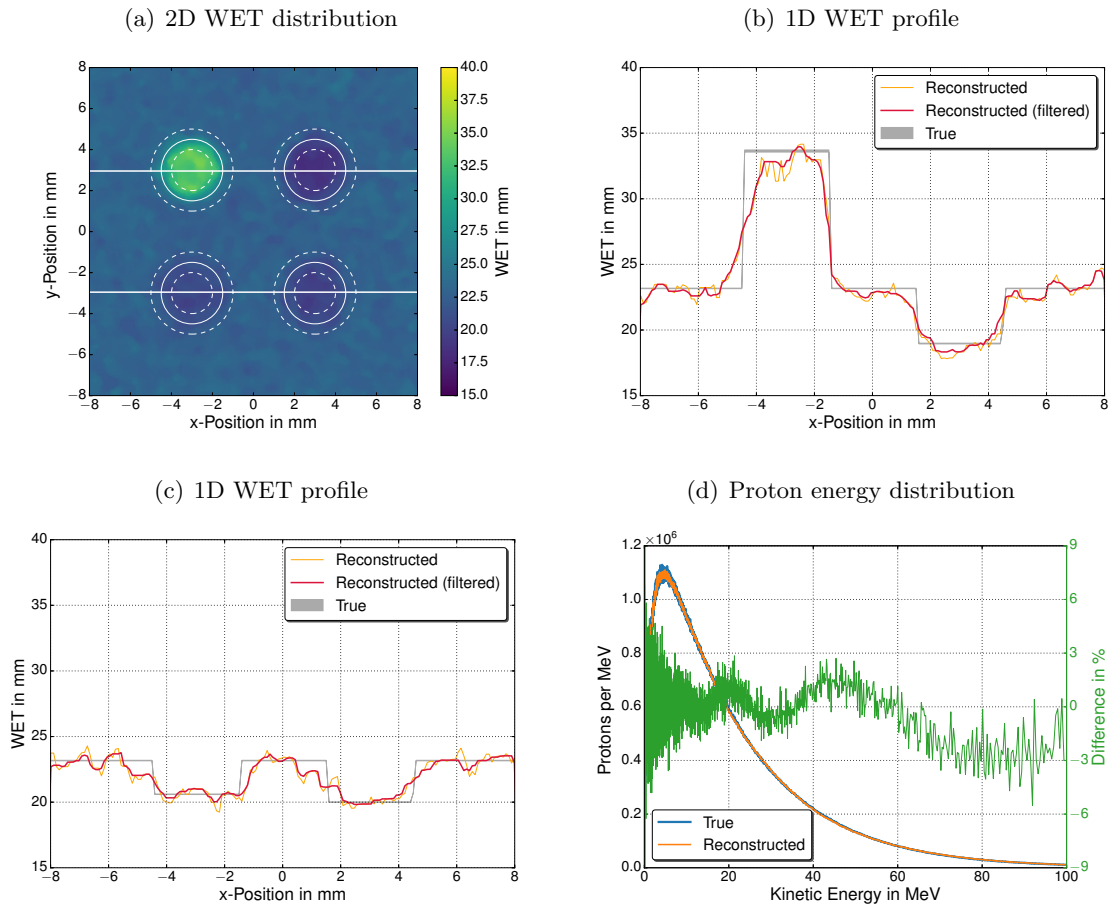
Figure 8.19: Reconstructed WET of the $2\,\text{cm}$ thick insert phantom in the RadEye radiography setup for higher proton energies. The primary particle number is 10^{10}. The 2D distribution is shown in (a), 1D profiles through the inserts are plotted in (b) and (c). The meaning of the colors is the same as in figure 8.8. In (d), the reconstructed proton energy distribution is compared to the true spectrum, similar as in figure 8.4.

the bone insert close to the interface with water. Agreement between the mean WET in the ROIs and the true WET for higher proton energies was found to be better than 1.1%.

8.4.3 Discussion

The main advantage of an imaging setup based on the RadEye detection system is the increased dynamic range of the detector as compared to the imaging setup relying on the Timepix detector. The higher saturation limit is an absolute requirement for radiography using laser-accelerated proton bunches, given the huge particle fluxes. The simulated energy deposition inside the detector pixels was found lower than the saturation limit, even for the highest simulated primary particle number which would correspond to up to 135 protons per pixel or $6 \times 10^6\ \text{protons/cm}^2$.

To avoid large fluctuations of the reconstructed WET values, caused by the relatively low particle number per pixel and the low detector thickness, 2×2 pixels were grouped

together for further evaluation. With this approach, the RMSE values obtained in this imaging setup were found comparable to the results from the Timepix radiography setup.

Although not performed within this simulation study, the larger area of the detector could potentially be exploited to image larger samples. Several sensor modules could be attached almost edge-less, resulting in FOVs of several tens of cm^2. Of course, this also implies that a spectrometer with a correspondingly larger area would be required.

When moving the imaging setup from vacuum to air, hardly any relevant degradation of the image quality in terms of density resolution was encountered. Additional scattering in the air gap between the phantom and imaging detector can therefore be neglected for a distance between phantom and detector of 5 mm. However, it would further increase with larger distances. On the other hand, beam hardening considerably reduces the imaging dose while practically preserving the image quality at distances between phantom and detector as low as 5 mm. The hardening of the spectrum is due to low-energy protons that are already absorbed or large-angle scattered inside the Kapton foil and air, before they eventually reach the phantom and deposit their energy close to its front surface.

For phantom thicknesses of some centimeters, corresponding to potential small-animal irradiations, proton energies up to 100 MeV are required. Increased scattering inside the phantom itself results in substantially larger image blurring, which is most pronounced at the interfaces between high- and low-WET material. Although the spatial resolution, quantified in linepairs per mm, decreases for the thicker phantom, sub-mm resolution was still obtained with an air gap between phantom and detector of 5 mm. With a larger margin defining the ROIs to take into account the increased scattering at the cost of smaller ROIs, the correct WET could still be assigned to the respective insert materials. However, an iterative reconstruction method accounting for scattering inside the phantom could potentially improve the image quality in terms of spatial resolution.

Due to the method to create the look-up tables for WET reconstruction, large-angle scattering and fluence reduction due to nuclear reactions are inherently taken into account in the reconstruction. However, it has to be stressed that the look-up table is based on the assumption that the proton fluence is laterally homogeneous over an area that is large compared to the pixel size. This will certainly be not true close to the interfaces between materials with huge WET differences, e.g. between the phantom and air.

In laser-ion acceleration, x-rays, gammas, fast electrons and heavier ions are typically co-emitted with the proton bunch. No detailed investigations were performed within this study to assess their impact on the final image quality. For the same energy per nucleon, the energy loss rate is considerably larger for ions heavier than protons. The number of heavy ions having a sufficiently high energy to traverse the object to be imaged can therefore assumed to be small. Nevertheless, provided that different ions can be distinguished within the spectrometer, their additional signal in the imaging detector could be accounted for by including their energy deposition versus water thickness to the conversion curves. This correction method is not possible for x-rays and gammas.

However, the RadEye sensor is rather insensitive to photons in that energy range due to its sensitive thickness of only $2\,\mu m$. According to MC simulations, the range in water of $10\,MeV$ electrons is around $5\,cm$. Hence, signal contribution by electrons could be more critical for quantitative imaging. An almost complete removal of electrons from the mixed particle beam could be achieved by including a dipole magnet with a very shallow magnetic field (e.g. $50\,mT$) perpendicular to the beam direction, upstream of the imaging setup. Such magnetic field over a dipole length of $10\,cm$, followed by a drift space of $10\,cm$ prior to the spectrometer would lead to a a lateral displacement of $10\,MeV$ electrons of $21.6\,mm$, while the displacement of protons in the other direction is $2.3\,mm$ and $1.2\,mm$ for $5\,MeV$ and $20\,MeV$, respectively. Given the broad proton field, a continuously decaying conversion curve for the WET reconstruction is still maintained since the displacement differences for protons in the energy range of interest is small.

Of course, the assumption of a laterally homogeneous proton energy distribution would then be corrupted and a pixelated spectrometer would be required. Nevertheless, the necessity of such dipole magnets needs to be studied based on measured absolute proton and electron distributions in the laser-accelerated particle bunches. If required, a more detailed simulation study based on these numbers could provide important information for a proper choice of the magnetic field strengths, positions and distances.

8.5 Summary & Conclusion

A detailed MC simulation study was performed to assess the feasibility of laser-driven proton radiography using two different silicon-based pixel detectors and a silicon TOF spectrometer in transmission prior to the phantom. The principle of WET reconstruction is based on a monotonically decreasing detector signal versus traversed depth in water, as it would result naturally from typical TNSA proton spectra.

The first setup consisted of the Timepix, while the second setup was based on the RadEye detector. Excellent WET resolution was obtained for both imaging detectors for a proton fluence at the imaging setup around $10^6\,protons/cm^2$. The agreement between mean reconstructed WET inside studied ROIs with the corresponding true WET was always below 1.5% and the NRMSE was typically within 3%.

Spatial resolution of proton imaging is limited by MCS within the phantom. Therefore, thicker phantoms and larger distances between the phantom and the imaging device deteriorate the spatial resolution. For a phantom thickness between 0.3 and 0.66 mm, sub-mm resolution was found for distances up to $20\,mm$. At experimentally reasonable distances of $5\,mm$, a spatial resolution of $\sim 5\,lp\,mm^{-1}$ was found for such thin phantoms. For a phantom thickness of $2\,cm$ and proton energies up to $100\,MeV$, the spatial resolution was still around $2\,lp\,mm^{-1}$. Moreover, no significant difference was found for both the spatial and the density resolution between the imaging setup in vacuum an in air.

Due to its relatively low saturation limit, the usability of the Timepix-based imaging setup

is limited to proton fluences that are far below fluences obtained in laser-ion acceleration experiments. Only the second investigated setup based on the RadEye detector may therefore be applicable for radiography with laser-accelerated proton bunches.

The major drawback of using such a broad proton energy distribution with exponentially decaying shape is the high dose which is required to obtain the high spatial and density resolution mentioned before. This limits the presented method to applications, where the dose to the object is not of concern. This becomes even more severe when tomographic imaging, requiring multiple projections from different angles, is desired. A dose reduction in the order of 50% while maintaining the image quality can only be obtained by modification of the energy spectrum, i.e. reducing the number of protons with an energy that is insufficient to cross the object of interest. Additional absorbers, like a thin foil that is anyway required as vacuum window when imaging in air, can reduce the dose close to the front surface of the phantom by more than 20% while hardly affecting the overall image quality.

The impact of the mixed radiation field on the reconstructed WET images was not investigated in detail in this study. While the influence of heavy ions, x-rays and gammas is estimated to be small, it seems possible that highly relativistic electrons could deteriorate the image quality. More detailed investigations based on measured electron spectra would be required to judge whether changes in the setup are required. For instance, the use of a very moderate magnetic field perpendicular to the beam direction could potentially solve this problem.

8.6 Outlook: Proof-of-Principle Experiments using an Energy-Modulated Proton Beam

The MC simulation study was based on available imaging detectors and aims for a practicable implementation in the near future. To this aim, this outlook presents first experimental results on proton radiography obtained using a passively energy-modulated proton beam (see section 4.3.1) at the Munich Tandem accelerator. A more general outlook comprising ideas beyond the possibilities of the investigated imaging setups will be given in the following chapter.

The entire experimental setup was placed inside a vacuum chamber, which was flange-mounted to the beamline with a $50\,\mu\text{m}$ thin Kapton foil separating the beamline vacuum ($p_{\text{BL}} \sim 10^{-7}\,\text{mbar}$) from the vacuum in the experimental chamber ($p_{\text{VC}} \sim 10^{-5}\,\text{mbar}$). One RadEye sensor in the Remote RadEye configuration (see section 4.2.3) was used as imaging detector. Thin ($d \approx 1\,\text{mm}$) 3D printed plastic phantoms were mounted on a horizontal motorized stage, such that the distance between phantom and detector was $3\,\text{mm}$. The phantom to be presented in the following had four trenches forming the letters *L*, *M* and *U* and a horizontal bar. The depth of these trenches was 80, 160, 240 and $120\,\mu\text{m}$ with respect to the $1\,\text{mm}$ substrate. A photograph of the experimental setup is
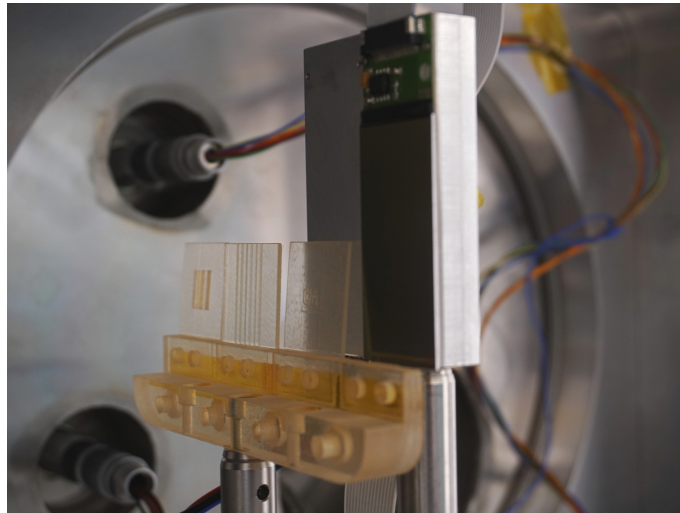
Figure 8.20: Photograph of the experimental setup for proton radiography at the Tandem accelerator. The yellowish transparent objects are phantoms mounted on a horizontal motorized stage.

shown in figure 8.20. Using the motorized stage, *open-field images*, i.e. images in absence of the phantom were additionally obtained. Also, dark frames were taken prior and after the imaging and were subtracted from the averaged beam-on image to account for the leakage current of the detector.

Unlike in the simulation study, the energy spectrum was obtained offline prior to the radiography experiments using a magnetic spectrometer as described in section 6.2.1. The measured proton energy distribution is shown in figure 8.21a.

The background-corrected, averaged radiography (figure 8.21c) was divided by the open-field image to account for the inhomogeneous lateral proton fluence in the FOV, resulting in a detector signal relative to the open-field (figure 8.21d). A conversion curve from relative detector signal to WET was created using the measured spectrum and the previously presented MC based look-up table (figure 8.21b). The mean relative detector signal within a small region behind the 1 mm substrate (WET = 1.096 mm) was used to scale the conversion curve accordingly.

The reconstructed WET distribution, where the three letters and the horizontal bar can nicely be seen in different shades of green, is shown in figure 8.21e. Although this reconstructed image relies on offline spectrum measurements and the knowledge of the detector signal for one given WET value (the substrate), it shows nicely the feasibility of this experimental imaging setup for proton radiography using a broad energy distribution. It is capable to resolve structures of sub-mm size and WET differences of $\sim 4\%$ can be distinguished. Further radiographic measurements at a laser-driven ion source are therefore foreseen to be performed in the near future, using the setup investigated in this chapter based on the RadEye detection system.
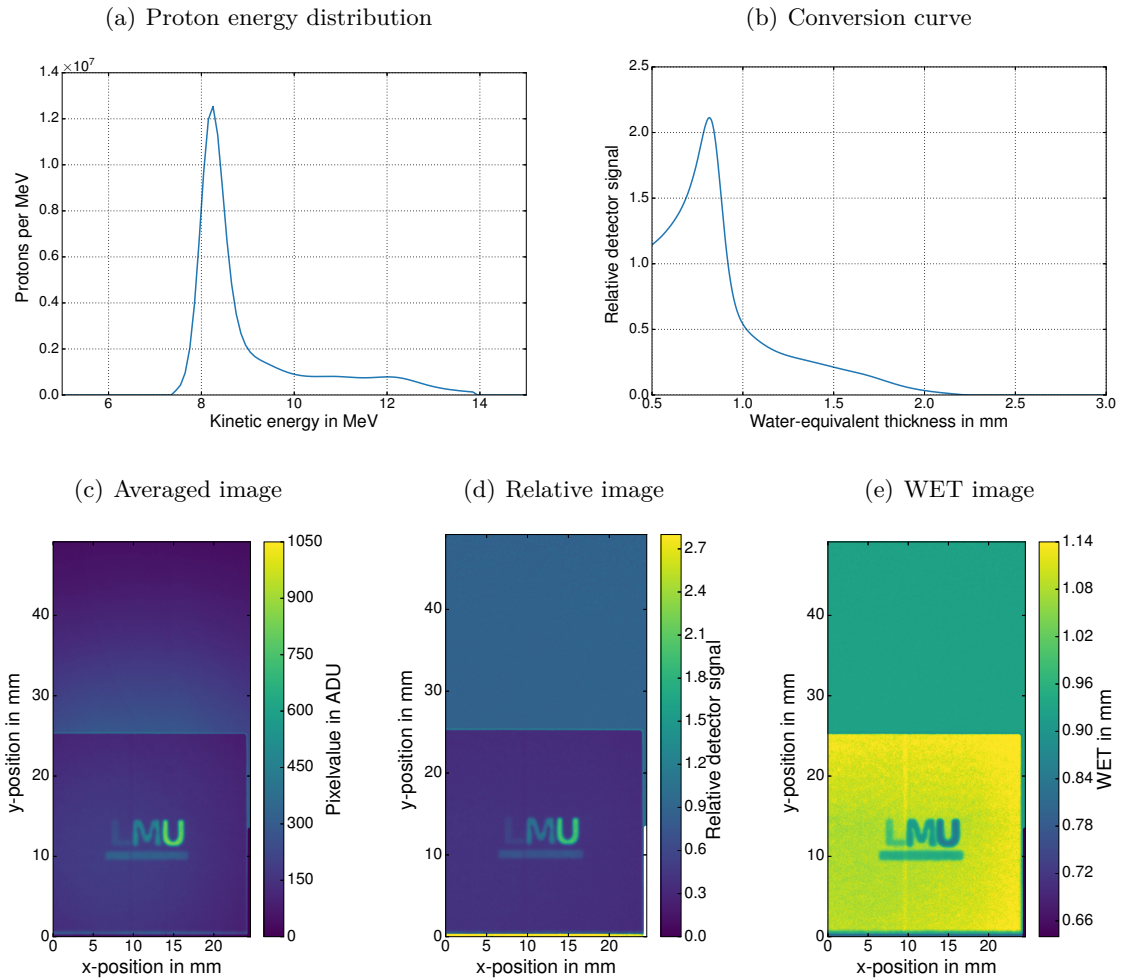
Figure 8.21: Experimental results for radiography using a passively energy-modulated proton beam from the Tandem accelerator. The energy distribution, measured offline using a magnetic spectrometer is shown in (a). The resulting conversion curve relating relative detector signal to traversed water thickness is plotted in (b). In (c) and (d), the detector image averaged over several image frames and the detector image divided by the open-field image are shown, respectively. Finally, (d) shows the reconstructed WET distribution.

Summary & Outlook

In several recently installed and upcoming research centers worldwide, multi-TW and PW laser systems are dedicated to the acceleration of ions from a laser-induced plasma. Kinetic energies of such laser-accelerated ions are approaching 100 MeV/n. Moreover, the transit from single-shot experiments to moderately high repetition rates ($\sim 1\,\mathrm{Hz}$), along with developments dedicated to beam focusing and guidance, give rise to a broad range of possible new applications. One field of interest is radiobiological studies in small-animal models. Such studies would highly benefit from accurate and precise dosimetric devices operating in parallel to an irradiation, as well as from radiographic or tomographic imaging of the object.

Due to the unique properties of laser-accelerated particle bunches, diagnostics commonly used in e.g. clinical ion beam facilities are not suitable for accurate characterization of such beams. The main detection devices in contemporary laser-ion acceleration experiments are still based on offline methods, such as nuclear track detectors (CR-39), IPs or RCFs. Within the past decade, many developments of online detection system have been proposed, showing interesting features on the one hand and shortcomings on the other hand. However, to this date no online diagnostic device is available, capable to accurately determine spatially resolved energy spectra of laser-accelerated ion bunches on a shot-to-shot basis and, above all, in parallel to an application.

9.1 Spectrometry of Laser-Accelerated Ion Bunches

Two approaches for characterization of laser-accelerated proton bunches in terms of energy spectrum have been investigated within the framework of this thesis. Prototype systems have been developed and were tested at a conventional electrostatic proton source. Experiments at a laser-driven ion source at LEX Photonics were performed for one of the two setups.

The first detection system is based on a thin silicon detector and is used to measure the TOF signal generated by the temporally divergent polyenergetic proton bunches. A

detailed preparatory study has been performed assessing the suitability of the detector and subsequent readout electronics, based on its radiation hardness and temporal characteristics. The properties found for the so-called Bridge microdosimeter have shown to be promising for TOF spectrometry experiments in the energy range of protons up to 20 MeV and to some extent even for higher energies.

To extract the absolute energy spectrum from the measured TOF signal current, a dedicated reconstruction method was developed. In contrast to TOF measurements of laser-accelerated ion bunches which had previously been published by other groups, the approach presented within this thesis explicitly takes into account the temporal response function of the detection system. This is essential, as TOF differences of protons in the (near-)relativistic energy range are in the same time scale as the detector response.

The approach was validated using an energy-modulated proton beam from a conventional electrostatic accelerator in the energy range up to 20 MeV and with ns-short proton bunches. Agreement between reconstructed energy distributions and the spectrum as expected from Monte Carlo simulations and measurements using a magnetic spectrometer was found very promising. Measurements were also performed at LEX Photonics using laser-accelerated proton bunches from thin target foils. TOF signals were acquired for an unperturbated TNSA spectrum, as well as for a focused proton beam. Despite the dominant high frequency noise caused by the EMP, reasonable agreement was found between the reconstructed spectrum using the TOF approach and measurements using the WASP or analytical calculations for an unfocused beam and for a beam focused by a pair of PMQs, respectively.

In a second spectrometric setup, the hybrid pixel detector Timepix was used in edge-on configuration, i.e. protons pass a thin collimator slit and impinge the sensor chip at its edge, penetrating parallel to the face of the chip. Besides information of the penetration depth in the sensor chip, which is related to the kinetic energy of the particle, spatial information along one axis perpendicular to the beam propagation direction is available with high resolution.

This edge-on spectrometry setup was calibrated at the Tandem accelerator with proton energies from 17 to 20 MeV and a reduced beam current, such that individual protons tracks were detected and could be extracted for creating an average model track for each proton energy. Based on these model tracks, a reconstruction method solving a linear least-squares problem was developed to obtain the initial energy spectrum from the measured signal. Since the approach is based on average proton tracks, more than 100 protons on the sensor chip are required to perform spectrum reconstruction with no spatial information but low statistical uncertainty. Maintaining the spatial information requires larger proton track numbers. However, this conflicting with the relatively low saturation limit of 7×10^3 protons/c^{2}m of the Timepix detector in edge-on configuration. Nevertheless, the presented method and technique itself could be applied to different detector types providing higher saturation limits.

Despite the very promising results obtained within this study, especially concerning the TOF approach, this was only one further step towards the development of a spatially resolved online monitoring system for laser-accelerated ion bunches providing spectral information on a shot-to-shot basis and in parallel to any application. The capabilities of the TOF approach have been shown for a thin silicon detector, which due to its segmentation could already provide some spatial information. Up to the limiting silicon wafer size, there is no reason why a detector composed by a larger number of segments cannot be produced. Moreover, the manufacturing techniques for reduction of the support substrate of the detector is available. Thus, the design and production of such pixelated, thin and large-area silicon detector is feasible and that project may be tackled within the following years. In the meantime, the previously mentioned U3DTHIN detector is a potential candidate to be used as online beam monitoring device, but without spatial information. Of course, studies investigating the actual performance of this detector for characterization of laser-accelerated ion bunches remain to be done.

9.2 Radiographic Imaging with Laser-Accelerated Ion Bunches and Beyond

A detailed Monte Carlo simulation study assessing the feasibility and the performance of laser-driven proton radiography was conducted in the framework of this thesis project. The study was based on typical proton spectra obtained in the TNSA regime with upper cutoff energies of $20\,\mathrm{MeV}$ and $100\,\mathrm{MeV}$. As quantitative transmission imaging with protons requires knowledge of the particle number and energy, a pixelated silicon spectrometer was modeled and used in transmission mode to determine the spectrum following the TOF technique. Phantoms composed by different tissue materials, water and PMMA and with thicknesses tailored to above mentioned the proton energies were exposed to the divergent polyenergetic beams downstream of the spectrometer. The thickness of the phantoms was up to $2\,\mathrm{mm}$ for the lower proton energy range and up to $23\,\mathrm{mm}$ for higher energies. The energy deposition of protons with a kinetic energy sufficient to entirely penetrate the phantom was measured in one out of two simplified models of actual pixel detectors (Timepix and RadEye). However, only the RadEye detector provided a sufficiently large dynamic range to be used for transmission proton radiography.

Using the information obtained from the online spectrometer, a calibration curve relating the signal in the imaging detector to the water-equivalent thickness of the traversed phantom was created during runtime of the image reconstruction for each detector pixel individually. Both for the low- and the high-energy proton source and regardless if the setup was in vacuum or air, sub-mm spatial resolution and a density resolution better than 3% was found for a particle fluence at the detector of around $10^6\,\mathrm{protons/cm^2}$. Yet, rather high dose values to the phantom (tens of mGy) were encountered for such image quality. Dose reduction would require a manipulation of the incoming proton spectrum

by reducing the number of low-energy protons.

Since spatial resolution is mainly affected by multiple Coulomb scattering inside the object to be imaged, the image quality decreases with thicker objects and larger distances between object and imaging detector. A distance of 5 mm has shown promising results and seems to be a realistic distance for future experiments.

All in all, according to the performed simulation study, the radiographic imaging setup based on the RadEye detector shows great potential to be implemented at a laser-driven ion source. First proof-of-principle experiments have already been performed with an energy-modulated proton beam at the Munich Tandem accelerator and satisfactory WET images have been obtained. Although the impact of high-energy electrons on the image quality still has to be investigated, first radiographic measurements could be performed at CALA in the near future, as soon as stable ion acceleration with the ATLAS-3000 laser system is possible and provided that the aforementioned online TOF spectrometry in transmission is operational.

Of course, there are several possible applications and modifications to the setup beyond the approach shown within this thesis. The co-emission of x-rays from the laser-plasma interaction can be exploited to perform bi-modal transmission imaging with protons and x-rays simultaneously. Such bi-modal radiographic images of crickets had been performed by a group of the department of medical physics within their beamtime at the Texas Petawatt Laser at the University of Texas in Austin, USA [Ostermayr, 2017]. Due to the different physics and absorber material dependences of ion energy loss and x-ray attenuation, such measurements could provide deeper insight to the actual composition of the object of interest. The experiments performed at the Texas Petawatt Laser were single shot experiments with offline detectors, i.e. one layer of CR-39 was used for proton detection, followed by a magnetic dipole field to deflect remaining protons and electrons, such that the non-deflected x-rays were detected by image plates. Replacing these offline detectors by online methods would be an ambitious task but not impossible. In such online setup, it has to be ensured that the proton detector does not significantly perturb the x-rays which can be detected behind a magnetic field using a commercial x-ray detection system.

Moreover, the polychromaticity of the spectrum could also be exploited to determine additional information of the object along the ion path. Additional information in such cases could be provided by taking into account the material-dependent scattering within the phantom [Raytchev and Seco, 2013]. In an analytical proof of principle study, the feasibility for such imaging with a multi-energetic proton beam was studied [Gianoli et al., 2018]. The measurement of the integral scattering power and the inverse stopping power (i.e. the residual energy) for different initial proton energies after an object of interest provides a system of non-linear equations. This can be solved by means of non-linear optimization and is (depending on object and beam energy parameters) capable to reconstruct inhomogeneities along the proton paths. Although the work of Gianoli et al. [2018] is based

on analytical calculations and assumes a perfect detector which is capable to determine the residual energy and integral scattering for individual energies of the polychromatic spectrum, it is worth spending a thought how this could be achieved in an experiment. An ideal detector, of course, would be capable to track and count every individual incoming proton. This, as previously discussed, is far from being achievable any time soon. The use of an offline detector like a stack of thin CR-39 detectors seems promising at first sight, since each layer corresponds to one energy bin and deconvolving the integral scattering power appears to be viable. However, the information from the stack of nuclear track detectors only provides information on the residual energy, but not on the initial energy which needs to be correlated with the scattering. In contrast, an imaging setup based on the TOF approach has the potential to yield such information. If the distance between source and object is large compared to the size of the object plus the distance to the detector, the additional TOF due to its slowing down within the object can be neglected. Hence, a thin TOF detection system providing also spatial resolution could be used to measure the energy-dependent integral scattering power of a laser-accelerated proton beam passing through an object of interest. This could potentially be exploited for online quasi-3D radiographic imaging.

Appendices

Online Detection of Laser-accelerated Helium-Ions at the LWS-20 Laser System

Introduction

In 2009, multi-MeV helium ions accelerated from a cluster-gas target by an ultrashort laser pulse of 150 mJ and 40 fs had been detected using a stack of solid state nuclear track detectors [Fukuda et al., 2009]. Based on this publication, an experimental campaign was conducted at the LWS-20 laser system installed at the Max Planck Institute of Quantum Optics (MPQ)[1] aiming to accelerate helium ions from supersonic gas jets and to detect them *online* using the hybrid silicon pixel detector Timepix. Experiments were performed in 6 experimental sessions between August and November 2015 in a collaboration with Dr. Daniel E. Cardenas and Prof. Dr. Lázló Veisz, formerly affiliated to the MPQ. The first sessions were dedicated to the optimization of the experimental setup.

Materials & Methods

The Experimental Setup

The setup for online detection of helium ions was installed in addition to the setup which is normally used for electron spectrometry. The laser beam was focused by an off-axis parabola onto the supersonic helium (or neon) gas jet. The accelerated particle bunches enter a first magnetic spectrometer through a pinhole. In the spectrometer, electrons are

---

[1]A description of the Light Wave Synthesizer 20 (LWS-20), which shortly after the last experimental session was dismantled and moved to Umeå University, Sweden, can be found in Rivas et al. [2017].

Figure A.1: Final experimental setup for the detection of laser-accelerated helium ions. Particles are coming from left and enter the first spectrometer (1), positively charged particles are deflected downwards. A second magnet (2) was used to further deflect charged particles to minimize the number of electrons hitting the detector. The Timepix detector was mounted inside the lead-shielded detector box (3). The second magnet and the detector box were mounted together on a motorized vertical stage.

deflected upwards by the perpendicular magnetic dipole field, where they are characterized using a Lanex scintillator screen. Positively charged particles are deflected downwards. An aluminum box with the Timepix detector was mounted on a motorized vertical stage 13 to 19 cm downstream with respect to the laser axis. The entrance window of the detector box was covered by a 3 µm thin gold foil (first experimental sessions) or by a 0.5 µm thin aluminum foil (last two experiments) to shield the detector against the intense laser light.

Throughout the 6 experimental sessions, the detection setup was optimized in order to minimize the amount of unwanted primary and secondary electrons reaching the Timepix detector. After the third experimental session, an additional pair of dipole magnets ($B > 600$ mT) was installed between the electron spectrometer and the detector box. Two 45 mm thick tungsten blocks were used to collimate the beam prior to the second magnet. The entrance slit to the second magnet was relatively broad (5 mm), making sure that helium ions deflected in the electron spectrometer could still enter the second magnet. Moreover, starting in experimental session 4, lead bricks were placed adjacent to the first spectrometer to keep the stray radiation low. Additionally, the detector box was covered with lead foil. In the last experimental session, the collimator was removed again and both magnets were brought closer together. This final setup is shown in figures A.1 and A.2.
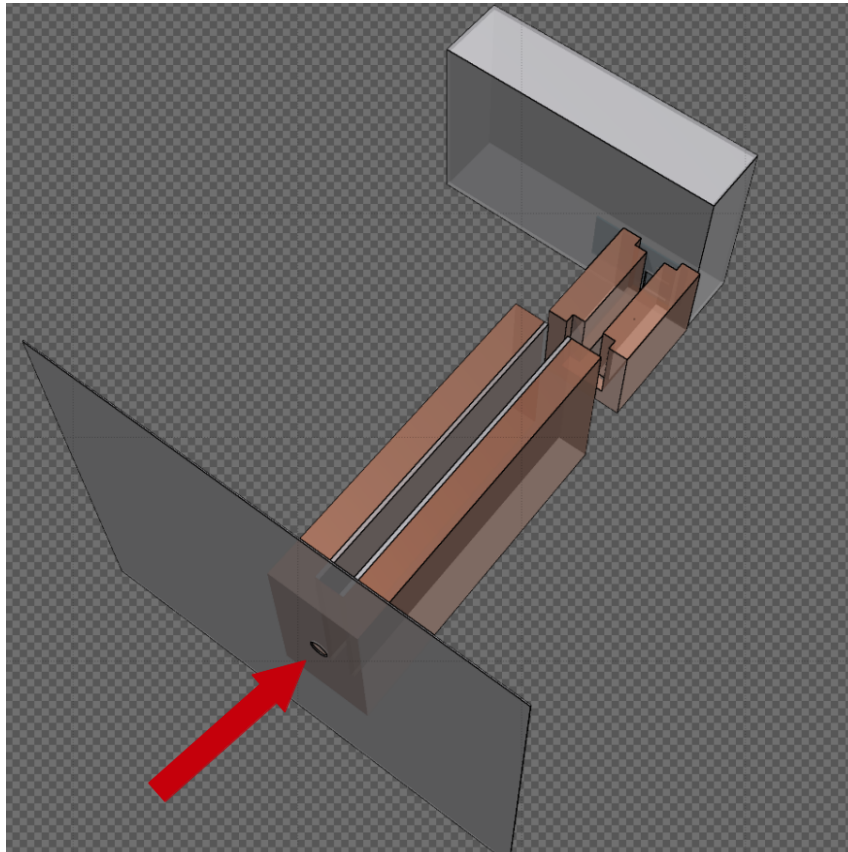
Figure A.2: 3D sketch of the experimental setup as described in the caption of figure A.1. The red arrow indicates the particle bunch direction.

The Detection System

The energy calibrated Timepix detector was operated in TOT mode and clusters were extracted and analyzed like in the experiments described in chapter 7. According to the shape and the size of each detected cluster, the particle species can be distinguished. Protons and heavier ions result in relatively round clusters (figure A.3), while electrons in the MeV range generally result in curly tracks. Small blobs or dots are generated by low-energy electrons or photons.

In addition to the Timepix detector, CR-39 nuclear track detectors were used for offline ion detection during the fifth experimental session. One plate (# 135) was mounted prior to the collimator, covering about one forth of the detector area. It was thus exposed to the particle beam within the entire experimental session. A second plate (# 126) was mounted between gas jet and entrance to first spectrometer for the last roughly 6000 shots of the experimental day. To obtain a background image of the CR-39, about half of the CR-39 plates was covered by a 30 µm thick aluminum foil, stopping all Helium ions with kinetic energies below 6.3 MeV. Since relatively low ion energies were expected, the CR-39 detectors were etched rather shortly (25 minutes) in 6M NaOH at 80 °C. After etching, the plates were washed in clear water, dried and manually analyzed using a confocal
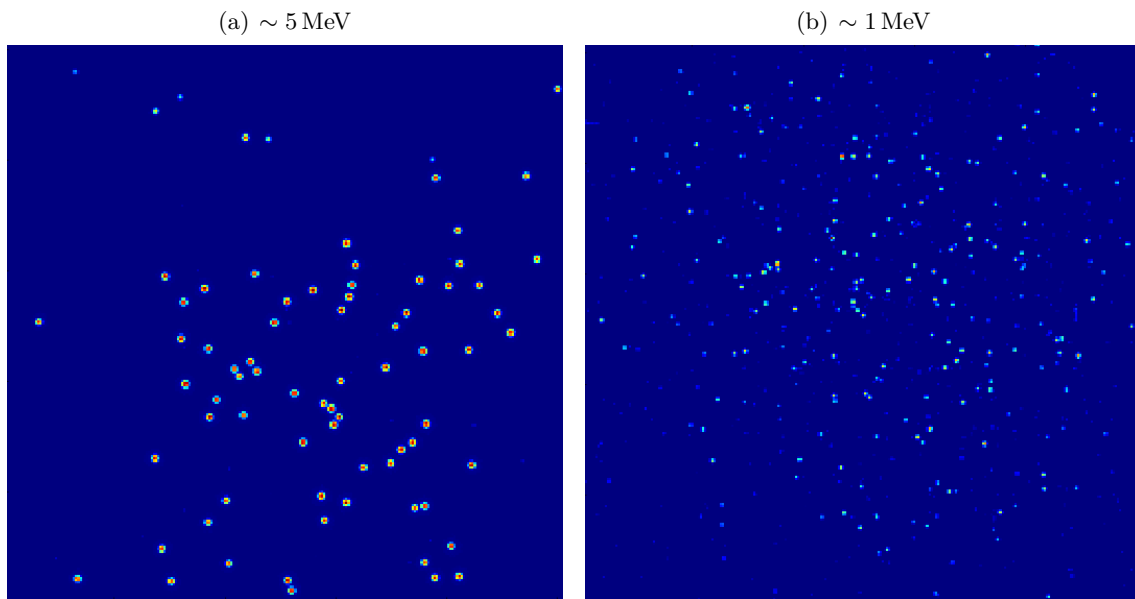
Figure A.3: Timepix frames showing α particles from a mixed nuclide source (^{239}Pu, ^{241}Am and ^{244}Cm) of energies around $5\,\text{MeV}$ and $1\,\text{MeV}$ are shown in (a) and (b), respectively. To obtain low-energy α particles, an additional absorber foil was placed between source and Timepix detector.

microscope.

Results & Discussion

First Experimental Sessions (August 7/12 and September 2, 2015)

Within the first experimental sessions, the detector was exposed to a huge number of (scattered) electrons, resulting in an almost homogeneous detector signal. Hence, no individual clusters could be extracted and an evaluation or search for ions was not possible. Examples of such frames are given in figure A.4.

Nevertheless, in some frames isolated clusters could be found with a shape resembling ion tracks. The cluster energies of all potential ion tracks were below $1.5\,\text{MeV}$. However, electrons in this energy range may also cause similar cluster shapes. Moreover, no significant difference in the number of extracted clusters was found between normal frames and frames in which an additional Lanex screen was accidentally left inside the beam path. The thickness of the Lanex screen would entirely stop helium ions of such kinetic energies. A further optimization of the experimental setup in terms of reducing the electrons hitting the detector was therefore required.

Experimental Sessions September 23/24, 2015

The use of the second dipole magnet and the collimator helped to considerably reduce the amount of electrons reaching the Timepix detector. Thus, all detected clusters could be
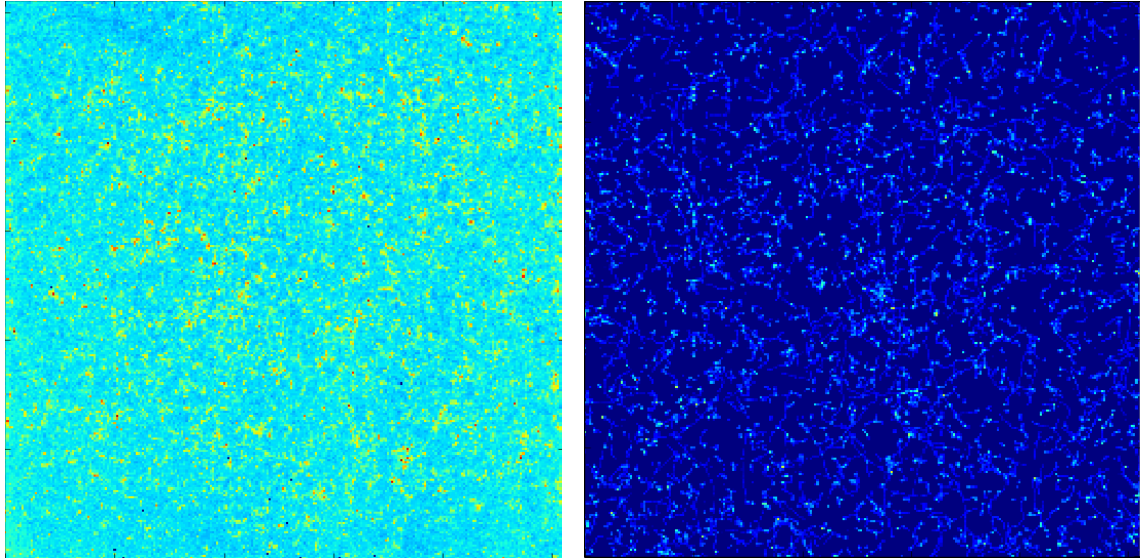
Figure A.4: Examples for Timepix frames within the first experimental sessions. Individual clusters could not been discriminated from the acquired Timepix frames due to the dominant electron background.

separated and analyzed independently.

Thus, 27 444 individual clusters could be extracted of which 1710 events had a cluster energy exceeding 1 MeV. However, the shape of these tracks clearly indicated that the clusters were generated by fast electrons. Only 16 clusters within the energy interval from 0.5 to 1 MeV had shown a cluster shape that could potentially be attributed to low-energy helium ions. Clusters with a total energy below 0.5 MeV were not analyzed.

In figure A.5, typical microscopic images of the uncovered and the covered part of the CR-39 detector # 135 are shown. The track-analysis of the CR-39 plates suggested the presence of helium ions. According to the spatial distribution of the circular pits on the CR-39, which was manifested in cloud-like distributions, many ions might have been accelerated within a relatively low number of laser shots. However, no energy information on the ions could be obtained since # 126 was mounted prior to the first spectrometer and # 135 was moved vertically with respect to the first spectrometer throughout the experimental session.

A measurement of the magnetic field of the electron spectrometer using a calibrated Hall probe revealed that its field strength was stronger than initially assumed. Therefore, the deflection of helium ions in the first magnet was so strong that ions with kinetic energy below 7 MeV could not pass the slit to enter the second dipole magnet.

Last Experimental Session (November 2015)

Based on the measured magnetic fields, the path of helium ions with different kinetic energies through both magnets towards the detector was calculated using Monte Carlo simulations. Using this information, two vertical positions of the second magnet and

<table>
<tr><td>(a) Uncovered</td><td>(b) Covered with Al foil</td></tr>
</table>
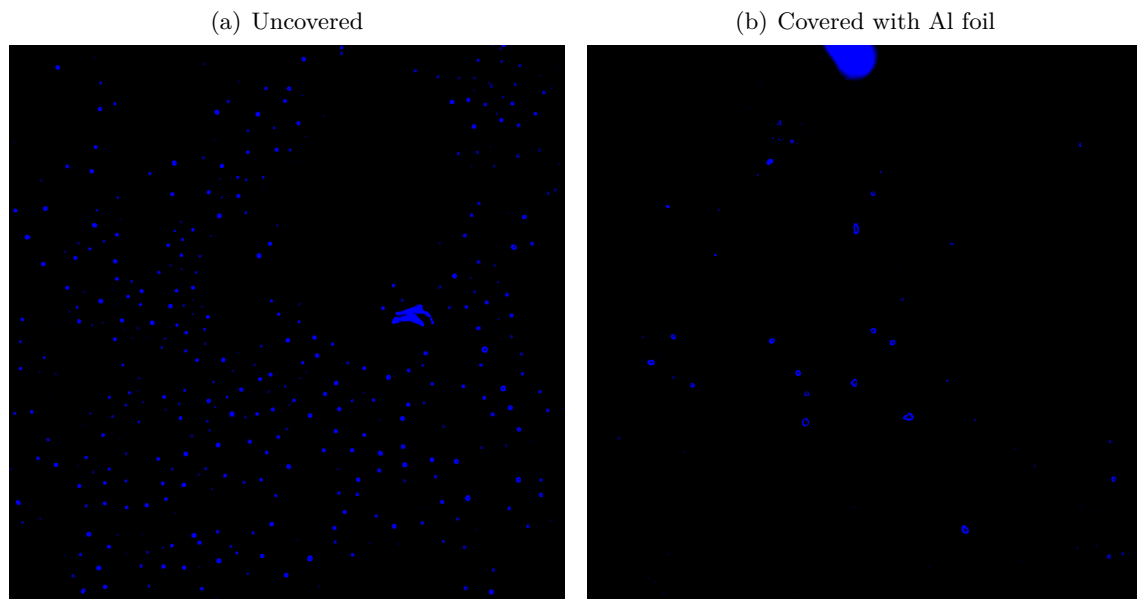
Figure A.5: Microscopic image of a CR-39 detector for helium ion detection. An example of the *uncovered* and *covered* part of the nuclear track detector is shown in (a) and (b), respectively. Ion tracks usually result in circles as they can be seen in (a), while the "tracks" in (b) not only have nicely round but also arbitrary shapes.

detector with respect to the first magnet were defined. The two magnets were separated by 40 mm and the collimators were not used anymore. In position A, only helium ions with energies above 1.5 MeV were able to hit the detector, while in the lower position B (-20 mm w.r.t position A), only ions with energies between 0.8 MeV and roughly 3 MeV could be detected on the Timepix sensor chip. Helium ions with energies below 0.8 MeV were not able to leave the second magnet.

Since clusters generated by low-energy helium ions may have the same shape as clusters from high-energy electrons, experiments with the same gas pressure settings and detector positions were run twice. In the first runs, the Lanex screen was intentionally kept inside blocking the particle beam for background measurement. In the second runs, no material was left inside the beam path. The electron density in these experiments was about 3×10^{20} cm^{-3}.

The cluster analysis resulted in 30 potential ion clusters with energies below 1 MeV out of a total number of 135 987 cluster events. One Timepix frame showing such potential ion clusters is shown in figure A.6. However, in the background measurements 21 potential ions were encountered out of 91 156 total clusters. Thus, no evidence for laser-accelerated helium ions with kinetic energies above 0.8 MeV was found in forward direction.

Additionally, experiments were performed with adding neon to the helium gas jet to create a higher electron density. In these experiments, only one cluster with an ion-like shape had been detected. The energy of that cluster was also below 1 MeV.
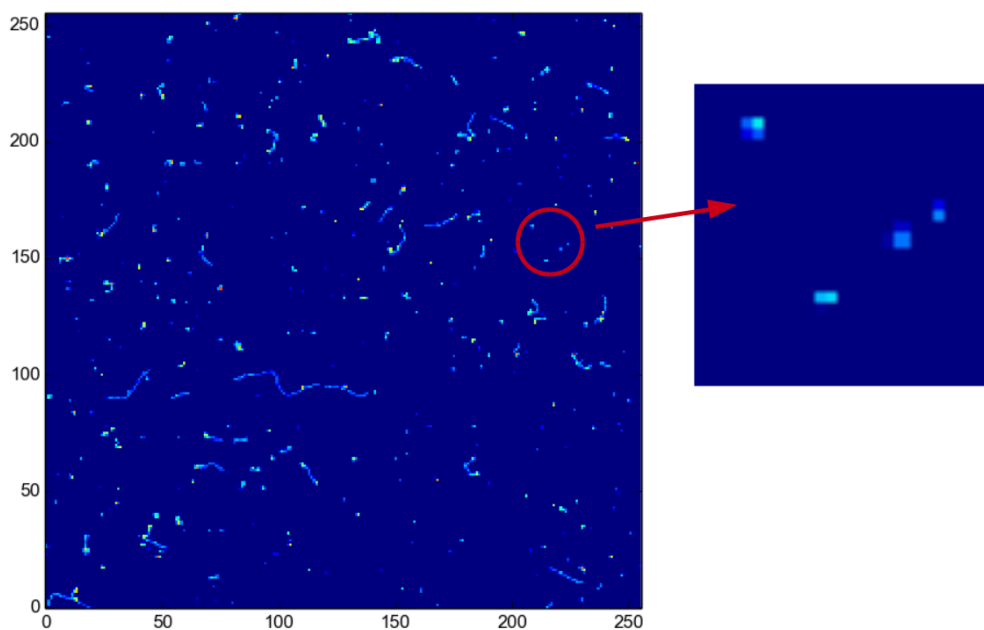
Figure A.6: Example of one acquired Timepix frame of the last experimental session for online helium ion detection. On the right, potential helium ions are shown in a magnification.

Conclusions

Within the six experimental sessions, online detection of laser-accelerated helium ions was not possible. The first experimental sessions were dedicated to the development of suitable electron background reduction. Even if there were helium ions hitting the Timepix detector, an identification would not have been possible due to the massive overlap of tracks in the detector signal. The setup was then improved to tremendously reduce the amount of electron tracks on the detector. However, since in the beginning the field strength of the first magnet was assumed to be smaller than it was, this "improvement" resulted in blocking all potential helium ions with energies below about 7 MeV. These errors in the experimental setup were eliminated and permitted a detection of helium ions with energies down to 0.8 MeV. However, the number of potential ion clusters did not significantly differ from background measurements. Nevertheless, the tracks observed on CR-39 could indicate the presence of accelerated helium ions, but no quantitative information on their energy and more importantly, no unambiguous proof that these encountered pits can really be attributed to ions was possible. The use of neon in the gas jet to increase the electron density did not show any considerable difference.

List of Scientific Contributions

Publications Related to this Project

2017

- **M. Würl**, S. Reinhardt, A. Rosenfeld, M. Petasecca, M. Lerch, L. Tran, S. Karsch, W. Assmann, J. Schreiber and K. Parodi. Experimental studies with two novel silicon detectors for the development of time-of-flight spectrometry of laser-accelerated proton beams, *Journal of Physics: Conference Series* **777** 012018 (2017)

- T. Rösch, P. Hilz, J. Bin, F. S. Englbrecht, Y. Gao, D. Haffa, J. Hartmann, S. Herr, F. H. Lindner, M. Speicher, **M. Würl**, K. Parodi, and J. Schreiber. Considerations on employing a PMQ-doublet for narrow and broad proton energy distributions, *Current Directions in Biomedical Engineering* **3** 2 pp339-342 (2017)

- F. S. Englbrecht, F.Balling, T. Rösch, **M. Würl**, F. H. Lindner, M. Speicher, K. Parodi, and J. Schreiber. Characterization of online high dynamic range imaging for laser-driven ion beam diagnostics using visible light, *Current Directions in Biomedical Engineering* **3** 2 pp343-346 (2017)

- F. H. Lindner, D. Haffa, J. Bin, F. Englbrecht, Y. Gao, J. Gebhard, J. Hartmann, P. Hilz, C. Kreuzer, S. Lehrack, T. Ostermayr, T. Rösch, M. Speicher, **M. Würl**, K. Parodi, J. Schreiber and P. Thirolf. Towards swift ion bunch acceleration by high-power laser pulses at the Centre for Advanced Laser Applications (CALA), *Nuclear Instruments and Methods in Physics Research Section B: Beam Interactions with Materials and Atoms* **402** pp354-357 (2017)

2018

- **M. Würl**, F. S. Englbrecht, S. Lehrack, C. Gianoli, F. H. Lindner, T. F. Rösch, D. Haffa, F. Olivari, M. Petasecca, M. L. F. Lerch, A. Pogossov, L. T. Tran, W.

Assmann, J. Schreiber, A. B. Rosenfeld and K. Parodi. Time-of-Flight Spectrometry of Ultra-Short, Polyenergetic Proton Bunches *submitted to Review of Scientific Instruments* (2018)

- F. S. Englbrecht, **M. Würl**, F. Olivari, A. Ficorella, C. Kreuzer, F. H. Lindner, M. Dalla Palma, L. Pancheri, G.-F. Dalla Betta, J. Schreiber, A. Quaranta and K. Parodi. An online, radiation hard proton energy-resolving scintillator stack for laser-driven proton bunches, *Radiation Protection Dosimetry*, **180** 1-4 pp291-295 (2018)

- D. Haffa, R. Yang, J. Bin, S. Lehrack, F.-E. Brack, H. Ding, F. Englbrecht, Y. Gao, J. Gebhard, M. Gilljohann, J. Götzfried, J. Hartmann, S. Herr, P. Hilz, S. Kraft, C. Kreuzer, F. Kroll, F. H. Lindner, J. Metzkes, T. M. Ostermayr, E. Ridente, T. F. Rösch, G. Schilling, H.-P. Schlenvoigt, M. Speicher, D. Taray, **M. Würl**, K. Zeil, U. Schramm, S. Karsch, K. Parodi, P. Bolton, W. Assmann and J. Schreiber. I-BEAT: New ultrasonic method for single bunch measurement of ion energy distribution, *submitted to Communications Physics* (2018)

Further Publications

- M. Bergemann, R.-P. Kudritzki, **M. Würl**, B. Plez, B. Davies and Z. Gazak. Red Supergiant Stars as Cosmic Abundance Probes. II. NLTE Effects in J-Band Silicon Lines, *The Astrophysical Journal* **764** 115 (2013)

- S. Reinhardt, **M. Würl**, C. Greubel, N. Humble, J. J. Wilkens, M. Hillbrand, A. Mairani, W. Assmann and K. Parodi. Investigation of EBT2 and EBT3 films for proton dosimetry in the 4–20 MeV energy range, *Radiation and Environmental Biophysics* **54** 1 pp71-79 (2015)

- **M. Würl**, F. Englbrecht, K. Parodi and M. Hillbrand. Dosimetric impact of the low-dose envelope of scanned proton beams at a ProBeam facility: comparison of measurements with TPS and MC calculations, *Physics in Medicine & Biology* **61** 2 pp958-973 (2016)

- B. Berndt, G. Landry, F. Schwarz, T. Tessonnier, F. Kamp, G. Dedes, C. Thieke, **M. Würl**, C. Kurz, U. Ganswindt, F. Verhaegen, J. Debus, C. Belka, W. Sommer, M. Reiser, J. Bauer and K. Parodi, Application of single- and dual-energy CT brain tissue segmentation to PET monitoring of proton therapy, *Physics in Medicine & Biology* **62** 6 pp2427-2448 (2017)

- M. Hillbrand, G. Landry, S. Ebert, G. Dedes, E. P. Pappas, G. Kalaitzakis, C. Kurz, **M. Würl**, F. Englbrecht, O. Dietrich, D. Makris, E. Pappas and K. Parodi. *submitted to Zeitschrift für Medizinische Physik* (2018)

Published Abstracts

- S. Reinhardt, **M. Würl**, C. Greubel, J. Wilkens, M. Hillbrand, A. Mairani, W. Assmann and K. Parodi. LET Dependence Correction of Radiochromic Films for Application in Low Energy Proton Irradiation, *Medical Physics* **42** 6 p3458 (2015)

- S. Reinhardt, **M. Würl**, C. Greubel, J. Wilkens, M. Hillbrand, A. Mairani, W. Assmann and K. Parodi. Correction of the LET dependence of radiochromic films for application in low-energy laser-driven proton irradiation, *Abstractband der 46. Jahrestagung der Deutschen Gesellschaft für Medizinische Physik*, p160 (2015)

- F. Englbrecht, **M. Würl**, D. Haffa, C. Kreuzer, S. Reinhardt, J. Schreiber and K. Parodi. Monte-Carlo studies for the development of laser-driven proton radiography *Abstractband der 46. Jahrestagung der Deutschen Gesellschaft für Medizinische Physik*, p162 (2015)

- **M. Würl**, F. Englbrecht, J. Hauffe, K. Parodi and M. Hillbrand. Dose output dependence on field size and spot spacing in scanned proton therapy - a comparison of measurements with TPS and MC calculations *Abstractband der 46. Jahrestagung der Deutschen Gesellschaft für Medizinische Physik*, p338 (2015)

- B. Berndt, T. Tessonnier, F. Schwarz, J. Bauer, **M. Würl**, F. Kamp, C. Thieke, C. Belka, F. Verhaegen, M. Reiser, W. Sommer, G. Dedes, G. Landry and K. Parodi. DECT Based Tissue Segmentation as Input to Monte Carlo Simulations for Proton Treatment Verification Using PET Imaging, *Medical Physics* **43** 6 p3877 (2016)

- **M. Würl**, S. Reinhardt, S. Karsch, W. Assmann, A. Rosenfeld, J. Schreiber and K. Parodi. Experimentelle Studien mit zwei neuartigen Siliziumdetektoren für die Entwicklung der Flugzeitspektrometrie laserbeschleunigter Ionenstrahlen, *Abstractband der 47. Jahrestagung der Deutschen Gesellschaft für Medizinische Physik*, p231 (2016)

- B. Berndt, T. Tessonnier, F. Schwarz, J. Bauer, **M. Würl**, F. Kamp, C. Thieke, C. Belka, F. Verhaegen, M. Reiser, W. Sommer, G. Dedes, G. Landry and K. Parodi. DECT basierte Gewebesegmentierung als Grundlage für Monte Carlo Simulationen zur Verifikation von Protonenbestrahlung mit Hilfe von PET-Bildgebung, *Abstractband der 47. Jahrestagung der Deutschen Gesellschaft für Medizinische Physik*, p248 (2016)

- **M. Würl**, F. Englbrecht, S. Lehrack, D. Haffa, C. Kreuzer, F. H. Lindner, T. F. Rösch, S. Reinhardt, S. Karsch, W. Assmann, L. T. Tran, M. Petasecca, M. Lerch, J. Schreiber, A. Rosenfeld, and K. Parodi. Development of TOF-Spectrometry of

Laser-Accelerated Proton Pulses using Silicon Microdosimeters *2017 European Conference on Lasers and Electro-Optics and European Quantum Electronics Conference* (2017)

- T. Rösch, D. Haffa, J. H. Bin, F. Englbrecht, Y. Gao, V. Gisbert, J. Gebhard, D. Hahner, J. Hartmann, M. Haug, S. Herr, P. Hilz, C. Kreuzer, S. Lehrack, F. H. Lindner, T. M. Ostermayr, E. Ridente, S. Seuferling, M. Speicher, **M. Würl**, R. Yang, K. Parodi and J. Schreiber. Laser-driven ION (LION) Acceleration at the Centre for Advanced Laser Applications (CALA), *2017 European Conference on Lasers and Electro-Optics and European Quantum Electronics Conference* (2017)

- **M. Würl**, F. Olivari, C. Gianoli, F. Englbrecht, A. Rosenfeld and K. Parodi. A new method for position-sensitive spectrometry of laser-accelerated proton bunches using the Timepix detector, *Abstractband der 48. Jahrestagung der Deutschen Gesellschaft für Medizinische Physik*, p437 (2017)

Conference Contributions

- **Poster**: *Dose output dependence on field size and spot spacing in scanned proton therapy – a comparison of measurements with TPS and MC calculations.* 46. Jahrestagung der Deutschen Gesellschaft für Medizinische Physik (DGMP), Marburg, Germany (2015)

- **Poster**: *Monte Carlo studies for the Development of Laser-Driven Proton Radiography.* Applications of Laser-driven Particle Acceleration, Venice, Italy (2015)

- **Oral**: *Experimental studies with two novel silicon detectors for the development of time-of-flight spectrometry of laser-accelerated proton beams.* Micro-Mini & Nano-Dosimetry & Innovative Technologies in Radiation Therapy, Hobart, Australia (2016)

- **Oral**: *Experimentelle Studien mit zwei neuartigen Siliziumdetektoren für die Entwicklung der Flugzeitspektrometrie laserbeschleunigter Ionenstrahlen.* 47. Jahrestagung der Deutschen Gesellschaft für Medizinische Physik (DGMP), Würzburg, Germany (2016)

- **Poster**: *Development of TOF-Spectrometry for Laser-Accelerated Protons using a Novel Silicon Detector.* 13th Symposium on Neutron and Ion Dosimetry, Krakow, Poland (2017)

- **Oral**: *Development of TOF-Spectrometry of Laser-Accelerated Proton Bunches using Silicon Microdosimeters.* The European Conference on Lasers and Electro-Optics, Munich, Germany (2017)

- **Poster**: *A new method for position-sensitive spectrometry of laser-accelerated proton bunches using the Timepix detector.* 48. Jahrestagung der Deutschen Gesellschaft für Medizinische Physik (DGMP), Dresden, Germany (2017)

- **Oral**: *Development of two prototype spectrometers for laser-accelerated proton bunches.* 17th International Symposium on Microdosimetry, Venice, Italy (2017)

- **Oral**: *Silicon detectors in medical applications and for characterization of laser-driven ion sources.* 13th "Trento" Workshop on Advanced Silicon Radiation Detectors, Munich, Germany (2018)

Awards and Scholarships

- $2014 - 2018$: Scholar of the "International Max Planck Research School of Advanced Photon Science (IMPRS-APS)"

- 2015: LMU Forscherpreis für exzellente Studierende

- 2015: Master's Thesis awarded by Springer "BestMasters"

- 2016: Travel grant of the DGMP

- 2016: Finalist in the "Young Investigator Award" of the DGMP

Table of Abbreviations

ADC	**A**nalog-to-**D**igital **C**onverter
ADU	**A**nalog-to-**D**igital **U**nit
ASCII	**A**merican **S**tandard **C**ode for **I**nformation **I**nterchange
ASE	**A**mplified **S**pontaneous **E**mission
ATLAS	**A**dvanced **T**itanium:sapphire **LAS**er
BP	**B**ragg **p**eak
CAD	Computer-**A**ided **D**esign
CALA	**C**entre for **A**dvanced **L**aser **A**pplications
CCD	**C**harge-**C**oupled **D**evice
CERN	**C**onseil **E**uropéen pour la **R**echerche **N**ucléaire
CMOS	**C**omplementary **M**etal-**O**xide-**S**emiconductor
CMRP	**C**entre for **M**edical **R**adiation **P**hysics
CPA	**C**hirped **P**ulse **A**mplification
CPU	**C**entral **P**rocessing **U**nit
CR-39	**C**olumbia **R**esin #**39** (allyl diglycol carbonate)
CTU	**C**zech **T**echnical **U**niversity
CSDA	**C**ontinuous **S**lowing **D**own **A**pproximation
CT	**C**omputed **T**omography
DC	**D**irect **C**urrent
DIL package	**D**ual **I**n-**L**ine package
ELI	**E**xtreme **L**ight **I**nfrastructure
ELIMAIA	**ELI** **M**ultidisciplinary **A**pplications of Laser-**I**on **A**cceleration
EMP	**E**lectro**M**agnetic **P**ulse
FC	**F**araday **C**up
FLAIR	**FL**UKA **A**dvanced **I**nte**R**face
FLUKA	**FLU**ktuierende **KA**skade
FOV	**F**ield-**O**f-**V**iew
FWHM	**F**ull **W**idth at **H**alf **M**aximum
GSI	**G**esellschaft für **S**chwer**I**onenforschung
GSM	**G**lobal **S**ystem for **M**obile communications

HU	**H**ounsfield **U**nit
I-BEAT	**I**on-**B**unch **E**nergy **A**coustic **T**racing
IEAP	**I**nstitute of **E**xperimental and **A**pplied **P**hysics
IP	**I**mage **Plate**
LET	**L**inear **E**nergy **T**ransfer
LEX Photonics	**L**aboratory for **EX**treme Photonics
LSF	**L**ine **S**pread **F**unction
MC	**M**onte **C**arlo
MCA	**M**ulti**C**hannel **A**nalyzer
MCP	**M**icro-**C**hannel **P**late
MCS	**M**ultiple **C**oulomb **S**cattering
MLL	**M**aier-**L**eibnitz-**L**aboratorium
MTF	**M**odulation **T**ransfer **F**unction
NRMSE	**N**ormalized **R**oot **M**ean **S**quare **E**rror
ND	**N**eutral **D**ensity
OD	**O**ptical **D**ensity
OTF	**O**ptical **T**ransfer **F**unction
PC	**P**ersonal **C**omputer
PHELIX	**P**etawatt **H**igh **E**nergy **L**aser of **I**on **EX**periments
PMMA	**P**oly**M**ethyl **M**eth**A**crylate $(C_5H_8O_2)_n$
PMQ	**P**ermanent **M**agnetic **Q**uadrupole
PMT	**P**hoto**M**ultiplier **T**ube
PSI	**P**aul **S**cherrer **I**nstitute
RCF	**R**adio**C**hromic **F**ilm
ROI	**R**egion **O**f **I**nterest
RMSE	**R**oot **M**ean **S**quare **E**rror
RPA	**R**adiation **P**ressure **A**cceleration
RSP	**R**elative **S**topping **P**ower
SiC	**Si**licon **C**arbide
SiPM	**Si**licon **P**hoto-**M**ultiplier
SOBP	**S**pread-**O**ut **B**ragg **P**eak
SOI	**S**ilicon-**O**n-**I**nsulator
SV	**S**ensitive **V**olume
TAC	**T**ime-to-**A**mplitude **C**onverter
TMAH	**T**etra**M**ethyl**A**mmonium **H**ydroxide
TNSA	**T**arget **N**ormal **S**heath **A**cceleration
TOF	**T**ime-**O**f-**F**light
TOT	**T**ime **O**ver **T**hreshold
UMTS	**U**niversal **M**obile **T**elecommunications **S**ystem
USB	**U**niversal **S**erial **B**us

WASP	**W**ide-**A**ngle magnetic **SP**ectrometer
WEPL	**W**ater **E**quivalent **P**ath **L**ength
WER	**W**ater **E**quivalent **R**atio
WET	**W**ater **E**quivalent **T**hickness

Bibliography

S. N. Ahmed. *Physics and Engineering of Radiation Detection.* Elsevier Science, 2014.

A. Alberigi-Quaranta, A. Taroni, and G. Zanarini. Plasma time in semiconductor detectors. *IEEE Transactions on Nuclear Science*, 15:373–380, 07 1968.

A. Alejo, D. Gwynne, D. Doria, H. Ahmed, D. C. Carroll, R. J. Clarke, D. Neely, G. G. Scott, M. Borghesi, and S. Kar. Recent developments in the Thomson Parabola Spectrometer diagnostic for laser-driven multi-species ion sources. *Journal of Instrumentation*, 11(10):C10005, 2016.

ALPA. Alpa - applications of laser-driven particle acceleration. `https://www.alpa.physik.uni-muenchen.de/protons.html`. Accessed on 2018-07-27.

W. Assmann, J. D. Boer, U. Meyer-Berkhout, S. Skorka, E. Huenges, P. Kienle, H. Morinaga, E. Nolte, H. Vonach, H. Münzer, L. Rohrer, and H. Schnitter. The Munich MP tandem. *Nuclear Instruments and Methods*, 122:191 – 203, 1974.

W. Assmann, S. Kellnberger, S. Reinhardt, S. Lehrack, A. Edlich, P. G. Thirolf, M. Moser, G. Dollinger, M. Omar, V. Ntziachristos, and K. Parodi. Ionoacoustic characterization of the proton Bragg peak with submillimeter accuracy. *Medical Physics*, 42(2):567–574, 2015.

F. H. Attix. *Introduction to Radiological Physics and Radiation Dosimetry.* A Wiley-Interscience publication. Wiley, 1986.

W. Barkas and D. Evans. *Nuclear Research Emulsions: Techniques and theory.* Pure and applied physics. Academic Press, 1963.

F. Belli, B. Esposito, D. Marocco, M. Riva, Y. Kaschuck, and G. Bonheure. A method for digital processing of pile-up events in organic scintillators. *Nuclear Instruments and Methods in Physics Research Section A: Accelerators, Spectrometers, Detectors and Associated Equipment*, 595(2):512 – 519, 2008.

M. Berger, J. Coursey, M. Zucker, and J. Chang. ESTAR, PSTAR, and ASTAR: Computer Programs for Calculating Stopping-Power and Range Tables for Electrons, Protons,

and Helium Ions (version 1.2.3), 2005. Available: http://physics.nist.gov/Star [2014, September 20].

H. Bethe. Zur Theorie des Durchgangs schneller Korpuskularstrahlen durch Materie. *Annalen der Physik*, 397:325–400, 1930.

J. Bin, K. Allinger, W. Assmann, G. Dollinger, G. A. Drexler, A. A. Friedl, D. Habs, P. Hilz, R. Hoerlein, N. Humble, et al. A laser-driven nanosecond proton source for radiobiological studies. *Applied Physics Letters*, 101(24):243701, 2012.

J. Birks. *The theory and practice of scintillation counting*. International series of monographs on electronics and instrumentation. Macmillan, 1964.

T. T. Böhlen, F. Cerutti, M. Chin, A. Fasso, A. Ferrari, P. G. Ortega, A. Mairani, P. Sala, G. Smirnov, and V. Vlachoudis. The FLUKA code: Developments and Challenges for High Energy and Medical Applications. *Nuclear Data Sheets*, 120:211–214, 2014.

N. Bohr. Lx. on the decrease of velocity of swiftly moving electrified particles in passing through matter. *The London, Edinburgh, and Dublin Philosophical Magazine and Journal of Science*, 30(178):581–612, 1915.

P. Bolton, M. Borghesi, C. Brenner, D. Carroll, C. De Martinis, A. Flacco, V. Floquet, J. Fuchs, P. Gallegos, D. Giove, et al. Instrumentation for diagnostics and control of laser-accelerated proton (ion) beams. *Physica Medica*, 30(3):255 – 270, 2014.

M. Borghesi, A. Schiavi, D. H. Campbell, M. G. Haines, O. Willi, A. J. MacKinnon, L. A. Gizzi, M. Galimberti, R. J. Clarke, and H. Ruhl. Proton imaging: a diagnostic for inertial confinement fusion/fast ignitor studies. *Plasma Physics and Controlled Fusion*, 43(12A):A267, 2001.

T. Bortfeld. An analytical approximation of the bragg curve for therapeutic proton beams. *Medical Physics*, 24(12):2024–2033, 1997.

T. Bowen. Radiation-induced thermoacoustic soft-tissue imaging. *IEEE Transactions on sonics and ultrasonics*, 29(3):187, 1982.

M. Branch, T. Coleman, and Y. Li. A subspace, interior, and conjugate gradient method for large-scale bound-constrained minimization problems. *SIAM Journal on Scientific Computing*, 21(1):1–23, 1999.

I. Brumer. Characterisation of Silicon Microdosimeters for Time-of-Flight Spectrometry of Laser-Accelerated Proton Bunches. Bachelor thesis, LMU München, 2017.

M. Bucciantonio, U. Amaldi, R. Kieffer, F. Sauli, and D. Watts. Development of a fast proton range radiography system for quality assurance in hadrontherapy. *Nuclear Instruments and Methods in Physics Research Section A: Accelerators, Spectrometers, Detectors and Associated Equipment*, 732:564 – 567, 2013.

S. Busold, D. Schumacher, O. Deppert, C. Brabetz, S. Frydrych, F. Kroll, M. Joost, A. Almomani, A. Blazevic, B. Zielbauer, et al. Focusing and transport of high-intensity multi-mev proton bunches from a compact laser-driven source. *Physical Review Special Topics: Accelerators and Beams*, 16, 10 2013.

S. Busold, D. Schumacher, O. Deppert, C. Brabetz, F. Kroll, A. Blazevic, V. Bagnoud, and M. Roth. Commissioning of a compact laser-based proton beam line for high intensity bunches around 10 MeV. *Physical Review Accelerators and Beams*, 17:031302, 2014.

S. Busold, D. Schumacher, C. Brabetz, D. Jahn, F. Kroll, O. Deppert, U. Schramm, T. Cowan, A. Blazevic, V. Bagnoud, and M. Roth. Towards highest peak intensities for ultra-short mev-range ion bunches. *Scientific reports*, 5:12459, 07 2015.

M. J. Butson, T. Cheung, and P. K. N. Yu. Scanning orientation effects on Gafchromic EBT film dosimetry. *Australasian Physics & Engineering Sciences in Medicine*, 29(3): 281–284, 2006.

M. Campbell. Photon counting detectors. Neutron & Photon Detector Workshop, 2012.

A. Cannavò, L. Torrisi, and L. Calcagno. SiC detector characterization for radiation emitted by laser-generated plasmas. *Journal of Instrumentation*, 11(05):C05008, 2016.

H. Chen, A. J. Link, R. van Maren, P. K. Patel, R. Shepherd, S. C. Wilks, and P. Beiersdorfer. High performance compact magnetic spectrometers for energetic ion and electron measurement in ultraintense short pulse laser solid interactions. *Review of Scientific Instruments*, 79(10):10E533, 2008.

I. W. Choi, C. M. Kim, J. H. Sung, I. J. Kim, T. J. Yu, S. K. Lee, Y.-Y. Jin, K. H. Pae, N. Hafz, and J. Lee. Absolute calibration of a time-of-flight spectrometer and imaging plate for the characterization of laser-accelerated protons. *Measurement Science and Technology*, 20(11):115112, 2009.

I. Choi Chang, H. Kang Byoung, K. Kim Yong, W. Choi Il, K. Do-Kyeong, L. Jongmin, and D. Kim Gi. Comparison between Proton Radiography Images Using a High-power Femtosecond Laser and a Tandem Van de Graff Accelerator. *Journal of the Korean Physical Society*, 59, 2011.

G. A. P. Cirrone, A. Tramontana, G. Candiano, M. Carpinelli, S. Cavallaro, M. Cutroneo, G. Cuttone, C. De Martinis, D. Giove, J. Krása, et al. A new Thomson Spectrometer for high energy laser-driven beams diagnostic. *Journal of Instrumentation*, 9(08):T08001, 2014.

A. M. Cormack. Representation of a function by its line integrals, with some radiological applications. *Journal of Applied Physics*, 34(9):2722–2727, 1963.

M. Cutroneo, P. Musumeci, M. Zimbone, L. Torrisi, F. La Via, D. Margarone, A. Velyhan, J. Ullschmied, and L. Calcagno. High performance sic detectors for mev ion beams generated by intense pulsed laser plasmas. *Journal of Materials Research*, 28(1):87–93, 2013.

H. Daido, M. Nishiuchi, and A. S. Pirozhkov. Review of laser-driven ion sources and their applications. *Reports on Progress in Physics*, 75:056401, 05 2012.

M. Dalla Palma, S. Carturan, M. Degerlier, T. Marchi, M. Cinausero, F. Gramegna, and A. Quaranta. Non-toxic liquid scintillators with high light output based on phenyl-substituted siloxanes. *Optical Materials*, 42:111 – 117, 2015.

G. Dollinger and T. Faestermann. Physics at the Munich Tandem Accelerator Laboratory. *Nuclear Physics News*, 28(1):5–12, 2018.

F. Englbrecht, F. Balling, T. Rösch, M. Würl, F. Lindner, K. Parodi, and J. Schreiber. Characterization of online high dynamic range imaging for laser-driven ion beam diagnostics using visible light. *Current Directions in Biomedical Engineering*, 3, 09 2017.

F. S. Englbrecht, M. Würl, F. Olivari, A. Ficorella, C. Kreuzer, F. Lindner, M. Dalla Palma, L. Pancheri, G.-F. Dalla Betta, J. Schreiber, A. Quaranta, and K. Parodi. An online, radiation hard proton energy-resolving scintillator stack for laser-driven proton bunches. *Radiation Protection Dosimetry*, page 291, 02 2018.

T. Esirkepov, M. Borghesi, S. V Bulanov, G. Mourou, and T. Tajima. Highly efficient relativistic-ion generation in the laser-piston regime. *Physical Review Letters*, 92:175003, 2004.

A. Y. Faenov, T. A. Pikuz, Y. Fukuda, M. Kando, H. Kotaki, T. Homma, K. Kawase, T. Kameshima, A. Pirozhkov, A. Yogo, et al. Ionography of nanostructures with the use of a laser plasma of cluster targets. *JETP Letters*, 89(10):485–491, 2009a.

A. Y. Faenov, T. A. Pikuz, Y. Fukuda, M. Kando, H. Kotaki, T. Homma, K. Kawase, T. Kameshima, A. Pirozhkov, A. Yogo, et al. Submicron ionography of nanostructures using a femtosecond-laser-driven-cluster-based source. *Applied Physics Letters*, 95(10): 101107, 2009b.

A. Ferrari, P. R. Sala, A. Fassó, and J. Ranft. FLUKA: a multi-particle transport code. *CERN-2005-10*, INFN/TC_05/11, SLAC-R-773, 2005.

P. Freiwang. Messung der Zeitstruktur eines gepulsten 20MeV-Protonenstrahl. Bachelor thesis, LMU München, 2014.

Y. Fukuda, A. Y. Faenov, M. Tampo, T. A. Pikuz, T. Nakamura, M. Kando, Y. Hayashi, A. Yogo, H. Sakaki, T. Kameshima, et al. Energy increase in multi-MeV ion acceleration

in the interaction of a short pulse laser with a cluster-gas target. *Physical Review Letters*, 103(16), 2009.

S. Gaillard, J. Fuchs, N. Renard-Le Galloudec, and T. E. Cowan. Study of saturation of CR39 nuclear track detectors at high ion fluence and of associated artifact patterns. *Review of Scientific Instruments*, 78(1):013304, 2007.

Y. Gao, J. Bin, D. Haffa, C. Kreuzer, J. Hartmann, M. Speicher, F. Lindner, T. Ostermayr, P. Hilz, T. Rösch, et al. An automated, 0.5 Hz nano-foil target positioning system for intense laser plasma experiments. *High Power Laser Science and Engineering*, 5:E12, 2017.

T. Gehrke, C. Amato, S. Berke, and M. Martisikova. Theoretical and experimental comparison of proton and helium-beam radiography using silicon pixel detectors. *Physics in Medicine & Biology*, 63:035037, 2018.

C. Gianoli, M. Würl, C. Seller Oria, M. Rädler, T. Ostermayr, J. Schreiber, and K. Parodi. "analytical proof of principle for a novel approach to imaging with multi-energetic proton beams". 2018 IEEE Nuclear Science Symposium and Medical Imaging Conference (accepted for oral presentation), 2018.

P. Gibbon. *Short Pulse Laser Interactions with Matter: An Introduction*. Imperial College Press, 2005.

B. Gottschalk. On the scattering power of radiotherapy protons. *Medical physics*, 37(1): 352–367, 2010.

B. Gottschalk, S. Tang, E. H. Bentefour, E. W. Cascio, D. Prieels, and H. Lu. Water equivalent path length measurement in proton radiotherapy using time resolved diode dosimetry. *Medical Physics*, 38(4):2282–2288, 2011.

T. Graeve and G. P. Weckler. High-resolution CMOS imaging detector. In L. E. Antonuk and M. J. Yaffe, editors, *Medical Imaging 2001: Physics of Medical Imaging*, volume 4320, pages 68–76, 2001.

C. Granja, Z. Vykydal, Y. Kopatch, J. Jakubek, S. Pospisil, and S. Telezhnikov. Position-sensitive spectroscopy of 252Cf fission fragments. *Nuclear Instruments and Methods in Physics Research Section A: Accelerators, Spectrometers, Detectors and Associated Equipment*, 574:472–478, 2007.

C. Granja, J. Jakubek, U. Köster, M. Platkevic, and S. Pospisil. Response of the pixel detector timepix to heavy ions. *Nuclear Instruments and Methods in Physics Research Section A: Accelerators, Spectrometers, Detectors and Associated Equipment*, 633:S198 – S202, 2011.

C. Granja, P. Krist, D. Chvátil, J. Solc, S. Pospisil, J. Jakubek, and L. Opalka. Energy loss and online directional track visualization of fast electrons with the pixel detector Timepix. *Radiation Measurements*, 59:245–261, 2013.

C. Granja, S. Polansky, Z. Vykydal, S. Pospisil, A. Owens, Z. Kozacek, K. Mellab, and M. Simcak. The SATRAM Timepix spacecraft payload in open space on board the Proba-V satellite for wide range radiation monitoring in LEO orbit. *Planetary and Space Science*, 125:114 – 129, 2016.

J. S. Green, M. Borghesi, C. M. Brenner, D. C. Carroll, N. P. Dover, P. S. Foster, P. Gallegos, S. Green, D. Kirby, K. J. Kirkby, et al. Scintillator-based ion beam profiler for diagnosing laser-accelerated ion beams. In *Laser Acceleration of Electrons, Protons, and Ions; and Medical Applications of Laser-Generated Secondary Sources of Radiation and Particles*, volume 8079, page 19, 05 2011.

D. Haffa, R. Yang, J. Bin, S. Lehrack, F.-E. Brack, H. Ding, F. Englbrecht, Y. Gao, J. Gebhard, M. Gilljohann, et al. I-BEAT: New ultrasonic method for single bunch measurement of ion energy distribution. 2018. (submitted; available: https://arxiv.org/abs/1809.02546).

S. P. Hatchett, C. G. Brown, T. E. Cowan, E. A. Henry, J. S. Johnson, M. H. Key, J. A. Koch, A. B. Langdon, B. F. Lasinski, R. W. Lee, et al. Electron, photon, and ion beams from the relativistic interaction of petawatt laser pulses with solid targets. *Physics of Plasmas*, 7(5):2076–2082, 2000.

M. Hegelich, S. Karsch, G. Pretzler, D. Habs, K. Witte, W. Guenther, M. Allen, A. Blazevic, J. Fuchs, J. C. Gauthier, et al. MeV ion jets from short-pulse-laser interaction with thin foils. *Physical Review Letters*, 89:085002, 2002.

A. Henig, D. Kiefer, M. Geissler, S. G. Rykovanov, R. Ramis, R. Hörlein, J. Osterhoff, Z. Major, L. Veisz, S. Karsch, et al. Laser-driven shock acceleration of ion beams from spherical mass-limited targets. *Physical Review Letters*, 102:095002, 2009.

A. Higginson, R. Gray, M. King, R. Dance, S. Williamson, N. Butler, R. Wilson, R. Capdessus, C. Armstrong, J. S. Green, et al. Near-100 MeV protons via a laser-driven transparency-enhanced hybrid acceleration scheme. *Nature Communications*, 9: 724, 2018.

V. Highland. Some practical remarks on multiple-scattering. *Nuclear Instruments and Methods*, 129(2):497–499, 1975.

I. Hofmann, J. Meyer-ter Vehn, X. Yan, A. Orzhekhovskaya, and S. Yaramyshev. Collection and focusing of laser accelerated ion beams for therapy applications. *Physical Review Special Topics: Accelerators and Beams*, 14(3), 2011.

J. Jakůbek. Semiconductor pixel detectors and their applications in life sciences. *Journal of Instrumentation*, 4(03):P03013, 2009.

J. Jakůbek. Precise energy calibration of pixel detector working in time-over-threshold mode. *Nuclear Instruments and Methods in Physics Research Section A: Accelerators, Spectrometers, Detectors and Associated Equipment*, 633:S262–S266, 2011.

J. Jakůbek, A. Cejnarova, T. Holy, S. Pospisil, J. Uher, and Z. Vykydal. Pixel detectors for imaging with heavy charged particles. *Nuclear Instruments and Methods in Physics Research Section A: Accelerators, Spectrometers, Detectors and Associated Equipment*, 591:155–158, 2008.

K.-W. Jee, R. Zhang, E. H. Bentefour, P. J. Doolan, E. Cascio, G. Sharp, J. Flanz, and H.-M. Lu. Investigation of time-resolved proton radiography using x-ray flat-panel imaging system. *Physics in Medicine & Biology*, 62(5):1905, 2017.

R. P. Johnson. Review of medical radiography and tomography with proton beams. *Reports on Progress in Physics*, 81(1):016701, 2018.

R. P. Johnson, V. Bashkirov, L. DeWitt, V. Giacometti, F. Hurley, P. Piersimoni, T. Plautz, H. F.-W. Sadrozinski, K. Schubert, R. Schulte, B. Schultze, and A. Zatserklyaniy. A Fast Experimental Scanner for Proton CT: Technical Performance and First Experience With Phantom Scans. *IEEE Transactions on Nuclear Science*, 63:1–1, 12 2015.

E. Jones, T. Oliphant, P. Peterson, et al. SciPy: Open source scientific tools for Python, 2001–. [Online; accessed 2018-06-18].

D. Jung, R. Hörlein, D. C. Gautier, S. Letzring, D. Kiefer, K. Allinger, B. J. Albright, R. Shah, S. Palaniyappan, L. Yin, et al. A novel high resolution ion wide angle spectrometer. *Review of Scientific Instruments*, 82(4):043301, 2011a.

D. Jung, R. Hörlein, D. Kiefer, S. Letzring, D. Gautier, U. Schramm, C. Hübsch, R. Öhm, B. Albright, J. Fernandez, D. Habs, and B. Hegelich. Development of a high resolution and high dispersion Thomson parabola. *Review of Scientific Instruments*, 82:013306, 2011b.

K.-i. Kamei, Y. Mashimo, Y. Koyama, C. Fockenberg, M. Nakashima, M. Nakajima, J. Li, and Y. Chen. 3d printing of soft lithography mold for rapid production of polydimethylsiloxane-based microfluidic devices for cell stimulation with concentration gradients. *Biomedical Microdevices*, 17(2):36, 2015.

L. V. Keldysh. Ionization in the field of a strong electromagnetic wave. *Soviet Physics JETP*, 20(5):1307–1314, 1965.

R. Kinsey, C. Dunford, J. Tuli, and T. Burrows. The NUDAT/PCNUDAT program for nuclear data. *Online (NuDat 2.7) - Available: http://www.nndc.bnl.gov/nudat2/ [2018, March 1]*, 1996.

L. Kinsler, A. Frey, A. Coppens, and J. Sanders. *Fundamentals of Acoustics.* Wiley, 2000.

D. Kirby, S. Green, H. Palmans, R. Hugtenburg, C. Wojnecki, and D. Parker. LET dependence of Gafchromic films and an ion chamber in low-energy proton dosimetry. *Physics in Medicine & Biology*, 55(2):417, 2010.

G. F. Knoll. *Radiation Detection and Measurement.* John Wiley & Sons, 2010.

A. M. Koehler. Proton Radiography. *Science*, 160:303–304, Apr. 1968.

S. L. Kramer, D. R. Moffett, R. L. Martin, E. P. Colton, and V. W. Steward. Proton imaging for medical applications. *Radiology*, 135(2):485–494, 1980.

J. Krása, A. Lorusso, D. Doria, F. Belloni, V. Nassisi, and K. Rohlena. Time-of-flight profile of multiply-charged ion currents produced by a pulse laser. *Plasma Physics and Controlled Fusion*, 47(8):1339, 2005.

J. Krása, K. Jungwirth, S. Gammino, E. Krouský, L. Láska, A. Lorusso, V. Nassisi, M. Pfeifer, K. Rohlena, L. Torrisi, J. Ullschmied, and A. Velyhan. Partial currents of ion species in an expanding laser-created plasma. *Vacuum*, 83(1):180 – 184, 2008.

V. Kraus, M. Holik, J. Jakubek, M. Kroupa, P. Soukup, and Z. Vykydal. FITPix — fast interface for Timepix pixel detectors. *Journal of Instrumentation*, 6(01):C01079, 2011.

M. Kroupa, S. Hoang, N. Stoffle, P. Soukup, J. Jakubek, and L. S. Pinsky. Energy resolution and power consumption of Timepix detector for different detector settings and saturation of front-end electronics. *Journal of Instrumentation*, 9(05):C05008, 2014.

M. Kroupa, T. Campbell-Ricketts, A. Bahadori, and A. Empl. Techniques for precise energy calibration of particle pixel detectors. *Review of Scientific Instruments*, 88(3): 033301, 2017.

E. L. Clark, K. Krushelnick, M. Zepf, F. Beg, M. Tatarakis, A. Machacek, M. I. K. Santala, I. Watts, P. A. Norreys, and A. E. Dangor. Energetic heavy-ion and proton generation from ultraintense laser-plasma interactions with solids. *Physical Review Letters*, 85: 1654–1657, 2000.

L. Landau. On the energy loss of fast particles by ionization. *J. Phys.(USSR)*, 8:201–205, 1944.

J. Lee, C. Kim, B. Min, J. Kwak, S. Park, S. B. Lee, S. Park, and S. Cho. Sparse-view proton computed tomography using modulated proton beams. *Medical Physics*, 42: 1129–1137, Feb. 2015.

S. Lehrack. *Investigating Accuracy and Precision of Ionoacoustics for Range Determination of Ion Beams in Water.* PhD thesis, LMU München, 2018.

W. R. Leo. *Techniques for Nuclear and Particle Physics Experiments.* Springer, 2nd edition, 1994.

F. Lindner, D. Haffa, J. Bin, F. Englbrecht, Y. Gao, J. Gebhard, J. Hartmann, P. Hilz, C. Kreuzer, S. Lehrack, et al. Towards swift ion bunch acceleration by high-power laser pulses at the Centre for Advanced Laser Applications (CALA). *Nuclear Instruments and Methods in Physics Research Section B: Beam Interactions with Materials and Atoms*, page 354, 03 2017.

F. Lindner, J. Bin, F. Englbrecht, D. Haffa, P. Bolton, Y. Gao, J. Hartmann, P. Hilz, C. Kreuzer, T. Ostermayr, et al. A novel approach to electron data background treatment in an online wide-angle spectrometer for laser-accelerated ion and electron bunches. *Review of Scientific Instruments*, 89(1):013301, 2018.

F. H. Lindner. Private communication. 2017.

U. Linz and J. Alonso. What will it take for laser driven proton accelerators to be applied to tumor therapy? *Physical Review Special Topics: Accelerators and Beams*, 10(9), 2007.

U. Linz and J. Alonso. Laser-driven ion accelerators for tumor therapy revisited. *Physical Review Special Topics: Accelerators and Beams*, 19(12), 2016.

X. Llopart and M. Campbell. First test measurements of a 64k pixel readout chip working in single photon counting mode. *Nuclear Instruments and Methods in Physics Research Section A: Accelerators, Spectrometers, Detectors and Associated Equipment*, 509:157–163, 2003.

X. Llopart, M. Campbell, R. Dinapoli, D. S. Segundo, and E. Pernigotti. Medipix2: A 64-k pixel readout chip with 55-μm square elements working in single photon counting mode. *IEEE Transactions on Nuclear Science*, 49:2279–2283, 2002.

X. Llopart, R. Ballabriga, M. Campbell, L. Tlustos, and W. Wong. Timepix, a 65k programmable pixel readout chip for arrival time, energy and/or photon counting measurements. *Nuclear Instruments and Methods in Physics Research Section A: Accelerators, Spectrometers, Detectors and Associated Equipment*, 581(1):485–494, 2007.

H.-M. Lu. A potential method for in vivo range verification in proton therapy treatment. *Physics in Medicine & Biology*, 53(5):1413, 2008.

G. Lutz. *Semiconductor Radiation Detectors: Device Physics.* Springer Berlin Heidelberg, 2007.

G. R. Lynch and O. I. Dahl. Approximations to multiple Coulomb scattering. *Nuclear Instruments and Methods in Physics Research Section B: Beam Interactions with Materials and Atoms*, 58(1):6 – 10, 1991.

A. Macchi, M. Borghesi, and M. Passoni. Ion acceleration by superintense laser-plasma interaction. *Reviews of Modern Physics*, 85:751–793, 2013.

T. H. Maiman. Stimulated optical radiation in ruby masers. *Nature*, 187:493–494, 08 1960.

A. Maksimchuk, S. Gu, K. Flippo, D. Umstadter, and V. Bychenkov. Forward ion acceleration in thin films driven by a high-intensity laser. *Physical Review Letters*, 84: 4108–4111, 2000.

V. Malka, S. Fritzler, E. Lefebvre, E. d'Humieres, R. Ferrand, G. Grillon, C. Albaret, S. Meyroneinc, J. Chambaret, A. Antonetti, and D. Hulin. Practicability of protontherapy using compact laser systems. *Medical Physics*, 31(6):1587–1592, 2004.

D. Margarone, J. Krása, L. Giuffrida, A. Picciotto, L. Torrisi, T. Nowak, P. Musumeci, A. Velyhan, J. Prokůpek, L. Láska, et al. Full characterization of laser-accelerated ion beams using Faraday cup, silicon carbide, and single-crystal diamond detectors. *Journal of Applied Physics*, 109(10):103302, 2011.

S. Marrone, D. Cano-Ott, N. Colonna, C. Domingo, F. Gramegna, E. Gonzalez, F. Gunsing, M. Heil, F. Käppeler, P. Mastinu, et al. Pulse shape analysis of liquid scintillators for neutron studies. *Nuclear Instruments and Methods in Physics Research Section A: Accelerators, Spectrometers, Detectors and Associated Equipment*, 490(1):299–307, 2002.

G. Marx. Interstellar vehicle propelled by terrestrial laser beam. *Nature*, 211(5044):22, 1966.

A. Merchant, M. Newall, S. Guatelli, M. Petasecca, M. Lerch, V. Perevertaylo, G. Milluzzo, G. Petringa, F. Romano, G. Cirrone, et al. Feasibility study of a novel multi-strip silicon detector for use in proton therapy range verification quality assurance. *Radiation Measurements*, 106:378–384, 2017.

F. A. Mettler, W. Huda, T. T. Yoshizumi, and M. Mahesh. Effective doses in radiology and diagnostic nuclear medicine: A catalog. *Radiology*, 248(1):254–263, 2008.

J. Metzkes, L. Karsch, S. D. Kraft, J. Pawelke, C. Richter, M. Schürer, M. Sobiella, N. Stiller, K. Zeil, and U. Schramm. A scintillator-based online detector for the angularly resolved measurement of laser-accelerated proton spectra. *Review of Scientific Instruments*, 83(12):123301, 2012.

J. Metzkes, K. Zeil, S. D. Kraft, L. Karsch, M. Sobiella, M. Rehwald, L. Obst, H.-P. Schlenvoigt, and U. Schramm. An online, energy-resolving beam profile detector for laser-driven proton beams. *Review of Scientific Instruments*, 87(8):083310, 2016.

X. Miao-Hua, L. Hong-Wei, L. Bi-Cheng, L. Feng, S. Lu-Ning, D. Fei, Z. Lu, Z. Yi, M. Jing-Long, D. Neely, et al. Development of a real-time ion spectrometer with a scintillator for laser-driven ion acceleration experiments. *Chinese Physics Letters*, 28 (9):095203, 2011.

G. Milluzzo, V. Scuderi, A. Amico, G. Cirrone, G.Cuttone, M. D. Napoli, J. Dostal, G. Larosa, R. Leanza, D. Margarone, et al. TOF technique for laser-driven proton beam diagnostics for the ELIMED beamline. *Journal of Instrumentation*, 12(03):C03044, 2017a.

G. Milluzzo, V. Scuderi, A. G. Amico, M. Borghesi, G. A. P. Cirrone, G. Cuttone, M. De Napoli, D. Doria, J. Dostal, G. Larosa, et al. Laser-accelerated ion beam diagnostics with TOF detectors for the ELIMED beam line. *Journal of Instrumentation*, 12:C02025, 2017b.

G. Molière. Theorie der Streuung schneller geladener Teilchen - II Mehrfachstreuung und Vielfachstreuung. *Zeitschrift für Naturforschung Teil A*, 3(2):78–97, 1948.

G. A. Mourou, T. Tajima, and S. V. Bulanov. Optics in the relativistic regime. *Reviews of Modern Physics*, 78:309–371, 2006.

A. A. Mustafa and D. F. Jackson. The relation between x-ray CT numbers and charged particle stopping powers and its significance for radiotherapy treatment planning. *Physics in Medicine & Biology*, 28(2):169, 1983.

S. Nakamura, Y. Iwashita, A. Noda, T. Shirai, H. Tongu, A. Fukumi, M. Kado, A. Yogo, M. Mori, S. Orimo, et al. Real-time optimization of proton production by intense short-pulse laser with time-of-flight measurement. *Japanese Journal of Applied Physics*, 45 (9):L913, 2006.

W. D. Newhauser and R. Zhang. The physics of proton therapy. *Physics in Medicine & Biology*, 60(8):R155, 2015.

F. Nürnberg, M. Schollmeier, E. Brambrink, A. Blažević, D. C. Carroll, K. Flippo, D. C. Gautier, M. Geißel, K. Harres, B. M. Hegelich, et al. Radiochromic film imaging spectroscopy of laser-accelerated proton beams. *Review of Scientific Instruments*, 80(3): 033301, 2009.

D. Offermann, K. Flippo, S. Gaillard, D. Gautier, S. Letzring, J. C. Cobble, G. Wurden, R. P. Johson, T. Shimada, D. Montgomery, et al. Carbon ion beam focusing using laser irradiated, heated diamond hemispherical shells. *Journal of Physics: Conference Series*, 244:022053, 2010.

T. Ostermayr. *Relativistically intense Laser-Microplasma Interactions*. PhD thesis, LMU München, 2017.

H. Paganetti. Range uncertainties in proton therapy and the role of monte carlo simulations. *Physics in Medicine & Biology*, 57(11):R99, 2012.

K. Parodi, H. Paganetti, E. Cascio, J. B. Flanz, A. A. Bonab, N. M. Alpert, K. Lohmann, and T. Bortfeld. PET/CT imaging for treatment verification after proton therapy: A study with plastic phantoms and metallic implants. *Medical Physics*, 34(2):419–435, 2007.

I. J. Paterson, R. J. Clarke, N. C. Woolsey, and G. Gregori. Image plate response for conditions relevant to laser–plasma interaction experiments. *Measurement Science and Technology*, 19(9):095301, 2008.

C. Patrignani et al. Review of Particle Physics. *Chinese Physics C*, 40(10):100001, 2016.

F. Pegoraro, T. Esirkepov, and S. Bulanov. Special relativity in action in laser produced plasmas. *Physics Letters A*, 347(1):133 – 142, 2005.

G. Pellegrini, F. García, J. Balbuena, E. Cabruja, M. Lozano, R. Orava, and M. Ullan. pages 115–118, 05 2009.

P. Pemler, J. Besserer, J. de Boer, M. Dellert, C. Gahn, M. Moosburger, U. Schneider, E. Pedroni, and H. Stäuble. A detector system for proton radiography on the gantry of the Paul-Scherrer-Institute. *Nuclear Instruments and Methods in Physics Research Section A: Accelerators, Spectrometers, Detectors and Associated Equipment*, 432(2): 483 – 495, 1999.

A. Picciotto, J. Krása, L. Láska, K. Rohlena, L. Torrisi, S. Gammino, A. Mezzasalma, and F. Caridi. Plasma temperature and ion current analysis of gold ablation at different laser power rates. *Nuclear Instruments and Methods in Physics Research Section B: Beam Interactions with Materials and Atoms*, 247(2):261 – 267, 2006.

M. N. Polyanskiy. Refractive index database. `https://refractiveindex.info`. Accessed on 2018-06-08.

M. Povoli, E. Alagoz, A. Bravin, I. Cornelius, E. Bräuer-Krisch, P. Fournier, T. E. Hansen, A. Kok, M. Lerch, E. Monakhov, et al. Thin silicon strip detectors for beam monitoring in micro-beam radiation therapy. *Journal of Instrumentation*, 10(11):P11007, 2015.

A. Poye, S. Hulin, M. Bailly-Grandvaux, J.-L. Dubois, J. Ribolzi, D. Raffestin, M. Bardon, F. Lubrano-Lavaderci, E. D'Humières, J. Jorge Santos, P. Nicolaï, and V. Tikhonchuk. Physics of giant electromagnetic pulse generation in short pulse laser experiments. *Physical Review E*, 91:043106, 2015.

R. Prasad, D. Doria, S. Ter-Avetisyan, P. S. Foster, K. E. Quinn, L. Romagnani, C. M. Brenner, J. S. Green, P. Gallegos, M. J. V. Streeter, et al. Calibration of thomson

parabola—mcp assembly for multi-mev ion spectroscopy. *Nuclear Instruments and Methods in Physics Research Section A: Accelerators, Spectrometers, Detectors and Associated Equipment*, 623(2):712 – 715, 2010.

D. L. Presti, D. Bonanno, F. Longhitano, D. Bongiovanni, G. Russo, E. Leonora, N. Randazzo, S. Reito, V. Sipala, and G. Gallo. Design and characterisation of a real time proton and carbon ion radiography system based on scintillating optical fibres. *Physica Medica*, 32(9):1124 – 1134, 2016.

PTCOG. Particle therapy co-operative group. `https://www.ptcog.ch`. Accessed on 2018-07-23.

M. Raytchev and J. Seco. Su-d-134-01: 3d proton radiography of simple inhomogeneities: Implications for tumor depth tracking. *Medical Physics*, 40:112–112, 2013.

S. Reinhardt. *Detection of laser–accelerated protons*. PhD thesis, LMU München, 2012.

S. Reinhardt, C. Granja, F. Krejci, and W. Assmann. Test of pixel detectors for laser-driven accelerated particle beams. *Journal of Instrumentation*, 6(12):C12030, 2011.

S. Reinhardt, W. Draxinger, J. Schreiber, and W. Assmann. A pixel detector system for laser-accelerated ion detection. *Journal of Instrumentation*, 8(03):P03008, 2013.

D. Rivas, A. Borot, D. E. Cardenas, G. Marcus, X. gu, D. Herrmann, J. Xu, J. Tan, D. Kormin, G. Ma, et al. Next generation driver for attosecond and laser-plasma physics. *Scientific Reports*, 7, 2017.

S. Roesler, R. Engel, and J. Ranft. *The Monte Carlo Event Generator DPMJET-III*, page 1033. 2001.

L. Rohrer, H. Jakob, K. Rudolph, and S. J. Skorka. The 4 gap double drift buncher at Munich. *Nuclear Instruments and Methods in Physics Research Section A: Accelerators, Spectrometers, Detectors and Associated Equipment*, 220(1):161–164, 1984.

T. Rösch. Private communication. 2018.

T. Rösch, P. Hilz, J. Bin, F. Englbrecht, Y. Gao, D. Haffa, J. Hartmann, S. Herr, F. Lindner, M. Speicher, et al. Considerations on employing a PMQ-doublet for narrow and broad proton energy distributions. *Current Directions in Biomedical Engineering*, 3, 2017.

H. H. Rossi and M. Zaider. *Microdosimetry and Its Applications*. Springer, 1996.

M. Roth, A. Blazevic, M. Geissel, T. Schlegel, T. E. Cowan, M. Allen, J.-C. Gauthier, P. Audebert, J. Fuchs, J. Meyer-ter Vehn, et al. Energetic ions generated by laser pulses: A detailed study on target properties. *Physical Review Special Topics: Accelerators and Beams*, 5:061301, 2002.

E. Rutherford. The scattering of alpha and beta particles by matter and the structure of the atom. *Philos. Mag.*, 21:669, 1911.

H. Ryu, E. Song, J. Lee, and J. Kim. Density and spatial resolutions of proton radiography using a range modulation technique. *Physics in Medicine & Biology*, 53(19):5461, 2008.

M. I. K. Santala, M. Zepf, F. N. Beg, E. L. Clark, A. E. Dangor, K. Krushelnick, M. Tatarakis, I. Watts, K. W. D. Ledingham, T. McCanny, et al. Production of radioactive nuclides by energetic protons generated from intense laser-plasma interactions. *Applied Physics Letters*, 78:19, 2001.

Y. Saraya, T. Izumikawa, J. Goto, T. Kawasaki, and T. Kimura. Study of spatial resolution of proton computed tomography using a silicon strip detector. *Nuclear Instruments and Methods in Physics Research Section A: Accelerators, Spectrometers, Detectors and Associated Equipment*, 735:485 – 489, 2014.

D. Schardt, T. Elsaesser, and D. Schulz-Ertner. Heavy-ion tumor therapy: Physical and radiobiological benefits. *Reviews of Modern Physics*, 82(1):383–425, 2010.

A. L. Schawlow and C. H. Townes. Infrared and optical masers. *Physical Review*, 112: 1940–1949, 1958.

S. Schell and J. J. Wilkens. Modifying proton fluence spectra to generate spread-out Bragg peaks with laser accelerated proton beams. *Physics in Medicine & Biology*, 54 (19):N459–N466, 2009.

C. Schinke, P. Christian Peest, J. Schmidt, R. Brendel, K. Bothe, M. R. Vogt, I. Kröger, S. Winter, A. Schirmacher, S. Lim, H. T. Nguyen, and D. MacDonald. Uncertainty analysis for the coefficient of band-to-band absorption of crystalline silicon. *AIP Advances*, 5(6):067168, 2015.

U. Schneider, E. Pedroni, and A. Lomax. The calibration of CT Hounsfield units for radiotherapy treatment planning. *Physics in Medicine & Biology*, 41(1):111, 1996.

U. Schneider, J. Besserer, P. Pemler, M. Dellert, M. Moosburger, E. Pedroni, and B. Kaser-Hotz. First proton radiography of an animal patient. *Medical Physics*, 31(5):1046–1051, 2004.

J. Schreiber, P. R. Bolton, and K. Parodi. Invited review article: "Hands-on" laser-driven ion acceleration: A primer for laser-driven source development and potential applications. *Review of Scientific Instruments*, 87(7):071101, 2016a.

J. Schreiber, P. R. Bolton, and K. Parodi. Laser-driven Ion Acceleration - The Role of Relativistic Laser-Plasma Engineering and Applications. G.I.T. Laboratory Journal 3-4/2016, 2016b.

H. Schwoerer, S. Pfotenhauer, O. Jäckel, K. U. Amthor, B. Liesfeld, W. Ziegler, R. Sauerbrey, K. W. D. Ledingham, and T. Z. Esirkepov. Laser-plasma acceleration of quasi-monoenergetic protons from microstructured targets. *Nature*, 439:445–448, 2006.

V. Scuderi, G. Milluzzo, A. Alejo, A. Amico, N. Booth, G. Cirrone, D. Doria, J. Green, S. Kar, G. Larosa, et al. Time of flight based diagnostics for high energy laser driven ion beams. *Journal of Instrumentation*, 12(03):C03086, 2017.

J. Seco, M. Oumano, N. Depauw, M. F Dias, R. P. Teixeira, and M. Spadea. Characterizing the modulation transfer function (MTF) of proton/carbon radiography using Monte Carlo simulations. *Medical Physics*, 40:091717, 2013.

F. H. Séguin, J. A. Frenje, C. K. Li, D. G. Hicks, S. Kurebayashi, J. R. Rygg, B.-E. Schwartz, R. D. Petrasso, S. Roberts, J. M. Soures, et al. Spectrometry of charged particles from inertial-confinement-fusion plasmas. *Review of Scientific Instruments*, 74 (2):975–995, 2003.

R. A. Snavely et al. Intense High-Energy Proton Beams from Petawatt-Laser Irradiation of Solids. *Physical Review Letters*, 85:2945–2948, 2000.

J. Son, C. H. Lee, J. Kang, D.-Y. Jang, J. Park, Y. H. Kim, Y. K. Kim, C. I. Choi, I. J. Kim, I. W. Choi, et al. Fine phantom image from laser-induced proton radiography with a spatial resolution of several μm. *Journal of the Korean Physical Society*, 65(1): 6–11, 2014.

M. Speicher, D. Haffa, M. A. O. Haug, J. Bin, Y. Gao, J. Hartmann, P. Hilz, C. Kreuzer, F. H. Lindner, T. M. Ostermayr, et al. Integrated double-plasma-mirror targets for contrast enhancement in laser ion acceleration. 2018. (accepted for publication).

H. Spieler. *Semiconductor Detector Systems*. Series on Semiconductor Science and Technology. OUP Oxford, 2005.

D. Strickland and G. Mourou. Compression of amplified chirped optical pulses. *Optics Communications*, 55(6):447 – 449, 1985.

D. Swanson. *Plasma Waves*. Elsevier Science, 2012.

K. Takahashi, K. Kohda, J. Miyahara, Y. Kanemitsu, K. Amitani, and S. Shionoya. Mechanism of photostimulated luminescence in BaFX: Eu2+ (X = Cl, Br) phosphors. *Journal of Luminescence*, 31:266–268, 1984.

A. Taroni and G. Zanarini. Space charge limited currents in p-n junctions. *Journal of Physics and Chemistry of Solids*, 30(7):1861 – 1871, 1969a.

A. Taroni and G. Zanarini. Plasma effects and charge collection time in solid state detectors. *Nuclear Instruments and Methods*, 67(2):277 – 282, 1969b.

J. T. Taylor, P. P. Allport, G. L. Casse, N. A. Smith, I. Tsurin, N. M. Allinson, M. Esposito, A. Kacperek, J. Nieto-Camero, T. Price, and C. Waltham. Proton tracking for medical imaging and dosimetry. *Journal of Instrumentation*, 10:C02015, 02 2015.

M. Testa, J. M. Verburg, M. Rose, C. H. Min, S. Tang, E. H. Bentefour, H. Paganetti, and H.-M. Lu. Proton radiography and proton computed tomography based on time-resolved dose measurements. *Physics in Medicine & Biology*, 58(22):8215, 2013.

J. J. Thomson. LXXXIII. Rays of positive electricity. *The London, Edinburgh, and Dublin Philosophical Magazine and Journal of Science*, 20(118):752–767, 1910.

V. T. Tikhonchuk. Physics of laser-assisted ion acceleration. *Nuclear Instruments and Methods in Physics Research Section A: Accelerators, Spectrometers, Detectors and Associated Equipment*, 620(1):1 – 13, 2010.

P. A. Tipler and R. Llewellyn. *Modern Physics*. W. H. Freeman, 2003.

C. A. Tobias, J. H. Lawrence, J. L. Born, R. K. McCombs, J. E. Roberts, H. O. Anger, B. V. A. Low-Beer, and C. B. Huggins. Pituitary irradiation with high-energy proton beams a preliminary report. *Cancer Research*, 18(2):121–134, 1958.

L. Torrisi. Coulomb-Boltzmann-Shifted distribution in laser-generated plasmas from 10^{10} up to 10^{19}W/cm^2 intensities. *Radiation Effects and Defects in Solids*, 171(1-2):34–44, 2016.

L. Torrisi, M. Cutroneo, G. Ceccio, A. Cannavò, D. Batani, G. Boutoux, K. Jakubowska, and J. Ducret. Near monochromatic 20 mev proton acceleration using fs laser irradiating au foils in target normal sheath acceleration regime. *Physics of Plasmas*, 23:043102, 04 2016.

L. T. Tran. *Advanced semiconductor silicon detector for dosimetry and microdosimetry in radiation protection and hadron therapy*. PhD thesis, University of Wollongong, Australia, 2014.

L. T. Tran, D. Prokopovich, M. Petasecca, M. Lerch, A. Kok, A. Summanwar, T.-E. Hansen, C. Da Via, M. I. Reinhard, and A. B. Rosenfeld. 3d Radiation Detectors: Charge Collection Characterisation and Applicability of Technology for Microdosimetry. *IEEE Transactions on Nuclear Science*, 61:1537–1543, 03 2014.

L. T. Tran, L. Chartier, D. Bolst, D. A. Prokopovich, S. Guatelli, M. Nancarrow, M. I. Reinhard, M. Petasecca, M. L. F. Lerch, V. L. Pereverlaylo, et al. 3d Silicon Microdosimetry and RBE Study Using C-12 Ion of Different Energies. *IEEE Transactions on Nuclear Science*, 62(6, 1):3027–3033, 2015a.

L. T. Tran, L. Chartier, D. A. Prokopovich, M. I. Reinhard, M. Petasecca, S. Guatelli, M. L. F. Lerch, V. L. Perevertaylo, M. Zaider, N. Matsufuji, et al. 3d-Mesa "Bridge"

Silicon Microdosimeter: Charge Collection Study and Application to RBE Studies in C-12 Radiation Therapy. *IEEE Transactions on Nuclear Science*, 62(2):504–511, 2015b.

L. T. Tran, L. Chartier, D. Bolst, A. Pogossov, S. Guatelli, M. Petasecca, M. L. F. Lerch, D. A. Prokopovich, M. I. Reinhard, B. Clasie, et al. Characterization of proton pencil beam scanning and passive beam using a high spatial resolution solid-state microdosimeter. *Medical Physics*, 44(11):6085–6095, 2017.

D. Turecek, T. Holy, J. Jakubek, S. Pospisil, and Z. Vykydal. Pixelman: a multi-platform data acquisition and processing software package for Medipix2, Timepix and Medipix3 detectors. *Journal of Instrumentation*, 6(01):C01046, 2011.

P. Vavilov. Ionization losses of high-energy heavy particles. *Soviet Physics - JETP*, 5: 749–751, 01 1957.

V. I. Veksler. The principle of coherent acceleration of charged particles. *The Soviet Journal of Atomic Energy*, 2(5):525–528, 1957.

V. Vlachoudis. FLAIR: A Powerful But User Friendly Graphical Interface For FLUKA. In *Proc. Int. Conf. on Mathematics, Computational Methods & Reactor Physics (M&C 2009)*, 2009.

S. Waheed, J. M. Cabot, N. P. Macdonald, T. Lewis, R. M. Guijt, B. Paull, and M. C. Breadmore. 3d printed microfluidic devices: enablers and barriers. *Lab Chip*, 16:1993–2013, 2016.

S. C. Wilks, A. B. Langdon, T. E. Cowan, M. Roth, M. Singh, S. Hatchett, M. H. Key, D. Pennington, A. MacKinnon, and R. A. Snavely. Energetic proton generation in ultra-intense laser–solid interactions. *Physics of Plasmas*, 8(2):542–549, 2001.

D. C. Williams. The most likely path of an energetic charged particle through a uniform medium. *Physics in Medicine & Biology*, 49(13):2899, 2004.

R. R. Wilson. Radiological Use of Fast Protons. *Radiology*, 47(5):487–491, 1946.

T. Wittmann, J. P. Geindre, P. Audebert, R. S. Marjoribanks, J. P. Rousseau, F. Burgy, D. Douillet, T. Lefrou, K. T. Phuoc, and J. P. Chambaret. Towards ultrahigh-contrast ultraintense laser pulses—complete characterization of a double plasma-mirror pulse cleaner. *Review of Scientific Instruments*, 77(8):083109, 2006.

J. L. Wiza. Microchannel plate detectors. *Nuclear Instruments and Methods*, 162(1):587 – 601, 1979.

M. Würl. *Towards Offline PET Monitoring at a Cyclotron-Based Proton Therapy Facility: Experiments and Monte Carlo Simulations*. BestMasters. Springer Fachmedien Wiesbaden, 2016.

M. Würl, S. Reinhardt, A. Rosenfeld, M. Petasecca, M. Lerch, L. Tran, S. Karsch, W. Assmann, J. Schreiber, and K. Parodi. Experimental studies with two novel silicon detectors for the development of time-of-flight spectrometry of laser-accelerated proton beams. *Journal of Physics: Conference Series*, 777(1):012018, 2017.

X-ray Imaging Europe GmbH. Private communication. 2018.

A. Yogo, H. Daido, A. Fukumi, Z. Li, K. Ogura, A. Sagisaka, A. S. Pirozhkov, S. Nakamura, Y. Iwashita, T. Shirai, et al. Laser prepulse dependency of proton-energy distributions in ultraintense laser-foil interactions with an online time-of-flight technique. *Physics of Plasmas*, 14(4):043104, 2007.

R. Zhang and W. D. Newhauser. Calculation of water equivalent thickness of materials of arbitrary density, elemental composition and thickness in proton beam irradiation. *Physics in Medicine & Biology*, 54(6):1383, 2009.

P. Zygmanski, K. P. Gall, M. S. Z. Rabin, and S. J. Rosenthal. The measurement of proton stopping power using proton-cone-beam computed tomography. *Physics in Medicine & Biology*, 45(2):511, 2000.

Danksagung

209